



High Temperature Corrosion in Waste-to-Energy Plants

A Thesis Submitted to
The University of Sheffield

By
Awassada Phongphiphat, B.Eng M.Eng

For the degree of Doctor of Philosophy
Project Supervisors:
Professor V.N. Sharifi and Professor J. Swithenbank

Department of Chemical and Process Engineering
The University of Sheffield

July 2008

SUMMARY

High temperature corrosion of the heat exchanger materials is the important factor that limits the efficiency of various energy systems. The problem becomes more serious when fuels containing alkali metal, heavy metals, chlorine, and sulphur are used. In combustion systems utilizing biomass and municipal solid waste, the steam temperatures are kept lower than 450°C in order to avoid the corrosion problems. This results in low overall plant efficiencies (e.g. 25 – 30%). Therefore, methods to prevent or control high temperature corrosion in these plants must be investigated.

The overall objectives of this PhD research study were to investigate (i) the factors affecting the high temperature corrosion in waste to energy plants and, (ii) to explore and test corrosion control methods in the real furnace conditions.

The experimental program was carried out at a UK waste to energy plant. Two air-cooled sampling probes were designed and placed at different locations in the furnace in order to simulate the corrosion process taking place on the superheater tubes and also to collect the deposits of combustion residues. Sampling probe sections were fabricated from different types of superalloys and were equipped with two corrosion control methods; sacrificial baffle and aluminide coated alloy. After approximately 800 hours of exposure to hot flue gas having temperature range of 730 – 813°C, each probe was carefully disassembled and analysed. Our study showed that both ‘temperature’ and ‘particle deposition’ had great effects on the high temperature corrosion inside this plant. Damages due to hot corrosion were significantly magnified when the metal surface temperature range (modelling results) increased from 363 – 440°C to 404 – 495°C. Tests showed that sulphates and chlorides of alkali metals (namely calcium, sodium, and potassium) and heavy metals (namely zinc, lead, and arsenic) were the main contributors to the hot corrosion. In this particular environment, tubes made of nickel based alloys were found to have higher corrosion resistance than iron based alloys. Test showed that

aluminide coating on the tube surfaces could significantly improve their corrosion resistance.

In addition, mathematical modelling using FLUENT code was carried out in order to simulate the flow characteristics and heat transfer inside the furnace and the region around the air cooled sampling probes. Results from the modelling corresponded with the plant information and explained the experimental results very well.

This PhD study has yielded valuable information that can be used by the operators of waste-to-energy plants. Our study showed that ‘aluminide coating’ is a promising corrosion control technique for superheater materials in the waste-to-energy plants. The coating is relatively cheap and simple but it can significantly increase the corrosion resistance of materials.

ACKNOWLEDGEMENT

First of all, I would like to thank my supervisors, Prof. Vida Sharifi and Prof. Jim Swithenbank, for their kind support, valuable advices, and great understanding throughout this study. I would also like to thank Dr. Adrian Leyland, Dr. Changkook Ryu, and Dr. Yao Bin Yang for their willingness to contribute time and guidance for all these years.

I would like to thank UK Engineering and Physical Science Research Council (EPSRC) and the Royal Thai Government for their financial support for this work. I really appreciate the UK incineration industry for providing chances for this study and following technical support. My experiment was successfully conducted with helps from a lot of experienced industrial staffs.

The achievement would have been much more difficult without helps and unlimited patience from staffs and students in the 'Department of Chemical and Process Engineering', 'Department of Engineering Materials', 'Department of Chemistry' at the University of Sheffield, and 'Materials and Engineering Research Institute' at Sheffield Hallam University. Special thanks to Prof. Bernard B Argent, Prof. Peter Styring, Dr. Hailiang Du, Dr. Injeti Gurrappa, Dr. Adrian Duncliff, Dr. Peter Korgul, Dr. Alan Cox, Dr. Gavin Reynolds, Dr. Tze Chean Ooi, Dr. David Poole, Dr. Nigel Russell, Dr. Catherine Shields, Dr. Hywel Jones, Andrew Ganguly, Gary Parsons, James Alice, Nigel Storey, Jakkaphol Phengpan, Jenny Louth, Johnny Wright, Kel Win Chua, Philip Staton, Maria Soto, Stuart Richards, and Oz McFarlane.

Last but not least, I would like to thank my beloved family and Winson Chung for their constant love, endless support and encouragement. Thank you for always be there for me and believe in me.

TABLE OF CONTENTS

	Page No.
Summary.....	i
Acknowledgements.....	iii
Table of Contents.....	iv
List of Figures.....	x
List of Tables.....	xvi
Nomenclature.....	xx
CHAPTER 1 INTRODUCTION.....	1
1.1 Biomass and Waste: Potential Sources of Renewable Energy	1
1.2 Overview: Degradation and Corrosion of Materials.....	3
1.2.1 Corrosion of Metals	3
1.2.2 Safety & Environmental Impacts.....	4
1.2.3 Economic Impact	4
1.2.4 UK Regulations and Standards Related to Corrosion.....	5
1.3 High Temperature Corrosion in the Energy Systems	6
1.4 Control Methods for High Temperature Corrosion	7
1.5 Problem Statement.....	7
1.6 Research Objectives.....	8
1.7 Layout of the Thesis.....	9
CHAPTER 2 LITERATURE REVIEW	11
2.1 Modes of High Temperature Corrosion and Degradation	11
2.1.1 Oxidation	11
2.1.2 Corrosion in Mixed Oxidants	12
2.1.3 Accelerated Corrosion Induced by Deposits	13
2.1.4 Erosion – Corrosion.....	17

2.2	High Temperature Corrosion in Energy Systems	17
2.2.1	Oil-Fired Boilers	17
2.2.2	Coal-Fired Energy Systems	18
2.2.3	Gas Turbines	21
2.2.4	Black Liquor Boilers.....	22
2.2.5	Nuclear Reactors.....	22
2.3	Energy Recovery Facilities Using Biomass and Waste	23
2.3.1	Corrosion Sensitive Areas	23
2.3.2	Typical Material Used for Superheater Tubes	24
2.4	High Temperature Corrosion in Biomass Power Plants	26
2.5	High Temperature Corrosion in Waste to Energy Plants.....	31
2.6	Evaluation of Corrosion Damage.....	39
2.7	Methods for Preventing or Controlling Metallic Corrosion	40
2.7.1	Corrosion Prevention Techniques.....	40
2.7.2	Corrosion Control by Coatings and Surface Modification	40
2.8	Summary	45
CHAPTER 3 THEORETICAL CONSIDERATION.....		46
3.1	Mechanisms of Fly Ash Formation.....	46
3.2	Deposition Mechanisms.....	49
3.2.1	Principal Mechanisms for Particle Deposition	50
3.2.2	Slagging and Fouling	51
3.3	Heat Transfer through Deposits	52
3.4	Electrochemical Corrosion Reactions.....	57
3.5	Forms of Metallic Corrosion.....	58
3.5.1	Uniform Corrosion (General Corrosion)	58
3.5.2	Galvanic Corrosion (or Dissimilar metal Corrosion)	60
3.5.3	Intergranular Corrosion	60
3.5.4	Crevice Corrosion.....	60
3.5.5	Pitting Corrosion.....	61
3.5.6	Selective Leaching.....	62
3.5.7	Erosion-Corrosion.....	62
3.5.8	Stress Corrosion.....	62

3.6	Analytical Methods for Deposits and Corrosion	62
3.6.1	Scanning Electron Microscopy and Energy Dispersive Spectroscopy (SEM/EDS)	62
3.6.2	X-Ray Diffraction.....	64
3.6.3	Simultaneous Thermal Analysis (STA).....	64
3.6.4	High Temperature Light Microscopy (HTLM)	65
3.6.5	Inductively Coupled Plasma Optical Emission Spectrometry (ICP-OES).....	65
CHAPTER 4 EXPERIMENTAL PROGRAM AND ANALYTICAL METHODOLOGY.....		66
4.1	Overview.....	66
4.2	Experimental Program at a UK Waste to Energy Plant.....	66
4.2.1	Description of the Plant	66
4.2.2	Calculations for heat transfer rate of superheater tubes and sampling probes	75
4.2.3	Locations in the furnace of the sampling probes	77
4.2.4	Fabrication of sampling probes and data logger.....	78
4.2.5	Technical data of metal alloys	83
4.2.6	Aluminide pack cementation coating procedure	86
4.2.7	The installation and the operation of sampling probes	87
4.2.8	Other collection points of combustion residues.....	88
4.3	Analytical Methodology for Combustion Residues and Deposits.....	89
4.3.1	Full elemental analysis	89
4.3.2	Differential Thermal Analysis	90
4.3.3	Crystalline phase study	91
4.3.4	Microstructure analysis.....	92
4.3.5	Corrosion rate measurement	94
4.3.6	Grain boundary analysis	95
4.3.7	Errors in analytical methods	96
CHAPTER 5 EXPERIMENTAL RESULTS		97
5.1	Identification of Samples from the Sampling Probes	97
5.2	Temperature Measurement by using an Air-cooled Suction Pyrometer.....	99

5.3	Temperature of cooling air inside the sampling probes.....	99
5.4	Sampling Probes after the Experiment	103
5.4.1	Sampling Probe No.1	103
5.4.2	Sampling Probe No.2.....	109
5.5	Physical Characteristics of Other Combustion Residues.....	114
5.6	Elemental Composition of the Probe Deposits and Other Combustion Residues	117
5.6.1	Combustion Residues	117
5.6.2	Deposit on Probes	122
5.6.3	Corrosion Products	127
5.7	Phase Study by Using X-Ray Diffractometer	131
5.8	Phase Transformation Study of Deposits and Other Combustion Residues	134
5.9	Corrosion Rates of Metal Alloy Samples	137
5.10	Grain Boundary Study of Metal Alloy Samples	140
5.11	Morphology and Elemental Composition of Corrosion Products and Alloy Samples	145
5.11.1	Results for Alloy 59.....	145
5.11.2	Results for the Coated Coupon of Alloy 59.....	148
5.11.3	Results for Alloy 625.....	154
5.11.4	Results for Alloy 556.....	156
5.11.5	Results for the Coated Coupons of Alloy 310	159
5.11.6	Results for Alloy 316 (Baffle).....	164
CHAPTER 6 3-DIMENSIONAL MODELLING OF THE FURNACE AND THE SAMPLING PROBES		166
6.1	Overview.....	166
6.2	FLUENT code modelling	167
6.3	Three-dimensional modelling of the furnace.....	168
6.3.1	Model description	168
6.3.2	Input data	169
6.3.3	Results: Velocity.....	171
6.3.4	Results: Temperature	173
6.3.5	Results: Chemical species of gases.....	173

6.3.6	Validity of the modelling results	174
6.4	Three-dimensional modelling of the sampling probe No.1	176
6.4.1	Model description	176
6.4.2	Input data	177
6.4.3	Results: Velocity.....	178
6.4.4	Results: Temperature	180
6.5	Three-dimensional modelling of the sampling probe No.2	185
6.5.1	Model description	185
6.5.2	Input data	187
6.5.3	Results: Velocity.....	187
6.5.4	Results: Temperature	189
6.6	Two-dimensional modelling of the sampling probe	194
6.6.1	Effects of welded sacrificial baffles.....	194
6.6.2	Effects of the particle size on the particle trajectory	196
6.7	Summary of the results from sampling probe models	198
CHAPTER 7 OVERALL DISCUSSION		201
7.1	Flue Gas Characteristics in the Superheater Areas	201
7.2	Characterization of the Combustion Residues and the Probe Deposits.....	202
7.3	Effects of Gas Stream Characteristics, Deposition and Alloy Temperatures.....	204
7.3.1	Gas Stream Characteristics and Deposition.....	204
7.3.2	Deposit and Alloy Temperatures	205
7.4	Effects of Heat Transfer Materials (Alloy 59, 556 and 625).....	207
7.4.1	Morphology of the Corroded Areas.....	207
7.4.2	Corrosion Rates	207
7.4.3	Overall Performance for Corrosion Resistance	208
7.4.4	Corrosion Products and Corrosion Mechanisms	209
7.5	Corrosion control by aluminum pack cementation.....	211
7.5.1	Aluminide Coating on Alloy 59	211
7.5.2	Aluminide Coating on Stainless Steel 310	212
7.6	Corrosion control by using sacrificial baffles.....	213
7.7	Problems and Errors.....	214

CHAPTER 8 CONCLUSIONS AND RECOMMENDATIONS FOR FUTURE	
WORK.....	215
8.1 Conclusions.....	215
8.1.1 Conditions of Flue Gas at the Sampling Points.....	215
8.1.2 Temperatures of Sampling Probes.....	216
8.1.3 Characterization of Deposits.....	216
8.1.4 Corrosion Products	217
8.1.5 Effects of Flue Gas Characteristics, Deposition and Alloy	
Temperatures	217
8.1.6 Effects of Heat Transfer Materials	218
8.1.7 Corrosion Control by Aluminide Pack Cementation.....	218
8.1.8 Corrosion Control by Using Sacrificial Baffles.....	219
8.2 Recommendations for Furture work	219
References.....	221
Appendix A: Chemical Composition of Various Engineering Alloys.....	A-1
Appendix B: Calculation for Heat Transfer and Surface Temperature.....	B-1
Appendix C: Corrosion Rates Measurement.....	C-1
Appendix D: List of Publications and Presentations.....	D-1

LIST OF FIGURES

	Page No.
Figure 1.1 The growth of renewable energy by technology (GWh/year) in European Countries.....	2
Figure 1.2 Distribution of corrosion costs for the United States in 1998.....	5
Figure 2.1 Schematic diagram showing the principal modes of high-temperature corrosion	12
Figure 2.2 The thermodynamically stable species of potassium in wheat straw combustion	14
Figure 2.3 Stability diagram of Fe-Cr-Ni-O-Cl at 727oC.....	14
Figure 2.4 Stability diagram of Fe-Ni-Cr-Mo-O-Cl at 500oC	14
Figure 2.5 Pathways of K, S, and Cl in a biomass power plant system	27
Figure 2.6 Corroded metal coupons covered under KCl and KSO ₄ : (a) SEM image, (b) schematic diagram.....	28
Figure 2.7 Main factors controlling the particle deposition and the corrosion rate on a heat recovery tube	33
Figure 2.8 Scale structure and corrosion mechanisms in Ni-Cr-Mo-(Nb, Fe) alloy	35
Figure 2.9 Summary of scale structure and corrosion reaction.....	37
Figure 2.10 The SEM image of deposits and corrosion products formed on 15Mo ₃ at 456oC	39
Figure 2.11 Aluminized HH309 stainless steel: (a) cross-sectional image, (b) concentration profiles of Al, Cr, Fe and Ni	42
Figure 3.1 Mechanisms of fly ash formation in the coal combustion processes	47
Figure 3.2 Mechanisms of fly ash formation in the woody biomass combustion processes	49
Figure 3.3 Typical structure of a fouling deposit.....	52
Figure 3.4 Heat transfer to and through ash deposits.....	54

Figure 3.5	Expected trends in deposit properties during their growth.....	56
Figure 4.1	Diagram showing the components of the waste-to-energy plant.....	68
Figure 4.2	Schematic diagram of the furnace (side view) and locations of 2 sampling probes	69
Figure 4.3	Motion of the Martin reverse-acting grate system.....	70
Figure 4.4	Superheater tube panels	72
Figure 4.5	C-shape sacrificing shields encasing superheater tubes	72
Figure 4.6	An overlay-welded superheater tube	72
Figure 4.7	Viewing port at the location of probe No.1	78
Figure 4.8	An opening hole after the viewing port was removed.	78
Figure 4.9	Gantry to the location of probe NO.1	78
Figure 4.10	Inner side of the wall at the location of probe No.1	78
Figure 4.11	Drawings of probe No.1 (top) and probe No.2 (bottom).....	79
Figure 4.12	Details of alloy rings, baffle, covering plate and connector flange	80
Figure 4.13	Sampling probe No.1 and the data logger before the experiment.	83
Figure 4.14	Installation of the sampling probe No.1.....	87
Figure 4.15	Data logger in operation	87
Figure 4.16	Operating sampling probe (No.1).....	87
Figure 4.17	Philips PW1710 Reflection Diffractometer.....	92
Figure 4.18	Siemens D500 Reflection Diffractometer.....	92
Figure 4.19	PHOENIX 400 Sample Preparation System.....	93
Figure 4.20	EMITECH K950X Carbon Coater	93
Figure 4.21	Mounted samples of alloy ring: polished, painted, and carbon coated samples.	93
Figure 4.22	Summary of range and spatial resolution of backscattered electrons, secondary electrons, X-rays and Auger electrons produced from an electron microprobe-scanning electron microscope	94
Figure 5.1	Diagram of a sampling probe and the abbreviations used for referring to the samples or locations on the sampling probe	97
Figure 5.2	Temperature profile of air inside the sampling probes: (a) probe No.1, (b) probe No.2.....	100
Figure 5.3	Probe No.1 after being exposed to the hot gas: (a) 387 hours – front side, (b) 769 hours – front side, (c) 769 hours – rear side	104

Figure 5.4	Diagrams for the formation of deposits (yellow) and corrosion products (brown) on the metal rings of probe No.1.....	105
Figure 5.5	Probe No.1 after the test: (a) wall/rear, (b) middle/rear, (c) end/rear	107
Figure 5.6	Baffles of probe No.1 after the test: (a) wall/rear, (b) end/rear	107
Figure 5.7	Probe No.1 after the test: (a) 2inch tube – rear, (b) baffle end – front, (c) end/bottom.....	108
Figure 5.8	Probe No.2 after being exposed to the hot gas: (a) 284 hours, (b) 811 hours.....	110
Figure 5.9	Probe No.2 after the test: (a) 1inchW and baffle wall – front, (b) wall/front, (c) 1inchM1 and coated coupons – front, (d) middle/front, (e) end/front, (f) 1inchE, coated coupons, baffle end - front	112
Figure 5.10	Combustion residues collected from the furnace: (a) BA, (b) SL1, (c) SL2, (d) SL2+Wh, (e) SL3, (f) SL3+Wh, (g) SH, (h) EC, (i) APC.....	115
Figure 5.11	XRD analysis for alloy rings and aluminide coated alloys.....	132
Figure 5.12	The results of Differential Thermal Analysis (DTA) for samples of combustion residues and probe deposits.	136
Figure 5.13	Corroded length (μm) of alloy rings from the sampling probes: (a) sampling probe No.1, (b) sampling probe No.2	137
Figure 5.14	Comparison of corrosion rate of alloy rings from the sampling probes (mm/year).....	139
Figure 5.15	Cross-sectional images of alloy 59 and its grain boundary structure.	142
Figure 5.16	Cross-sectional images of alloy 625 and its grain boundary structure.	143
Figure 5.17	Cross-sectional images of alloy 556 and its grain boundary structure.	144
Figure 5.18	Back scattered electron image of alloy 59: SP1 - end/top.....	145
Figure 5.19	Corrosion products of alloy 59: SP1 – end/top: (a) back scattered electron image, (b) elemental composition results	146

Figure 5.20	Elemental mapping of alloy 59 and its corrosion products: SP1 – end/top	146
Figure 5.21	Line scan results of alloy 59: (a) SP1 – end/bottom, (b) SP2 – end/top, (c) SP2 – end/bottom	147
Figure 5.22	Elemental mapping of coated alloy 59 and its corrosion products: SP2 - end/top.....	149
Figure 5.23	Elemental mapping of coated alloy 59 and its corrosion products: SP2 - wall/top.....	149
Figure 5.24	Results of line scan and point scanning for coated alloy 59: SP2 - end/top	150
Figure 5.25	Line scan results of coated alloy 59: (a) SP2 - end/top, (b) & (c) SP2 - wall/top.....	151
Figure 5.26	Coated alloy 59: (a) SP2 - end/bottom, (b) SP2 - end/middle, (c) SP2 - end/top, (d) SP2 - wall/top	153
Figure 5.27	Elemental mapping of alloy 625 and its corrosion products: SP1 – end/top	154
Figure 5.28	Line scan results for alloy 625: SP2 – end/bottom	155
Figure 5.29	Elemental mapping of alloy 556 and its corrosion products: SP1 – end/top	156
Figure 5.30	Point scan results for alloy 556 and its corrosion products: SP1 – end/top	157
Figure 5.31	Line scan results for alloy 556: SP2 – end/top	158
Figure 5.32	Elemental mapping of coated steel310 and its corrosion products: (a) SP2 – end/top, (b) SP2 – wall/middle	160
Figure 5.33	Line scan results of coated steel 310: (a) & (b) SP2 – wall/middle, (c) SP2 – wall/bottom, (d) SP2 – end/middle	162
Figure 5.34	Coated steel 310: (a) end/middle, (b) end/bottom, (c) wall/top, (d) wall/middle	163
Figure 5.35	Backscattered electron images for stainless steel 316: SP1 - wall	164
Figure 5.36	Elemental mapping results for alloy 316: SP1 – end.....	165
Figure 6.1	Schematic diagram (side view) and dimension of the furnace model	170
Figure 6.2	Isometric view of the furnace model.	170

Figure 6.3	Input data for the furnace model: (a) temperature (K) of the combustion gaseous products, (b) velocity magnitude (m/s) of the combustion gaseous products.	171
Figure 6.4	Contours of velocity magnitude (m/s) of the gases in the furnace model	172
Figure 6.5	Velocity vectors coloured by the velocity magnitude (m/s) of the gases in the furnace model.....	172
Figure 6.6	Path lines coloured by the residence time (s) of the gases in the furnace model	173
Figure 6.7	Contours of temperature (K) of the gases in the furnace model	173
Figure 6.8	Contours of mole fractions of chemical species presented in the furnace model	175
Figure 6.9	Isometric view of the model 'sampling probe No.1 with deposit' created by GAMBIT software	177
Figure 6.10	Contours of velocity magnitude (m/s) of the model 'sampling probe No.1'	179
Figure 6.11	Velocity vector, coloured by the velocity magnitude (m/s) of the flow across the model 'sampling probe No.1'	179
Figure 6.12	Contours of temperature (K) of the model 'sampling probe No.1'	180
Figure 6.13	Contours of temperature (K) of the model 'sampling probe No.1' at various cross-sections	181
Figure 6.14	Surface temperature (K) of alloy 59 rings in the model 'sampling probe No.1'	182
Figure 6.15	Surface temperature (K) of alloy 556 rings in the model 'sampling probe No.1'	182
Figure 6.16	Surface temperature (K) of alloy 625 rings in the model 'sampling probe No.1'	183
Figure 6.17	Surface temperatures (K) of deposits in the model 'sampling probe No.1'	185
Figure 6.18	Isometric view of the model 'sampling probe No.2 with deposits' created by GAMBIT software	186
Figure 6.19	Contours of velocity magnitude (m/s) of the model 'sampling probe No.2'	188

Figure 6.20	Velocity vector, coloured by the velocity magnitude (m/s) of the flow across the model 'sampling probe No.2'	188
Figure 6.21	Contour of temperature (K) of the model 'sampling probe No.2'	189
Figure 6.22	Contour of temperature (K) of the model 'sampling probe No.2' at various cross-sections	190
Figure 6.23	Surface temperature (K) of alloy 59 rings in the model 'sampling probe No.2'	191
Figure 6.24	Surface temperature (K) of alloy 556 rings in the model 'sampling probe No.2'	191
Figure 6.25	Surface temperature (K) of alloy 625 rings in the model 'sampling probe No.2'	191
Figure 6.26	Surface temperatures (K) of deposits in model 'sampling probe No.2'	193
Figure 6.27	Velocity vectors of the flow passing the baffle for 2-D modelling	196
Figure 6.28	Temperature contour of the tube and connected baffle for 2-D modelling	196
Figure 6.29	Particle tracks coloured by particle residence time: particles with diameter of 1 μm	197
Figure 6.30	Particle tracks coloured by velocity magnitude: particles with diameter of 1 μm	197
Figure 6.31	Particle tracks coloured by particle residence time: particles with diameter of 10 μm	197
Figure 6.32	Particle tracks coloured by velocity magnitude: particles with diameter of 10 μm	197
Figure 6.33	Particle tracks coloured by particle residence time: particles with diameter of 100 μm	197
Figure 6.34	Particle tracks coloured by velocity magnitude: particles with diameter of 100 μm	197

LIST OF TABLES

	Page No.
Table 2.1	Melting temperature (T_m) and the temperatures that chloride vapours equal to 10^{-4} atm (T_4) of various metal chlorides..... 15
Table 2.2	Melting temperatures for different species and binary mixtures 16
Table 2.3	Operating conditions and modes of corrosion/degradation for component materials in coal-fired systems..... 20
Table 2.4	Key variables and limiting step of material corrosion/degradation in coal-fired systems 20
Table 2.5	Comparison of corrosion and degradation problems (surface oriented problems) for gas turbine applications..... 21
Table 2.6	Operating conditions of boiler components in a WTE plant in the Netherlands. 23
Table 2.7	Chemical composition (wt%) of material commonly used in the fabrication of superheater tubes in biomass and waste derived energy systems 25
Table 2.8	Biomass fuel properties (the unit is in wt% unless indicated otherwise; elemental compositions is on a dry basis)..... 26
Table 2.9	Experience on corrosion rates for boilers components of Dutch WTE plants 33
Table 3.1	Potential mechanisms for the formation of fouling and slagging 53
Table 3.2	Suggested chemical classification developed by CHEC 63
Table 4.1	Designs of over-fire air nozzles 71
Table 4.2	Typical plant emissions compared with Environment Agency permit limits..... 74
Table 4.3	Input parameters used in calculations of heat transfer and surface temperature 76
Table 4.4	Results of calculation for heat transfer and surface temperature 76
Table 4.5	Locations and relative distances of points of interest in the furnace 77

Table 4.6	Typical chemical composition of metal alloy regarded in this study (wt%).....	84
Table 4.7	Samples of combustion residues: description and collection points.....	88
Table 4.8	List of samples and analysis program.....	89
Table 5.1	Description of the abbreviations used for referring to the samples or locations on the sampling probes.....	98
Table 5.2	Gas temperatures at the position of sampling probe No.2 - measured by an air-cooled suction pyrometer	99
Table 5.3	Average temperatures of air inside probe No.1 at different locations (°C)	102
Table 5.4	Average temperatures of air inside probe No.2 at different locations (°C)	102
Table 5.5	Modelled surface temperature values of metal and deposit at different locations on the sampling probes	103
Table 5.6	The thickness and position of scales at various locations on probe No.1.....	105
Table 5.7	Changes (%) in the thickness of alloy rings (measured by a vernier caliper) and the characteristics of corrosion products.	108
Table 5.8	The thickness of deposits and the availability of corrosion products at various locations on probe No.2.....	111
Table 5.9	Changes (%) in thickness of metal rings after deposits and spalled corrosion products were removed.....	114
Table 5.10	Elemental composition of 10 combustion residue samples (m/kg)	119
Table 5.11	Major elemental composition (>1%) of 10 samples of combustion residues (wt.%)	120
Table 5.12	Major molecular composition of 10 samples of combustion residues ($\times 10^{-3}$ mol/kg)	120
Table 5.13	The typical compounds found in fly ash collected from waste to energy plants	122
Table 5.14	Elemental composition of deposit collected from probe No.1 (mg/kg).....	123
Table 5.15	Major elemental composition (>1%) of the deposit collected from probe No.1 (wt.%)	124

Table 5.16	Major molecular composition of deposit collected from probe No.1 ($\times 10^{-3}$ mol/kg).....	124
Table 5.17	Elemental composition of deposit collected from probe No.2 (mg/kg).....	125
Table 5.18	Major elemental composition (>1%) of the deposit collected from probe No.2 (wt.%)	126
Table 5.19	Major molecular composition of deposit collected from probe No.2 ($\times 10^{-3}$ mol/kg).....	126
Table 5.20	Elemental composition of corrosion products (mg/kg)	128
Table 5.21	Major elemental composition (>1%) of the corrosion products (wt.%)	129
Table 5.22	Major molecular composition of corrosion products ($\times 10^{-3}$ mol/kg).....	129
Table 5.23	Crystalline substances detected in the scale/corrosion products of alloy samples.....	133
Table 5.24	Common minerals in solid residues from MSW combustion and their melting temperatures	135
Table 5.25	Average corrosion rates of alloy rings from sampling probe No.1	138
Table 5.26	Average corrosion rates of alloy rings from sampling probe No.2	138
Table 5.27	Elemental composition results of corrosion products of coated alloy 59: SP2 - end/top.....	150
Table 5.28	Elemental composition results for point scan of alloy 556: SP1 - end/top (atomic%).....	157
Table 5.29	Elemental composition results for point scan of alloy 556: SP1 - end/top (weight%).....	158
Table 6.1	Principal equations used in FLUENT code for the furnace and sampling probe models	168
Table 6.2	The chemical composition (by wt%) of the typical MSW in UK	170
Table 6.3	The proximate analysis results of the typical MSW in UK	170
Table 6.4	Comparison of results from the FLUENT modelling and the on-line recorded values	174
Table 6.5	Details of deposit thickness and their locations in the model 'sampling probe No.1'	177

Table 6.6	Physical and thermal properties of probe materials at 773 K.....	178
Table 6.7	Temperature (K/°C) of the air jet inside sampling probe No.1.....	181
Table 6.8	The average values of alloy surface temperatures from model 'sampling probe No.1' (K).....	183
Table 6.9	The average values of alloy surface temperatures from model 'sampling probe No.1' (°C).....	183
Table 6.10	The average values of deposit surface temperatures from the model 'sampling probe No.1'.....	185
Table 6.11	Details of deposit thickness and their locations in model 'sampling probe No.2'.....	186
Table 6.12	Temperature (K/°C) of the air jet inside the model 'sampling probe No.2'.....	190
Table 6.13	The average values of alloy surface temperatures from model 'sampling probe No.2' (K).....	192
Table 6.14	The average values of alloy surface temperatures from model 'sampling probe No.2' (°C).....	192
Table 6.15	The average values of deposit surface temperatures from model 'sampling probe No.2'.....	194
Table 6.16	Average temperatures on surface of tube equipped with a baffle in 2-D modelling (K).....	195
Table 6.17	Average temperatures of the air at different locations – comparison of 2 models (K).....	198
Table 6.18	Average temperatures of the air at different locations – comparison of 2 models (°C).....	198
Table 6.19	Temperatures of the metal surface at different locations – comparison of 2 models (K).....	198
Table 6.20	Temperatures of the metal surface at different locations – comparison of 2 models (°C).....	198
Table 6.21	Surface temperatures of the deposits at different locations – comparison of 2 models (K).....	199
Table 6.22	Surface temperatures of the deposits at different locations – comparison of 2 models (°C).....	199

NOMENCLATURE

Symbol	Description
A	Surface area; Cross-sectional area(m^2)
A	Stoichiometric coefficient
a	Radiation absorption coefficient (m^{-1})
$a_{\epsilon,i}$	Emissivity weighting factor for the i^{th} fictitious gray gas
b	Stoichiometric coefficient
C	Concentration ($kg\ m^{-3}$)
$C_{1\epsilon}, C_{2\epsilon}$	Model constant
C_p	Specific heat capacity at constant pressure ($J\ kg^{-1}\ K^{-1}$)
$[C_{j,r}]$	Molar concentration of species j in reaction r ($mol\ m^{-3}$)
D_e	Effective diffusion coefficient of gas A through the 'ash layer'
d	Spacing between the planes in the atomic lattice (m)
d_d	Sum of the tube diameter and the deposit thickness (m)
d_e	Inside diameter (m)
d_{io}	Outer tube diameter (m)
E	Total energy, activation energy (J, kJ, cal, Btu)
ϵ	Turbulent dissipation rate ($m^2\ s^{-3}$)
\bar{F}	Force vector (N)
\bar{g}	Gravitational acceleration ($m\ s^{-2}$); standard values = $9.80665\ m^2\ s^{-1}$
H	Enthalpy of formation ($J\ kg^{-1}$)
h_i	Convection heat transfer coefficient inside the tube ($W\ m^{-2}\ K^{-1}$)
h_o	Convection heat transfer coefficient outside the tube ($W\ m^{-2}\ K^{-1}$)
h_s	Conduction heat transfer coefficient ($W\ m^{-2}\ K^{-1}$)
I	Radiation intensity (energy per area of emitting surface per unit solid angle)
J	Mass flux; diffusion flux ($kg\ m^{-2}\ s^{-1}$)

Symbol	Description
k	Kinetic energy per unit mass (J kg^{-1})
k	Reaction rate constant (units vary)
k	Thermal conductivity ($\text{W m}^{-1}\text{K}^{-1}$)
k_{eff}	Effective thermal conductivity ($\text{W m}^{-1}\text{K}^{-1}$)
Nu	Nusselt number
n	Refractive index; Number of moles
P	Pressure (N/m^2 , Pa, atm)
P_{Cl_2}	Partial pressure of chloride (Pa, atm)
P_{O_2}	Partial pressure of oxygen (Pa, atm)
Pr	Prandtl number ($C_p \mu / k$)
Q	Overall heat transfer (kJ)
R	Process rate ($\text{kg m}^{-3}\text{s}^{-1}$), Universal gas constant ($8.314472 \text{ J K}^{-1} \text{ mol}^{-1}$)
$R_{k,r}$	Arrhenius molar rate of creation/destruction of species k in reaction r (mol s^{-1})
Re	Reynolds number
\vec{r}'	Position vector
S	Modulus of mean rate of strain tensor (s^{-1}) Stoichiometric coefficient
S_{ij}	Mean rate-of-strain tensor (s^{-1})
St	Stanton number
\vec{s}	Direction vector
\vec{s}'	Scattering direction vector
T	Temperature (K, °C)
ΔT	Temperature difference (K, °C)
T_4	Temperatures that chloride vapours equal to 10^{-4} atm (K, °C)
T_m	Melting Temperature (K, °C)
t	Time (s)
U	Overall heat transfer coefficient ($\text{W m}^{-2}\text{K}^{-1}$)
u, v, w	Velocity magnitude (m s^{-1}); also written with directional subscripts (e.g., v_x, v_z, v_r)

Symbol	Description
V	Volume (m^3)
\bar{v}	Overall velocity vector (m s^{-1})
X	Mole fraction (dimensionless)
x	Corrosion depth (m)
Y	Mass fraction (dimensionless)
α	Surface absorptivity
ϵ	Surface emissivity
θ	Angle between the incident X-ray beam and the scattering atomic planes
λ	Wavelength of x-rays, and moving electrons, protons, and neutrons
μ	Dynamic viscosity (cP, Pa-s, kg/ms)
ρ	Density (kg m^{-3})
ρ_B	Molar density of B in the 'material'
σ	Stefan-Boltzmann constant ($5.67 \times 10^{-8} \text{ W m}^{-2} \text{ K}^{-4}$)
σ	Surface tension (kg m^{-1})
σ_s	Radiation scattering coefficient (m^{-1})
τ	Stress tensor (Pa)
Φ	Parameter to be solved; Phase function
Ω'	Solid angle (sr)

Subscript	Description
cr	Solid
d	Deposit
g	Gas
l	Liquid
s	Solid
$s, steam$	Superheated steam
$wall - in, i$	Inner side of superheater wall
$wall - out, o$	Outer side of superheater wall
x	Integers ≥ 1
y	Integers ≥ 1

Abbreviation	Meaning
1in – E/ M/W	Main tube (diameter 1 inch) alloy 625 – End/Middle/Wall
2in	Brace tube (diameter 2 inch) alloy 625
556	Iron-based alloy 556
59	Nickel-based alloy 59
625	Nickel-based alloy 625
Al	Aluminium
AlCl ₃	Aluminium trichloride; Aluminium(III) chloride
Al ₂ O ₃	Aluminium oxide; Alumina
AISI	American iron and steel institute
APC	Air pollution control system
B	Bottom side of the probe (looking from the end)
BA	Bottom ash pit
BFE	Baffle – end section
BFW	Baffle – wall section
Br	Bromine
BS	British standards
BSE	Back scattered electron
C	Carbon
C310	Coated stainless steel 310
C59	Coated nickel-based alloy 59
Ca	Calcium
CaCl ₂	Calcium dichloride; Calcium(II) chloride
CaO	Calcium oxide; Lime
CaSO ₄	Calcium sulphate
CCD-ICP	Simultaneous charge-coupled device - Inductively coupled plasma
CDR	Closed drain wastes
Cd	Cadmium
CdCl ₂	Cadmium dichloride; Cadmium(II) chloride
CFD	Computational fluid dynamics
CH ₄	Methane
CHEC	Combustion and harmful emission control research centre

Abbreviation	Meaning
CHN	Carbon – hydrogen – nitrogen
Cl	Chlorine
Cl ⁻	Chloride ion
Cl ₂	Molecular chlorine
CO	Carbon monoxide
CO ₂	Carbon dioxide
Co	Cobalt
CoCl ₂	Cobalt dichloride; Cobalt(II) chloride
Cr	Chromium
Cr ₃ C ₂	Chromium carbide
CrCl ₂	Chromium dichloride; Chromium(II) chloride
CrCl ₃	Chromium trichloride; Chromium(III) chloride
Cr ₂ O ₃	Chromium sesquioxide; Chromium(III) oxide
CrO ₃	Chromium trioxide; Chromium(VI) oxide
Cu	Copper
DO	Discrete ordinate model
DTA	Differential thermal analysis
DSC	Differential scanning calorimetry
E	End section of the probe
EC	Economiser
EDS	Energy dispersive spectrometer
EN	European standards
F	Front side of the probe that directly faces the flue gas flow
Fe	Iron
FeAl	Iron aluminide (intermetallic phase)
FeAl ₂	Iron aluminide (intermetallic phase)
Fe ₃ Al	Iron aluminide (intermetallic phase)
FeCl ₂	Iron dichloride; Iron(II) chloride
FeCl ₃	Iron trichloride; Iron(III) chloride
Fe ₂ Cl ₆	Dimeric iron(III) chloride

Abbreviation	Meaning
FeO	Iron(II) oxide; Ferrous oxide
Fe ₂ O ₃	Iron(III) oxide; Ferric oxide
Fe ₃ O ₄	Iron(II, III) oxide; Ferrous ferric oxide
Fe _x O _y	Iron oxides such as FeO, Fe ₂ O ₃ and Fe ₃ O ₄
FeS ₂	Iron disulphide
Fe ₂ (SO ₄) ₃	Iron sulphate
GDP	Gross domestic product
H	Hydrogen
H ₂	Molecular hydrogen
HCl	Hydrochloric acid
HF	Hydrofluoric acid
HNO ₃	Nitric acid
H ₂ O	Water
H ₃ PO ₄	Phosphoric acid
H ₂ S	Hydrogen sulphide
H ₂ SO ₄	Sulphuric acid
HTLM	High temperature light microscopy
HVOF	High-velocity oxy-fuel spraying Technique
ICP-OES	Inductively coupled plasma optical emission spectrometry
ISO	International organization for standardization
K	Potassium
KCl	Potassium chloride
K ₂ CrO ₄	Potassium chromate
KOH	Potassium hydroxide
K ₂ SO ₄	Potassium sulphate
La	Lanthanum
LCV	Lower calorific value (MJ kg ⁻¹)
M	Middle section of the probe
Mg	Magnesium
MgCl ₂	Magnesium dichloride; Magnesium(II) chloride
MgO	Magnesium oxide

Abbreviation	Meaning
Mn	Manganese
MnCl ₂	Manganese dichloride; Manganese(II) chloride
Mo	Molybdenum
MoCl ₂	Molybdenum dichloride; Molybdenum(II) chloride
MoCl ₃	Molybdenum trichloride; Molybdenum(III) chloride
MoCl ₄	Molybdenum tetrachloride; Molybdenum(IV) chloride
MoO ₂	Molybdenum dioxide; Molybdenum(IV) oxide
MoO ₃	Molybdenum trioxide; Molybdenum(VI) oxide
MSW	Municipal solid waste
N	Nitrogen
N ₂	Molecular nitrogen
NACE	The national association of corrosion engineers
Na	Sodium
NaBr	Sodium bromide
NaCl	Sodium chloride
Na ₂ CO ₃	Sodium carbonate
Na ₂ CrO ₄	Sodium chromate
NaOH	Sodium hydroxide
Na ₂ S	Sodium sulphide
Na ₂ SO ₄	Sodium sulphate
Na ₂ S ₂ O ₃	Sodium thiosulphate
Nb	Niobium
Nb ₂ O ₅	Niobium pentoxide; Niobium(V) oxide
NH ₃	Ammonia
NH ₄ Cl	Ammonium chloride
Ni	Nickel
NiAl	Nickel aluminide (intermetallic phase)
Ni ₃ Al	Nickel aluminide (intermetallic phase)
NiCl ₂	Nickel dichloride; Nickel(II) chloride
NiCr ₂ O ₄	Nickel chromite spinel
NiFe ₂ O ₄	Nickel ferrite spinel

Abbreviation	Meaning
NiO	Nickel(II) oxide
Ni(OH) ₂	Nickel (II) hydroxide
NO _x	Nitrogen oxides such as NO (nitric oxide), NO ₂ (nitrogen oxide), N ₂ O (Nitrous oxide), and N ₂ O ₃ (dinitrogen trioxide)
O	Oxygen
O ₂	Molecular oxygen
OFA	Over-fire air system
P	Phosphorus
PAC	Powdered activated carbon
Pb	Lead
PbCl ₂	Lead dichloride; Lead(II) chloride
pH	Potential of Hydrogen
PM ₁₀	Particles of 10 micrometres or less
PREN	Pitting resistance equivalent number
PTA	Purified terephthalic acid
Pt	Platinum
PVC	Polyvinyl chloride
R	Rear side of the probe
S	Sulphur
SEM	Scanning electron microscope
SH	Superheater
Si	Silicon
SiO ₂	Silicon dioxide; Silica
SL	Slag
Sn	Tin
SO ₂	Sulphur dioxide; Sulphur(IV) oxide
SO ₃	Sulphur trioxide; Sulphur(VI) oxide
SO ₄	Sulphate
SP	Sampling probe
STA	Simultaneous thermal analysis
T	Top of the probe

Abbreviation	Meaning
Ta	Tantalum
TG	Thermogravimetry
Ti	Titanium
UFA	Under-fire air system
UK	United Kingdom
V	Vanadium
V ₂ O ₅	Vanadium pentoxide; Vanadium(V) oxide
VPS	Vacuum plasma spraying technique
W	Tungsten
W (probe)	Wall section of the probe (close to the furnace wall)
WEEE	Waste of electrical and electronic equipment
Wh	White precipitates in the fly ash
WTE	Waste-to-energy plant
XRD	X-ray diffraction
Y	Yttrium
Y ₂ O ₃	Diyttrium trioxide; Yttrium (III) oxide; Yttria
Zn	Zinc
ZnCl ₂	Zinc dichloride; Zinc(II) chloride
ZnSO ₄	Zinc sulphate
Zr	Zirconium
ZrO ₂	Zirconium dioxide; Zirconium(IV) oxide; Zirconia

CHAPTER 1

INTRODUCTION

1.1 Biomass and Waste: Potential Sources of Renewable Energy

Global concern about the environment has become a strong force to drive the use of renewable energy into a worldwide interest. The contribution of renewable energy to the overall energy consumption during 2000 – 2005 in European countries is 8.5% and it is set to reach 20% in 2020. Biomass and waste are major sources of renewable energy. The most common technologies to utilize biomass and waste are the thermo-chemical conversion treatments which include combustion, gasification, pyrolysis and liquefaction (McKendry, 2002). The average contribution of biomass and waste sources to the overall renewable energy sources in 2005 for European countries is 67.8%, which can be categorized as 3.8% biofuels, 52.2% wood, 8.2% municipal solid waste, and 3.6% biogas (European Communities, 2007). The growth of renewable energy by technology in European countries is shown in Figure 1.1.

In the United Kingdom alone, about 30 million tonnes of municipal solid waste (MSW) are generated annually. This is equivalent to the energy produced from 10 million tonnes of coal per year, which equals to 1/4 – 1/3 of total coal consumption per year (Swithenbank et al., 2000). Therefore, the combustion of waste and biomass with energy recovery is a very promising alternative that should be promoted. This technique not only satisfies the economical and environmental aspects, it also solves the social problems related to waste disposal. Nevertheless, the limitations of this technique includes; pollution related problems, the corrosive conditions in the furnace and subsequently the low efficiency of the plants (Swithenbank et al., 2000). Therefore, further investigation to decrease these limitations is necessary. In this thesis, the focus is on material behaviour in thermal energy conversion systems.

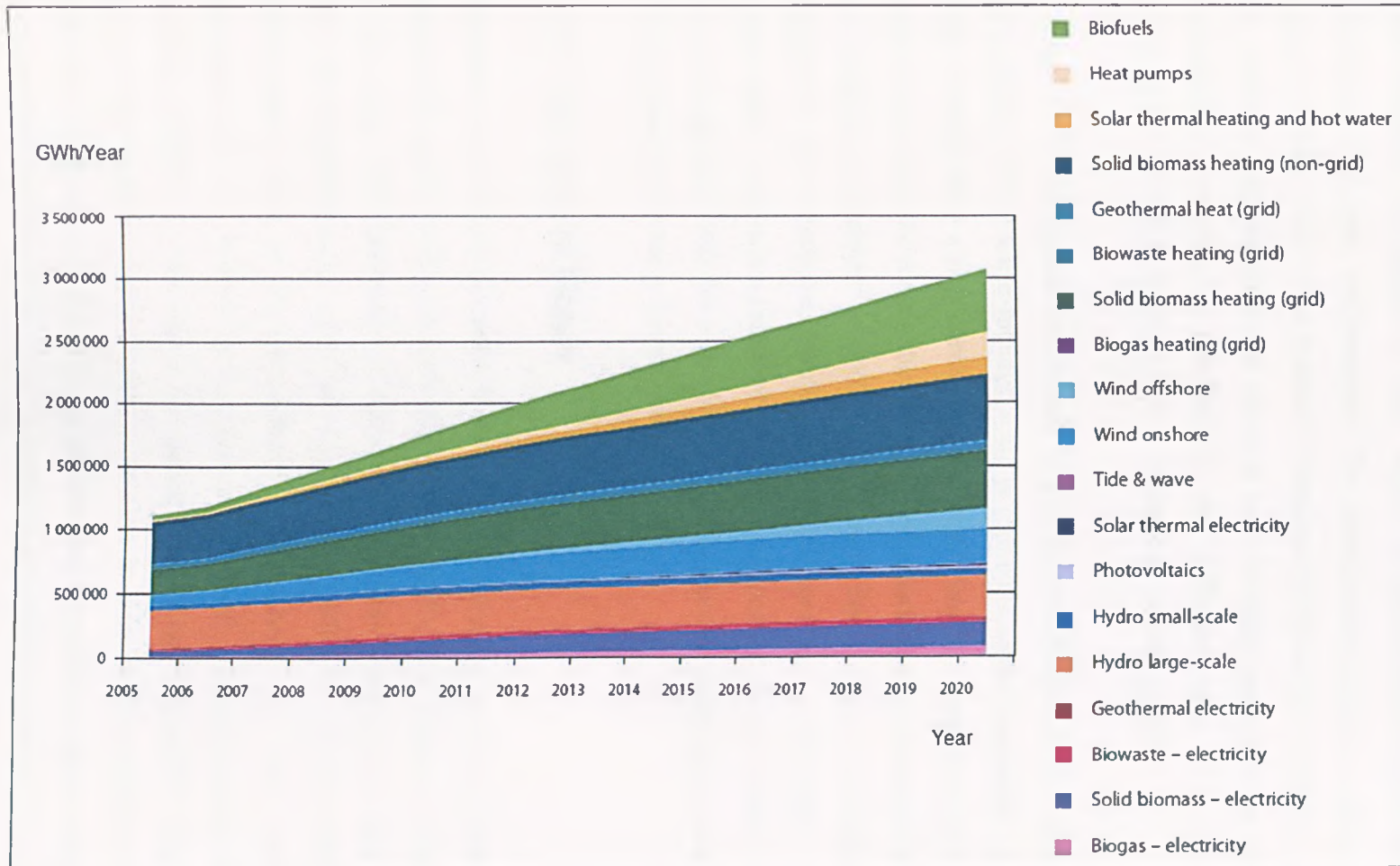


Figure 1.1 The growth of renewable energy by technology (GWh/year) in European Countries (European Communities, 2007)

1.2 Overview: Degradation and Corrosion of Materials

Most materials are subject to some degree of deterioration depending on their interactions with their environments. The deterioration results in either the mass change or impairment of the material's properties such as the mechanical properties (the ductility and strength), the physical and chemical properties, or appearance. Deterioration has varying mechanisms for different types of materials. The deterioration process is normally called 'corrosion' or 'degradation'.

Corrosion of *metallic materials* results in actual material loss either by dissolution or by oxidation, where a non-metallic scale is formed. *Ceramic materials* on the other hand normally have a high corrosion resistance. Thus, the corrosion process usually takes place at elevated temperatures or in a very corrosive environment. Mechanisms and products for *polymer materials* are different from metals and ceramics. They deteriorate by dissolution, swelling, bond rupture and weathering. The term 'degradation' is therefore commonly used for polymers (Callister, 2007). This study is concerned only with the corrosion of metals. Further information related to this topic is discussed in the following sections.

1.2.1 Corrosion of Metals

Corrosion of a metal is generally an electrochemical reaction, which normally takes place at the surface of the component (Callister, 2007). The reaction is very familiar. It is a result of the material's compositional elements attempting to return to their most thermodynamically stable state (Schweitzer, 2007). It regularly takes place in environments such as the atmosphere, aqueous solutions, soils, acids, bases, inorganic solvents, molten salts, liquid metals, and even the human body. An obvious example of corrosion is the rusting detected in automobiles, structures and pipes. Under normal circumstances, corrosion is retarded by protective layers of corrosion products or oxides. Corrosion rates can be predicted and measured under the controlled conditions. However, variables such as pH, temperature and stress can adversely influence the prediction and corrosion control technology.

1.2.2 Safety & Environmental Impacts

Metallic corrosion involves three primary concerns: safety, economics and conservation. The most obvious concern of corrosion problem to human beings is the failure of structures, for examples the corrosion of highways and bridges.

Corrosion of metals and alloys potentially cause harm to humans and the environment, when they are released from buildings as 'corrosion-induced metal runoff'. This mechanism is considered to be a major source of the diffuse dispersion of metals. However, the information about this issue and its environmental fate from source to recipient is limited. Therefore, extensive long-term research about this issue is being conducted by a group of researchers from Sweden, France and Italy (Wallinder et al., 2008). The objectives of their study are to provide quantitative data on metal runoff, and to investigate the chemical speciation and bioavailability both at the immediate release situation and after environmental interaction and retention.

1.2.3 Economic Impact

Corrosion of metals causes significant economic loss. Money and time are spent enormously to prevent corrosion, for maintenance or to replace the components that are damaged as a result of corrosion reactions. Indirect costs of corrosion, which include plant shut-down, loss of efficiency, contamination or loss of products also contribute largely to the economic damage. Approximately 5% of an industrialized nation's income is spent on this issue (Callister, 2007). The data from the last few years show that the United States spends somewhere between \$9 and \$90 billion per year on issues related to corrosion (Schweitzer, 2007).

Research funded by the Federal Highway Administration of the United States of America (NACE International, 2002) revealed that the corrosion cost in 1998 was 3.1% of gross domestic product (GDP) or \$276 billion. The largest corrosion costs are incurred in the 'transportation and utilities' (34.9%) and 'manufacturing' (31.5%) sectors of industry. A diagram showing the distribution of corrosion cost in each sector is presented in Figure 1.2.

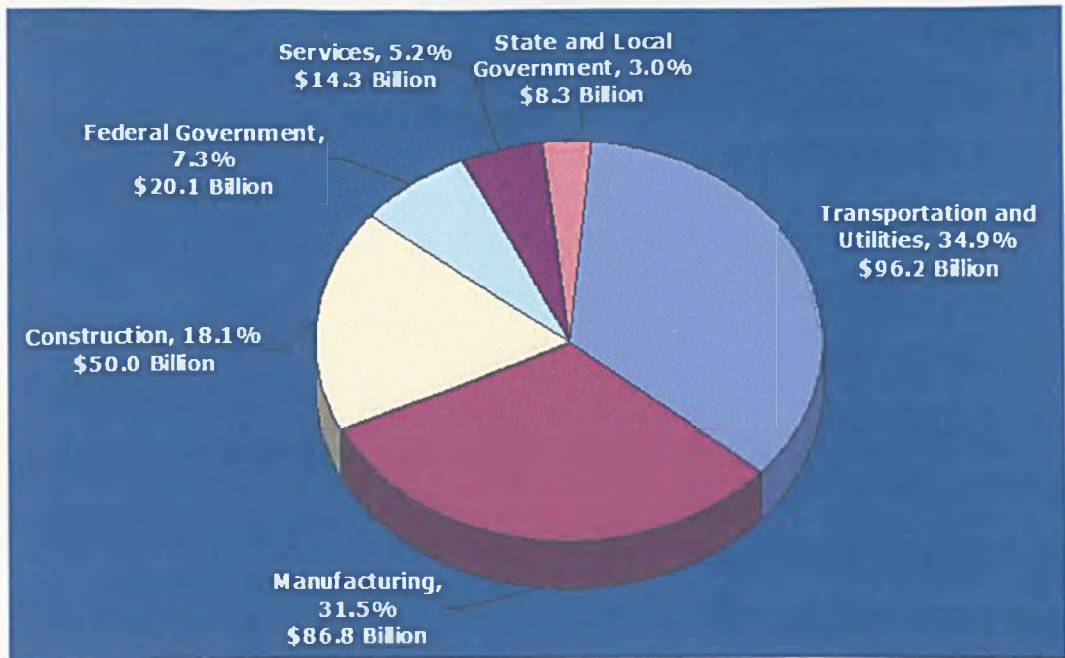


Figure 1.2 Distribution of corrosion costs for the United States in 1998. (Total cost is \$276 billion) (NACE International, 2002)

1.2.4 UK Regulations and Standards Related to Corrosion

Corrosion control of metal components is mentioned for various groups such as crafts, leisure and culture, metal detecting, metal recycling, metal licences, environmental protection, special waste collections, carriage of goods, water supply, traffic and vehicles, and electricity (Office of Public Sector Information, 2008). These regulations generally mention that corrosion of metallic material should be carefully considered. Materials must have corrosion resistance to an acceptable level for each particular operation.

The important British standards (BS) are shown as follows.

BS 7545:1991	Method for removal of corrosion products from corrosion test specimens of metals and alloys
BS EN 12499:2003	Internal cathodic protection of metallic structures
BS EN 12500:2000	Protection of metallic materials against corrosion. Corrosion likelihood in atmospheric environment. Classification, determination and estimation of corrosivity of atmospheric environments
BS EN ISO 10062:2008	Corrosion tests in artificial atmosphere at very low concentrations of polluting gas(es)
BS EN ISO 11130:1999	Corrosion of metals and alloys. Alternate immersion test in salt solution

BS EN ISO 7539-1:1995	Corrosion of metals and alloys. Stress corrosion testing. General guidance on testing procedures
BS EN ISO 8044:2000	Corrosion of metals and alloys. Basic terms and definitions
BS EN ISO 9400:1996	Determination of resistance to intergranular corrosion
BS EN ISO 9227:2006	Corrosion tests in artificial atmospheres. Salt spray tests.
BS ISO 11463:1995	Corrosion of metals and alloys. Evaluation of pitting corrosion
BS ISO 11844	Corrosion of metals and alloys. Classification of low corrosivity of indoor atmospheres.

1.3 High Temperature Corrosion in the Energy Systems

Operations in energy-producing systems or in energy-converting systems generally require a high operating temperature. Their efficiency depends on the high temperature of the heat exchanger materials or the steam. This leads to the corrosion problems of the materials in the furnace. For that reason, the corrosion of materials often limits the efficiency of the systems (Stringer, 1986).

Stringer (1986) proposed that the most serious high temperature corrosion problems can generally be divided into 2 major classes: (1) molten salt induced accelerated oxidation, and (2) mixed oxidant attack. The molten salt induced accelerated oxidation is often called 'hot corrosion'. It occurs in the presence of certain compounds, i.e. sulphates and chlorides of alkali metals and heavy metals such as V, Pb, and Zn in the fuels. The most common form of gaseous mixed oxidant attack is combined sulphidation and oxidation.

Other modes of corrosion at high temperature include carburization and nitridation (Lai, 1990). Other factors that induce high temperature corrosion also include; particle impact and the high velocity of flue gas, and the presence of a reducing atmosphere (Swithenbank et al., 2000).

The energy systems and other industries that experience high temperature corrosion include (1) fossil fuel power generation, (2) biomass/waste power plants, (3) aerospace and gas turbines, (4) nuclear, (5) automotive, (6) pulp and paper, (7) refining and petrochemical processing, (8) chemical processing, (9) mineral and

metallurgical processing, (10) heat treating, (11) ceramic, electronic, and glass manufacturing (Lai, 1990).

1.4 Control Methods for High Temperature Corrosion

High temperature corrosion problems in the energy systems depend greatly on the system. Therefore, the best solution for corrosion control is specific to the system. The most common and easiest approach to prevent the corrosion is to select suitable materials. However, the materials that can withstand the corrosive environments in energy systems often have a very high cost.

Other possible techniques include operational changes and design changes. These techniques can often be achieved by using the Computational Fluid Dynamics (CFD) modelling (Swithenbank et al., 2000), which can optimize the flow, gas mixing conditions, heat transfer and particle trajectories inside the furnace. Using cooling tiles and a co-flow superheater also reduces the corrosion problem (Swithenbank et al., 2000). Another possible approach is to use the addition, of for example MgO, which can reduce the corrosion due to the presence of V_2O_5 . Sacrificial equipment might be used as a sacrificial anode, or as a flow diverter to reduce the erosion.

Coating is a popular corrosion control techniques used in recent studies. It provides a combination of ‘the excellent mechanical properties of the substrate material’ and ‘the good corrosion control resistance of the surface’ (Tsaur et al., 2005). These properties are not easy to attain solely by alloy development. Examples of effective surface coating to prevent high temperature corrosion are Al_2O_3 and Cr_2O_3 (Houngninou et al., 2004; Tsaur et al., 2005).

1.5 Problem Statement

High temperature corrosion of the heat exchanger materials is the important factor that limits the efficiency of energy systems. The problem becomes more serious when fuels containing alkali metals, heavy metals, Cl, and S are used. In energy

systems utilizing biomass and MSW, the steam temperatures are kept lower than 450°C to avoid these problems. Hence, the plant's efficiency is restricted to a very low level compared to a furnace burning traditional fuels. This represents a crucial drawback of these clean energy systems.

To increase the plant's efficiency and to lower the corrosion damage, methods to prevent or control high temperature corrosion must be investigated. Additionally, a comprehensive knowledge about the factors affecting high temperature corrosion and its significance is required.

This study proposes corrosion control methods to be investigated as follows: (1) new high grade alloys (both Ni-based and Fe-based alloys), (2) aluminide coatings, and (3) sacrificial baffles. Similar studies carried out so far by other researchers have only been conducted in the simulated conditions in the laboratory, or only for short exposure periods in the real plants. Therefore, it is appropriate to perform this research in a waste-to-energy (WTE) plant for an extended exposure period.

Such a study carried out in a WTE plant may result in further benefits. Firstly, the results can be applied to other systems such as in a coal-fuelled power plant since the condition in a WTE plant is one of the most corrosive environments. Secondly, the results may contribute to an improvement in the system's efficiency. This can subsequently promote the combustion of biomass and waste with energy recovery.

1.6 Research Objectives

The overall objectives of this research are:

1. to investigate the factors affecting the high temperature corrosion in waste-to-energy plants and,
2. to explore and test corrosion control methods in the real furnace conditions.

In order to achieve the above objectives, the research work was divided into five stages. The description of each stage and its sub-objectives are as follows:

1. Literature review

- a. To understand the mechanisms of high temperature corrosion.
- b. To review the corrosion problems in various energy systems.
- c. To review the available techniques used for corrosion control.

2. Experimental work

- a. To investigate the actual conditions in the plants and the sampling points for probes.
- b. To collect the combustion residues at various locations in the plants.
- c. To design the air-cooled sampling probes which can be used to investigate the effects of temperatures, effects of particle depositions and the performance of different corrosion control techniques. Techniques to be tested are the use of high grade alloys, baffles, and aluminide coatings.

3. Analytical work

- a. To analyse the samples of combustion residues and probe deposits for their chemical composition, crystalline phase and melting temperatures.
- b. To analyse the samples of corrosion products for their crystalline phase and chemical composition.
- c. To analyse the samples of alloys for morphology, corrosion rate and grain boundary corrosion.

4. Mathematical modelling

- a. To simulate the conditions (temperatures and gas velocity) of the furnace and the flue gas around the sampling points
- b. To simulate the sampling probes in order to obtain the local temperatures of alloys and deposits.
- c. To investigate the performance of flow diverted sacrificial baffles.

1.7 Layout of the Thesis

This PhD thesis consists of 9 chapters as described in the following:

Chapter 1 Introduction describes the background of this study. Then, it states the problems and the objectives of the study.

Chapter 2 Literature Review presents an overview of research related to the high temperature corrosion of metal alloys and the available prevention methods.

Chapter 3 Theoretical Considerations lays out the principal knowledge required for the study of high temperature corrosion in energy systems. It includes the mechanisms of fly ash formation, ash deposition, models of heat transfer in the deposits, corrosion reactions, and analytical theory.

Chapter 4 Experimental Program and Analytical Methodology describes the waste to energy plant, the fabrication and installation of the sampling probes, the collection of combustion residues and finally the analytical methodology.

Chapter 5 Experimental Results presents the results obtained from the experiments and the analytical work.

Chapter 6 Mathematical Modelling presents the methodology of modelling and the results. The CFD work consisted mainly of 3-dimensional models of the furnace, sampling probe No. 1, and sampling probe No. 2.

Chapter 7 Overall Discussion presents an overall discussion by using results from both experiments and mathematical modelling.

Chapter 8 Conclusions and Recommendations for Future Work concludes the work that has been presented so far, summarizes the important findings and finally gives suggestions for further work.

CHAPTER 2

LITERATURE REVIEW

This chapter presents an overview of research work carried out related to the high temperature corrosion of metal alloys and the available prevention methods. Firstly, the principal modes of high temperature corrosion and degradations of metals are introduced. Then, the high temperature corrosion problems in various energy systems are presented. The chapter focuses specifically on the corrosion mechanisms and alloy behaviour in biomass power plants and WTE plants (i.e. in both laboratory scale and the real operating plants). In addition techniques commonly used to evaluate the corrosion damage are summarized. Finally the available corrosion prevention approaches are discussed.

2.1 Modes of High Temperature Corrosion and Degradation

Metal alloys used in high temperature applications experience different modes and degrees of damage depending on the nature of the operating conditions and intrinsic properties of alloys. Principal modes of high temperature corrosion and degradation can be categorized as follows: (1) oxidation, (2) mixed oxidant (corrodent) attack, (3) deposit induced corrosion, and (4) erosion (Pettit and Goward, 1983b; Stringer, 1986). The relation of oxidation, mixed oxidants and deposits in high temperature corrosion are summarized schematically in Figure 2.1.

2.1.1 Oxidation

The oxidation resistance of alloys depends on the selective oxidation of elements such as Al, Cr or Si, and the adhesion of the oxide scales. The oxidation rate of a metal can be the limiting factor that determines its operating temperature. An example is the use of Cr₂O₃-forming alloys at elevated temperatures especially in high velocity of gas streams. This is due to the evaporation of Cr as in the following

reaction: $Cr_2O_3(s) + \frac{1}{2}O_2(g) \rightarrow 2CrO_3(g)$. The rate of reaction is determined by mass transfer through the gaseous boundary layer, and the thickness of this layer depends on the velocity of the gas stream. Continuous loss of oxide scales (e.g. Al_2O_3 and Cr_2O_3) by the exfoliation on thermal cycling followed by the re-formation of these scales can contribute largely to the damage of alloys especially the Al_2O_3 formers. Exfoliation also occurs on the steam side of boilers due to growth stress. The oxide scales are mainly Fe_3O_4 .

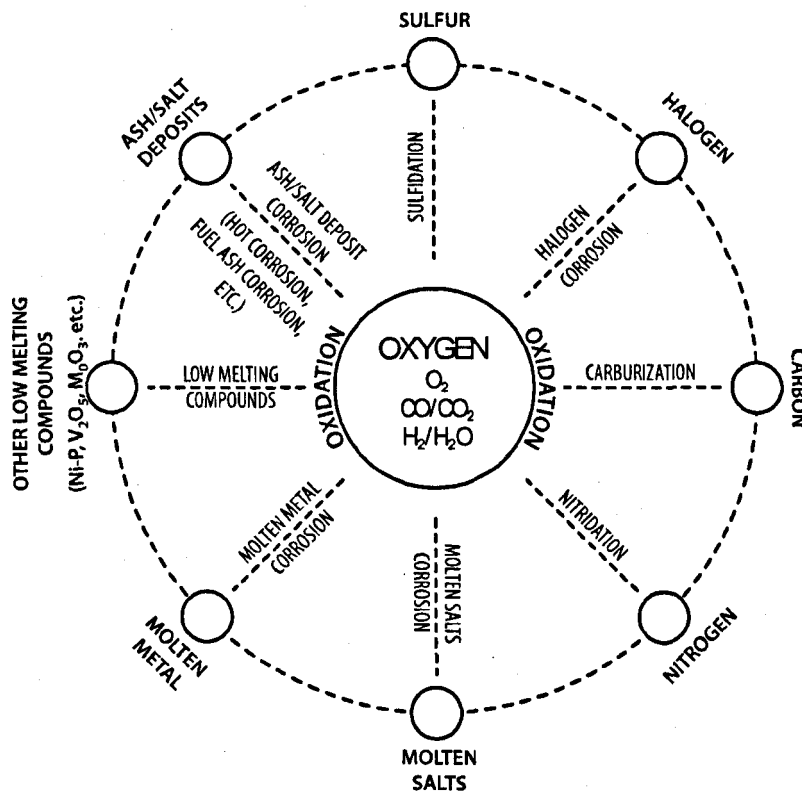


Figure 2.1 Schematic diagram showing the principal modes of high-temperature corrosion (adapted from Lai (1990))

2.1.2 Corrosion in Mixed Oxidants

Corrosion becomes more severe and the mechanical properties of alloys are degraded when there are other oxidants such as S, C, and Cl involved. S and C may transport through the protective oxide layer and react with the metals internally to form carbides or sulphides with elements responsible for forming the protective oxide layer. These oxidants may also accumulate either at the scale-metal interface

or in the deposits, resulting in the increase of the scale growth stress and deposit induced corrosion.

The rates of damage increase in the order: oxidation only < oxidation and internal sulphidation < oxidation and internal chlorination < hot corrosion by sulphate salts < hot corrosion by sulphate and chloride salts (Mohanty and Shores, 2004).

2.1.3 Accelerated Corrosion Induced by Deposits

The integrity of the protective oxide layer can be destroyed when it was covered under the deposits either by (1) dissolution which often involves molten salts such as the dissolution of oxides by molten V_2O_5 , or by (2) alteration of a newly formed oxide layer to become less protective compounds. There is no clear evidence of certain sequences and the exact time for which protective oxide products remain stable before the damages occur (Michelsen et al., 1998).

This type of corrosion is often mentioned as 'hot corrosion'. Hot corrosion is the process where the metal undergoes accelerated oxidation when it is covered under deposits containing S and/or Cl in an oxidizing atmosphere at the elevated temperature. The corrosion products include the un-protective oxide scale, internal sulphide compounds and internal chloride compounds. The reaction of hot corrosion consists of 2 stages: (1) an initial incubation stage where the continuous protective oxide layer is formed and the corrosion rate is slow as there is no deposit and (2) a propagation stage where the reaction rate becomes very fast since the protective oxide scale is destroyed or changed due to depositions (Mohanty and Shores, 2004; Sidhu et al., 2005). However, the presence of Cl in the gas phase often reduces or eliminates the initial incubation stage (Nielsen et al., 2000).

The presence of compounds in deposits and corrosion products is related to the Gibb's free energy, partial pressures of gaseous species and temperature of the environment. They can be determined by considering their thermodynamical stability. A diagram of thermodynamic stable species of K in wheat straw combustion is shown in Figure 2.2. This system considers the presence of C, H, O, N, S, Cl, Na, K, and Si.

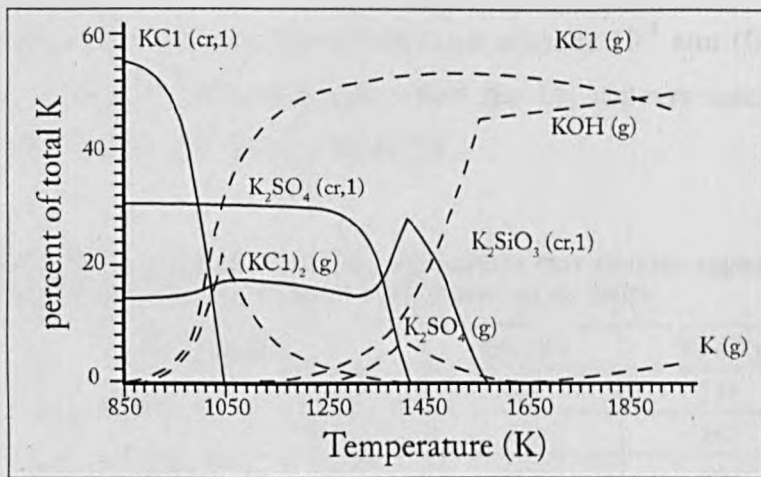


Figure 2.2 The thermodynamically stable species of potassium in wheat straw combustion (Michelsen et al., 1998)

The stability of metal oxides and chlorides in terms of Cl_2 and O_2 partial pressures ($P_{\text{Cl}_2}, P_{\text{O}_2}$) at a specific temperature can be explained by Ellingham – Pourbaix stability diagrams (Nielsen et al., 2000). For example, stability of corrosion products from the corrosion of superheater alloys composed mainly of Fe, Cr, and Ni at 727°C is shown in Figure 2.3. The stability of corrosion products of Fe-Ni-Cr-Mo alloys at 500°C calculated by using commercial software named THERMO-CALC is shown in Figure 2.4.

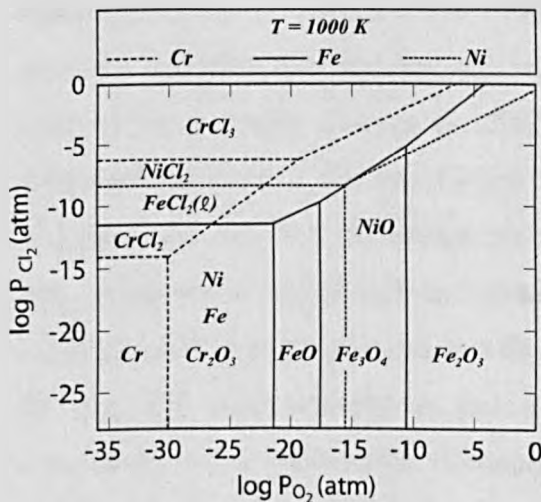


Figure 2.3 Stability diagram of Fe-Cr-Ni-O-Cl at 727°C (Grabke, 1991; Nielsen et al., 2000)

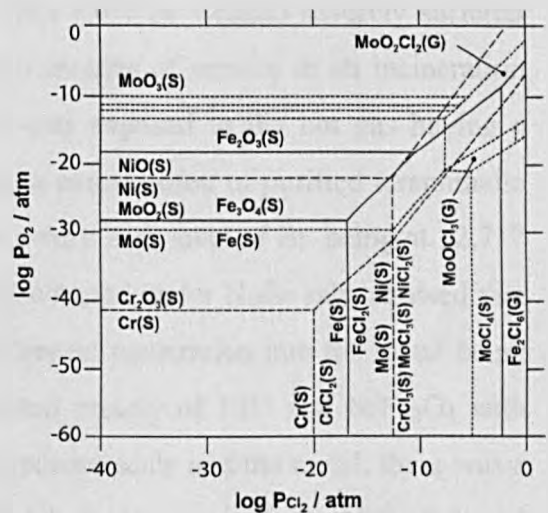


Figure 2.4 Stability diagram of Fe-Ni-Cr-Mo-O-Cl at 500°C (Kawahara, 2002)

Metal chlorides have high vapour pressures and can evaporate even at low temperature resulting in rapid loss of metals. Volatilization can be the governing

corrosion mechanism when the vapour pressure exceeds 10^{-4} atm (Grabke, 1991). The melting points and temperatures at which the Cl_2 vapours reach 10^{-4} atm of different metal chlorides are listed in Table 2.1.

Table 2.1 Melting temperature (T_m) and the temperatures that chloride vapours equal to 10^{-4} atm (T_4) of various metal chlorides (Grabke, 1991; Nielsen et al., 2000)

Metal Chlorides		T_m ($^{\circ}\text{C}$)	T_4 ($^{\circ}\text{C}$)
Iron chlorides	FeCl_3	676	536
	FeCl_2	303	167
Nickel chloride	NiCl_2	1030	607
Chromium chlorides	CrCl_2	820	741
	CrCl_3	1150	611

Deposits containing eutectic mixtures of alkali-metal chlorides have very low melting temperatures (eutectic temperatures) compared to their original constituent compounds. Once the deposits become melted, the corrosion rate increases significantly. The melting temperatures of various compounds and binary mixtures are presented in Table 2.2. Extensive lists of this data can be found in Rademakers et al. (2002).

Bromine may play a vital role in corrosion. The thermowell made of Inconel 600 (Ni balance, Cr 14.0 – 17.0%, Fe 6.0 – 10.0%, Mn 1.0% by weight) severely suffered from the high temperature corrosion within 6 months of service in an incineration plant in Saudi Arabia (Yin et al., 2005). It was exposed to the hot gas having a temperature of 950°C . The fuel for this plant, a combination of purified terephthalic acid slurry and closed drain wastes, contains a very high level of Br^- being at 12,717 ppm. Cross section images of the thermowell covered under NaBr salts showed that it experienced intergranular attack with the deepest penetration into the metal being $800\ \mu\text{m}$. The outermost porous scale consisted mainly of NiO and NiFe_2O_4 with some threads of Cr/Mn-oxides. Between this porous scale and the metal, there was a continuous non-protective oxide layer of nickel chromite spinel (NiCr_2O_4) and $\text{Cr}_2\text{O}_3\cdot\text{NiO}$. These Ni/Cr oxides together with NaBr salts were also found in the cracks along the grain boundaries. However, the author pointed out that the role of Br was not certain and the main reason of failure might come from the use of an inappropriate substrate material. The Cr content in Inconel 600 was not enough to

form a continuous protective oxide (Cr_2O_3) layer as at least 18 – 20% Cr is required (Lai, 1990). Furthermore, the Cr_2O_3 possibly evaporates at a temperature higher than 980 – 1000°C (Lai, 1990) which was barely higher than the operating temperature of this plant.

Table 2.2 Melting temperatures for different species and binary mixtures (Nielsen et al., 2000; Rademakers et al., 2002).

System	Melting/Eutectic temperature (°C)	Composition at eutectic point (mol% alkali)	Reference
NaCl	801		(1)
KCl	772		
FeCl_2	677		
FeCl_3	300		
NaCl – FeCl_2	370 – 374	≈ 56	
NaCl – FeCl_3	151	45.3	
KCl – FeCl_2	340 – 393	45.8 – 91.8	
KCl – FeCl_3	202 – 202	24 – 47	
CrCl_2	845		
CrCl_3	947		
NaCl – CrCl_2	437	53.7	
NaCl – CrCl_3	544 – 593	68 – 95	
KCl – CrCl_2	462 – 475	36 – 70	
KCl – CrCl_3	700 – 795	54 – 89	
Na_2CrO_4	792		
K_2CrO_4	980		
NaCl – Na_2CrO_4	557		
KCl – K_2CrO_4	650	68.4	
$\text{Na}_2\text{Cr}_2\text{O}_7$	356.7		
$\text{K}_2\text{Cr}_2\text{O}_7$	398		
NaCl – $\text{Na}_2\text{Cr}_2\text{O}_7$	592	30	
KCl – $\text{K}_2\text{Cr}_2\text{O}_7$	366 – 368	25 – 27.5	
48 ZnCl_2 + 52 KCl	250		
82 ZnCl_2 + 18 KCl	262		
84 ZnCl_2 + 16 KCl	262		
73 ZnCl_2 + 27 PbCl_2	300		
31 NaCl + 69 PbCl_2	410		
21 KCl + 79 PbCl_2	411		
17 NaCl + 83 PbCl_2	415		
39 ZnCl_2 + 50 KCl + 11 PbCl_2	275		
35 ZnCl_2 + 48 NaCl + 17 PbCl_2	350		
16 NaCl + 40 KCl + 44 PbCl_2	400		
K_2SO_4 + Na_2SO_4 + ZnSO_4	384		
KCl + ZnCl_2 + K_2SO_4 + ZnSO_4	292		

[Note: (1) from Nielsen et al. 2000, (2) from Rademakers et al. 2002]

In WTE plants, Br may come from the plastic waste of electrical and electronic equipment (WEEE). The effect of Br on corrosion was investigated in order to find

out the possibility of co-firing WEEE waste with MSW (Rademakers et al., 2002). It was found that in a mixed fuel having 3% WEEE (Cl increase 0.15 wt%, Br increase 0.05 wt%), Cl-induced corrosions are still the primary mechanisms, and the difference in corrosion rates is not noticeable. The formation of free Br₂ can be avoided by limiting raw gaseous Br to 300 mg/m³.

Thermal cycling significantly induces hot corrosion to take place at a higher rate. An example of the process with thermal cycling and hot corrosion is the induration (sintering) furnaces for taconite pellet production where the temperature cycled from ambient to approximately 900°C and deposits were mainly composed of Na₂SO₄, K₂SO₄, NaCl, and KCl. Thermal cycling also induces cracking and mechanical failures of the scale which subsequently increases the exposure of metal to the corrosive environments (Mohanty and Shores, 2004).

2.1.4 Erosion – Corrosion

Erosion significantly complicates existing corrosion mechanisms especially at elevated temperatures. Degradation becomes more severe especially in the combination of erosion-hot corrosion because abrasive particles remove outer scales and alloy is exposed more to molten corrosive deposits. The effects of erosion depends on various parameters such as the particle velocity and size, particle composition, loading and shape, temperature and the corrosive conditions. Coatings that can prevent high temperature corrosion and erosion are not yet developed. However, it should be as dense as ceramic coatings and adherent to the alloy.

2.2 High Temperature Corrosion in Energy Systems

2.2.1 Oil-Fired Boilers

The metal temperatures at the fire-side of the heat exchanger system in oil-fired boilers are relatively low being less than 650°C. The materials are often made of plain carbon steel, low alloy ferritic steels (e.g. Fe-2¼Cr-1Mo) and for the last section, austenitic stainless steels such as 304 (Fe-18Cr-10Ni) are used. The corrosion problems in these systems are largely related to the accumulation of

deposit containing V_2O_5 and alkali sulphates primarily Na_2SO_4 . Methods for corrosion prevention include (1) reducing the excess air to minimize the formation of V_2O_5 , (2) use of co-extruded tube with an outer layer of high Cr alloys (e.g. Ni-50Cr) as Cr satisfactorily resists attack of V (Stringer, 1986), (3) avoiding austenitic steel as it is very susceptible to sulphidation (McKendry, 2002), (4) use of additives, mainly MgO, in order to form higher melting point compounds with V (Fichera et al., 1987).

Sulphur present in diesel is the major contribution to the corrosion in diesel fuel systems. Repeated economizer tube failures and intermittent failures at the condensate preheater, and economizer in power plants using high-speed diesel in India are reported (Srikanth et al., 2003). The failures include pitting and thinning on the fireside especially on locations covered by deposits. No significant corrosion or deposit was detected on the waterside surfaces. The authors suggested that $Fe_2(SO_4)_3$ present in the deposits on the evaporator (metal temperature 300 – 450°C) and economizer (metal temperature 225 – 290°C) contribute largely to this problem. No significant corrosion was detected on the superheater (metal temperature 500 – 550°C) because there is no formation of sulphates. $Fe_2(SO_4)_3$ is thermodynamically stable only at temperatures lower than 500°C.

Water vapour released as a result of burning emulsified diesel oil can also cause high temperature corrosion in boiler materials made of carbon steel (Wang and Pan, 2003). The study was conducted in a furnace at the temperatures 750 and 850°C.

2.2.2 Coal-Fired Energy Systems

There are various technologies developed to convert coal into energy. Table 2.3 shows the service conditions and modes of degradation for the main components that are present in various coal-fired energy systems. The main corrosion factors and the limiting steps for the corrosion processes are listed in Table 2.4.

Coal-fired boilers generally experience two corrosion problems; superheater and waterwall. Firstly, the superheater is attacked by the molten alkali- SO_4 salts that are stabilized by the relatively high local SO_3 partial pressure. Secondly, accelerated

wastage of the waterwall takes place in areas where metal temperatures are lower than 450°C. This corrosion occurs in the presence of (1) slag deposit containing unoxidized pyrite (FeS₂) and uncombusted char particles, (2) low concentration of O₂ due to the misalignment of the burner, (3) significant levels of CO (1 – 10 vol%), and possibly (4) Cl-containing compounds (Stringer, 1986; Meadowcroft, 1987; Li et al., 2007). The effects of Cl on corrosion in coal fired boilers are not clear. Disagreements are discussed in various literatures (Ho and Doane, 2002).

Using Inconel alloy 740 (Ni-24Cr-20Co) in simulated environments for a pulverized coal-fired boiler has been studied at 550 and 700°C (Zhao et al., 2005). Results have shown that after the protective scale of Cr₂O₃ is created, damages start from internal sulphidation, followed by the hot corrosion fluxing of oxide and molten salts.

Corrosion can be prevented by using coextruded tubes with an outer layer of 310 stainless steel (Fe-25Cr-20Ni) or equivalent. High Cr alloys are ideal since Cr exhibited good resistance against this environment (Li et al., 2007). Additives are sometimes useful. Plasma sprayed coating is also beneficial. Other approaches could be correcting the combustion design and avoiding using high Cl coals (Meadowcroft, 1987).

Coal-fired fluidized bed boilers often contain deposits rich in CaSO₄ as a result of limestone addition in order to capture S. Corrosion especially internal sulphidation are often found on the metal that is covered under these deposits and has temperatures above 500°C. Erosion in the bed can increase damage by aggravating carburization, sulphidation and oxidation of alloys. In this case, coatings are not particularly helpful due to the high loadings of flue-gas entrained particles resulted from fluidized bed operation. Coated layers can be easily eroded as particles attack the surface. However, chromizing could be the best available method.

Coal Gasifier consists mainly of C-containing gases and to a lesser extent S and O. Forms of corrosion can be a combination of carburization, sulphidation, and oxidation. Presence of HCl could further complicate the problems. Aluminide coatings are susceptible in the presence of HCl. Coextruded tubes might be a suitable solution but there are little concrete evidence (Meadowcroft, 1987)

Table 2.3 Operating conditions and modes of corrosion/degradation for component materials in coal-fired systems (Natesan, 1993)

Technologies	Gas environment	Gas temperature (°C)	Metal temperature (°C)	Deposit type	Particulate	Mode of degradation
<i>Heat exchangers</i>						
Pulverized coal fired boilers	Oxidizing	1300 – 1600	400 – 700	Alkali, sulphates, ash	Fly ash, < 20m/s	Alkali corrosion, fouling
Fluidized bed combustion	Oxidizing, locally reducing	850	400 – 850	CaSO ₄ , CaO, carbon, fly ash	Sorbent bed, fly ash, ≥ 3 m/s	Oxidation – sulphidation, erosion
Gasification	Reducing, moderate to high H ₂ S	900 – 1100	400 – 650	Fly ash, alkalis, chlorides	Fly ash, < 20 m/s	Sulphidation – erosion, fouling.
Magnetohydrodynamic system	Oxidizing	1400 – 1600	400 – 700	K ₂ SO ₄ , fly ash – slag	Fly ash, < 20 m/s, seed	Potassium corrosion, fouling
<i>Turbines</i>						
Combined cycle (gasification)	Oxidizing	850 – 900	850 – 900	Fly ash – slag, alkali	Slag, 200 – 500 m/s	Hot corrosion – erosion
Fluidized bed combustion effluent	Oxidizing	850 – 900	850 – 900	Alkali sulphates, feldspars, aluminosilicates, sorbent	Fly ash, sorbent, 200-500 m/s	Hot corrosion – erosion
Direct-fired turbines	Oxidizing	1000	1000	Alkalis, chlorides, fly ash – slag	Fly ash, 200 – 500 m/s	Hot corrosion - erosion

Table 2.4 Key variables and limiting step of material corrosion/degradation in coal-fired systems (Natesan, 1993)

Phenomenon	Key variables	Possible rate-limiting step
Boiler-tube corrosion	Alkali content, chlorine level, temperature, fly ash	Alkali condensation, oxide-sulphate reaction
Substoichiometric combustion (also gasification)	Oxygen and sulphur partial pressures, temperature, downtime condensate, alkali-slag deposit	Fracture of oxide scale, oxidation-sulphidation, pitting and crevice formation
Fluidized bed combustion in-bed corrosion-erosion	Bed chemistry, local particle velocity, particle size and loading	Oxidation-sulphidation of base metals, arrival rate of particles, fracture of surface scales
Low temperature hot corrosion	Temperature, salt-film thickness, temperature gradient, sulphur level, alkali level	Sulphidation of transient oxides, transport of base metals (i.e. Co, Ni)
Hot corrosion-erosion	Alkali level, temperature, particle size, loading, and velocity	Fracture of scale, sulphidation of transient oxides, transport of base metals

2.2.3 Gas Turbines

Gas turbines are widely used in various applications. The processes that require high quality turbine materials in order to withstand the harsh environments are the aviation industry, marine industry, and electric power generation (Pettit and Goward, 1983a). The severity of corrosion and degradation present in these applications are compared in Table 2.5.

Table 2.5 Comparison of corrosion and degradation problems (surface oriented problems) for gas turbine applications (Pettit and Goward, 1983a)

Applications	Oxidation	Hot corrosion	Interdiffusion	Thermal fatigue
Aircraft propulsion	Severe	Moderate	Severe	Severe
Electric utility	Moderate	Severe	Moderate	Mild
Marine propulsion	Moderate	Severe	Mild	Moderate

In general, the hot corrosion is more severe in the electric utility and marine applications due to the quality of fuels used. Gas turbines in aviation (gas inlet temperatures up to 1350°C, and metal temperatures of 850 – 900°C) usually burn clean fuel. Therefore, impurities mostly come from the air. Industrial applications (gas inlet temperatures around 1150°C, and metal temperatures of 850°C) suffer severe hot corrosion mainly due to impurities existing in the liquid fuel, namely V and Na. Na removal by washing it out from fuel is straightforward whereas removal of V can be a problem. Using a large amount of MgO results in the formation of deposits, leading to a reduction in the plant's efficiency. For all applications, salt contamination from the surrounding environment (particularly in the oceanic regions) is another potential source of corrosion. In addition, when aircraft is in operation close to desert regions, it is susceptible to erosion – corrosion, due to sand ingestion.

Hot corrosion on gas turbines occurs in 2 stages; (1) at temperatures ranging from 825 to 950°C by Na₂SO₄ and to a lesser extent MgSO₄ and CaSO₄ and (2) at temperatures ranging from 700 to 800°C by complex sulphates containing Co and Na under a relatively high local partial pressure of SO₃ (Stringer, 1986).

Generally, materials used in gas turbines at elevated temperatures in the high velocity gas stream are Al_2O_3 formers, and coatings are principally pack aluminide with possible additions of Cr or Pt. Minor additions of Si are found to significantly increase the quality of these aluminide coatings.

Hot corrosion could be efficiently prevented by using coatings containing M-Cr-Al-Y where M represented Co or Co/Ni. These coatings could be applied by either electron beam physical vapour deposition or vacuum plasma spraying techniques. Additionally, Y_2O_3 -stabilized ZrO_2 plasma sprayings over M-Cr-Al-Y coatings could be applied as thermal barrier coatings. However, Y_2O_3 can be destroyed under V-containing deposits (Pettit and Goward, 1983a).

2.2.4 Black Liquor Boilers

In the Kraft pulping process where the operating temperature is typically 170°C , wood chips are cooked in liquor containing NaOH and Na_2S resulting in a mixture of cellulose fibers and black liquor. The black liquor consists of (1) organic extractives, (2) products from lignin fragmentation reactions, and (3) residual inorganic chemicals such as Na_2S , Na_2SO_4 , $\text{Na}_2\text{S}_2\text{O}_3$, Na_2CO_3 , NaOH and, to a lesser extent, NaCl. Organic constituents in black liquor are the main factors governing the low temperature corrosion of carbon steel equipment (Singh and Anaya, 2007).

Problems of high temperature corrosion arise in the co-combustion of this black liquor with oil or gas to recover the energy. Inorganic constituents become the major factors as a considerable amount of Na_2SO_4 and Na_2CO_3 produced in the combustion chamber induces hot corrosion processes (Bernath et al., 1998). Using high alloy materials such as Ni-50Cr with coextrusion by the same material can prevent the corrosion (Stringer, 1986).

2.2.5 Nuclear Reactors

The high temperature corrosion in nuclear reactors occurs due to the impurities present in the coolants which react with material particularly ferritic steel (e.g. Fe-9Cr). Impurities such as CO, H_2O and hydrocarbons induce the formation of internal

precipitates principally of carbides at grain boundaries. This deteriorates mechanical properties of alloys and causes physical disruption of the Fe_3O_4 layer. A prevention method may be oxide deposition applied by sol-gel or equivalent coatings that can hinder the carbon transport (Stringer, 1986).

2.3 Energy Recovery Facilities Using Biomass and Waste

2.3.1 Corrosion Sensitive Areas

The energy recovery facilities using biomass and waste commonly consist of (1) the fuel receiving area and the fuel storage, (2) fuel feeding system, (3) furnace, (4) boiler or heat recovery system and steam turbine, (5) air pollution control system, (6) residue treatment equipment, and (7) control unit.

The problems related to high temperature corrosion take place in the furnace areas especially on the heat transfer surfaces, namely the waterwalls in the first pass of the boilers, screen tubes between the passes, and the superheater tubes. Further details are discussed in section 2.4 and 2.5.

The corrosion process and the degree of damage are governed by various factors including the metal temperature and the flue gas temperature. The metal temperature depends largely on the operating conditions of steam or the coolants for that boiler, and the surrounding temperatures (of hot flue gases). The operating temperatures of a WTE plant in the Netherlands are shown in Table 2.6.

Table 2.6 Operating conditions of boiler components in a WTE plant in the Netherlands (Rademakers et al., 2002).

Boiler part	Steam system	Metal temperature (°C)	Gas temperature (°C)
Waterwall	Evaporator 265°C	~ 300	~ 1000 – 800
Screen tubes	Evaporator 265°C	~ 300	~ 800 – 700
Superheaters	Steam 400°C	~ 450	~ 700 – 600

In general, modern biomass power plants or WTE plants are designed to produce superheated steam that has temperatures of approximately 400°C at the pressures of 40 bar (Rademakers et al., 2002). However, the designs are greatly varied. For example, an outgoing steam having a temperature of 450°C and a pressure of 61 bars were achieved in a 10.7 MW wheat straw plant at Rudhøbing KVV, Denmark (Michelsen et al., 1998). The temperatures of flue gas around the superheater locations range from 725 to 750°C.

2.3.2 Typical Material Used for Superheater Tubes

Throughout the world, different categories of superheater materials are reported ranging from low-alloyed steels to Ni-based alloys. The chemical compositions of these alloys are compared in Table 2.7. For some alloys, the maximum steam temperatures for their application in straw-fired boilers are given. The theory of alloys and the role of additive elements are further discussed in the 'Chapter 3 Theory'.

The most common material used for the fabrication of superheater tubes in the WTE plants in UK is carbon steel 15Mo3. This type of low alloyed steel has revealed its lack of ability to withstand the harsh environment in the furnace. Therefore, other types of materials are increasingly introduced either to replace or to reinforce the strength by overlay welding and coating. Ni-based alloys, for example alloy 625 and alloy 59, are the most common choice. These alloys are widely applied in fabricating the tubing materials for heat recovery systems in advanced WTE plants due to their high corrosion resistance and/or heat resistance. Commercial Ni-based alloys that could be used in WTE plants are, for example (Mankins et al., 1990):

1. *Alloy 625*: Ni-Cr-Mo alloy with an addition of Nb.
2. *Alloy C-276*: Ni-Mo-Cr alloy with an addition of W and Mn.
3. *Alloy 556*: Fe-Ni-Cr-Co alloy
4. *Alloy 800*: Fe-Ni-Cr.

Table 2.7 Chemical composition (wt%) of material commonly used in the fabrication of superheater tubes in biomass and waste derived energy systems. (The values of maximum steam temperature are subject to application in straw-fired boilers)

Alloy	C	Cr	Fe	Mn	Mo	Ni	Nb	V	Others	Max. steam temp.	Ref.
ST35.8	0.2		Bal	0.6					P, S, Si: trace		(1)
15Mo3	0.12-0.20		Bal.	0.40-0.90	0.25-0.35				P, S: ≤0.035, Si: 0.10-0.35	< 450°C (1)	(2)
13CrMo44	0.13	1.00	Bal.		0.50						(3)
10CrMo910	0.10	2.25	Bal.	0.50	1.00						(3)
HCM2S	0.06	2.25	Bal.		0.30		0.05	0.25	N, B: trace, W: 1.60		(3)
P91	0.10	9.00	Bal.		1.00		0.07	0.23	N: trace		(3)
NF616	0.10	9.00	Bal.		0.50		0.06	0.20	N,B: trace, W: 1.80		(3)
X20CrMoV121	0.2	11.2	Bal	0.5	1.0	0.5		Trace	P, S, Si: trace	< 470°C (1)	(1)
HCM12	0.10	12.00			1.00		0.05	0.25	W: 1.00		(3)
Esshete1250	0.1	15.0	Bal	6.3	1.0	9.5	Trace	Trace	B: Trace		(1)
C-276	≤0.010	14.5 16.5	4.0 7.0	≤1.0	15.0 17.0	Bal		≤0.35	Co: ≤2.5, P: ≤0.025, S: ≤0.010, Si: ≤0.08, W: 3.0 – 4.5		(4)
X3CrNiMoN1713	0.03	17.00	Bal.		2.25	13.00			N: trace		(3)
TP347H FG	0.07	18.00	Bal.			10.00	1.00			< 540°C	(3)
AISI 347FG	0.07	18.0	Bal.	2.0		12.0	Nb+Ta:≤1.2	≤0.5	Si: <0.75		(5)
Super304H	0.10	18.00	Bal.			9.00	0.40		N: trace, Cu: 3.0		(3)
NF709	0.07	20.00	Bal.		1.50	25.00	0.25		Ti: 0.05		(3)
625	≤0.10	20.0 23.0	≤5.0	≤0.50	8.0 10.0	Bal (>58.0)	Nb+Ta: 3.15- 4.15		Al: ≤0.40, Co: ≤1.0, P: ≤0.015, S: ≤0.015, Si: ≤0.50, Ti: ≤0.40		(6)
556	0.10	22	Bal. (>31.0)	1.0	3	20			Al: 0.2, Co: 18.0, La: 0.02, N: 0.2, Si: 0.4, Ta: 0.6, W:2.5, Zr: 0.02		(7)
59	≤0.01	22.0 24.0	≤1.5	≤0.5	15.0 16.5	Bal.			Al: 0.1 – 0.4, Co: ≤0.3, P: ≤0.015, S: ≤0.005, Si: ≤0.10		(8)
HR3C	0.06	25.00	Bal.			20.00	0.40		N: trace		(3)
HR6W		23.00	Bal.		1.00	43.00	0.20		Ti: 0.10, W: 6.00		(3)
Sanicro28	0.02	27.0	Bal	1.7	3.5	31.0			Cu: Trace		(1)

Note: (1) for Persson et al. (2007), (2) for E-Pipe Co. Ltd. (2007), (3) for Nielsen et al. (2000), (4) for Mankins et al. (1990), (5) for Nielsen et al. (1999), (6) for ThyssenKrupp VDM (2002b), (7) for Haynes International Inc. (1998), and (8) for ThyssenKrupp VDM (2002a)

2.4 High Temperature Corrosion in Biomass Power Plants

There are different types of biomass and each has different composition and combustion characteristics. Table 2.8 presents the estimated variations of conventional properties of biomass species.

Table 2.8 Biomass fuel properties (the unit is in wt% unless indicated otherwise; elemental compositions is on a dry basis) (Yang et al., 2005)

Moisture	Volatile matter	Fixed carbon	Ash	LCV	Particle diameter	Bulk density
5 – 50	65 – 85	7 – 20	0.5 – 20	15 – 22 MJ/kg	1 – 100 mm	20 – 710 kg/m ³
C	H	O	N	S	Cl	Thermal conductivity
38 – 53	4.5 – 7.0	32 – 45	0.15 – 2.7	0.02 – 0.35	0 – 0.5	0.07 – 0.5 W/mK

The high temperature corrosion in biomass power plants is often found to be related to the particulate deposition on the superheater tubes, particularly when the deposits contains alkali chloride compounds (such as KCl). Critical corrosion can take place at temperatures below the melting points of the salts (Michelsen et al., 1998; Nielsen et al., 1999).

The main constituents of biomass deposits are K, Si, Ca and possibly high levels of S and Cl depending on the type of biomass (Nielsen et al., 2000). Cl plays a vital role in corrosion of the furnace (Baxter et al., 1998). It was estimated that Cl 0.1 wt% in biomass is roughly equivalent to 100 ppmv of gas phase Cl₂ in the furnace.

Studies on the inorganic content of different types of biomass (Baxter et al., 1998; Michelsen et al., 1998) revealed that the weight percentages (on a dry basis) of K, Cl and S in Danish biomass species vary in the range of 0.033 – 1.66 wt%, 0.025 – 2 wt%, and 0.1 – 0.2 wt% respectively. In general, straw and grasses contain a higher concentration of alkali metals and Cl when compared with wood. A straw derived deposit having Cl content as high as 38% was reported (Nielsen et al., 2000).

The schematic pathways of K, Si and Cl in a biomass-fired system are shown in Figure 2.5.

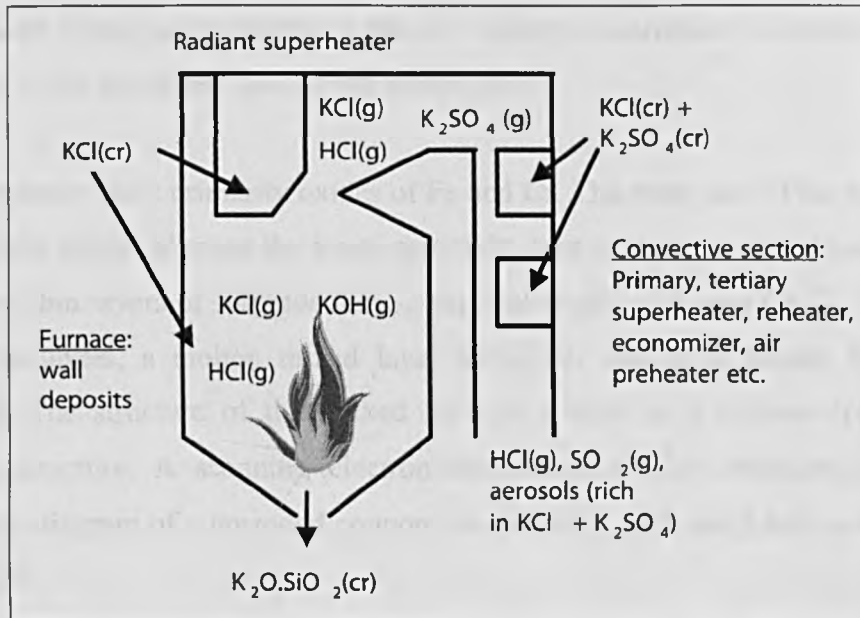


Figure 2.5 Pathways of K, S, and Cl in a biomass power plant system (Nielsen et al., 2000)

The deposit-induced corrosion in biomass energy systems causes a significantly higher corrosion rate at 2 - 20 times higher than the rate typically detected in coal-fired power plants, despite the relatively low S content of biomass. One way to prevent corrosion traditionally is to keep the steam temperature to below 450°C (Nielsen et al., 1999; Nielsen et al., 2000).

The high temperature corrosion of superheater tube material in straw-fired boilers was studied in the laboratory (Nielsen et al., 1999). Metal coupons of boiler tube steel (ferritic X20CRMV121 and austenitic AISI 347FG) were covered with (1) KCl, (2) K₂SO₄, (3) a mixture of KCl and K₂SO₄ and (3) real deposits from a straw-fired grate boiler. Test elements were then exposed to a synthetic flue gas (composed of 6 vol% O₂, 12 vol% CO₂, 400 ppmv HCl, 60 ppmv SO₂, balance N₂) in electrically heated ovens having a temperature of 550°C. Exposure times varied from 1 week to 5 months. The results show that corrosion damage was greater in the metal coupons covered with deposits containing KCl compared to the samples covered solely by K₂SO₄ or by no deposit at all. The austenitic AISI 347 was more resistant to the Cl-induced corrosion than the ferritic X20. The corrosion by KCl was generally uniform with minor internal attacks. However, a 200 μm deep crack having Cl at the bottom of the pit was detected. The corrosion rates, determined as the thickness of the oxide

layers, were found to fit a parabolic rate law where the corrosion is controlled by the diffusion of the gas phase through the oxide layer.

The corrosion yields primarily oxides of Fe and Cr. The outer part of the oxide layer was mainly Fe_xO_y , whereas the inner part right next to the base metal occasionally contained thin layers of sulphide (Cr_xS_y) and traces of Fe_xCl_y and Cr_xCl_y . On top of the oxide layers, a molten mixed layer of K_2SO_4 and with threads Fe_xO_y was detected. The structure of this mixed layer is similar to a laminar (pin-striped) eutectic structure. A scanning electron microscope (SEM) micrograph and the schematic diagram of a corroded coupon covered with KCl and K_2SO_4 are shown in Figure 2.6.

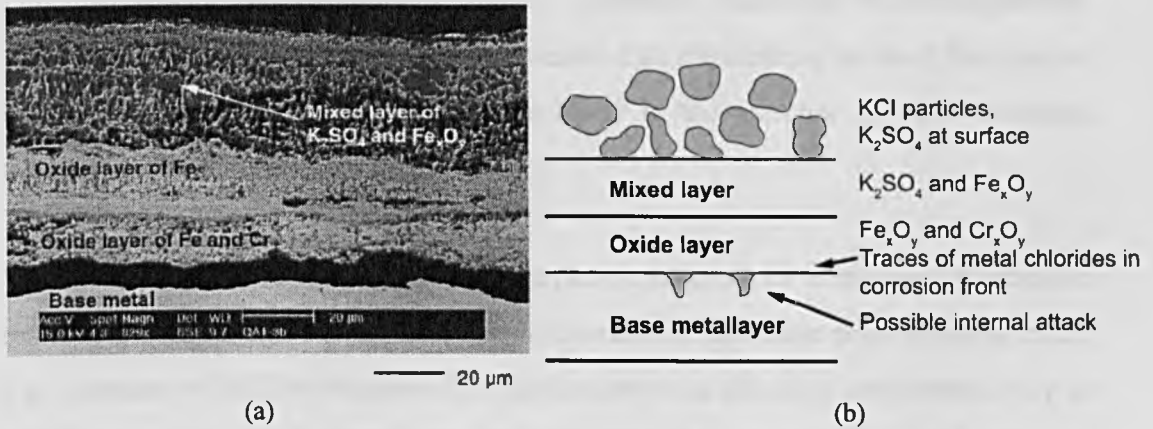


Figure 2.6 Corroded metal coupons covered under KCl and K_2SO_4 : (a) SEM image, (b) schematic diagram (Nielsen et al., 1999)

The authors suggest that KCl formed a melt mixture with K_2SO_4 and iron compounds (Fe_xO_y and $FeCl_2$) on top of the oxide layer. These mixtures accelerate the sulphation reaction which yields HCl and Cl_2 according to the equations:

1. $2KCl(s) + SO_2(g) + 1/2O_2(g) + H_2O(g) \rightarrow K_2SO_4(s) + 2HCl(g)$ and
2. $2KCl(s) + SO_2(g) + O_2(g) \rightarrow K_2SO_4(s) + Cl_2(g)$.

The sulphation also can occur by SO_3 as a result of catalytic conversion from SO_2 (g) by the Fe_xO_y in the deposits.

Furthermore, gaseous chlorine species can also be created from (1) the reaction of alkali chlorides with the metal oxides (Na_2CrO_4 , $\text{Na}_2\text{Fe}_3\text{O}_4$), or (3) the reaction of alkali chlorides with Cr_3C_2 .

The gaseous chlorine products (HCl , or Cl_2) then diffuse back to the metal surface through the oxide layer and react with metals (particularly Fe and Cr) to form volatile metal chloride compounds. These compounds are thermodynamically stable at the interface between metal and oxide, where the partial pressure of O_2 is low. When they diffuse to the outer scale where the partial pressure of O_2 is higher, they are readily oxidized to form an un-protective oxide layer. The liberated gaseous Cl_2 may subsequently diffuse back to the base metal and react with Fe and Cr again.

This mechanism can explain the shift in corrosion behaviour with temperature. Simultaneous thermal analysis (STA) revealed that the melting point of the mixture $\text{KCl-K}_2\text{SO}_4\text{-Fe}_x\text{O}_y$ is 577°C , and is even lower in the presence of other corrosion products such as FeCl_2 .

Nielsen et al. (1999) concluded that Cl can cause accelerated corrosion by increased oxidation, metal loss, internal attack, void formations and loose non-adherent scales. The presence of HCl in biomass-fired boilers even in the high concentration up to 1000 ppmv might not cause a corrosion problem due to the gaseous attack, but may increase sulphidation of water-walls in the local reducing atmosphere in boilers of both pure biomass, and coal and biomass co-fired systems. Gases of HCl and Cl_2 may increase the volatilization of alkali elements from coal in the co-fired power plant. The most severe corrosion induced by Cl is often related to deposits of alkali chlorides by the following mechanisms: (1) intra-deposit sulphation of alkali chlorides by SO_2 which release HCl(g) and $\text{Cl}_2\text{(g)}$ close to the metal surface, (2) reactions of alkali chlorides and metal scale or Cr_3C_2 which releases gaseous Cl species close to the metal surface, (3) accelerated corrosion due to the molten alkali sulphates. Moreover, there is evidence that Cl-containing deposits are not only able to diffuse through the protective oxide layer but they also can destroy the protective oxide layer and create ways to the metal surface. However, the mechanisms are still unclear.

The effects of temperatures on the severity of corrosion are obvious in the study conducted by Michelsen et al. (1998) in a 10.7 MW wheat straw-fired boiler in Rudkøbing, Denmark (Michelsen et al., 1998; Frandsen, 2005). The experiments can be divided into 2 parts: (1) analysis of mature deposit on the existing superheater tube, and (2) the probe experiment. There was negligible corrosion occurring on the existing superheater tube at steam temperatures of 450°C. An air-cooled probe with surface temperatures of 460°C and 550°C was inserted in the furnace to collect the deposits in the flue gas with temperature between 725 to 750°C (just before the superheater). The probe was made of stainless steel and had an outer diameter of 38 mm. The sampling times were 2, 4 and 14-16 hours.

The results revealed that corrosion takes place when the metal temperature is over 520°C. The upstream side deposit on the probe consisted mainly of fly ash and large amounts of condensed KCl, while the downstream side deposit appeared as powdery. The upstream deposits were darker and denser. Deposits consisted mainly of K and Cl, which accounted for 40 – 80%, and other minor components such as Si, Ca and S. On the 550°C probe, the inner layer of deposit was very dense and consisted of almost pure KCl. The structure and the density of the layer indicate that molten phases have been present in the dense layer next to the metal oxide layer. For the 460°C probes the inner layer was thinner and consisted of individual angular particles and was not as dense as on the 550°C probes. The difference between the inner layer of the deposit and nearby molten phases may play the determining role in the corrosion of superheater tubes. Corrosion probe studies revealed that the corrosion rate increased moderately in the steam temperature interval 490 – 520°C and markedly at temperatures above 520°C. Selective corrosion is observed at steam temperatures above 490°C where Cr and to a lesser extent Fe are removed from the alloy leaving a degraded metal phase enriched in Ni.

Another similar study was carried out at the 33 MW_{th} straw-fired Masnedø combined heat and power plant (Hansen et al., 2000). Two types of deposit were analysed: (1) approximately one year old superheater deposits and (2) deposit collected on an air/water-cooled stainless steel probe. Probes were placed at two positions: on the top of the furnace (6 h with a metal temperature of 550 – 700°C)

and on the top of the convective pass (6 h, with a metal temperature of 540 – 620°C). The flue gas temperatures at sampling points were about 1000°C.

Deposits on the probe consisted of an inner layer of KCl and Fe_xO_y and an outer layer of sintered fly ash. The threads of Fe_xO_y in the layer of KCl were noticed.

The mature deposits from the superheater were relatively thick; some were up to 10 cm in thickness. The deposits were shown to have a layered structure as follows: from the metal surface (1) a white thin layer of Fe/Cr-oxide, (2) a grey thin dense layer of K₂SO₄ with white threads of Fe_xO_y, (3) a light coloured thicker porous layer of KCl crystals, (4) a relatively thick massive layer of amorphous KCl, (5) a relatively thick massive layer of KCl with ash particles, (6) a porous layer of sintered fly ash particles mainly consisting of K, Ca, and Si. The massive layers, starting from the fourth layer, showed that the temperature of the deposits was higher than 770°C (melting point of KCl). For mature deposits, threads of Fe_xO_y commonly found in a K₂SO₄ layer are not found in a KCl layer. The authors suggest that K₂SO₄ was the result of sulphation of KCl by gaseous SO₂ or most likely SO₃ as this equation: $2KCl + SO_2 + 1/2 O_2 + H_2O \rightarrow K_2SO_4 + 2HCl$. Sulphation might be accelerated by the high operation temperature of this plant. However, the sulphation is a slow reaction and is related to the presence of Fe_xO_y. Fe_xO_y provides one or more species that form eutectic mixtures with KCl and also increase the rate of SO₃ formation. The low corrosion detected in this plant might be due to the dense layer of K₂SO₄ that does not enhance corrosion for temperatures below 700°C.

2.5 High Temperature Corrosion in Waste to Energy Plants

Corrosion problems in WTE plants can be divided into 2 basic types according to the temperature and the locations that problems emerge: (1) low temperature corrosion and (2) high temperature corrosion (Klasen and Gerner, 2000). Low temperature corrosion is driven by the acid products of the reactions between SO₃, Cl₂, CO₂ and H₂O. It occurs at the cold end of the plants and will not be further addressed in this present study.

Klasen and Groner (2000) state 3 main mechanisms of high temperature corrosion:

1. **Liquid phase corrosion** caused by molten alkali metal salts that are eutectic mixtures having a very low melting points.
2. **Cl-induced corrosion** usually occurs at temperatures above 475°C. Cl generally existing in the fuel leads to the formations of HCl, Cl₂, and other Cl-containing compounds in the deposits. Damage is increased in the presence of the compounds of Pb, Zn and Sn (Oksa, 2006).
3. **Corrosion due to non-uniform furnace atmosphere:** reducing environments allow CO and H₂S to react with the protective oxide layer of metal oxides. The reactions take place in the temperature range of 400 – 600°C.

The corrosion rate occurring in the boiler or furnace depends largely on:

1. **The properties of the heat exchanger materials.** This topic is discussed further in the following sections.
2. **The design of the furnace and the air supply.** Efficient design should provide oxidizing and well-mixed conditions throughout the plant (Klasen and Groner, 2000).
3. **The operating conditions of the plant** such as the fuel properties, temperatures of hot gases and temperatures of the metal surfaces. These factors determine the composition, and the phases of compounds existing in the furnace. Operating conditions significantly control the deposition rate of the deposit and its characteristics including gas permeability and gas penetrating properties (HCl and O₂), deposit thickness, and corrosive components (Cl, SO₄, alkaline and heavy metals). Burning inhomogeneous fuel and the application of soot blowing result in temperature fluctuation and possibly cause a local reducing atmosphere in the furnace.

A brief diagram illustrating the factors affecting particle deposition and corrosion on the heat recovery tubes is shown in Figure 2.7.

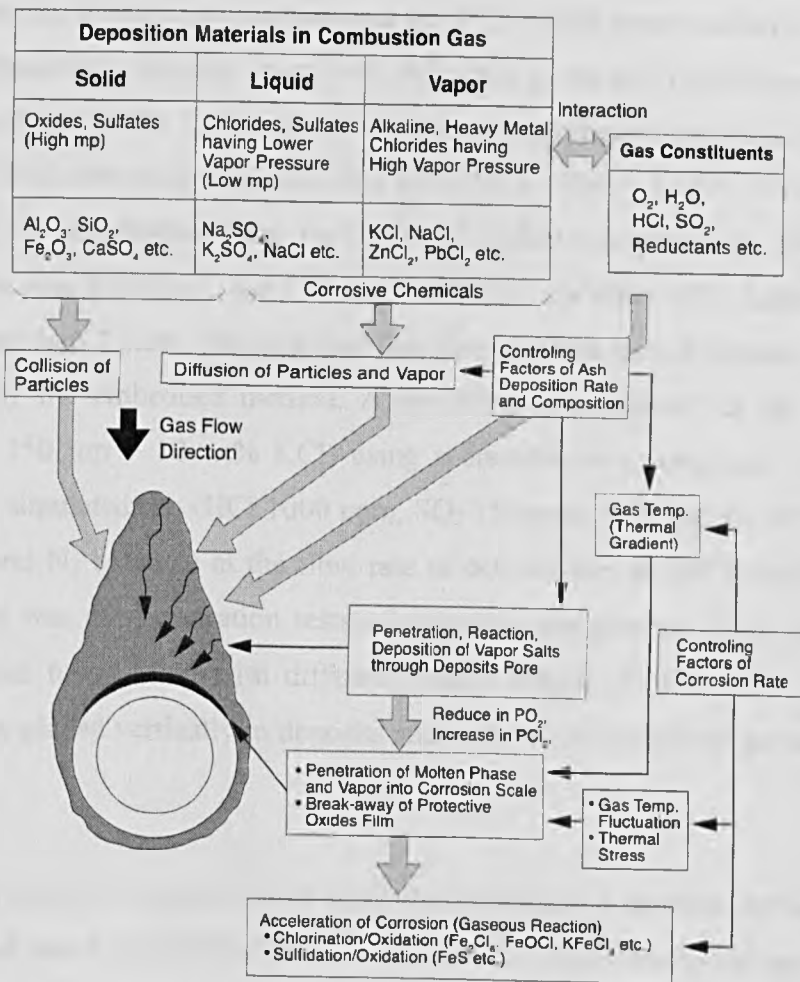


Figure 2.7 Main factors controlling the particle deposition and the corrosion rate on a heat recovery tube (Kawahara, 2002)

Experience on the corrosion rates for boiler components of several WTE plants in the Netherlands is summarized in Table 2.9.

Table 2.9 Experience on corrosion rates for boilers components of Dutch WTE plants (Rademakers et al., 2002)

Boiler part	Evaporator tubes	Superheater tubes
Tube wall temperature	~ 200 – 300°C	~ 400 – 530°C
Tube arrangement	Membrane wall	Bundles
Material	Carbon steel (ST 35.8)	Low alloy steel (15Mo3)
Typical corrosion rates	0.15 – 0.30 mm/year	0.20 – 0.40 mm/year
High corrosion rates	0.30 – 2.0 mm/year	0.40 – 4.0 mm/year

High temperature corrosion mechanisms in WTE plants were studied by analysing corrosion products collected from both full-scale plant and conducting laboratory tests (Kawahara, 2002). In the plant, two typical superheater materials, SA213-T12 (1Cr - 0.52Mo) low alloy steel and alloy 625 (21Cr - 9Mo - 3.5Nb - Ni based) were exposed to the combustion gases for 3000 and 13,800 h respectively. The metal/gas temperature was 550/635°C for T12 and 465/650°C for alloy 625. Laboratory tests were divided into 2 parts. The first part was the corrosion test of various superheater materials by the embedded method. A specimen is embedded in the real boiler deposit ($< 150 \mu\text{m} + 10 \text{ wt}\% \text{ KCl}$) using a crucible as a container. It was then exposed to simulated gas (HCl 1000 ppm, SO₂ 150 ppm, CO₂ and O₂ 10 vol%, H₂O 20 vol%, and N₂ balance) at the flow rate of 600 ml/min at 600°C for 200 h. The second part was the penetration tests of corrosive components from deposits into oxides. Glass tubes filled with different oxides (Fe₂O₃, Fe₃O₄, Cr₂O₃, SiO₂, and Al₂O₃) were placed vertically in deposits and were heated in mixed gas at 550°C for 200 h.

Corrosion products formed on both steels have protective lamellar oxide structures of Fe₃O₄ and dual Cr₂O₃/MoO₂/Nb₂O₅ - Fe₃O₄/NiO. This is due to the environmental change during operation that affects the stability of oxides and chlorides of these metallic elements. The stabilities of oxides and chlorides of metallic elements are in the order of Cr > Mo ~ Fe > Ni and Cr > Fe > Ni ~ Mo, respectively. At the scale-alloy interface, comparatively soft metal chlorides, oxides, and sulphides were found. The reaction takes place at the scale-alloy interface during steady state corrosion therefore seems to be gaseous corrosion, where simultaneous chlorination, sulphidation, and oxidation occur. Oxy-chlorination could be the main reaction, while electrochemical reaction with molten salt corrosion can occur at the initial stage of reaction. Penetration of corrosive components including molten phases, volatile chlorides having high vapor pressures (ZnCl₂, NaCl, KCl, etc.) and gas components (HCl, Cl₂, SO₂, O₂, etc.) into scale occurs through the defects in the scale or oxide film. The penetrating extent of deposits is reduced in the following order: Fe₂O₃ >> Fe₃O₄ > Cr₂O₃ > Al₂O₃ > SiO₂ which corresponds to the vulnerability of these oxides to chlorination. In the soot blower-affected zone, deposit removal consequently causes scale defects through which a molten phase of deposits can penetrate. This increases initial molten salt corrosion. Furthermore, the

soot blower causes high P_{O_2} condition at the outer part of the corrosion products, while a high P_{Cl_2} condition occurs at the corrosion products-alloy interface. Accordingly, peeling and falling of the scales takes place and accelerates the continuous supply of Cl from the outside and induces oxy-chlorination. In summary, the corrosion models were presented as shown in Figure 2.8.

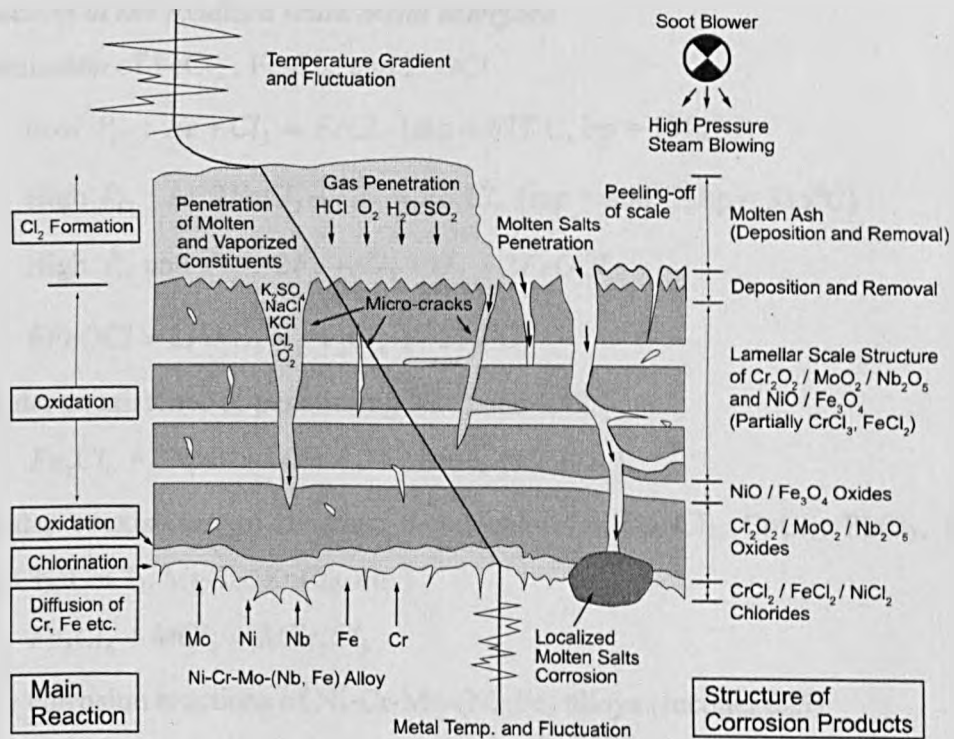
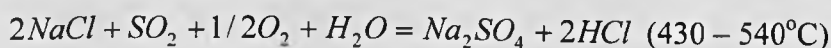


Figure 2.8 Scale structure and corrosion mechanisms in Ni-Cr-Mo-(Nb, Fe) alloy (Kawahara, 2002)

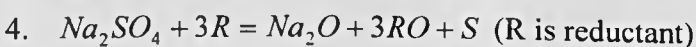
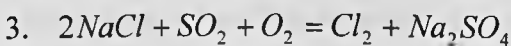
The authors divided corrosion mechanisms into 3 sections: reaction in deposits, reaction in scale, interface between oxidized scale and metal. All possible reactions are summarized and illustrated in Figure 2.9.

a. Reaction in deposits: gas permeation and HCl/Cl₂ production

1. Hargreaves reaction:



2. Deacon reaction: $4HCl + O_2 = 2Cl_2 + 2H_2O$ (catalytic reaction)

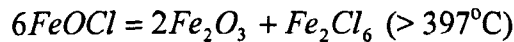
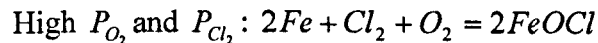
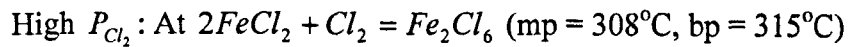
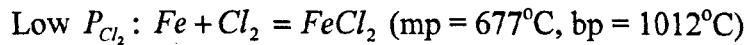


b. Reaction in scale:

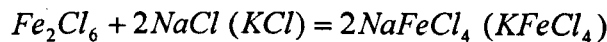
1. Protective film of Fe_2O_4
2. Penetration of molten phase and gaseous components through scale defects which lead to a change in P_{Cl_2} and P_{O_2} at the interface, and hence to the reaction rate.

c. Reaction at the oxidized scale/metal interface

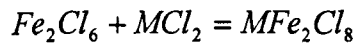
1. Formation of $FeCl_2$, Fe_2Cl_6 , and $FeOCl$



2. Under coexistence of penetrating NaCl and KCl

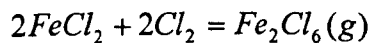
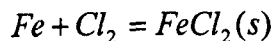
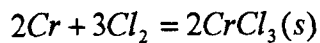


3. Under coexistence of divalent metal chlorides ($MnCl_2$, $CoCl_2$, $PbCl_2$, $NiCl_2$, $CdCl_2$, $CaCl_2$, $MgCl_2$, $ZnCl_2$, etc.)

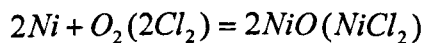
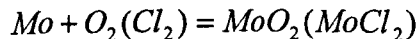


4. For corrosion reactions of Ni-Cr-Mo-(Nb,Fe) alloys (Inconel 625)

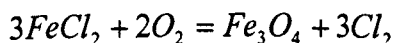
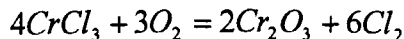
- Selective chlorination of Cr, Fe, or initially formed oxides such as Cr_2O_3 and Fe_3O_4



- Formation of Fe/Ni- and Cr/Mo/Nb rich oxides and chlorides in the interfaces



- Oxidation of chlorides



- Formation of lamellar structure of $Cr_2O_3/MoO_2/Nb_2O_5$ and NiO/Fe_3O_4

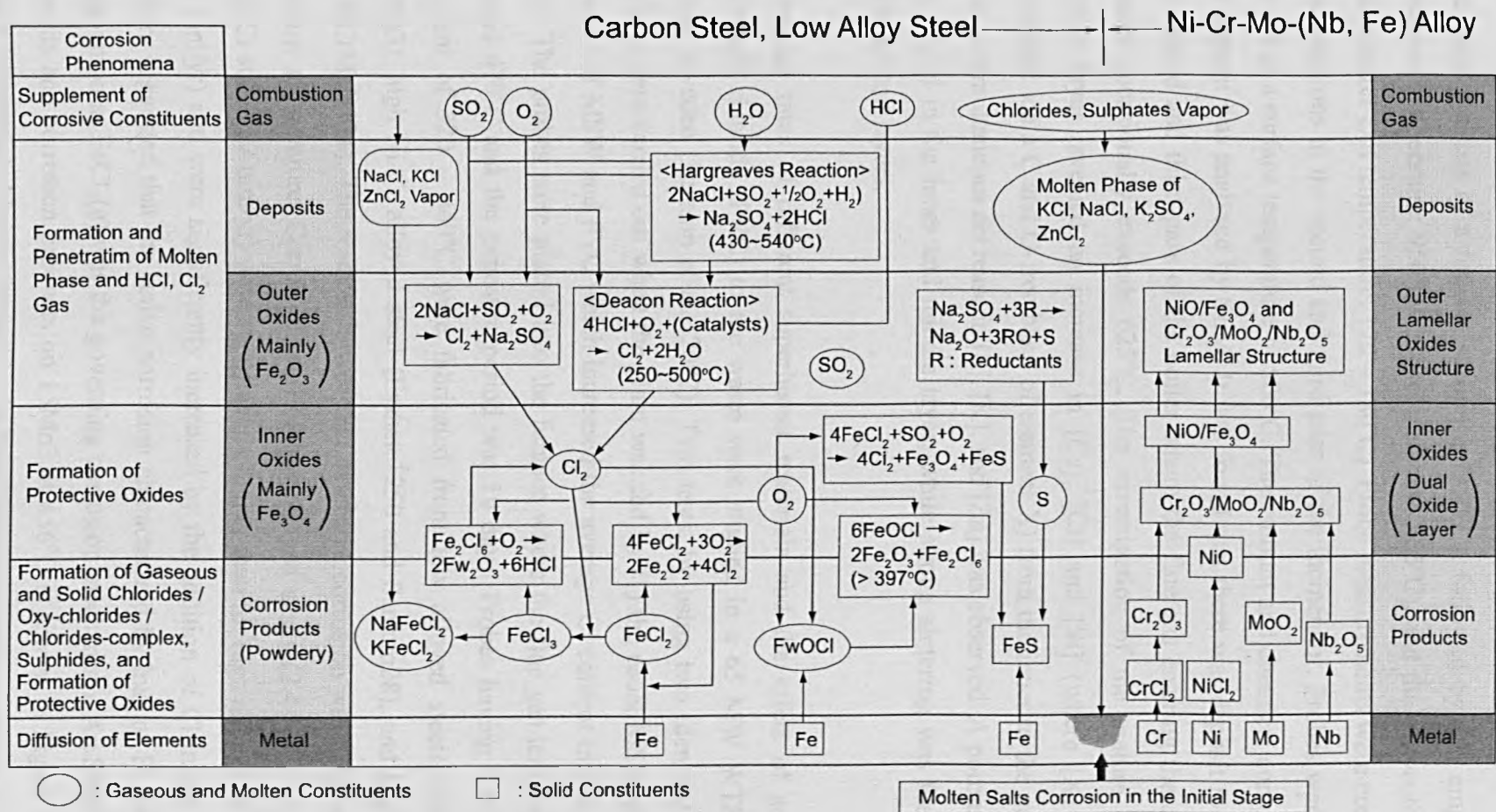


Figure 2.9 Summary of scale structure and corrosion reaction (Kawahara, 2002)

A Danish MSW incineration plant was investigated for ash and deposit formation (Frandsen, 2005). Its maximum incineration capacity is 20 tonnes/h at 11.72 MJ/kg. The plant consists of a furnace section (~1150°C), followed by two empty passes (entrance temperature: 950°C, exit temperature: 625°C), and the convective section (economizer exit temperature: 170 – 180°C). Probe measurements were conducted in four locations in the second and third pass of the incinerator. Probes were exposed for 4 h at a surface temperature of 500°C. The amount and chemical composition of the deposit was analysed by SEM. It was found that there was deposit formation in the second and third pass of the boiler where the flue gas entering the convective system occasionally exceeds 625°C. The investigation of the mature (in-boiler) deposit layer revealed an increase in [Ca], [Cl] and [Si] (where [X] is the % (mol/mol), on a C and O-free base, of element X) from the inner to the outer layers while a simultaneous decrease in [S], [K], and [Zn] was observed. A porous structure was found in the inner and middle layer, while strong sintering was found in the outer deposit layers.

Corrosion rates of different superheater materials and the effect of addition of polyvinyl chloride (PVC) to the waste were studied in a 65 MW WTE plant in Umeå, Sweden (Persson et al., 2007). Two tests, by using two identical sampling probes, were carried out when the plant was fed by (1) the usual MSW and (2) the mixture of MSW and PVC which increased the average Cl content in the fuel up to 13%. The probes were placed into the furnace where the flue gas temperature was around 470°C and the exposure period was 10 days. Probes having a temperature gradient of 320 – 460°C were fabricated from low alloyed steels (ST35.8 and 15Mo3), high Ni-Cr alloyed steel (Esshete1250 and Sanicro28), and high Cr steel (X20CrMoV121). The results showed that extensive corrosion was detected even at this low temperature. Corrosion rates of low alloyed steels (2.4 – 3.7 mm/yr) and high Cr steel (2.2 mm/yr) were significantly higher than for high alloyed steels (0.9 – 1.1 mm/yr) and were significantly increased by the addition of Cl in the fuel. The authors suggested that the active corrosion characterized by loss of Fe through the evaporation as $\text{FeCl}_2(\text{g})$ was the governing corrosion mechanism. An SEM image of deposits and corrosion products on 15Mo3 at 456°C is shown in Figure 2.10. The author differentiated layers formed in the metal/deposit interface. On top of the metal layer (a), there was under a thin layer of Cl compounds (b) possibly Fe_xCl_y . A thick

layer of Fe_xO_y (c) was detected under the initial metal surface boundary (d). Layer (e) was the oxide layer that developed outward in the deposit layer (f) which was mainly compounds of alkali sulphates.

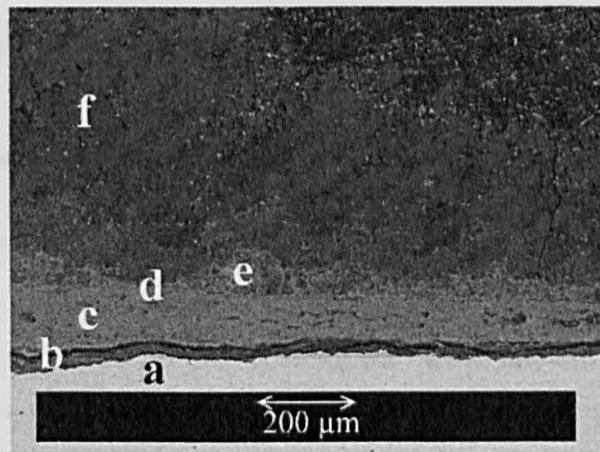


Figure 2.10 The SEM image of deposits and corrosion products formed on 15Mo3 at 456°C (Persson et al., 2007)

2.6 Evaluation of Corrosion Damage

Corrosion damage for metal alloys in any system is very specific and depends on the process, the operating conditions, and characteristics of materials.

The extent of corroded metals can be measured by using an optical microscope in which the metal loss can be expressed either as corroded length or loss area. A digital weighing scale is also used, and the corrosion loss is expressed as weight gained, especially by the oxidation process.

Chemical composition and morphology of the corrosion products can be analysed by using a Scanning Electron Microscope / Energy Dispersive Spectrometer (SEM/EDS). X-Ray Diffraction (XRD) is used widely to study the phase of compounds. Using an SEM/EDS on the etched sample can reveal the effects of corrosion on the grain boundary structures of metals.

Simultaneous thermal analysis (STA) and related thermal analysis techniques are useful in analysing the melting temperatures of deposits and oxide mixtures. The results also clearly show the exothermic and endothermic behaviour of the deposits.

2.7 Methods for Preventing or Controlling Metallic Corrosion

2.7.1 Corrosion Prevention Techniques

The most common and easiest approach to prevent the corrosion is to select suitable materials once the nature of corrosion in that system is characterized. However, there often are problems related to the cost of the most durable material and other approaches must be found. Other possible ways are to change the characteristics of environment, for example, by ensuring good mixing conditions in the plant, and by using MgO to prevent corrosion due to V_2O_5 . Sacrificial equipment might be used as a sacrificial anode, or as a flow diverter.

2.7.2 Corrosion Control by Coatings and Surface Modification

Coating that could be used as high temperature protection must be both chemically and mechanically compatible with the substrate materials, and the coating technology should be practical, reliable, economical and suit the time requirement (Sidhu et al., 2005). Coatings are used only when the resistance to the environment cannot be combined with the necessary properties of the material to perform the required tasks, or when the fabrication of alloys becomes too expensive compared to coatings. One of the most effective coatings for the elevated temperature conditions is $\alpha\text{-Al}_2\text{O}_3$. It develops good resistance to oxidation degradation and mixed gas attack. It may be used to prevent the hot corrosion but SiO_2 may perform better in the presence of highly acidic deposits (Pettit and Goward, 1983b).

In general, coatings could be categorized into 4 groups: (a) diffusion coatings, (b) overlay coatings, (c) ion implantation, and (d) other surface modification methods (Stringer, 1986; Schutze et al., 2006):

a. Diffusion Coatings

This type of coating is the most common process in current use. However, it usually needs furnaces or reaction vessels. Therefore it is not applicable in the field and is not suitable for large components such as heat exchanger panels. Joining, welding and repairing of coated components at a site require other approaches such as weld overlay or flame spraying. Furthermore, the heat required in the coating process might change properties or damage the substrate.

Pack aluminizing or the aluminized pack cementation technique is widely used for applying the alumina onto the surface of stainless steels or Ni-based alloys. It is inexpensive and suitable for application on small parts. Material is packed with an Al source, a diluent (usually Al_2O_3) and a halide activator (often NH_4Cl). This assembly is then held at elevated temperature in the absence of oxidizing agents or under inert gases for a certain time until the required coating thickness forms. The resulting coatings comprise an outer layer of aluminides, and an inner layer of Al-diffused area.

The effect of aluminizing pack coating on the oxidation resistance of heat resistant austenitic stainless steel HH309 (26 wt% Cr, 10 wt% Ni) was studied (Sharafi and Farhang, 2006). Specimens were coated using a powder mixture consisting of 85 wt% Al_2O_3 , 10 wt% Al and 5 wt% NH_4Cl under the inert gas at $1,050^\circ\text{C}$ for 6 hours. The cross sectional SEM image of the coating and the concentration profiles of Al, Cr, Fe and Ni are shown in Figure 2.11. The coating formed on the metal surface consists of two layers. The outer layer contains Fe-Al intermetallic phases such as FeAl and $\text{Fe}_{24}\text{Al}_{78}$. Residual of coating process Al_2O_3 and its oxidized product Fe_2O_3 were also found. The interdiffusion layer contains (1) precipitates of NiAl and Ni_3Al , and (2) a matrix of ferrite with a high concentration of Al. The coated and bare specimens were oxidized in air at $1,100^\circ\text{C}$. The results showed that Al_2O_3 formed by coating provided the substrate with a greater high temperature oxidation resistance compared to a bare specimen that had only Fe_3O_4 . A layer of Al_2O_3 on the surface of stainless steel gives a better high temperature oxidation resistance since it prevents the loss of Cr_2O_3 through volatilization (in the form of CrO_3) at high temperatures; Cr_2O_3 is destabilized at temperatures higher than $1,000^\circ\text{C}$ (Lai, 1990).

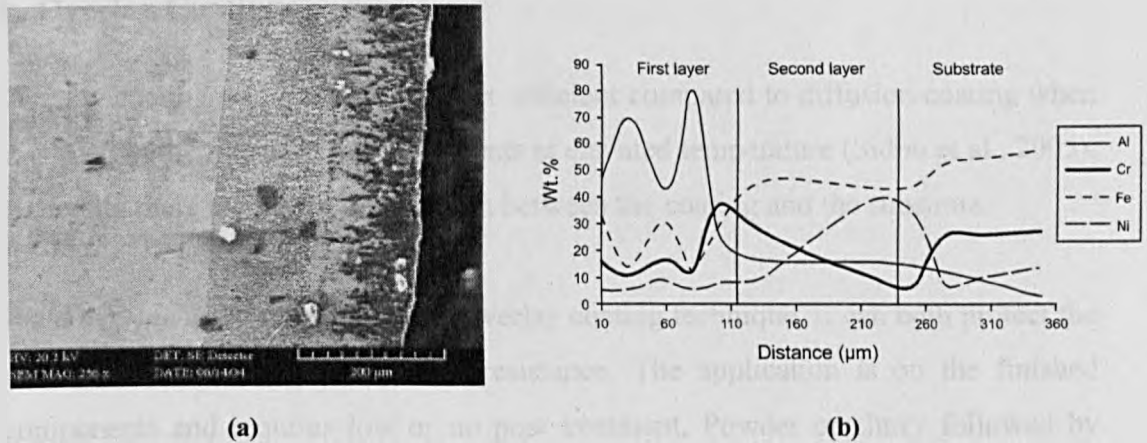


Figure 2.11 Aluminized HH309 stainless steel: (a) cross-sectional image, (b) concentration profiles of Al, Cr, Fe and Ni (Sharafi and Farhang, 2006)

Iron aluminide - based alloys coated with aluminizing pack coatings showed improving resistance against high temperature oxidation and cyclic oxidation (Juzon et al., 2007). The coatings were prepared by using a powder mixture composed of Al_2O_3 82 wt%, Al 15 wt% and NH_4Cl 3 wt% under an Ar atmosphere at $1,000^\circ\text{C}$ for 5 hours. The samples were then tested at the temperature of $1,100^\circ\text{C}$. Zr addition in the substrate alloy improves the adherence of the $\alpha\text{-Al}_2\text{O}_3$ layer. It also reduces the rate of scale growth by blocking the outward diffusion of Al cat-ions through the grain boundaries, and simultaneously enhances O_2 diffusion. The coating layer can be divided into 3 layers: (1) FeAl_2 , (2) FeAl , (3) interdiffusion zone.

Chromizing coating is another type of diffusion coating. It can be applied either by the pack process or a gas phase diffusion process. Coatings of chromizing coupled with aluminizing are under development.

Carburizing, nitriding and its combination are the most widely used surface modification techniques. They increase the wear resistance, and also improve the fatigue properties of materials. Co-application with aluminizing might produce a great resistance to high temperature erosion and corrosion.

b. Overlay Coatings

Overlay coating was found to be more efficient compared to diffusion coating when it is used in the aggressive environments at elevated temperature (Sidhu et al., 2005). Generally there is no alloying reaction between the coating and the substrate.

Weld overlay is the most important overlay coating technique. It can both protect the material surface and provide wear-resistance. The application is on the finished components and requires low or no post treatment. Powder or slurry followed by flame or laser melting achieve a thinner coating. However, thermal stress cracking is possible and care should be taken.

Roll bonding, explosive bonding, hot isostatic pressing, and coextrusion create metallurgical bonds between the protective coatings and the substrate at relatively low temperatures. These coatings are applied as a thin sheet or foil except for coextrusion coating which is relatively thick. The advantage of these methods is that the coating material can be controlled. However, weld overlay essentially substitutes these techniques at joints.

Flame and plasma spraying techniques melt the coating material by injected it into a flame or plasma, then the droplets are projected toward the substrate surface. The quality of coating is governed by the atomization, the melting of the coating particles, the oxidation of the droplets and the impact velocity. Application with a spraying gun allows these techniques to be applicable for large scale components. It is easy to repair or reapply. However, the coatings are generally porous and have poor bonding with the substrate. Methods such as using a base coating, hot isostatic pressing, or surface remelting can be used to improve the density.

The *Vacuum plasma spraying technique (VPS)* which reduces the pressure during the process can provide a more dense coating because it increases the impact velocity and might also limit oxidation. However, the price for large components is not economic.

High-velocity oxy-fuel (HVOF) spraying Technique is a new and promising technology. In comparison with VPS, it is cheaper and flexible and could provide coatings having low porosity, high hardness, high yield stress, high abrasive resistance, and great high temperature corrosion resistance. The coating particles are fed into a hot gas stream where they are melted. Then they are applied to the substrate surface by using a spray gun that injects particles at a supersonic velocity. Fuel gases can be hydrocarbon or pure H₂. Further tests of this coating in real aggressive environments are needed (Sidhu et al., 2005).

Vapour Deposition and Related Techniques can produce very high quality and reliable coatings. However, a high vacuum chamber is essential so the cost is very expensive. Physical vapour deposition involves evaporating elements from the source to form coatings in a high vacuum chamber, and condensing of these elements on the components. Similarly, chemical vapour deposition consists of volatilisation of molecules containing coating elements, decomposition of these molecules, and deposition of the coated element on the surface. Related technique such as **ion plating** is the process where volatilized atoms are ionized and a potential difference between the coating source and the substrate is created. The **Sputtering** technique dislodges atoms from the coating source by bombarding them with inert gas ions. Reactive species might be introduced into the vapour of coating elements so that a compound is formed that deposits on the surface.

Oxide deposition applies coatings either as an aqueous solution or a gel (usually of nitrates) on the warm substrate material. The nitrate coating is then decomposed and the oxide is formed on the surface when the system is heated up to a temperature of approximately 400°C. **Chromating** occurs when Cr₂O₃ coatings are created from hot chromate solutions.

c. Ion Implantation

High energy ions of coating material bombard the substrate surface and penetrate deep into the substrate for a few nanometres. This is followed by annealing at moderate temperature in order to mend the damage from the collisions. Applications are, for example, Y and La implantation on the heat-resisting alloys.

d. Other surface Modification Methods

Surface remelting followed by rapid solidification produces a chemically homogeneous structure of single phase that is either microcrystalline or amorphous. For the best results, a laser is widely used together with surface chemical modification processes such as boronizing which induce the growth of an amorphous layer.

Cold working and recrystallization forms a very-fine-grained surface on the components. The protective oxide is well formed by the rapid diffusion paths through the metal grain boundaries.

2.8 Summary

The presence of species such as alkali, chloride, sulphur and heavy metals in the deposits derived from burning fuels like biomass and MSW leads to serious corrosion problems in heat and power generation plants. The steam temperatures are kept lower than approximately 450°C to avoid these problems, and hence limit the plant's efficiency. Methods to prevent or control high temperature corrosion must be studied.

Work carried out so far by other researchers, have only studied the mechanisms of corrosion, the use of higher grade alloys and coatings for high temperature applications in simulated conditions in the laboratory, or only for short exposure periods in real plants. Therefore, the application of new high grade alloys and the application of coatings need further investigation in real plant conditions, with longer exposure periods.

CHAPTER 3

THEORETICAL CONSIDERATION

This chapter lays out the principal knowledge required for the study of high temperature corrosion in the energy systems. It begins with the sections of mechanisms related to the fly ash formation and the ash deposition followed by the models of heat transfer in the deposits. Then, it moves on to the corrosion topics comprising the electrochemical reactions for corrosion, and the forms of metallic corrosion. Finally, the theory of analytical techniques for deposit study as well as corrosion products is presented.

3.1 Mechanisms of Fly Ash Formation

The formation of fly ash in the coal combustion process depends on the fuel characteristics and the operating conditions in which the ash is developed. The inorganic elements in the coal are the governing constituents and they are composed of both the mineral matter present either in crystalline or amorphous form, and the organically-bound elements such as Na, K and Ca.

The mechanisms of ash formation begin with the decomposition of fuel, followed by different processes undergone by inorganic constituents such as fusion – coalescence – agglomeration, separation – fragmentation, vaporisation, condensation, quenching, and solidification (Couch, 1994). A schematic diagram illustrating the mechanisms of fly ash formation in the coal combustion process is shown in Figure 3.1.

The fly ash created in biomass combustion processes typically has a bimodal particle size distribution: (1) the coarse fly ash having particle size ranges from 1 μm up to about 250 μm , and (2) the aerosol fraction consisting of particles with a size smaller than 1 μm . Coarse fly ash is simply entrained into the gas stream from the fuel bed

whereas the formation of aerosol is more complicated and affected by the presence of the coarse fly ash (Obernberger and Brunner, 2005; Kaer et al., 2006).

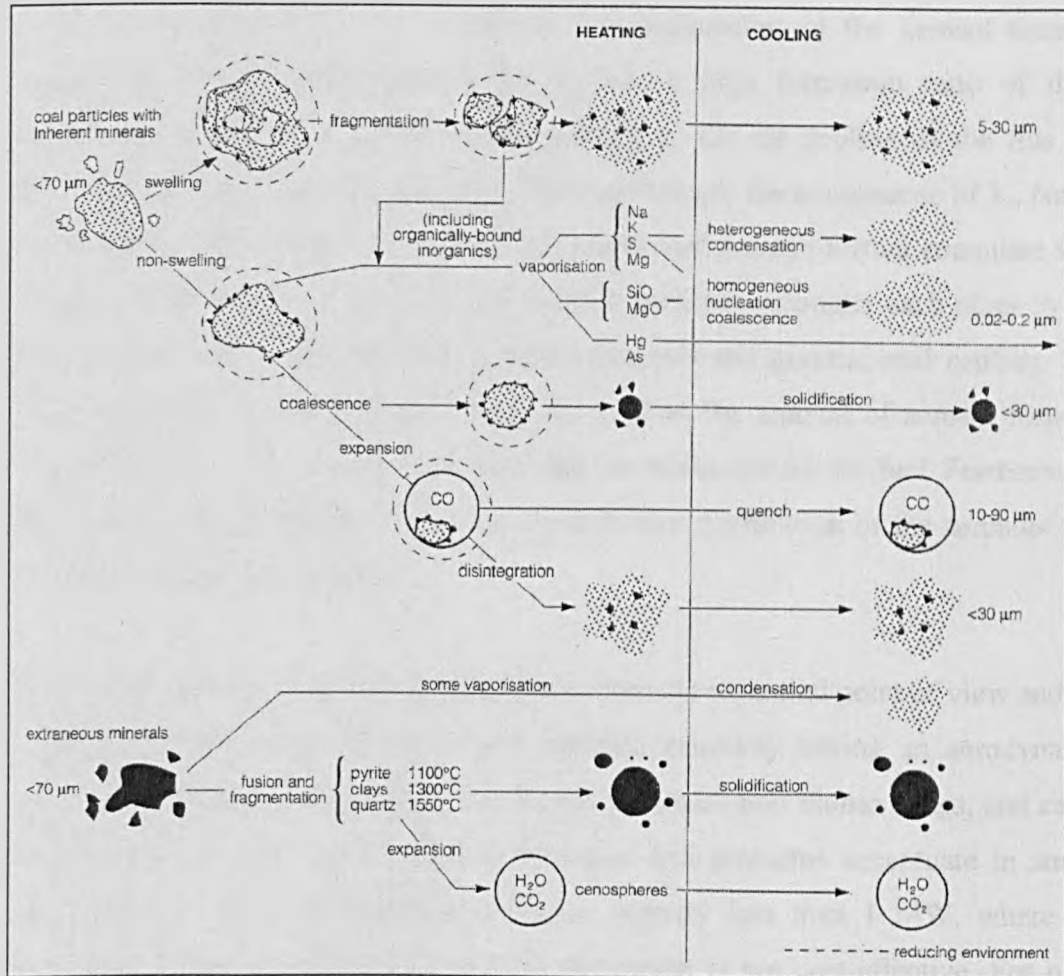


Figure 3.1 Mechanisms of fly ash formation in the coal combustion processes (Couch, 1994)

The coarse fly ash has 2 forms: porous irregular shaped particles and spheres. Particles in the first group are composed of the non volatile inorganic matrix and mainly consist of Ca, K and O and to a lesser extent of Mg and P. Small amounts of heavy metals such as Zn, and Pb compounds as well as Cl and S are also found on the surface of these particles as the result of condensation of the vapour phases. Particles in the latter group, spherical particles, often contain mineral impurities and consist mainly of Ca, Si, Mg, Al and O. The formation of coarse fly ash depends on the characteristics of the fuel, the combustion technology, the load on the combustion unit, and the conditions in the fuel bed. Generally, the amount of coarse fly ash is lower when the fuel has: less ash content and a smaller particle size, the

operation is fixed-bed rather than fluidised bed, operating load is smaller, and the primary combustion air is distributed appropriately.

Aerosols are formed by the nucleation or condensation of the aerosol forming vapours on the existing surfaces due to: (1) a high formation ratio of these compounds which increase the partial pressure or (2) the cooling of the flue gas which reduces the saturation pressure. The vapours are the compounds of K, Na, S, Cl as well as Zn, Pb and Cd. The newly formed particles can further coagulate with others or with coarse fly ash particles as these particles encounter each other by the Brownian motion, turbulent eddies, thermophoresis and gravitational settling. The mass of aerosols formed in the system depends on the amount of aerosol forming species (K, Na, S, Cl, and heavy metals) that are released from the fuel. Furthermore, the mass produced directly affects the particle size distribution of the aerosols as a result of coagulation process.

The aerosol fraction is of most concern from both the industrial point of view and the study of human health effects. These particles generally having an aerodynamic diameter less than 10 μm (PM_{10}), can deeply penetrate into human lungs, and cause adverse health effects. The emission increases and problems accentuate in small-scale plants, notably with plants having a capacity less than 1 MW, where the installation of efficient pollution control equipment is not cost-effective. For plant operators, the problems often relate to the constituents present in aerosols, notably alkalis, S, Cl and heavy metals. Compounds of these elements significantly contribute to the slagging, fouling and subsequently hot corrosion of the heat exchanger systems.

One method to tackle these problems is to predict the formation of these aerosols and their behaviour in the furnace by using the mathematical modelling or computational software (Baxter et al., 1998; Delay et al., 2001; Swithenbank et al., 2005; Ryu et al., 2006; Poole et al., 2008).

Figure 3.2 shows a schematic diagram of the ash formation mechanisms in the biomass combustion processes.

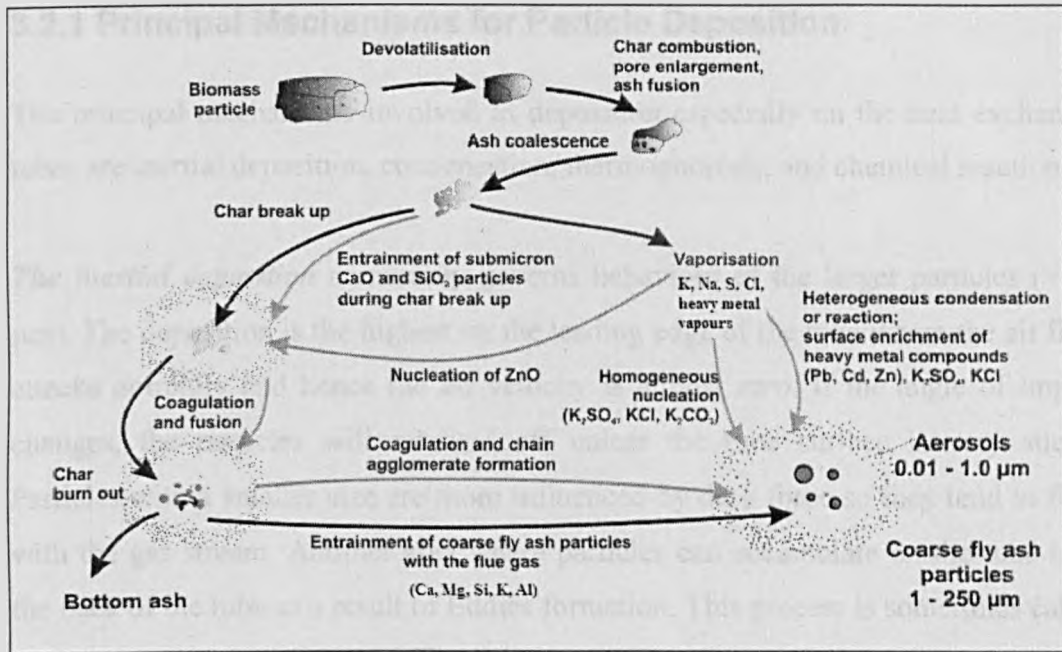


Figure 3.2 Mechanisms of fly ash formation in the woody biomass combustion processes (Oberberger and Brunner, 2005)

3.2 Deposition Mechanisms

The actual deposition mechanisms in each energy system depend on various factors as follows (Couch, 1994; Wang and Harb, 1997; Joller et al., 2007):

1. Chemical and physical characteristics of the fuel,
2. Operating conditions of the furnace including gaseous temperature, residence time, fluid dynamics, the locally oxidizing or reducing environment and the use of soot blowing,
3. Transport mechanisms of the gaseous phases including molecular and Brownian diffusion, thermal diffusion, eddy diffusion, gravity effects, and electrostatic effects,
4. Fly ash particles and aerosols characteristics such as physical state, particle stickiness, particle size, and momentum.
5. Conditions of heat transfer surfaces such as the ash and wall stickiness

The deposition always occurs simultaneously with erosion, shedding and re-entrainment of particles. These processes strongly influence the extent of deposition. Generally, the larger particles are assumed to rebound more and for several times before deposition compared to the submicron particles.

3.2.1 Principal Mechanisms for Particle Deposition

The principal mechanisms involved in deposition especially on the heat exchanger tubes are inertial deposition, condensation, thermophoresis, and chemical reaction.

The inertial deposition commonly governs behaviour of the larger particles ($> 10 \mu\text{m}$). The deposition is the highest on the leading edge of the tube where the air flow attacks normally and hence the air velocity is almost zero. If the angle of impact changes, the particles will rebound off unless the tube surface is very sticky. Particles with a smaller size are more influenced by drag force so they tend to flow with the gas stream. Another area where particles can accumulate on the tube is at the back of the tube as a result of Eddies formation. This process is sometimes called 'turbophoresis'. The Eddies effects are greater in the region having a higher gas velocity in the lower temperature regions such as at the economiser panels.

Condensation occurs when the gaseous phases or vapours come into contact with a cool surface. The surface areas can be the heat exchanger surface, the entrained particles, or the deposited particles. In general the condensed deposits are uniform and smooth. The condensed layer may be sticky due to the radiative heat from the furnace, or insufficient heat transfer through the thick deposit layer.

Thermophoresis is where particles migrate to the cool surface due to a steep temperature gradient between the gases and the surface (of the wall or heat exchanger tubes). The movement force arises in the gases and acts on the particles themselves. This mechanism affects mainly the small particles. The adherence increases when the particles are sticky, the surface is rough, or there is chemical reaction involved. The deposits that result from this mechanism are finer and more evenly distributed than those from inertial deposition.

Another similar mechanism that may contribute to the particle deposition is electrophoresis. Particles may be held on to the surface by a combination of Van der Waals and electrostatic forces.

Chemical reaction takes place when a particle reaches the tube or the deposit surface. It controls the growth of deposit as well as the physical state of the deposit surface. The important reactions include

1. Oxidation of the residual char that is entrained in the gas stream with the inorganic part can reduce C in the fouling to less than 2% and almost none in the slagging.
2. Sulphation: especially the sulphation of NaOH, KOH, NaCl, and KCl.
3. Alkali absorption: Si absorbs alkalis and forms silicate compounds (Alkali-SiO₂) which have a much lower melting temperature compared to Si.
4. The formation of low temperature eutectics by species of alkali salts, and heavy metals.

Chemical reactions are significantly affected by the temperature. Therefore, the magnitude and the rate of reactions vary by the location in the furnace.

3.2.2 Slagging and Fouling

Slagging is the deposition that takes place in the region where radiative heat transfer is dominant. Therefore, the target components include the burners, the main boiler waterwalls, the bottom hopper and the bottom of the first banks of heat exchanger tubes. In general, the waterwall surface has a temperature of 200 to 400°C. Firstly, dry powdery particles are deposited on the surface. Then, the surface will become so sticky that most of the particles that come into contact are retained. Hence, the slagging generally has an overall chemical composition similar to the bulk fly ash in the region, especially near the surface. Once the deposit is thick enough, the temperature of the deposit surface increases until eventually it turns into a so-called running layer. This fluid may contain either melted compounds or amorphous phases containing small solid particles. It can be partially vaporized later on.

Fouling occurs in the regions where convective heat transfer prevails. For high temperature fouling such as in the superheater and reheater regions, the major bonding components in the deposit tend to depend on the presence of silicate liquids, whereas sulphate compounds are the main components for lower temperature fouling, such as in the economiser area. The fouling begins with the deposition of condensed vapours, notably of alkali metals (Ca, Na, or K) that may be in the

compounds as sulphates as a result of reactions between alkali oxides or hydroxides and gaseous SO_3 . Low melting temperature eutectic compounds can also be formed. As the deposit thickness increases, the surface temperature subsequently increases and the surface becomes sticky. Hence, almost all impacting particles are captured, particularly at the leading edge where gas stream attacks normally. Consequently, fouling is composed of several deposit layers that have different chemical compositions, microstructure, porosity, and particle size. The typical structure of fouling is shown in Figure 3.3.

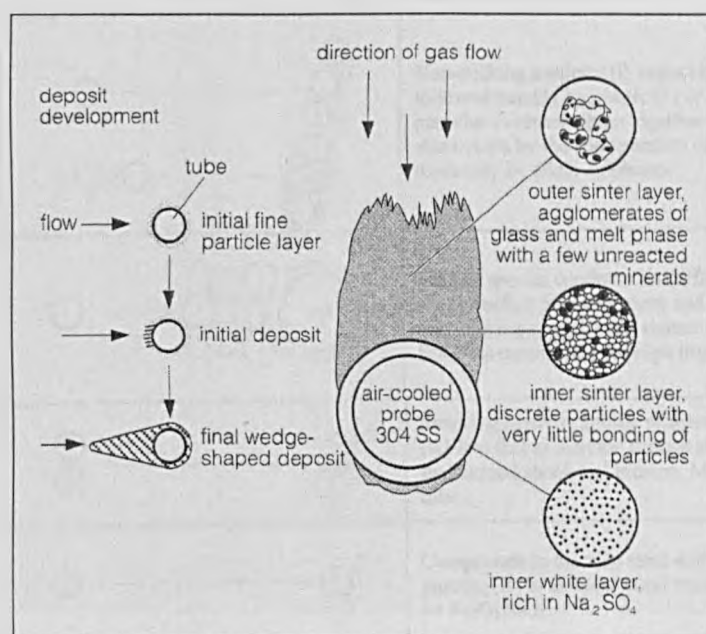


Figure 3.3 Typical structure of a fouling deposit (Couch, 1994)

Potential mechanisms that govern the formation of fouling and slagging are presented in Table 3.1.

3.3 Heat Transfer through Deposits

The initial layer of deposit, adjacent to the heat transfer surface, generally consists of a continuous phase of condensed vapours and discrete solid particles. This layer has high porosity, and therefore its thermal conductivity is very low compared to the outer layer that often occurs as a fused solid continuous phase. As a result, this inner layer largely contributes to the overall effective thermal conductivity of the deposit.

Table 3.1 Potential mechanisms for the formation of fouling and slagging (Couch, 1994)

Mechanism	Schematic diagram	Description
Adherence to a sticky surface		Particle impacts with a sticky or fluid surface and is held there. It tends to coalesce with the material on the surface
Condensation on ash particles		Vapour condensed on non-reactive particle (P): vapour of Na ₂ SO ₄ on quartz particle
Surface reaction on ash particles		Condensate on surface reacts with reactive particle (R) to form plastic product: NaCl condensate on Al ₂ O ₃ .6SiO ₂ particle
Plastic flow		Plastic particle (P) deforms to conform with surface, becomes mechanically attached, and may react later: CaSO ₄ at 540-815°C
Cementation on surface		Non-sticking particles (I) impact the surface followed quickly by plastic (P) or liquid (L) particles to cement them together. Cementation also occurs by the condensation of vapour species especially by alkali sulphates.
Surface condensation		Vapour species condense on surface to provide a sticky surface for entrapment and cementing of non-sticking particles (I): vapour of Na ₂ SO ₄ . Build-up occurs only for high impact angles.
Sintering on the surface		Sintering between similar or dissimilar particles (R1 and R2) to increase deposit strength against the thermal shock and erosion. May include the tube.
Reaction with target tube		Compounds in the tube react with impacted particle (R) to increase bond strength: Fe ₂ O ₃ +SiO ₂ → Fe ₂ O ₃ .SiO ₂
Incomplete reaction due to short residence time		Inadequate residence time in the combustor for complete reaction leaves sticky surface: incompletely burned coal particles covered in tars.
Reducing reactions		Reduction by carbon particles (C) will lower the viscosity if iron (or other reducible oxide) is present. Typical reduction of fouling temperature is 90°C.
Deposition/Erosion		Mildly fouled surface by gassy siliceous particles (P) of high viscosity (e.g. 104 poise) may be eroded by semi-inert particles (I) of high abrasiveness such as mullite or quartz.
Temperature gradients in the deposit		For constant tube temperature, surface sintering increases with gas temperature.

A schematic diagram of heat transfer from the flue gas to and through the deposits is shown in Figure 3.4. In the utility boilers, heat is initially transferred from the hot flue gases (T_g) to the deposit surface (T_d) by radiation and convection. Then it is conducted through the deposit, and through the tube wall (T_t). Finally, heat is transferred to the steam (T_s) by convection (Zbogar et al., 2005).

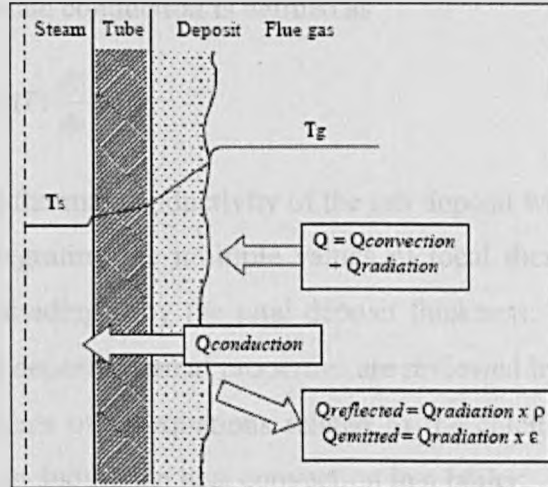


Figure 3.4 Heat transfer to and through ash deposits (Zbogar et al., 2005)

The heat transfer through the heat exchanger is interrupted by the deposit mainly because of the insulating nature of the deposit, and because the deposit changes the radiation properties of the surface. The overall heat transfer equation is

$$Q_{conduction} = Q_{convection} + Q_{radiation} - Q_{reflected} - Q_{emitted} \quad \text{Equation 3.1}$$

If the heat conduction through the tube wall and steam film is neglected, and the flame emissivity is assumed to be unity, then Equation 3.1 for a cylindrical geometry tube can be written as follows:

$$Q_{conduction} = \frac{T_d - T_t}{\frac{d_d}{2\pi k_d} \ln \frac{d_d}{d_{to}}} = h_{conv}(T_g - T_d) + \alpha \cdot \sigma \cdot T_g^4 - \epsilon \cdot \sigma \cdot T_d^4 \quad \text{Equation 3.2}$$

Where T_d is the temperature at the deposit surface, T_t is the temperature of the tube wall, T_g is the temperature of flue gas, d_d equals to sum of the tube diameter and the deposit thickness, d_{to} is the outer tube diameter, k_d is the thermal conductivity of deposit layer, α is the surface absorptivity, ϵ is the surface emissivity, σ is the Stefan-Boltzmann constant ($5.67 \times 10^{-8} \text{ W/m}^2\text{K}^4$). From this equation, heat convection

from the flues gases to the deposit and conduction through the deposit are the prevailing thermal resistances in the overall heat transfer (Zbogar et al., 2005).

The thermal conductivity of ash deposit is often represented by an effective thermal conductivity, k_{eff} . It concerns both the conductive and radiative heat transfers that may occur either in parallel or in series. The effective thermal conductivity for one-dimensional steady-state conduction is defined as

$$\frac{dQ}{dy} = -\frac{d}{dy} \left[k_{eff}(T) \frac{dT}{dy} \right] = 0 \quad \text{Equation 3.3}$$

The overall effective thermal conductivity of the ash deposit with different layers can be calculated by integrating the multiple values of local thermal conductivity and thickness and then dividing it by the total deposit thickness. Numerous models for estimation of the ash deposit thermal properties are reviewed by Zbogar et al. (2005). The paper also presents other equations related to the calculation of heat transfer through the deposit, including the heat convection in a boiler.

The thermal properties of the deposit, particularly its thermal conductivity and the surface emissivity, are the most important factors in the calculation of heat transfer. These properties are directly affected by the deposit physical structures such as the particle size distribution, the porosity and the degree of sintering. The conductive properties depend on deposit properties throughout the whole thickness whereas the radiative properties depend exclusively on the condition at the deposit surface. The emissivity is mainly affected by the surface nature (particulate, partly fused or completely molten), the size distribution of particles in the surface layer, and the chemical composition (colour of the deposit). The effects of important factors controlling the thermal properties of the deposit are explained in detail as follows:

a. Effect of Temperature

Rising temperature directly increases the thermal conductivity of the deposit due to the change of void space between particles. The high temperature can also increase the particle size at the deposit surface due to sintering, and as a result the emissivity is increased.

b. Chemical composition

The chemical composition indirectly affects the deposit structure at a given temperature. An example is the lower sintering temperatures that occur in a deposit containing Si and Fe. Sintering can increase the thermal conductivity of the deposit. The emissivity is also affected by the presence of colouring agents (e.g. Fe) in the deposit, which results in increasing absorptivity. The change of particle size distribution by sintering also has an influence on the emissivity.

c. Particle size

Increase in particle size leads to an increase in the effective thermal conductivity particularly at high temperature (above 800 K). For the emissivity, effects of particle size always link with the sintering process. Under the sintering temperature, an increase in particle size results in less reflection of the incident radiation, and consequently an increase in the emissivity. The relationships between the growth of deposit and its thermal properties are shown in Figure 3.5. Below the sintering temperature, the emissivity decreases when the temperature increases, and then increases sharply as the sintering and fusion of ash occur at the higher temperatures.

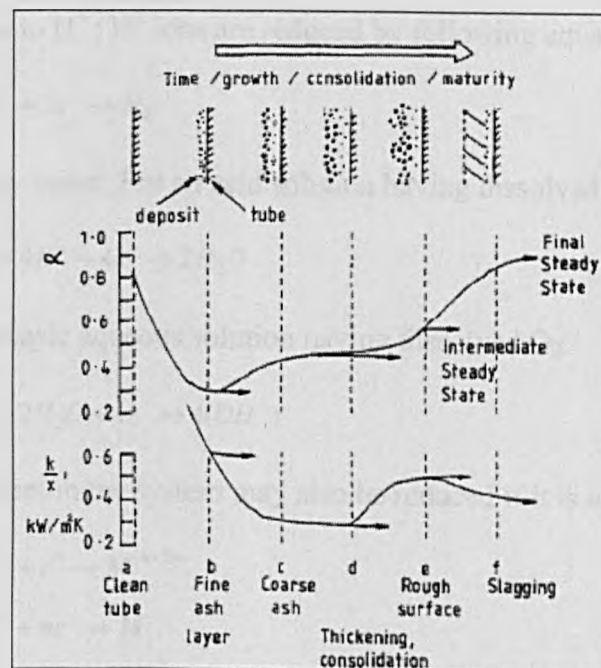


Figure 3.5 Expected trends in deposit properties during their growth (Wall et al., 1995)

d. Porosity

Porosity in the deposit is often affected by the sintering condition and time. A decrease in porosity generally increases the effective thermal conductivity.

3.4 Electrochemical Corrosion Reactions

Metallic corrosion is normally electrochemical in which there is transfer of electrons from one chemical species to another. The reaction where metal atoms lose electrons is called an oxidation reaction. The reaction can be written as shown in Equation 3.4 – 3.6. The site where oxidation takes place is called the anode. Therefore, the oxidation reaction is sometimes called an anodic reaction.



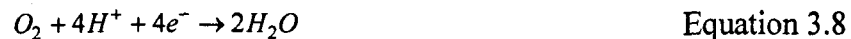
For examples; $Fe \rightarrow Fe^{2+} + 2e^{-}$ Equation 3.5



The electrons generated from the oxidation are then transferred to another chemical species, resulting in a reduction reaction. The location at which the reduction takes place is called the cathode. For example, metals in acid solutions are oxidized and their ions are given to H^{+} ; H^{+} ions are reduced by following equation:



Other reactions may occur. For an acid solution having dissolved O_2 :



Or for a neutral or basic aqueous solution having dissolved O_2 :



Any metal ion present in the system may also be reduced if it is a multivalent ion:



The sum of the oxidation reaction and the reduction reaction is the overall electrochemical reaction. For every corrosion system, the net electrical charge

transferred between cathode and anode equals zero; the total rate of oxidation must equal the total rate of reduction (Callister, 2007).

3.5 Forms of Metallic Corrosion

Metallic corrosions can be categorized by their physical appearance into 9 groups: uniform attack, galvanic corrosion, crevice, pitting, intergranular corrosion, selective leaching, erosion-corrosion, stress corrosion cracking, and biological corrosion (Callister, 2007; Schweitzer, 2007). The mechanisms for each corrosion form are explained as follows:

3.5.1 Uniform Corrosion (General Corrosion)

Uniform attack is the most common corrosion form. It occurs over the entire exposed area at an even corrosion rate. The rate of corrosion is predictable therefore the corrosion control system can be designed easily. The mechanisms are metal loss due to chemical attack or the dissolution of the metallic component into metallic ions. In high temperature processes, metal loss is usually a result of metallic oxide formation (un-protective scale) rather than simple loss of metallic ions. Metal can resist this general corrosion by forming a protective or passive film on the surface when it is exposed to air for a certain period of time. The efficiency of the film depends on the composition, temperature and the aggressiveness of the surrounding environments.

a. Passive Film on Fe

The oxide film on Fe consists of Fe_2O_3 and Fe_3O_4 . The Fe_2O_3 layer accounts for the passivity, while the Fe_3O_4 layer is an essential state required for the formation of a higher oxidizing state. This formation occurs at a relatively slow rate compared to the rapid formation on Ni. The thickness of the oxide layer is 1 – 4 mm.

b. Passive Film on Ni

The oxide film on Ni can be formed faster than that on Fe but results in a thickness of 0.9 – 1.2 mm. There are two theories regarding its composition: (1) it is NiO with

a small content of nonstoichiometry which increases Ni^{3+} cation vacancies, or (2) it is composed of an inner layer of NiO and an outer layer of anhydrous $\text{Ni}(\text{OH})_2$.

The nickel oxide film in Ni-based alloys has a good corrosion resistance against cyclic exposures to high temperatures, reducing environments both with acids and alkalis, carburizing environments, and nitriding, when alloyed with Cr and Fe. Additionally, Ni-based alloys have a high resistance to thermal fatigue and can maintain an austenitic structure. However, this passive film does not have a good corrosion resistance in oxidizing environments containing HNO_3 , chlorides or halides.

Additions of some other elements into material can improve the stability of the oxide film and improve the corrosion resistance (Mankins et al., 1990). Cr provides both oxidation and carburization resistance at temperatures higher than 760°C in Ni-Cr alloy (>15% Cr). It promotes the formation of a protective surface oxide and enhances sulphidation resistance at high temperature. Fe reduces the susceptibility to internal oxidation when the alloy is in atmospheres that are oxidizing to Cr but reducing to Ni. Mo and Ni offer higher degrees of nobility and resistance to chloride pitting and crevice corrosion. Co provides a low coefficient of expansion, a constant modulus of elasticity, and high strength in a Ni-Fe matrix. Al, Nb, Ta and Ti are used to stabilize reactions with C. This prevents precipitation of Cr_3C_2 which causes a depletion of corrosion-resisting elements in the area surrounding the grain boundary of austenitic stainless steels (C-Fe-Cr). W combines excellent high-temperature strength with outstanding resistance to oxidization environments up to 1150°C . It also helps to protect against Cl-induced corrosion.

c. Passive film on Austenitic Stainless Steel

The passive film on austenitic stainless steel consists of an inner layer of oxide film and an outer deposit of hydroxide or salt film. The film formation initiates by the rapid formation of surface-absorbed hydrated complexes of metals, followed by the reaction with water forming a hydroxide phase. Finally, this hydroxide phase deprotonates to form an insoluble surface oxide film. Components such as Cr, Ni, Mn and N significantly contribute to its passivity (Schweitzer, 2007).

3.5.2 Galvanic Corrosion (or Dissimilar metal Corrosion)

Galvanic corrosion occurs when two different metals are electrically connected while they are surrounded by a conductive solution (electrolyte). The electric potential difference created provides a driving force for the dissolution of anodic elements (higher electrically negative or less noble) and reduce the dissolution of cathodic elements (lower electrically negative). An example is the corrosion of steel tubes when they are jointed with Cu in a domestic water heater. The evaluation of corrosion and the galvanic flow are possible by considering the galvanic series. The prevention methods include (1) select closer metal components in the galvanic series if the coupling of dissimilar metals is required, (2) provide anode components with a large area, (3) electrically insulate the components, and (4) use sacrificial components that are anodic metal.

3.5.3 Intergranular Corrosion

Intergranular corrosion is a localised corrosion where the grain boundary and/or the adjacent zones are preferentially attacked. The corrosion often takes place rapidly and the damage is detected at a deep level from the surface. It leaves components with less ductility and strength, and finally the components disintegrate. The causes of this corrosion are (1) segregation of specific elements or compounds at the grain boundary (Al, or Ni-Cr alloys), (2) enrichment of an element at the grain boundary (brass), and (3) depletion of the corrosion resistant element at the grain boundary (stainless steel). The most common intergranular corrosion is carbide precipitation. This takes place both in stainless steel as a result of welding (weld decay) and in the Ni-based alloys. Other heat treatments and thermal processing including stress relief also create the possibility for this type of corrosion. The prevention approaches are: reducing the C content in alloys as well as adding some elements such as Nb, Ti and Ta to prevent the precipitation of chromium or molybdenum carbides (for example, Cr_3C_2 and Mo_3C_2).

3.5.4 Crevice Corrosion

Crevice corrosion is a localised corrosion that takes place at (1) areas having local differences in O_2 concentrations, (2) areas covered under deposits, (3) gaskets, lap

joints, crevices or voids where liquid can be trapped and become stagnant. Crevice corrosion occurs on any metal in any corrosive environment. Once it starts, the process is rapid, especially in the presence of Cl. The corrosion process inside the crevices starts off with the same mechanisms as at other exposed areas and continues until O₂ is depleted. Then, the electrons escape to further areas where there is sufficient O₂ for reduction by passing through the metal. This leads to a concentration cell (differential aeration) between the crevice and the other areas. The concentrated cations inside the crevice significantly induce Cl⁻ to migrate resulting in the formation of OH⁻ and HCl. Consequently, newly formed acids destroy the passive film and accelerate the dissolution of metal inside the crevice. The control methods include (1) using proper design of the components to avoid gaps or crevices, (2) avoiding operation under high temperature conditions and in the presence of Cl or acidity, (3) preventing the accumulation of deposits, and (4) using improved alloys to which have been added corrosion resistant elements such as Cr, Ni, Mo and N.

3.5.5 Pitting Corrosion

Pitting is a localised form of corrosion that causes rapid loss of metal. It is hard to detect since the resulted pits are often covered by the corrosion products and the weight change is too small to detect. It can cause structural failure due to the localized weakening and stress concentration it created. Pitting corrosion often associates with other types of corrosion, especially crevice corrosion. The corrosion rate is very rapid once it starts and the mechanisms are accelerated in the presence of halide ions. Pitting corrosion can occur in: areas where dissimilar metals are attached, the metal surface having irregular chemical and physical structure, dirty surfaces, or on those areas where the flow is stagnant. It usually occurs on the upper surface and grows downward according to the gravity force. Stainless steels and alloys of Al are the most vulnerable components whereas carbon steels are more resilient. The performance of alloys against pitting is often represented as pitting resistance equivalent number (PREN). This number is calculated as follows: $PREN = \%Cr + 3.3(\%Mo) + 30(\%N)$. A higher PREN number yields better pitting resistance.

3.5.6 Selective Leaching

Selective leaching occurs in the solid alloys where one element is preferentially removed from the matrix. The process is also called de-alloying or de-zincification. The most common example is the removal of Zn from a brass alloy leaving a porous skeleton of copper and corrosion products. It significantly reduces the tensile strength and the ductility. Selective leaching may occur in other alloy systems where Al, Fe, Co, Cr and other elements are susceptible.

3.5.7 Erosion-Corrosion

Erosion-corrosion is a combination of chemical attack and mechanical abrasion as a result of fluid movement. The degree of corrosion is higher when bubbles and suspended particulates are present in the fluid stream.

3.5.8 Stress Corrosion

Stress corrosion occurs when metal components undergo tensile stress under a corrosive environment. Cracks are formed and then grow perpendicularly to the direction of stress, possibly resulting in a brittle-like failure. It might be inherently initiated from the stress in alloys such as the residual stress from rapid temperature changes, or the difference in the coefficient of expansion in phases existing in alloys. An appropriate anneal treatment may be used to solve the problem. Other methods to decrease the stress such as reducing the external load or increasing the stress-bearing areas are also suggested.

3.6 Analytical Methods for Deposits and Corrosion

3.6.1 Scanning Electron Microscopy and Energy Dispersive Spectroscopy (SEM/EDS)

Samples are embedded in epoxy resin, cross-sectioned, ground and subsequently polished. Then they are carbon coated in order to avoid charging during analysis. The samples are bombarded by a high energy electron beam providing two types of images: secondary electron images (SE) and back scattered electron images (BSE).

Secondary electron images show the general topography or microstructure of the area whereas the back scattered electrons give information about the average atomic number of the focused spot. The higher level of brightness represents the elements that have a heavier molecular weight. X-ray mappings showing the chemical composition in layers of deposit or corrosion products can be created by this method (Hansen et al., 2000). The chemical compositions may be categorized into mineral categories as shown in Table 3.2. The work is suggested by the Combustion and Harmful Emission Control Research Centre (CHEC) (Frandsen, 2005).

The corrosion can be calculated by measuring (1) the thicknesses of internal attack, (1) the thickness of oxide layer, and (2) the thickness of the mixed layer (of K₂SO₄ and iron oxides) via using the BSE images from SEM. The results can be plotted against the exposure time in order to show the corrosion rate and corrosion behaviour of alloys (Nielsen et al., 1999).

Table 3.2 Suggested chemical classification developed by CHEC research centre (Frandsen, 2005)

Original coal-based CCSEM chemistry				Biomass	Waste
Quartz	Montmorill.	Ca aluminate	Apatite	K ₂ SO ₄	ZnCl ₂
Iron oxide	Illite	Pyrite	Ca-Al-P	K-Al silicate	Gypsum+ZnCl ₂
Periclase	Fe-Al silicate	Pyrrhotite	KCl	C-Ca silicate	ZnSO ₄
Rutile	Ca-Al silicate	Oxi. pyrrho.	Gypsum-rutile	KCl + silicate	Zn-Ca silicate
Alumina	Na-Al silicate	Quartz-pyrite	Gypsum Al-Si	K-Phosphate	Zn-Ca rich
Calcite	Alum. silicate	Clay-pyrite	Si-rich	K-Mg phos.	PbCl ₂
Dolomite	Mixed silicate	Fe-Cr oxide	Ca-rich	Uncl. chloride	Pb-rich chl.
Ankerite	Fe silicate	Cr-Fe oxide	Ca-Si rich	Uncl. sulphate	Ca-Pb rich
Kaolinite	Ca silicate	Gypsum	Unknown	Uncl. silicate	Pb-rich

In general, corrosion rates are assumed to be linear or parabolic. The linear rate law assumes that the diffusion has no limit and the chemical reactions at the metal surface are the rate-controlling step. The rate law for gaseous chlorine corrosion is traditionally regarded as being linear because the porous oxide layer formed provides no protection against further attack. Equation 3.12 describes the linear rate law:

$$x = k_1(T) \cdot t \quad \text{Equation 3.12}$$

Where x is the corrosion depth, t is the exposure time, T is the temperature, and k_1 is a constant. The parabolic rate law, presented in Equation 3.13, assumes that

corrosion is controlled by diffusion of gas-phase reactants through the corrosion product layer. Oxidation of metals is often governed by this law.

$$x_2 = k_2(T) \cdot t \quad \text{Equation 3.13}$$

For the reaction: $A(g) = bB(s) = C(s) + D(g)$, the value of $k_2(T)$ can be calculated from

$$k_2(T) = \frac{2 \cdot b \cdot D_e \cdot C_{Ag}}{\rho_B} \quad \text{Equation 3.14}$$

Where D_e is the effective diffusion coefficient of gas A through the 'ash layer', ρ_B is the molar density of B in the 'material', C_{Ag} is the gas-phase concentration of component A , and b is the stoichiometric coefficient (Levenspiel, 1972; Nielsen et al., 1999).

3.6.2 X-Ray Diffraction

X-Ray diffraction is principally used for qualitative and quantitative phase analysis such as for phase identification and for quantification of phase composition, and for determination of lattice parameters (Rafaja et al., 2008). It can also determine the residual stresses, preferred orientation as well as grain size. The results are achieved by measuring the elastic scattering of x-rays from crystal structures, and utilizing the Bragg's law (Equation 3.15). The diffraction data is interpreted by comparing with the results in a database such as the one provided by the International Centre for Diffraction Data.

$$n\lambda = 2d \cdot \sin \theta \quad \text{Equation 3.15}$$

Where n is an integer (>1), λ is the wavelength of x-rays, and moving electrons, protons, and neutrons, d is the spacing between the planes in the atomic lattice, and θ is the angle between the incident X-ray beam and the scattering atomic planes.

3.6.3 Simultaneous Thermal Analysis (STA)

Thermal analysis can be used to indicate the material properties as a function of temperature (Frandsen, 2005). STA requires the sample and an inert reference material to be placed in a furnace during a heating program, typically from 20 to 1,300°C at the heating rate of 10°C/min. The sample weight (by Thermogravimetry-

TG) and the sample temperature (by Differential Thermal Analysis-DTA or Differential Scanning Calorimetry-DSC) are continuously measured during the heat-up process. Heat produced or consumed by the sample, and chemical and physical processes occurring in the sample can be estimated from this analysis. The number of processes involved when ash is heated includes vaporization, crystallization, devitrification, phase transition, melting, etc. However, STA might not be able to provide quantification data related to the ash melting, especially when the ash contains a glassy structure.

3.6.4 High Temperature Light Microscopy (HTLM)

A high-temperature light microscope (HTLM) is used for monitoring the melting properties of ashes. The instrument consists of an electrically heated oven which can operate at variable heating rates, equipped with a microscope and a charge-coupled device (CCD) video camera. The influences of ash particle shape and composition on the melting behaviour are observed by varying the temperature and heating rate. An image processing program allow sequences of images to be saved and retrieved (Frandsen, 2005).

3.6.5 Inductively Coupled Plasma Optical Emission Spectrometry (ICP-OES)

ICP-OES can measure elemental concentrations to ppb (parts per billion) levels. It utilizes plasma to heat the analysing elements causing their electrons to be excited and raised to higher energy levels. When these electrons return to their ground states, they emit certain wavelengths of electromagnetic radiation. The measured radiations including their intensities are then compared with calibration curves previously constructed by standard solutions in order to give quantitative results of elemental component in the sample. The main advantage of this method compared to the atomic absorption technique is that it can analyse various elements at one time. With a relatively large signal and importantly the lowest detection limit it is suitable for analysis of a wide range of combustion samples (Iländer and Vaisanen, 2007).

CHAPTER 4 EXPERIMENTAL PROGRAM AND ANALYTICAL METHODOLOGY

4.1 Overview

The experimental program was carried out at a UK waste to energy plant. Two air-cooled sampling probes were designed and placed at different locations in the furnace in order to simulate the corrosion process taking place on the superheater tubes, and also to collect the deposits of combustion residues. Sampling probe sections were fabricated from different types of superalloys and were equipped with two corrosion control methods; a sacrificial baffle and aluminide coated alloy. After approximately 800 hours of exposure to hot flue gas, each probe was carefully disassembled. The alloy materials and deposit samples along with other combustion residues collected from this plant were analysed and characterized in our laboratories.

This chapter consists of two sections. The first section contains a description of the WTE plant, the fabrication and installation of the air cooled sampling probes, and samples of combustion residues collected from the plant. Finally, the second section looks into the analytical methodology and instrumentations used in this research.

4.2 Experimental Program at a UK Waste to Energy Plant

4.2.1 Description of the Plant

This research was carried out in a modern UK energy recovery facility using the mass-burn process to incinerate municipal waste at high temperature. The plant was first commissioned in December 1993, and was re-equipped with a new system to reduce NO_x emissions of in August 1998. The emissions released from the plant are well-controlled and meet the new European Directives, i.e. the integrated pollution control provisions of the environmental protection act 1990. The plant has the

capacity of handle 520,000 tonnes of waste per annum which results in electricity to serve 48,000 homes. The plant consists of 2 parallel incineration processes that run simultaneously. Each process line operates continuously for 6 months before it is shut down for a week of routine maintenance. A schematic diagram of the plant in question and its facilities are shown in Figure 4.1.

a. Control Room

The operation and the performance of the plant are controlled by a fully computerized system located in the control room. Manual intervention is also applicable as required. Technicians are available 24 hours a day to ensure the plant is operating efficiently with acceptable pollution emissions.

b. Waste Loading and Feeding System

Waste collected from homes in the neighbourhood and some businesses are transported to the plant by waste collection vehicles. On arrival and departure from the plant, the vehicles are weighed on the automatic weighbridge providing an accurate amount of waste input. The vehicles then proceed to the tipping hall where the waste is transferred into the waste bunker. The typical storage of this bunker is 4500 tonnes with a maximum capacity of 6000 tonnes.

Above the bunker, there are two semi-automatic cranes. These cranes are used to mix waste in the bunker to increase its homogeneity, and for carrying the waste to the feed hopper. Each crane can grab up to 5 tonnes of waste. Waste is sent through a feed chute, and is then directed to a sloped grate where it undergoes the combustion process at a burning rate up to 30 tonnes/h (per a process line). The calorific value of the waste is approximately 8.6 MJ/kg.

c. Furnace and Heat Recovery System

The furnace consists of 4 connected passes. The first pass of the furnace comprises mainly of an incineration grate system, air supply systems, and overboard region. Waste coming from the feed hopper falls onto a moving incineration grate where the combustion process begins.

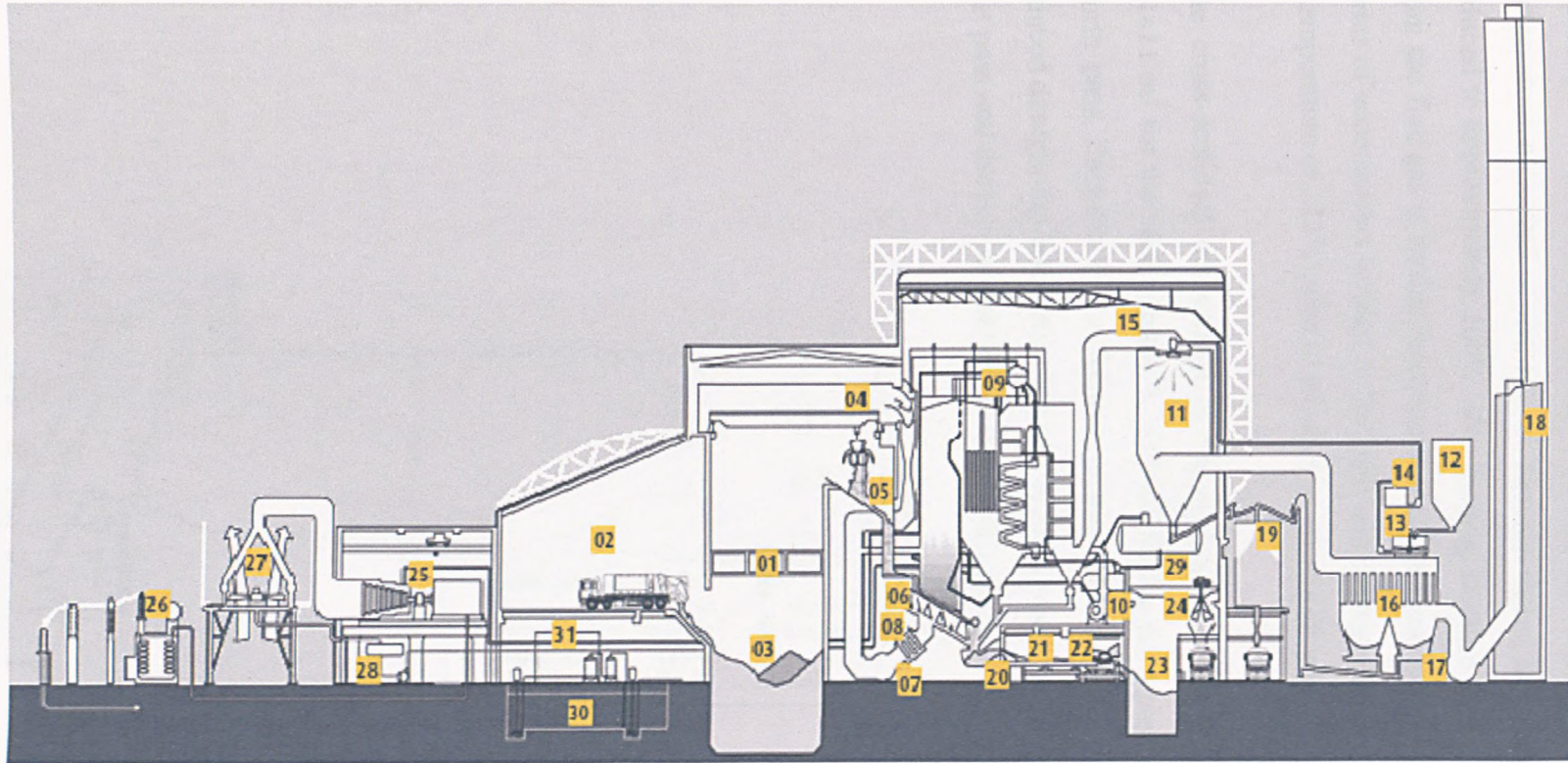


Figure 4.1 Diagram showing the components of the waste-to-energy plant

- | | | | |
|-----------------------|--------------------------------|-----------------------------------|--|
| 1. Control room | 9. Steam boiler | 17. Induced draught fan | 25. Steam turbine and generator |
| 2. Tipping hall | 10. Over fire fan | 18. Chimney stack | 26. Electrical substation |
| 3. Bunker | 11. Gas treatment scrubber | 19. Air pollution control residue | 27. Air cooled condenser |
| 4. Handling crane | 12. Lime silo | 20. Ash discharge | 28. Condensate tank |
| 5. Feed hopper | 13. Lime preparation | 21. Residue handling conveyors | 29. De-aerator |
| 6. Incineration grate | 14. Prepared lime storage | 22. Magnetic separator | 30. Water treatment plant |
| 7. Under fire fan | 15. Activated carbon injection | 23. Bottom ash pit | 31. Future heat exchanger for district heating |
| 8. Air heater | 16. Bag house filter | 24. Residue handling crane | |

The vigorously burning waste could reach a temperature of 1500°C. Gaseous products of the combustion flow up to the overboard region and subsequently to the second pass which consists of superheater panels as shown in Figure 2. The gas temperature measured at the top of furnace varies between 804 – 828°C and is reduced to approximately 500°C after passing through superheater panels. The heat from the flue gas is further recovered by a vaporizer located in the third pass, and a series of economisers located in the third and fourth pass. The resulting flue gas has a temperature of 227°C prior to an entry of plant's air pollution control system.

The cross-sectional dimensions of the furnace are 4.9×11 m² for the first pass, 4.4×11 m² for the second pass, 3.2×11 m² for the third pass and 3.0×11 m² for the fourth pass. Pressure in the furnace is controlled to approximately 0.5 bar by an induced draught fan installed at the end of the furnace. The schematic diagram of the first pass and the second pass of the furnace is shown in Figure 4.2.

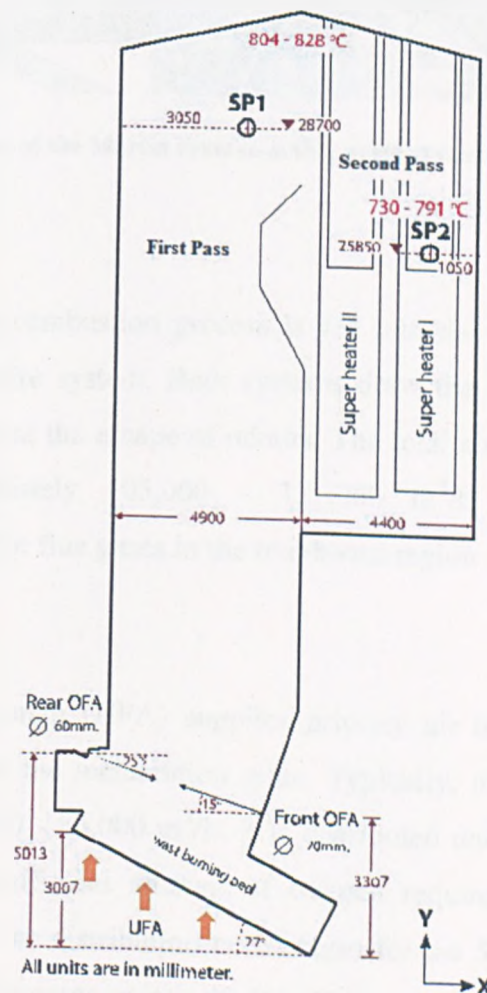


Figure 4.2 Schematic diagram of the furnace (side view) and locations of 2 sampling probes

The Incineration Grate

The incineration grate system used in this plant is a Martin reverse-acting grate. The grate is inclined at an angle of 26° in the direction of waste transport. The motion of Martin reverse-acting grate is illustrated in Figure 4.3. To start up the combustion process, a burner situated just above the grate heats up the furnace at the rate of 50°C/h for 12 -14 hours. When temperature is constantly high, the waste is then fed. The height of waste bed reduces from 60 mm at the beginning of the grate to 40 mm at the end.

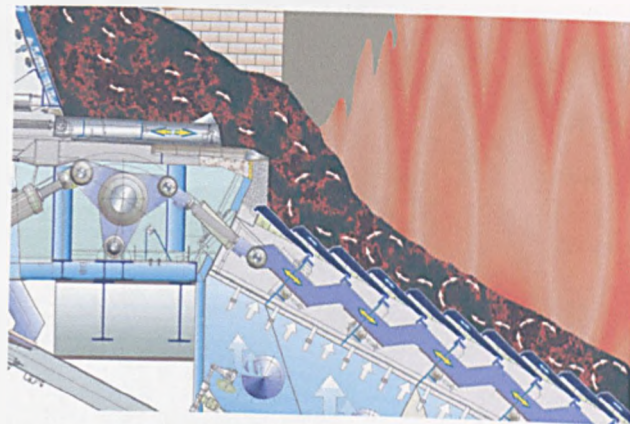


Figure 4.3 Motion of the Martin reverse-acting grate system (Martin GmbH, 2007)

Air Supply System

Air supplied for the combustion process is fed into the furnace by an under-fire system and an over-fire system. Both systems draw the air from areas above the waste bunker to prevent the escape of odours. The total air flow rate throughout the process is approximately $105,000 - 121,000 \text{ m}^3/\text{h}$. Consequently, the O_2 concentration of the hot flue gases in the overboard region is approximately 8.5% by weight.

The under-fire air system (UFA) supplies primary air to the furnace through 5 hoppers located under the incineration grate. Typically, the total primary air flow rate varies from $65,000 - 83,000 \text{ m}^3/\text{h}$. It is distributed unevenly to each hopper in order to provide a sufficient amount of oxygen required for each step in the combustion process. The distribution percentages for the 5 hoppers are 10.8% (the first part of the waste burning grate), 42.3%, 31.4%, 15.5% and 0% (the last part of

the waste burning grate). The air is pre-heated by an air heater to 125 – 140°C before it is sent through hoppers.

The over-fire air system (OFA) supplies secondary air to the furnace through a series of nozzles. These nozzles are located in the front and rear wall of the furnace just above the waste burning grate (Figure 4.2). The secondary air ensures complete combustion of waste and also provides a well-mixed and oxidizing atmosphere. The designs of the front and rear wall nozzles are different as summarized in Table 4.1.

Table 4.1 Designs of over-fire air nozzles

Design parameters	Total flow rate (m ³ /h)	Feed pressure (bar)	Diameter of nozzles (mm)	Number of nozzles	Average velocity of air (m/s per nozzle)
Front wall System	21,836 – 22,383	40	70	35	45.60
Rear wall System	16,664 – 16,745	45	60	33	49.73

Heat Recovery System

The heat recovery system, in the order of gas transport direction, consists of 2 superheaters located in the second pass, a vaporizer located in the third pass, and 2 economisers located in the third and the fourth pass. Heat recovered from the flue gas in each process line can produce approximately 80 tonnes/h of superheated steam. The steam leaving the superheater outlet has a temperature of 395°C and a pressure of 46 bars. It is then fed directly into a single 35 MW steam turbine generator.

Superheater: Corrosion and Prevention

The superheater tubes are made of a high temperature steel grade 15Mo3, according to DIN17175 (German Institute for Standardization). The tube has an inner diameter of 25.4 mm and an outer diameter of 38 mm, resulting in a thickness of 6.3 mm. Corrosion on the surface of superheater tubes, as shown in Figure 4.4, is commonly encountered due to the high temperature and extremely corrosive environment in the furnace. Deposition of particles on these tubes also significantly contributes to corrosion problems. These corroded superheater tubes would be replaced or

equipped with one of the corrosion control techniques during the plant's bi-annual maintenance.

There are two corrosion control techniques that are currently used in order to prevent further corrosion, deposition of fly ash on tubes, and tube explosion. The first method is to encase the tubes with C-shaped plates made of mild steel (0.05 – 0.15% Carbon) as shown in Figure 4.5. These plates are known as sacrificing shields. However, these shields will become severely corroded after 6 months of operation and therefore require major replacement. The second method is to overlay-weld superheater tubes by alloy Inconel 59 which has a higher corrosion resistance than carbon steel 15Mo3. (The details of the chemical composition and properties of these alloys are discussed in section 4.2.5) The overlay thickness is 0.75 – 1 mm. A sample of an overlay-welded tube is shown in Figure 4.6.



Figure 4.4 Superheater tube panels



Figure 4.5 C-shape sacrificing shields encasing superheater tubes



Figure 4.6 An overlay-welded superheater tube (15Mo3 overlay welded by Inconel 59)

d. Steam Turbine and Electrical Generator

Superheated steam exiting from the heat recovery system is fed directly into a single 35 MW steam turbine generator. Steam rotates a turbine engine to create mechanical energy which is subsequently converted to electricity by an electrical generator. Electricity having a voltage of 11 kV is transformed to 132 kV before it is exported to the local grid system.

e. Treatment of Steam and Water

Steam leaving the turbine is used for pre-heating the combustion air, after which, it is sent to the air cooled condenser where the low pressure steam is cooled down to water. This condensate is kept and pumped back into the heat recovery system. Prior to re-use, the water is pre-treated by a de-aerator. The de-aerator is used for removing dissolved oxygen from the water so that metal surfaces of the superheater tubes could be protected from inside corrosion.

f. Air pollution Control System (APC)

The air pollution control system is mainly composed of a carbon injection system, a gas treatment scrubber, and a bag house filter. Powdered activated carbon (PAC) is injected into the gas stream in order to absorb any remaining organic compounds and heavy metals such as Hg and Cd from the flue gas. The PAC injection flow rate is 6 kg/h/boiler. In the gas treatment scrubber, liquid lime is sprayed into the gas stream in order to absorb acid gases. The amount of injected lime varies with the amount of incoming acid gases. The air pollution control residues and fly ash are removed from the gas stream as it passes through a bag house filter. The filter is made of approximately 3000 individual bags that are each periodically cleansed by a pulse of compressed air.

Finally, clean gases are released to the atmosphere via a 100 m tall chimney equipped with emission monitoring equipment. The typical plant emission complies with the current Waste Incineration Directive and regulations issued by the

Environment Agency. Emissions from this plant recorded in October 2006 are shown in Table 4.2.

Table 4.2 Typical plant emissions compared with Environment Agency permit limits

Release substance	Typical plant emissions (mg/Nm ³)	Environment Agency permit limits (mg/Nm ³)
Particulates	<3	10
Hydrogen Chlorides	<7	10
Hydrogen Fluoride	<1.0	1
Sulphur Dioxide	<20	50
Oxides of Nitrogen (as NO ₂)	<180	200
Volatile Organic Compounds (as C)	<1	10
Cadmium & Thallium	<0.01	0.05
Mercury	<0.03	0.05
Other metals	<0.1	0.5
Carbon Monoxide	<8	50
Dioxins	<0.07 (ng/Nm ³)	0.1 (ng/Nm ³)
Nitrous Oxide	<5	15
Ammonia	<5	-

Collected fly ash and APC residues are kept in 2 storage silos. These residues are later on transported to a licensed hazardous waste site by tankers.

g. Bottom Ash Handling

At the end of the incineration grate, non-combustible residues drop into an ash discharge. Residues are cooled down by water-filled quench baths immediately. Then, the residues are carried by conveyors to a screening process where the oversize materials are separated. After which, residues are transferred to a magnetic separator. This machine, comprised of a large rotating drum with an internally attached electro-magnet, is used to recover ferrous materials from the residues. Approximately 3 tonnes of ferrous metals for every 100 tonnes of waste are recovered. Both the bottom ash and recovered materials are sent to an off-site company where around 1.5% of ferrous metals and up to 1.5% of non-ferrous metals can be further recovered. The rest of the bottom ash is processed to be used as high grade aggregate.

4.2.2 Calculations for heat transfer rate of superheater tubes and sampling probes

Heat transfer of superheater tube materials is an important factor affecting the plant's efficiency. It governs the surface temperature of superheater tubes which directly affects the corrosion process. Therefore, the heat transfer coefficient and the surface temperature of existing superheater tubes were calculated. Results from these calculations were consequently taken into account when the sampling probe was designed. There was an attempt to design a sampling probe that has the same heat transfer value as the superheater tubes. However, it could not be achieved exactly because only compressed air could be used as coolant in this experiment while the heat transfer in the superheater tubes was governed by the superheated steam. Therefore the heat transfer rate and surface temperature of the probe was calculated based on compressed air as the coolant.

The methods of calculation, equations used and gas properties were mainly obtained from 'Coulson and Richardson's Chemical Engineering' Volume 1 by J.M. Coulson et al (1999), and Volume 6 by R.K. Sinnott et al (2005), and 'Heat Transfer' by J.P. Holman (2001). Additionally, properties of superheated steam were acquired from 'Superheated Steam Region – Steam Table' by Spirax-Sarco Limited (2007). Physical properties of carbon steel 15Mo3 were extracted from 'Introduction to Heat Transfer' by F.P. Incropera (1990). Physical properties of alloy 59 were extracted from 'Nicrofer 5923 hMo-Alloy59' by ThyssendKrupp (2002a).

Input parameters and results from the calculation are summarized in Table 4.3 and Table 4.4 respectively. The details of all calculations can be found in Appendix B.

In summary, the overall heat transfer coefficient in the superheater tube was found to be $32.08 \text{ W/m}^2\text{K}$ whereas the calculated value for the air cooled sampling probe was $31.41 \text{ W/m}^2\text{K}$. The heat transfer rates of the superheater tube and the sampling probe are $16,760.89 \text{ W/m}^2$ and $24,797.77 \text{ W/m}^2$ respectively. The average temperature of the superheater tube is approximately 339°C (612 K) while it is 163°C (436 K) for the air-cooled sampling probe.

Table 4.3 Input parameters used in calculations of heat transfer and surface temperature

Parameter for calculations	Superheater tube	Sampling probe
1. Properties of coolant		
Coolant type	Superheated steam	Compressed air
Pressure	46 bar	4.5 bar
Velocity of steam	25 m/s	20.5 m/s
Average temperature for calculation	600.73 K	350.00 K
Density	18.99 kg/m ³	4.54 kg/m ³
Viscosity	2.11×10 ⁻⁵ kg/ms	2.08×10 ⁻⁵ kg/ms
Thermal conductivity	4.61×10 ⁻² W/mK	3.00×10 ⁻² W/mK
Specific heat capacity	2768.04 J/kgK	1009.00 J/kgK
Pr	-	0.70
2. Properties of tube material		
Material name	Carbon steel - 15Mo3	Inconel - 59
Outer diameter	0.038 m	0.0318 m
Inner diameter	0.0254 m	0.0254 m
Thickness	0.0063 m	0.00635 m
Average temperature for calculation	610 K	430 K
Thermal conductivity	43.67 W/mK	43.98 W/mK
Specific heat capacity	587.85 J/KgK	582.43 J/KgK
3. Properties of hot combustion gases		
	Assumed to be equal to those of N ₂	
Temperature	1123.15 K	
Velocity (normal direction to tube)	5 m/s	
Pressure	1 atm	
Density	0.30 kg/m ³	
Viscosity	4.28×10 ⁻⁵ kg/ms	
Thermal conductivity	7.13×10 ⁻² W/mK	
Specific heat capacity	1190.94 J/kgK	
Pr	0.72	

Table 4.4 Results of calculation for heat transfer and surface temperature

Results of calculations	Superheater tube	Sampling probe
Convection heat transfer coefficient inside the probe (W/m ² K)	2097.60	260.59
Convection heat transfer coefficient outside the probe (W/m ² K)	32.77	36.08
Conduction heat transfer coefficient (W/m ² K)	5705.59	3539.12
Overall heat transfer coefficient (W/m ² K)	32.08	31.41
Heat transfer (W/m ²)	16,760.89	24,797.77
Surface wall temperature (K)	612.66	435.78
Surface wall temperature (°C)	338.51	162.63

4.2.3 Locations in the furnace of the sampling probes

Two air cooled sampling probes namely probe No.1 (SP1) and probe No.2 (SP2) were fabricated for this experimental program. These probes were installed in the furnace at different locations. The schematic diagram showing the probe locations is presented in Figure 4.2. Probe No.1 (SP1) was installed in the first pass of the furnace at 19.38 m from the incineration grate. At the height of 22.16 m from the incineration grate, the temperature of the hot combustion gas was measured to be around 804 - 828°C. Therefore the temperature at the location of probe No.1 was estimated to be around 850°C. The combustion gas passing through the probe location generally flows in the upward direction.

Probe No.2 (SP2) was installed in the second pass of the furnace. The location was at 28.78 m from the incineration grate and 0.47 m above the top of superheater panels. The temperature of hot gases, flowing downward, at this position measured by the plant operators was found to be between 730 and 791°C. Relative distances from different points of interest such as the incineration grate, roof thermometer, the top of the furnace, superheater, and 2 sampling probes are presented in Table 4.5.

Table 4.5 Locations and relative distances of points of interest in the furnace

Points of interest	Relative distance from points of interest (m)			
	From ground	From the grate	From the roof thermometer	From the top of the furnace
Incineration grate	9.32	-	22.16	22.66
Sampling probe No.1	28.70	19.38	2.77	3.27
Roof thermometer	31.47	22.16	-	0.50
Top the furnace	31.97	22.66	0.50	-
Sampling probe No.2	25.85	28.78	5.62	6.12
Top of the superheaters	25.38	29.25	6.09	6.59
End of the superheaters	18.50	36.13	12.97	13.47

Sampling probes were placed into the furnace via existing furnace's viewing ports. The viewing port and the square covering plate, Figure 4.7, were removed in order to provide an opening for the sampling probe and a new plate, Figure 4.8. The gantry to the location of sampling probe No.1 is shown in Figure 4.9. The yellow line in the Figure 4.9 was the compressed air pipeline supplied by a plant's compressor. The inner side of the probe location is shown in Figure 4.10.



Figure 4.7 Viewing port at the location of probe No.1



Figure 4.8 An opening hole after the viewing port was removed.



Figure 4.9 Gantry to the location of probe NO.1



Figure 4.10 Inner side of the wall at the location of probe No.1

4.2.4 Fabrication of sampling probes and data logger

The designs of both probes were relatively similar. Illustrations of probe No.1 and probe No.2 are shown in Figure 4.11. Details of alloy rings, baffle, a connector flange and a covering plate for both probes are presented in Figure 4.12.

The main components of the sampling probes are

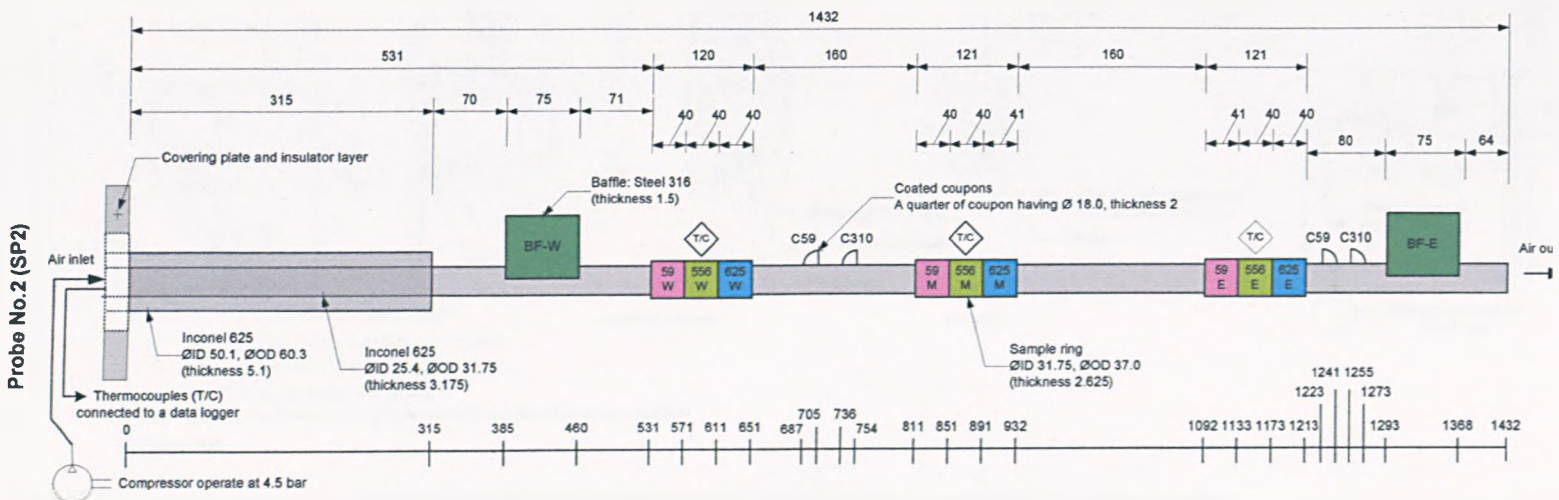
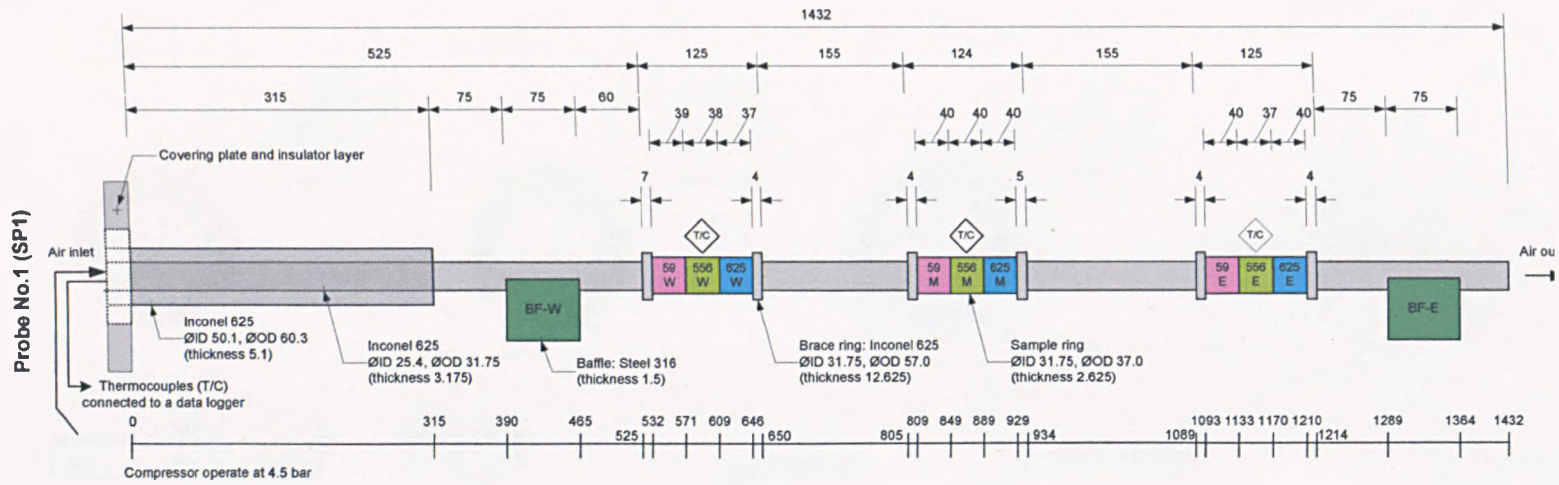


Figure 4.11 Drawings of probe No.1 (top) and probe No.2 (bottom)

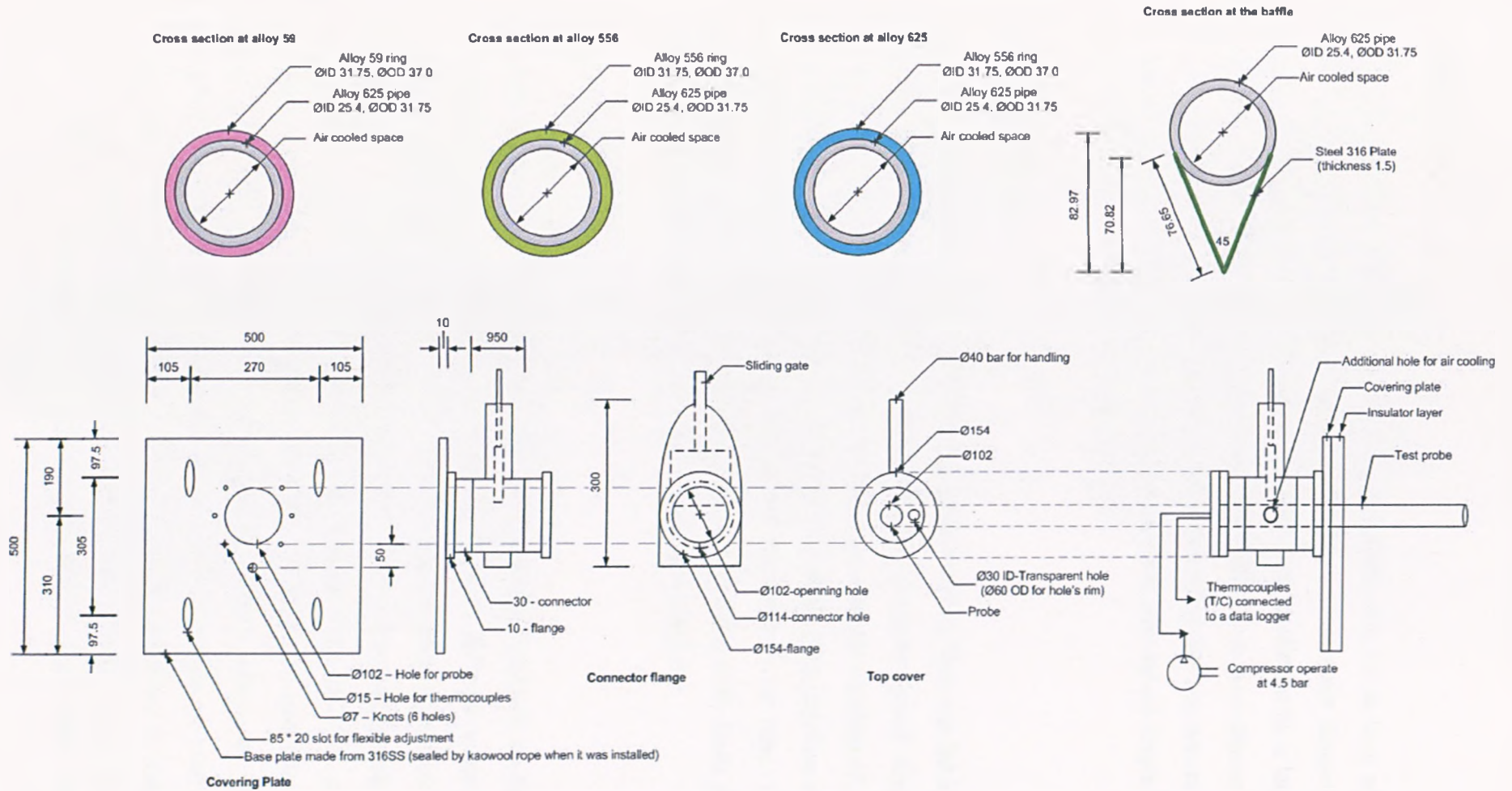


Figure 4.12 Details of alloy rings, baffle, covering plate and connector flange

a. Main tube

The main structure of the sampling probes was made of a 1.5 m long tube of alloy 625. The tube had an inner diameter of 25.40 mm and an outer diameter of 31.75 mm. For safety reason, the wall-end of this tube was reinforced by a larger tube of alloy 625. This reinforcing tube had a length of 0.400 m, an inner diameter of 50.10 mm and an outer diameter of 60.30 mm. The wall-end of the tube was mounted to a connector flange which is located outside the furnace. The actual length of the tube inside the furnace was calculated to be 1.432 m.

b. Compressed air

The tube temperature was controlled by the compressed air that was fed into the tube via the connector flange. The air passing through the tube flowed freely into the furnace at the other end. Additionally, there was a secondary pipeline of compressed air connected to the furnace through the covering plate. This pipeline supplied the compressed air to the surrounding area of the wall-end of the tube. This was to prevent tube failure due to excess heat from the furnace wall. Both pipelines of compressed air were supplied by the plant's existing compressor.

c. Alloy rings

The effects of tube material and the effects of temperature gradient on the corrosion process were studied by inserting rings that are made of different types of alloy on the probe, at different locations. Three identical sets of alloy rings were fabricated, slid on and welded onto the main tube at 0.59 m (wall section), 0.68 m (middle section) and 1.16 m (end section) from the furnace wall. Each set of rings was composed of 3 individual rings made of alloy 59, alloy 556 and alloy 625. (The details of chemical composition and properties of these alloys are discussed in section 4.2.5) Each ring had an inner diameter of 31.75 mm, and an outer diameter of 37.00 mm. The fabrication of these rings was carefully carried out in order to ensure that the inner diameter of the rings had full contact with the main tube. This was done to prevent any air space between the rings and the main tube. The length of each ring was approximately 40 mm.

d. Sacrificial baffle

The corrosion control method by using a sacrificial baffle was studied for both probes. Sacrificial baffles made from stainless steel 316 were welded to the sampling probes at 0.43 and 1.33 m from the furnace wall. For probe No.1, the baffles were welded at the bottom of the main tube since the hot gas stream flows upward to the probe. Contrarily, the baffles welded on probe No.2 were on the top of the main tube since the hot gas stream flowed downward to the probe. Sacrificial baffles were fabricated in a triangular shape. The dimensions of the baffle were 76.65 mm × 75 mm, with an angle of 45°.

e. Coated alloy

A corrosion control method by applying coating on the tube surface was studied on sampling probe No.2. Alloys 59 and 310 were selected to be used as substrate materials for this study. Firstly, 2 coupons of each alloy were prepared. Each coupon was cut as a quarter of a round disk having a diameter of 3.6 mm, with a thickness of 2 mm. Then, the coupons were coated according to the procedure described in section 4.2.6. Coupons of each alloy were welded to the main tube at 0.72 m and 1.25 m from wall.

f. Thermocouple and data logger

The temperatures inside the probe were measured by three thermocouple junctions. The thermocouples wires were inserted into the middle of the main tube at 0.59 m (wall section), 0.68 m (middle section) and 1.16 m (end section) from the furnace wall. This was done carefully to ensure that each thermocouple did not come into contact with any of the wall sections of the tube. The temperatures read by thermocouples were recorded in a data logger every half an hour. For safety reasons, a thermocouple was set also outside the furnace to measure the wall temperature.

g. Connector flange and covering plate

The connector flange and the covering plate were made of stainless steel 316 since it is economical and it is not exposed to a very high temperature environment. The

connector flange was also used to house (1) the compressed air inlet for the probe and (2) the connection board of the thermocouples wires that run inside the main tube and wires leading to the data logger. The covering plate with an insulator layer was installed to replace the void that resulted from the removal of plant's viewing port. It had an inlet of secondary compressed air which was used for cooling the wall-end of the probe.

Figure 4.13 shows an image of the sampling probe No.1 and the data logger before it was installed at the plant.

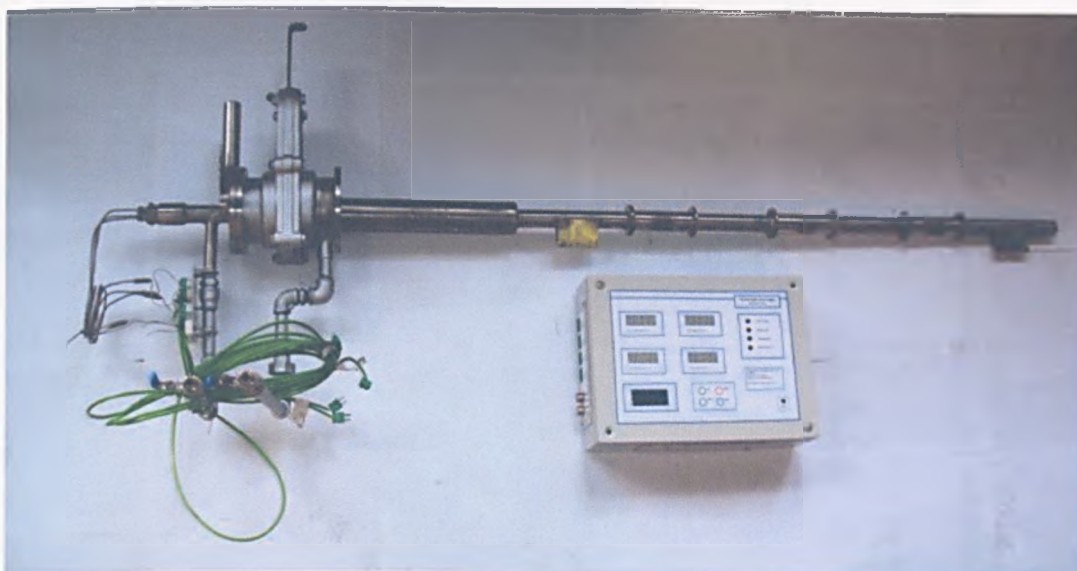


Figure 4.13 Sampling probe No.1 and the data logger before the experiment.

4.2.5 Technical data of metal alloys

Six types of metal alloy were studied in this project. Alloys 59, 556, 625, 310 and 316 were used in fabrication of the sampling probes, and carbon steel 15Mo3 which was the plant's superheater material. Alloys 59, 556, 625 and 15Mo3 are classified as corrosion resistant and high temperature alloys whereas alloys 310 and 316 are commonly known as austenitic stainless steel. The typical chemical compositions of these alloys are compared in Table 4.6. It should be noted that alloys from different producers could have some minimal difference in chemical composition.

Table 4.6 Typical chemical composition of metal alloy regarded in this study (wt%)

Alloy	Al	C	Co	Cr	Fe	Mn	Mo	Ni	P	S	Si	Ti	Others	Reference
59	0.1 0.4	Max 0.010	Max 0.3	22.0 24.0	Max 1.5	Max 0.5	15.0 16.5	Bal.	Max 0.015	Max 0.005	Max 0.10			(1)
556	0.2	0.10	18	22	Bal. (31)	1.0	3	20			0.4		W 2.5 Ta 0.6 N 0.2 La 0.02 Zr 0.02	(2)
625	Max 0.40	Max 0.10	Max 1.0	20.0 23.0	Max 5.0	Max 0.50	8.0 10.0	58.0 Min	Max 0.015	Max 0.015	Max 0.50	Max 0.40	Nb+Ta 3.15 – 4.15	(3)
310		Max 0.25		24.0 26.0	Bal.	Max 2.00		19.0 22.0	Max 0.045	Max 0.030	Max 1.75			(4)
316		Max 0.08		16.0 18.0	Bal.	Max 2.00	2.0 3.0	10.0 14.0	Max 0.045	Max 0.030	Max 0.75		N <0.10	(5)
15Mo3		0.12 0.20			Bal.	0.40 0.90	0.25 0.35		Max 0.035	Max 0.035	0.10 0.35			(6)

Note: (1) for ThyssenKrupp VDM (2002a), (2) for Haynes International Inc. (1998a), (3) for ThyssenKrupp VDM (2002b), (4) for Sandmeyer Steel Company (2007a), (5) for Sandmeyer Steel Company (2007b), and (6) for E-Pipe Co. Ltd. (2007).

a. Alloy 59

Alloy 59 is a Ni-Cr-Mo alloy with a very low content of C and Si. Nicrofer®5923hMo produced by ThyssenKrupp VDM is an example of alloy 59. It is commercially promoted as having excellent corrosion resistance and high mechanical strength. It was approved for pressure-vessel use with wall temperatures varying from -196 to 450°C. Alloy 59 has a face-centered-cubic structure. This alloy markedly withstands a wide range of corrosive mediums under both oxidizing and reducing conditions. It has an excellent resistance to chloride ions and mineral acids such as HNO₃, H₃PO₄, and in particular to H₂SO₄ and HCl mixtures. Typical applications of alloy 59 are in the chemical, petrochemical and pharmaceutical industries, energy production, pollution control equipment, and especially in processes involving acids and/or chlorides (ThyssenKrupp VDM, 2002a).

b. Alloy 556

Alloy 556 is an Fe-Ni-Cr-Co alloy. HAYNES®556TM produced by Haynes international is an example of alloy 556. The alloy has effective resistance to oxidation, sulphidization, carburization and chlorine attacks at high temperature. It could also resist the corrosion by molten chlorides and molten zinc compounds. Typical applications are in elevated temperature and 'moderately to severely corrosive environments' such as in municipal and industrial waste incinerators, minerals processing, land-based gas turbines burning low-grade fuels, rotary calciners, processes involving high-sulphur petroleum feedstocks, and also various high temperature applications in the aerospace industry (Haynes International Inc., 1998a).

c. Alloy 625

Alloy 625 is a Ni-Cr-Mo-Nb alloy with a low content of C. HAYNES®625 produced by Haynes international and Nicrofer®6020hMo produced by ThyssenKrupp VDM were examples of the commercial alloy 625. It has corrosion resistant ability similar to those of alloy 59 but with a different limitation in terms of operating temperatures. It has excellent strength up to approximately 816°C (1500°F). Long term applications of this alloy are restricted to about 595°C (1100°F).

It is widely used in chemical industries, sea water and power plant scrubbers (Haynes International Inc., 1998b; ThyssenKrupp VDM, 2002b).

d. Alloy 310 and 316

Alloy 310 and 316 are very common austenitic stainless steels used in industry. These alloys have a fair corrosion resistance and generally good strength at elevated temperatures. They are widely used for elevated temperature applications such as in furnace and heat exchanger parts. They can also be used in chemical processes that require exposure to hot concentrated acids, NH_3 , SO_2 , acetic and citric acid. Alloy 316 contains Mo which gives it a better corrosion resistance than alloy 310 (AK Steel, 2000; Sandmeyer Steel Company, 2007a; Sandmeyer Steel Company, 2007b).

e. Alloy 15Mo3

Alloy 15Mo3 is a high temperature steel with the addition of C and Mo. It is typically used for boiler parts or heat exchanger pipes in power plants globally. However, it is an old material and its performance is generally superceded by modern types of superalloys (Vencl et al., 2004; E-Pipe Co.Ltd., 2007).

4.2.6 Aluminide pack cementation coating procedure

The aluminide pack cementation coating of samples was conducted by the “Advanced Material Research Institute, School of Engineering, University of Northumbria at Newcastle”. The coating procedure for each alloy substrate depended on its chemical composition which in turn determines the adhesiveness and coating quality between the coat layer and substrate material: The procedures used in this experiment are discussed as follows:

Firstly, coupons of alloy 59 and alloy 310 were ground up to 600 SiC grit finish. Then, each coupon was heated in a ceramic crucible packed with aluminide chemicals in the furnace. For coupons of alloy 59, the aluminide mixture was composed of 15%Al + 3% NH_4Cl + 82% Al_2O_3 by weight. These coupons were heated at a temperature of 1,000°C for 5 hours. For coupons of alloy 310, the aluminide mixture was composed of 4%Al + 2% AlCl_3 + 94% Al_2O_3 by weight. These coupons were heated at a temperature of 850°C for 5 hours.

4.2.7 The installation and the operation of sampling probes

The installation of the probe was carried out during scheduled plant shut down for maintenance. The viewing port at the probe location was taken out and replaced by the insulating plate, the covering plant and the connection flange. The probe was carefully inserted into the furnace (Figure 4.14). Then compressed air at a pressure of 4.5 bars was set up and fed through a valve into the probe at a flow rate of 1320 ft³/h (37.38 m³/h). Approximately the same amount of compressed air was used as a secondary air jet for cooling around the wall-end of the probe. Finally, thermocouples were connected to the data logger (Figure 4.15) which was pre-programmed to record the temperatures of air in the probes every half an hour. The installed and operating sampling probe is shown in Figure 4.16.



Figure 4.14 Installation of the sampling probe No.1

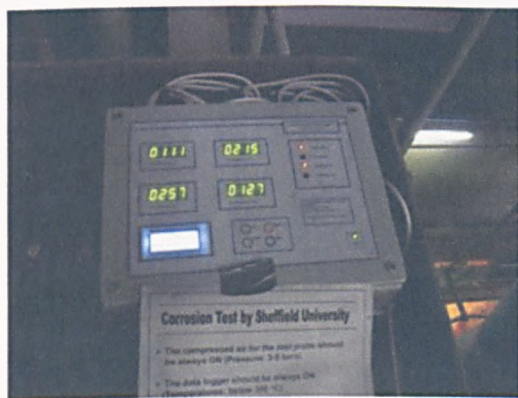


Figure 4.15 Data logger in operation



Figure 4.16 Operating sampling probe (No.1)

Sampling probe No.1 was installed on 15 October 2006 and was taken out on 16 November 2006. The period of operation for the second probe began on 5 April 2006 and ended on 9 May 2006. This resulted in an exposure time of 769 h for probe No.1

and 811 h for probe No.2. At each probe removal, the flange and covering plate was left at the plant until the next scheduled maintenance. The viewing port was only replaced after all experiments were completed. During the experiment, probes No.1 and No.2 were taken out to check their general conditions. The checking times for probe No.1 and No.2 were on day 14, and day 12 respectively.

4.2.8 Other collection points of combustion residues

Samples of combustion residues were collected from various locations inside the furnace. These samples were subsequently analysed for their chemical composition. The results could be used to explain the elemental flux of waste constituents that were released from the waste burning bed and travelled to the air pollution control system. The samples' description and collection points are summarized in Table 4.7.

Table 4.7 Samples of combustion residues: description and collection points

No.	Identity	Type of sample	Collection points
1	BA	Bottom ash	Bottom ash pit
2	SL1	Slagging from the furnace wall	1 st pass, at 19.5 m from ground or at 10.2 m above the waste burning bed
3	SL2	Slagging from the furnace wall	1 st pass, at 25.1 m from ground or at 15.8 m above the waste burning bed
4	SL2+Wh	White deposit accumulated on the wall slagging	1 st pass, at 25.1 m from ground or at 15.8 m above the waste burning bed
5	SL3	Slagging from the furnace wall	1 st pass, at 28.7 m from ground or at 19.4 m above the waste burning bed (the same area as the sampling probe no.1)
6	SL3+Wh	White deposit accumulated on the wall slagging	1 st pass, at 28.7 m from ground or at 19.4 m above the waste burning bed (the same area as the sampling probe no.1)
7	SH1	Fouling on the superheater tube - sample 1	2 nd pass, at 25.35 m from ground or at 0.5 m lower than the location of sampling probe no.2
8	SH2	Fouling on the superheater tube - sample 2	2 nd pass, at 25.35 m from ground or at 0.5 m lower than the location of sampling probe no.2
9	EC	Fouling or combustion residues that deposited on the economiser.	Ash bunker located under the economiser (at the beginning of the 3rd pass)
10	APC	Air pollution control residues	Storage silo of the air pollution control residues (particulates filtered out from the gas stream by the bag house filter)

4.3 Analytical Methodology for Combustion Residues and Deposits

After the sampling probes were removed from the furnace, deposits and corrosion products were collected from various positions on both probes with labels carefully marked on each sample container. Then the alloy rings covered with a thin layer of corrosion products were disassembled and cut to appropriate sizes which are required for further analytical work. Baffles and coated coupons were also cut out from the main probe. Table 4.8 is a list of all samples and the analysis carried out.

Table 4.8 List of samples and analysis program

Sample	Analysis program					
	Full elemental analysis	Differential thermal analysis	Crystalline phase study	Micro-structure analysis	Corrosion rate analysis	Grain boundary analysis
Combustion residues	√	√	√			
Deposits on probes	√	√	√			
Corrosion products	√		√			
Alloy rings			√	√	√	√
Baffle				√		
Coated coupons			√	√		

4.3.1 Full elemental analysis

a. Sample preparation

Sample preparation for deposits and corrosion products were carried out at the Department of Chemical and Process Engineering. Initially the samples were manually ground using a mortar until the particles were smaller than 212 μm . Then the samples were kept in air-tight containers prior to sending them for analysis.

b. Analytical details

The full elemental analysis was conducted by the Centre for Analytical Science, Department of Chemistry. Samples in powdered form were digested in an acid

solvent, namely “aqua regia”. This solvent was a mixture of HNO_3 and HCl at the ratio of 3:1. After which, the solvents were injected into the “Spectro Genesis – Simultaneous Charged Coupled Device – Inductively Coupled Plasma (CCD-ICP) Spectrometer” for elemental analysis. It was noted that the results of Si from this analysis were not accurate. This is because the analysis of Si requires HF solvent which was not permitted in this experiment. Measurement of Cl and Br were also not accurate due to the sensitivity limitation of the system.

Further analysis for C, H and N was carried out by using a “Perkin Elmer 2400 Elemental Analyser for C-H-N Analysis”. The elements existing in the sample were separated into gas form for detection by the combustion/reduction technique.

Chlorine was determined by using a standard titration method. The sample was burnt in the presence of O_2 in a flask containing an absorbance solution. This solution was then titrated with $\text{Hg}(\text{NO}_3)_2$ to give the Cl concentration.

4.3.2 Differential Thermal Analysis

a. Sample preparation

Samples of deposit and corrosion products were prepared using the same method as described in section 4.3.1.a.

b. Analytical details

The analysis was carried out using a “Perkin Elmer - Differential Thermal Analyser DTA7 (N538-1045)” at the Material Characterization Laboratory, Department of Engineering Materials. A sample was weighed to be approximately 25 mg and placed into the alumina crucible. It was then heated up in the furnace containing nitrogen gas from 50°C to 1400°C at the rate of $10^\circ\text{C}/\text{min}$. The temperature of the reference standard, the sample and the furnace were recorded. The final result was used to plot a graph of the temperature difference between the reference and the sample against the furnace temperature.

4.3.3 Crystalline phase study

a. Sample preparation

Different methods were used to prepare the powdered-form and the metal alloy samples since they were analysed using different instruments. Samples of deposit and corrosion products were prepared using the same method as described in section 4.3.1.a. Samples of coated coupons did not need preparation since the flat surface of the coated coupons was compatible with the instrument requirement. However, the preparation for the alloy rings was different since they did not have a flat surface. Only part of the flat surface of the rings could be exposed to the radiation beam in order to provide precise phase analysis. Therefore the alloy rings were partially cold-mounted in epoxy resins. The rings were arranged in the way that only a flat surface, of approximately 0.5×0.5 cm was exposed out of the resin. There was no grinding or polishing required for this cold mounting.

b. Analytical details

Crystalline phase study was carried out at the X-Ray Diffraction Laboratory, Department of Engineering Materials. Samples of deposits and corrosion products were analysed by using “Philips PW1710 Reflection Diffractometer (Copper System)” with the software named “STOE WinX^{POW} and Hiltonbrooks XRD Link”. The 2θ range used in this analysis was $5 - 80^\circ$.

Samples of coated coupons and alloy rings were analysed using “Siemens D500 Reflection Diffractometer (Copper Radiation)” with the software named “Diffrac plus XRD commander”. The analysis was carried out for two scan types; “locked coupled” (θ - 2θ analysis) and “detector-scan” (glancing angle analysis). The 2θ range used in this analysis was $10 - 105^\circ$. The glancing angle used was 8° . Analysed depths of samples were approximately $25 \mu\text{m}$ for the locked coupled scan, and $2 \mu\text{m}$ for the detector scan.

The radiation beam in both machines consists of $\text{CuK}_\alpha 1$ and $\text{K}_\alpha 2$, and operates at 40 kV and 30 mA. Phillips PW1710 Reflection Diffractometer and Siemens D500 Reflection Diffractometer are shown in Figure 4.17 and Figure 4.18 respectively.



Figure 4.17 Philips PW1710 Reflection Diffractometer



Figure 4.18 Siemens D500 Reflection Diffractometer

4.3.4 Microstructure analysis

a. Sample preparation

Microstructure analysis of the alloy rings, baffles, and coated coupons were carried out only on a cross section surface of these samples. The sample preparation was conducted in the Department of Chemical and Process Engineering and in the Micropreparation Lab, Department of Engineering Materials. Firstly, these metal samples were cut to the sizes that could fit into a 24 mm mount as required by the analytical instrument. Alloy rings were cut quarterly and a sample of baffle was cut into 1 cm × 1 cm. Coated coupons having the smallest size did not require cutting.

Cut samples were cold mounted in epoxy resin with a diameter of 24 mm. After they were allowed set for 24 hours, the samples were ground using abrasive grinding paper up to a grit finish of 600 SiC (median diameter 15.3 μm) to create the cross section surface. Then, the mounted samples were polished with diamond polishing abrasives solution until a diamond size of 3 μm was achieved. Grinding and polishing were carried out by using a “PHOENIX 400 Sample Preparation System” as shown in Figure 4.19. 6-8 pounds of force was used for both grinding and polishing. Revolutions used for grinding and polishing were 250 rpm and 150 rpm respectively.

Prior to the analysis, the polished samples were painted with “Silver in Methyl Isobutyl Ketone Electrodag” also known as silver dag solution in order to improve

the electrical conductivity between the samples and the sample holder inside the instrument. In some cases, samples were carbon-coated in order to reduce the charging effect. The carbon coating machine used in this study was “EMITECH K950X Carbon Coater” as shown in Figure 4.20. Polished samples, painted samples and carbon-coated samples are shown in Figure 4.21.



Figure 4.19 PHOENIX 400 Sample Preparation System



Figure 4.20 EMITECH K950X Carbon Coater

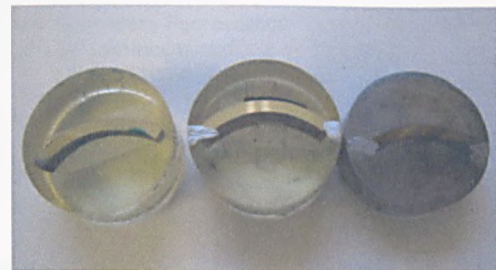


Figure 4.21 Mounted samples of alloy ring: polished, painted, and carbon coated samples.

In the processes of sample preparation, alloy samples were kept dried as much as possible and only Isopropanol was used for washing and lubricating during the cutting process.

b. Analytical details

Microstructure analysis was carried out in the “Materials and Engineering Research Institute (MERI), Sheffield Hallam University” by using “Environmental Scanning Electron Microscopy - Phillips XL30 ESEM-FEG” with a software named “Inca”.

The scanning electron microscope operated with a typical accelerating voltage of 20 keV. The working distance between the electron gun and the sample was 10 cm.

Surface images of the samples were obtained using a secondary electron beam. It is therefore important for one to note that the results of elemental composition determined by the backscattered electron beam might be different. This is because the backscattered electrons penetrate deeper into the sample compared to secondary electrons. The schematic diagram of the range and spatial resolutions of backscattered electron and secondary electrons is shown in Figure 4.22.

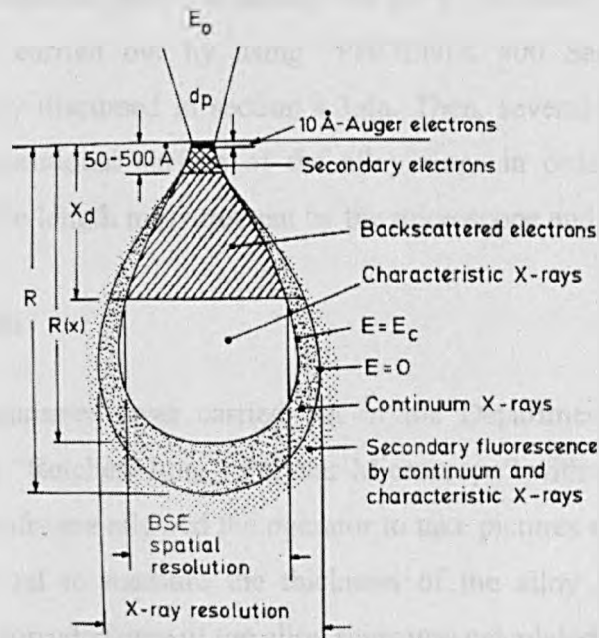


Figure 4.22 Summary of range and spatial resolution of backscattered electrons, secondary electrons, X-rays and Auger electrons produced from an electron microprobe-scanning electron microscope (Goldstein, 1974)

Another important issue whilst using ESEM analysis is that the results of some elements overlap. Pairs of elements that produce overlapping results are W – Si, Mo – S, and Fe – Cu.

4.3.5 Corrosion rate measurement

Corrosion rates on alloy rings were analysed by 2 methods. Firstly, the thickness of the alloy rings was measured by a digital vernier calliper with a precision of up to a

hundredth of a millimetre (10 μm). Secondly, the corrosion rates of alloy rings were measured by an optical microscope. The latter method is discussed in the following:

a. Sample preparation

Alloy rings were cut into half and mounted in epoxy resins having a diameter of 38 mm. After it was left to set for 24 h, the samples were ground using abrasive grinding paper up to a grit finish of 600 SiC (median diameter 15.3 μm) to create the cross section surface. Then, the mounted samples were polished with diamond polishing abrasives solution until a diamond size of 3 μm was achieved. Grinding and polishing were carried out by using “PHOENIX 400 Sample Preparation System” as previously discussed in section 4.3.4a. Then, several radius lines were drawn on the cross-sectional surface of the alloy rings in order to create some reference marks for the length measurement by the microscope and its software.

b. Analytical details

Corrosion rate measurement was carried out in the Department of Engineering Materials by using a “Reichert Jung - Polyvar Microscope” with a software named “KS Run 3.0”. The software allowed the operator to take pictures of the sample with high magnification and to measure the thickness of the alloy rings. Hence, the corroded length and corroded area of the alloy rings was calculated.

4.3.6 Grain boundary analysis

a. Sample preparation

The samples of alloy rings were prepared using the same method as described in section 4.3.5a.

b. Etchant preparation

Etchant No. 105, also known as etchant 92-5-3, was made of 5 ml H_2SO_4 + 3 ml HNO_3 + 90 ml HCl . The solution was prepared under the fume hood.

c. Analytical details

Corrosion rate measurement was carried out in the Department of Chemical and Process Engineering and the Department of Engineering Materials. Sample surfaces were swabbed by the etchant solution for 10-30 seconds. Then, the samples were washed with distilled water and dried. The dried samples were placed under the optical microscope "Reichert Jung - Polyvar Microscope" for grain boundary analysis.

4.3.7 Errors in analytical methods

Multiple errors were accounted for the whole experimental program. However, some errors were reduced by calibration of instruments whereas others required multiple readings and measurements to obtain averages. Another error that was not accounted for was during preparation by cutting the alloys. Cutting the alloys at high temperature caused them to stretch and distort which causes some errors during corrosion rate measurements. Furthermore, some of the compounds might have been disintegrated or transformed due to atmospheric moisture absorption while transporting the probes from the plant.

CHAPTER 5

EXPERIMENTAL RESULTS

This chapter presents the results obtained from the experiments and the analytical work that were previously described in Chapter 4. Firstly, the abbreviations used for identifying samples are introduced. Then, the chapter shows the results of the temperature measurements that consist of (1) gas temperature measurement by using a suction pyrometer and (2) temperature profiles of the air inside the probes during the exposure in the furnace. Next, the visual characteristics of various combustion residue samples are discussed, followed by the description of the probes after they were withdrawn from the furnace. Subsequently, the analytical results for alloy specimens, corrosion products, probe deposits and other combustion residues are presented. These results include (1) elemental composition, (2) crystalline phase identification for coating and corrosion products, (3) temperatures of phase transformation of deposits, (4) corrosion rates, (5) grain boundary analysis, and (6) morphology of corroded areas and corrosion products.

5.1 Identification of Samples from the Sampling Probes

A systematic identification system was designed in order to standardize the names of locations of samples collected from the probes. The abbreviations to be used and their positions on the probe are shown in Figure 5.1. All abbreviations and their descriptions are listed in Table 5.1.

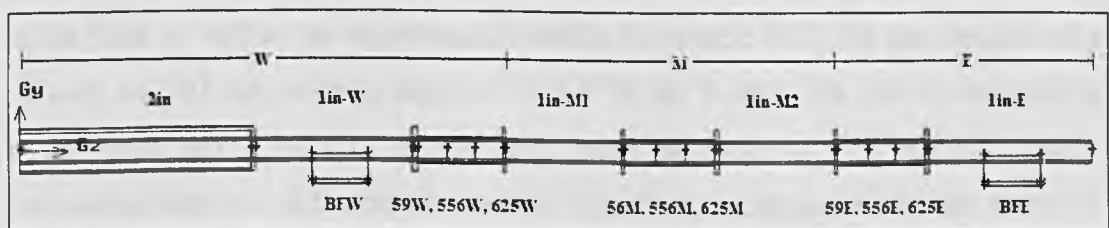
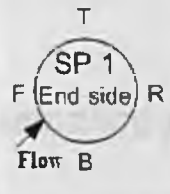



Figure 5.1 Diagram of a sampling probe and the abbreviations used for referring to the samples or locations on the sampling probe

Table 5.1 Description of the abbreviations used for referring to the samples or locations on the sampling probes

Type	Abbreviation	Description	Distance (m) from wall	
			Probe No.1	Probe No.2
Main probe (Alloy625)	2 in	The 2inch diameter	0 – 0.315	0 – 0.315
	1in – W	The 1inch diameter at the wall section	0.315 – 0.525	0.315 – 0.531
	1in – M1	The 1inch diameter at the middle section	0.650 – 0.805	0.651 – 0.811
	1in – M2	The 1inch diameter at the middle section	0.934 – 1.089	0.932 – 1.092
	1in – E	The 1inch diameter at the end section	1.214 – 1.432	1.213 – 1.432
Alloy rings	Ring W	Area of ring 59W, 556W and 625W	0.532 – 0.646	0.531 – 0.611
	Ring M	Area of ring 59M, 556M and 625M	0.809 – 0.929	0.811 – 0.932
	Ring E	Area of ring 59E, 556E and 625E	1.093 – 1.210	1.092 – 1.213
	59W	Ring of alloy59 at the wall section	0.532 – 0.571	0.531 – 0.571
	556W	Ring of alloy556 at the wall section	0.571 – 0.609	0.571 – 0.611
	625W	Ring of alloy625 at the wall section	0.609 – 0.646	0.611 – 0.651
	59M	Ring of alloy59 at the middle section	0.809 – 0.849	0.811 – 0.851
	556M	Ring of alloy556 at the middle section	0.849 – 0.889	0.851 – 0.891
	625M	Ring of alloy625 at the middle section	0.889 – 0.929	0.891 – 0.932
	59E	Ring of alloy59 at the end section	1.093 – 1.133	1.092 – 1.133
	556E	Ring of alloy556 at the end section	1.133 – 1.170	1.133 – 1.173
625E	Ring of alloy625 at the end section	1.170 – 1.210	1.173 – 1.213	
Baffles	BFW	Baffle close to the wall	0.390 – 0.465	0.385 – 0.460
	BFE	Baffle close to the end of the probe	1.289 – 1.364	1.293 – 1.368
Coated coupons	C59W	Coated coupon of alloy59 close to the wall	-	0.687 – 0.705
	C310W	Coated coupon of alloy310 close to the wall	-	0.736 – 0.754
	C59E	Coated coupon of alloy59 close to the end	-	1.223 – 1.241
	C310E	Coated coupon of alloy310 close to the end	-	1.255 – 1.273
Directions	F / front	Front side of the probe (side facing gas stream directly)		
	R / rear / back	Rear side of the probe (side not facing the gas stream directly)		
	T / top	The top half of the probe		
	B / bottom	The bottom half of the probe.		

The direction of the gas stream passing through the probe was different for each probe. Mathematical modelling (Chapter 6) was used to calculate the direction of the gas flow. The calculated results corresponded reasonably with the flow observation at the plant as well as the experimental results. For probe No.1, the gas stream had a velocity of 3.05 m/s, with an angle of -138.4° to the Y-axis. The gas stream passing probe No.2 had a velocity of 4.83 m/s, with an angle of 4.83° to the Y-axis. Schematic diagrams of the probes and the flow direction of gas stream are shown in Table 5.1. The drawing illustrates the view as one is looking from the end of the probe.

5.2 Temperature Measurement by using an Air-cooled Suction Pyrometer

The flue gas temperatures at the position of probe No.2 were measured by using an air-cooled suction pyrometer. The pyrometer was placed at 3 positions: 0.53, 0.98 and 1.43 m from wall which were approximately equivalent to the position of alloy ring W, alloy ring M, and the end of the sampling probe. Results from the pyrometer compared with the data obtained from the plant operators are shown in Table 5.2.

Table 5.2 Gas temperatures at the position of sampling probe No.2 - measured by an air-cooled suction pyrometer

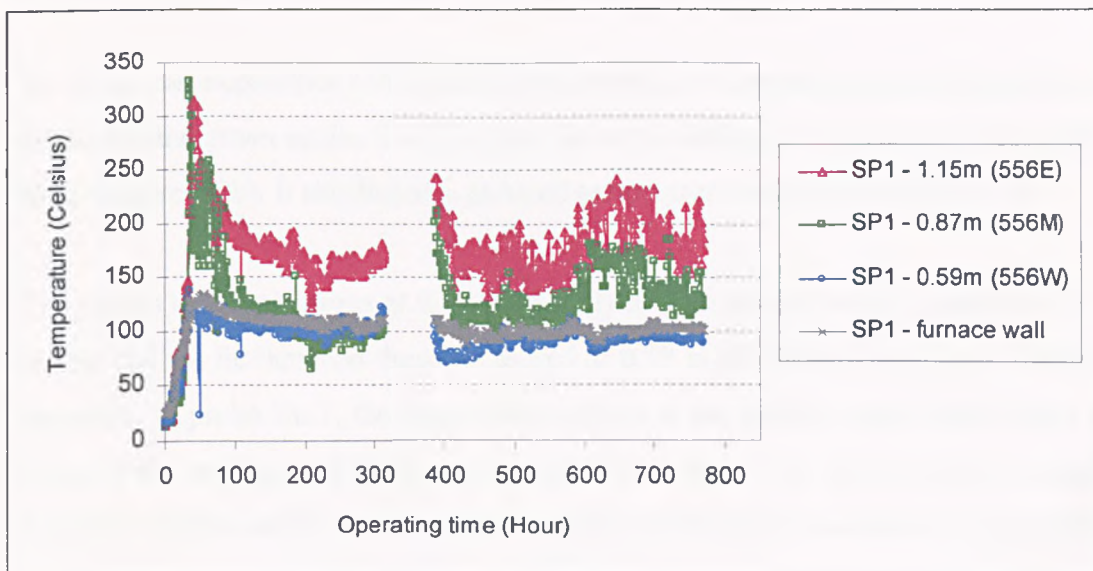
Distance (m)	Temperatures measured by the suction pyrometer (°C)	Temperatures measured by the plant's equipment (°C)
1.43 m from wall (probe's end)	600 – 650	730 – 791
0.98 m from wall (ring M)	515	
0.53 m from wall (ring W)	482	

The results show that probe No.2 was exposed to temperatures ranging from 482°C at ring-wall to 650°C at the end of the probe. These values were lower than the plant's data (730 – 791°C) in spite of the fact that the suction pyrometer was designed to eliminate the effect of heat loss through radiation. The reason is that the plant's probe is located further away from the waterwall and also at a higher position (close to the first pass of furnace).

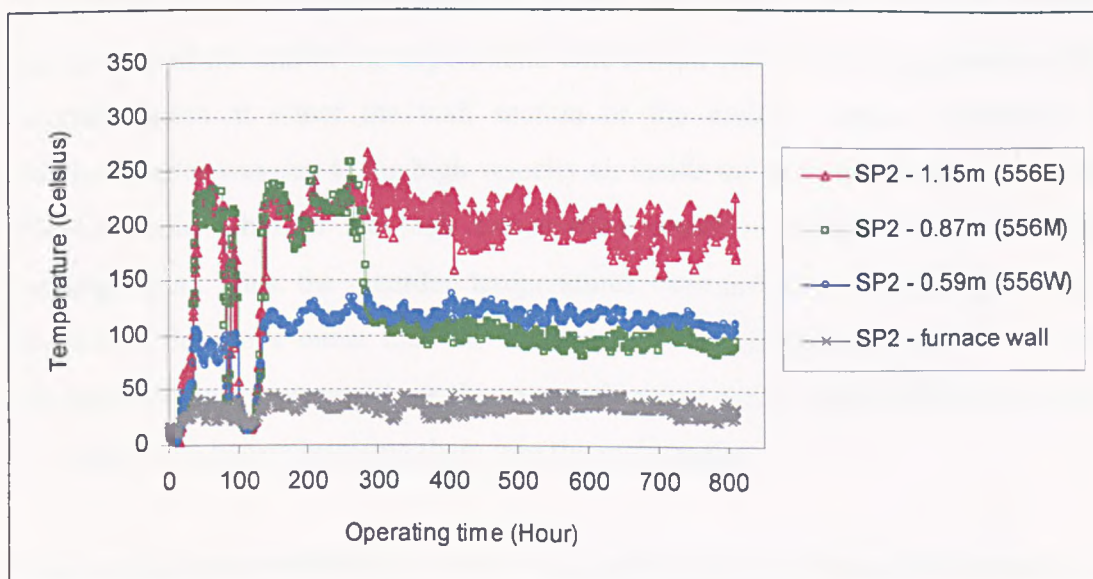
5.3 Temperature of cooling air inside the sampling probes

The temperature profiles of air inside the sampling probes are shown in Figure 5.2. The results are composed of profiles of air temperature measured at 0.59 (556W), 0.87 (556M) and 1.15 m (556E) from the wall, and also the temperature at the furnace wall. The sampling probes were placed in the furnace during the plant maintenance shutdown. After the maintenance jobs are accomplished, the auxiliary burner heats up the furnace at a rate of 50°C/h until the operating temperature is reached. Therefore, the recorded temperatures of air inside the probes started at the room temperature and sharply increased before being stabilized during the following day. The total exposure times of sampling probe No.1 and No.2 were 769 hours (32 days), and 811 hours (34 days) respectively. In general, the temperature of the

cooling air increased as it passed through the probe, i.e. the temperatures at the end section were greater than those at the wall section. The temperature profiles of both probes gradually decreased as time progressed. This was the result of deposit accumulation, as the deposit has a low thermal conductivity, which significantly reduces the heat transferred to the probe.



(a)



(b)

Figure 5.2 Temperature profile of air inside the sampling probes: (a) probe No.1, (b) probe No.2

The data recorded for probe No.1 (Figure 5.2a) between hour 314 and 387 are not available due to a burn out of the fuse in the data logger. A higher grade fuse was

inserted and the experiment continued. The temperature profile consists of two peaks of increased temperature; in the period of hour 0 – 100 and hour 600 – 700. One reason for the first peak may be the effect of deposit accumulation as previously discussed. The later temperature increase may have occurred after the lower part of the deposit cracked and fell away from the probe. The evidence showing the loss of the thick deposit layer from the lower part of the probe is presented in section 5.4.1.

The plant can experience some difficulties during the start-up process and the burner might be shut down again. This problem occurred during the experiment with probe No.2 (Figure 5.2b). It resulted in a reduced temperature profile in hour 80 - 136.

The results of temperatures at 0.87 m (556M) in both probes were inconsistent. The results did not lie between those measured at 0.59 m (556W) and 1.15 m (556E) as expected. In probe No.1, the temperatures of air at the middle section were close to those of the wall section from about hour 100 to hour 314. In probe No.2, results from the middle section were similar to those of the end section from the beginning of the experiment until hour 281. After that, the recorded temperatures immediately dropped to be lower than temperatures at the wall section and remained relatively constant until the end of the experiment. One reason can be the displacement of the thermocouples at either the wall section or the middle section. Movement of thermocouples was due to the high velocity air inside the probe or the ductility of the thermocouple tubes in the high temperature condition which causes significant misalignment. Thus, the recorded temperatures were probably affected by the inner surface of the probe rather than the air temperature. This problem can be solved in the future by incorporating these thermocouple wires with a small stainless steel tube (or round bar) before inserting them into the main probe.

The average temperatures at 3 positions as well as the temperature differences (ΔT) between the end section and the wall section for probe No.1 and No.2 were calculated. The values are shown in Table 5.3 and Table 5.4 respectively. The average temperatures were calculated for 3 different ranges of time in order to observe the effects of deposit accumulation. The ranges are (1) the first period: hour 150 – 400, (2) the last period: from hour 400 to the end, and (3) the total experimental period: from hour 150 to the end.

Table 5.3 Average temperatures of air inside probe No.1 at different locations (°C)

Position of the air temperature measurement (from the wall) in probe No.1	Range of temperatures for calculating the average values		
	Hour 150 – 400	Hour 400 - End	Hour 150 – End
0.59 m (556W)	100	90	94
0.87 m (556M)	104	131	122
1.15 m (556E)	167	179	175
$\Delta T (T_{556E} - T_{556W})$	67	89	82

Table 5.4 Average temperatures of air inside probe No.2 at different locations (°C)

Position of the air temperature measurement (from the wall) in probe No.2	Range of temperatures for calculating the average values		
	Hour 150 – 400	Hour 400 - End	Hour 150 – End
0.59 m (556W)	118	117	117
0.87 m (556M)	142	97	110
1.15 m (556E)	219	198	204
$\Delta T (T_{556E} - T_{556W})$	102	81	87

The average temperatures for probe No.1, calculated from hour 150 to the end, at the wall section, middle section and end section were 94, 122 and 175°C respectively. The average values for probe No.2 were 117, 110 and 204°C respectively. The temperatures for probe No.2 were generally higher than probe No.1. The reason may be the displacement of thermocouples as discussed previously.

The temperature difference of the air flow inside the probe calculated from the wall section to the end section was 82°C for probe No.1, and 87°C for probe No.2. Therefore, the design of these probes provides an average temperature difference of 84°C. The differences of average temperatures between the first period (hour 150 – 400) and the last period (hour 400 – end) confirm the effect of deposit accumulation.

These measured temperatures were used as the reference for the modelling work, which will be further explained in Chapter 6. Modelling of the sampling probes can provide an estimate of the surface temperature of the metal and deposit as shown in Table 5.5 (summarized results from Chapter 6). For probe No.1, the surface temperatures of the metal and deposits vary in the range of 404 – 543°C and 489 – 680°C respectively. For probe No.2, the surface temperatures of the metal and deposits vary in the range of 363 – 474°C and 400 – 616°C respectively. These

results will be referred to and used to explain the corrosion process later on. However, the modelling results for the air temperature inside the probes were lower than the measured temperatures. Therefore, it should be noted that the real surface temperatures of metal and deposit were higher than the modelling results.

Table 5.5 Modelled surface temperature values of metal and deposit at different locations on the sampling probes

Surface temperature (°C)	Location (section)	Sampling probe No.1		Sampling probe No.2	
		No deposit	With deposit	No deposit	With deposit
Metal surface temperature	0.59 m (W)	452 – 496	404 – 427	397 – 434	363 – 378
	0.87 m (M)	477 – 518	435 – 462	419 – 453	385 – 401
	1.15 m (E)	504 – 543	468 – 495	441 – 474	418 – 440
Deposit surface temperature	0.59 m (W)	n.a.	489 – 680	n.a.	399 – 598
	0.87 m (M)		514 – 641		419 – 596
	1.15 m (E)		542 – 631		616

5.4 Sampling Probes after the Experiment

5.4.1 Sampling Probe No.1

The probe was taken out from the furnace at hour 387 (day 16) for a brief inspection. It was covered all around by deposits as shown in Figure 5.3a. The deposit on the front side (directly facing the gas stream) was generally thicker than on the rear side of the probe. Cracks separating deposits into a top and bottom part were observed on the side, in the middle and the end of the probe. After 769 hours of exposure, probe No.1 was finally withdrawn from the furnace. The front side and the rear side of the probe are shown in Figure 5.3b and Figure 5.3c respectively.

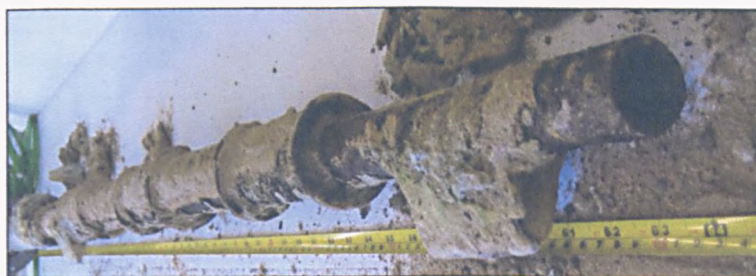
It was found that a major portion of the thick deposits detected earlier had fallen off in the furnace. The top part of the front side of the probe was the only area where a thick deposit was found. The other areas were covered by a very thin layer of deposit except the end section of the rear side where deposit was barely detected.

Scale or substance accumulating on sampling probe No.1 was composed of (1) a thick layer of deposit at the outmost, (2) hard lamella layers of corrosion products

which were easily detached from the probe, and (3) at the scale-metal interface, a very thin film of dense and powdery corrosion products.



(a)



(b)



(c)

Figure 5.3 Probe No.1 after being exposed to the hot gas: (a) 387 hours – front side, (b) 769 hours – front side, (c) 769 hours – rear side

a. The Thickness and the Forms of Scale

The thickness and the formation of scale layers on the probe varied depending on their position on the probe and the type of alloys in that particular area. Table 5.6 presents the thickness (measured by a vernier caliper) and positions of the scale at various locations on the probe. A simplified diagram showing the position and the formation of scale on the alloy rings is presented in Figure 5.4. The thickness values of corrosion products presented in Table 5.6 and Figure 5.4 were mainly of the

detachable corrosion products (hard lamella layers). It was not possible to measure the thickness of the thin film at the scale-metal interface by a vernier caliper.

Table 5.6 The thickness and position of scales at various locations on probe No.1

Locations	Deposit		Corrosion products	
	Thickness (mm)	Covered area (to the Y-axis)	Thickness (mm)	Covered area (to the Y-axis)
2in 625	10 – 35			
1in –W	9 – 16			
BFW	3.5		1	All
59W	8	-120° to 30°	Barely detectable	-180° to 30°
556W	15	-120° to 30°	2	-90° to 135°
625W	13	-120° to 30°	1	-180° to 30°
1in – M1	13			
59M	7	-105° to 20°	<1	All round but thicker at -200° to 30°
556M	8	-105° to 20°	2.5	-120° to 90°
625M	8	-105° to 20°	0.5	All round but thicker at -200° to 30°
1in – M2	7			
59E	8	-90° to 0°	1	All round but thinner at the bottom side
556E	5	-90° to 0°	2	-90° to 30°
625E	6	-90° to 0°	0.5	All round but thinner at the bottom side
1in – E	7			
BFE	3.5 - 4		1	All

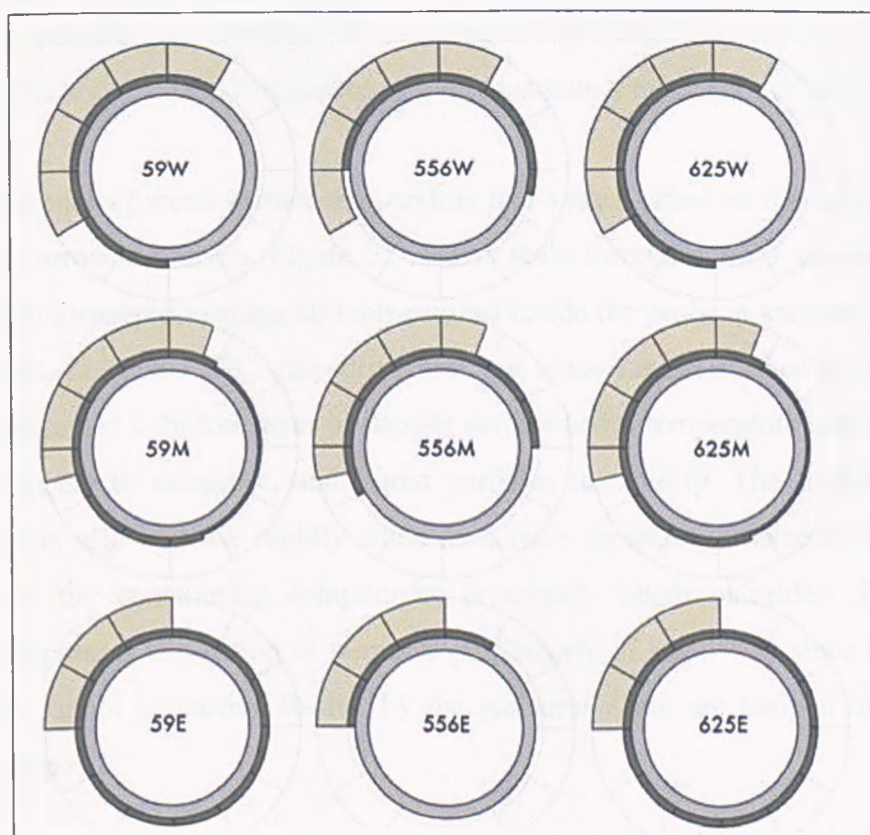


Figure 5.4 Diagrams for the formation of deposits (yellow colour) and corrosion products (brown colour) on the metal rings of probe No.1

Deposit found to be thicker on the front side of the probe could be clearly explained by using the mathematical modelling (further described in Chapter 6). In summary, the front side of the probe was the area where the gas and particles impinged on the probe directly, and with the highest velocity. Therefore, the deposit was maintained by the force of the flue gas flow. This result agreed with a previous study which proved that the inertia-controlled transport is the dominant transport mechanism of particles. The study had considered the deposition rate which resulted from the change in heat transfer, diffusion and thermophoresis processes (Van Beek et al., 2001).

Important factors that cause the deposits to fall off during the exposure time are:

1. The weight of deposit
2. The easily detached layer of corrosion products – it is porous due to the loss of metal elements from the vaporization during the oxidation process (spallation). Therefore, it cannot carry the increasing weight of deposit.
3. Cracking due to the temperature difference in the probe – the temperature gradient of 82°C for a distance of 0.56 m can lead to a difference in expansion, and consequently cracking and spalling of the deposit.
4. The shock due to fluctuation of the gas stream temperature or velocity

The difference of metal surface temperature had a great effect on the deposit amount and the corrosion process. Figure 5.5 shows scale formation on 3 sections of alloy rings. The measured average air temperatures inside the probe at sections W, M, and E were 94, 122 and 175°C, respectively. It was clear that the surface having a lower temperature had a thicker layer of deposit since a lower temperature surface allowed more vapours to condense, and liquid particles to solidify. The thickness of the deposit can also increase rapidly when its surface temperature exceeds the melting points of the constituting compounds, principally alkali chlorides. The molten deposit increases deposition of particles particularly of small size since these small particles cannot be carried further by the gas stream but are trapped in the sticky molten deposit.

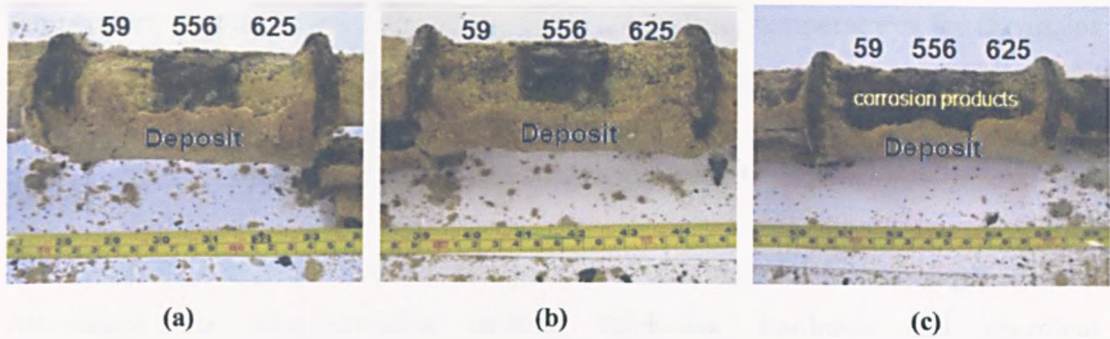


Figure 5.5 Probe No.1 after the test: (a) wall/rear, (b) middle/rear, (c) end/rear

The temperature significantly contributes to the corrosion process as can be clearly identified in Figure 5.6. The main tube (1 inch) at the near wall position (Figure 5.6a) still had a shiny metallic surface, whereas the end section (Figure 5.6b) had corrosive surface damage. It is concluded that the rate of the corrosion process increases with temperature.



Figure 5.6 Baffles of probe No.1 after the test: (a) wall/rear, (b) end/rear

b. Characteristics of Deposits

The deposit on probe No.1 was composed mainly of fine yellow particles. It had the same visible characteristic as the deposit collected from the surrounding furnace walls. As the deposition continued, larger particles, especially flake-shaped particles, were accumulated on the old deposit surface. It was found that the upper layer of the thick deposit was brown in colour and contained larger particles. The evidence of molten deposit was detected in locations such as on the thickest deposit covering the 2 inch tube (Figure 5.7a) and on the baffles (Figure 5.7b). On the molten areas, deposits had a mixed colour of light green, white and grey. This observation agrees with the modelling work showing that the surface temperatures of deposits covering the 2 inch tube were as high as 680°C. This temperature is higher than the melting

temperature of various eutectic compounds. The melting temperatures for the major constituents of the deposit were previously shown in Table 2.2.

c. Corrosion Products of Alloys 59, 556, and 625

The chemical composition of the different substrate material (metal rings) directly determines the characteristics (colour, thickness, hardness and chemical composition) of the corrosion products and the protective oxide layer. The detachable lamella layers (as shown in Figure 5.7c) of corrosion products are an un-protective oxide layer resulting from the oxidation of metal from the substrate followed by the volatilization of metals to the atmosphere (Kawahara, 2002). Such layers tend to be hard and brittle, with low cohesive strength; each layer could be separated by a slight force. They could be easily removed from the parent ring material, leaving a thin film covering the metal surface. The colours of the thin films formed on each alloy are described in . After the spalled layers of corrosion products were removed, the thickness of each ring was measured. The values were then calculated in order to find out the changes (%) in the thickness of each alloy ring. The results are shown in Table 5.7.

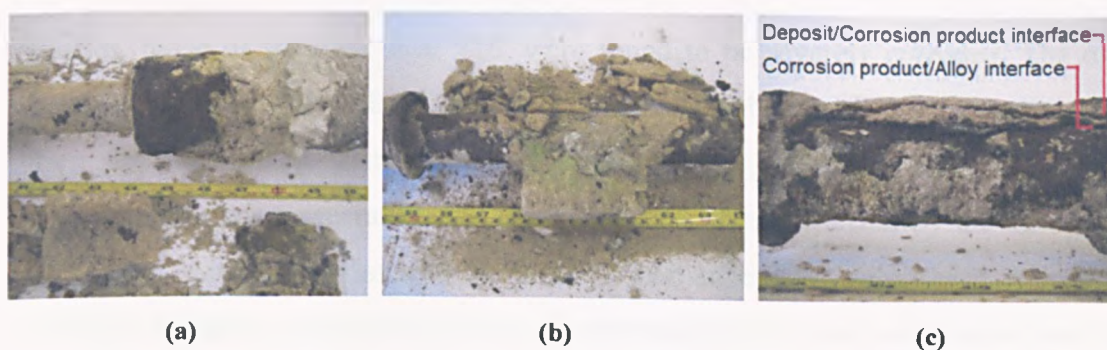


Figure 5.7 Probe No.1 after the test: (a) 2inch tube – rear, (b) baffle end – front, (c) end/bottom

Table 5.7 Changes (%) in the thickness of alloy rings (measured by a vernier caliper) and the characteristics of corrosion products.

Material	59			556			625			1in (625)				2in
	W	M	E	W	M	E	W	M	E	W	M1	M2	E	
Change (%)	+	-	-	-	-	-	+	+	+	+	+	+	+	-
	4.67	23.1	1.95	2.57	3.62	2.81	5.71	6.43	4.38	11.97	5.24	5.63	2.64	0.39
Corrosion products	Greenish brown Max. thickness = 1 mm			Black and soft Max. thickness = 2 mm			Dark green/ brown Max. thickness = 0.5 mm			Dark green/ brown Max. thickness = detectable				

The results do not give a conclusive idea about the affect of temperature, but they clearly show the effect of alloy composition on the thickness loss. Alloy 556 experienced the most thickness loss, followed by alloy 59. This implies that oxidized products of alloy 556 spalled off easily and were not protective. Conversely, the thickness of alloy 625 increased after the test. This could mean that the scale formed on alloy 625 is more adherent to the metal substrate. Therefore it can be a protective layer preventing further diffusion of oxidants (particularly O₂ and Cl₂) and subsequently slow down corrosion reaction of this alloy. Further investigations and their results supporting this idea are described in the section 5.9 – 5.11.

Alloy 625 and alloy 59 are both nickel-based alloys. Therefore, their corrosion products have a similar colour which is greenish brown whereas the corrosion products of alloy 556 were black. A decrease in diameter of the 2 inch tube might be the result of corrosion due to the molten salts. Nevertheless, one should note that the thickness measurement was possibly misread. This is due to the presence of a thin film that could not be removed from the metal surface. Hence, some changes (%) were positive values.

d. Corrosion of Baffles

Baffles, made of stainless steel 316, were found to be severely corroded. The oxide layers were black with a slight amount of dark reddish brown. The baffle at the end of the probe was broken. They were covered by fused deposits. This was mainly due to the higher surface temperature since the baffles were not affected by the air-cooling. The voids between baffles and the main 1 inch tube were filled with yellow fine particles. Spallation (expanded layers) of corrosion products are common especially at the edge where baffles were welded to the probes. There was no evidence that these baffles can prevent or reduce the corrosion of the 1 inch tube in the area where they were welded.

5.4.2 Sampling Probe No.2

Probe No.2 was taken out from the furnace for a brief inspection after 284 hours (day 12) as shown in Figure 5.8a. The overall experiment was completed after 811 hours

of exposure. Figure 5.8b shows the probe and its deposit as it was brought back to the lab.



(a)



(b)

Figure 5.8 Probe No.2 after being exposed to the hot gas: (a) 284 hours, (b) 811 hours

a. The Thickness and the Forms of Scale

The accumulation of deposits detected after 284 hours was similar to the findings at 811 hours. There was a thick layer of deposit formed on the top half of the probe whereas the bottom half was coated by a thin film of deposit. The top half was the side directly facing the flue gas stream. The relatively symmetric shape of deposit formed on the top side corresponded with the fact that gas stream flowed downward and relatively vertical. It also agreed with the mathematical modelling results.

The amount of deposit found on this probe was more than that of probe No.1. The thick layers of deposit were found on the whole length of the probe as shown in Table 5.8. The deposit thickness varied from 40 mm at the beginning of the probe to 16 mm at the end. The factors inducing a larger amount of deposit on this probe are: (1) the lower temperature of the probe and the environment promoting more droplets

to condense on the surface, and (2) the position of the probe against the flue gas stream which allows gravity to promote more deposition.

The thick deposits easily fell off approximately 10 minutes after the probe had been withdrawn from the furnace. The exposed areas, earlier covered by deposit, look relatively similar to the bottom side of the probe. The only exception is that at the same position along the probe, the visible corrosion products on the bottom side of the probe were slightly thicker than those on the top side.

The amounts of visible corrosion products detected on this probe were less than those of probe No.1. Metallic, shiny surfaces were still detected on the 2 inch tube, 1 inch W, 59W and 625W. Figure 5.9 shows probe sections after the thick layer of deposit was removed. Visible corrosion was detected on alloy 556 (W-E), 1 inch tube M2, ring E, 1 inch tube E, and baffles. However, thin films of a dark oxide layer were also present randomly on 59M, 625M, and coated coupons E.

The locations of visible corrosion products at various positions on probe No.2 are shown in Table 5.8. It was not possible to measure the thickness of these corrosion product layers since they were very thin and firmly attached to the metal surface. There is no spallation except for alloy 316 (baffles). Nevertheless, the corrosion products of alloy 556 E were noticeably thicker than for alloys 59 and 625. Results from Table 5.8 confirm the fact that temperature plays a vital role in the formation of deposits as well as the corrosion products.

Table 5.8 The thickness of deposits and the availability of corrosion products at various locations on probe No.2

Locations	Deposit thickness (mm)	Corrosion products	Locations	Deposit thickness (mm)	Corrosion products
2 in	40	n.a.	556M	20	++
1 in - W		n.a.	625M		+
BFW	40 (100% covered)	++++	1 in - M 2	20	+
59W	24	n.a.	59E	16	++
556W		+	556E		+++
625W		n.a.	625E		++
1 in - M 1		n.a.	1 in - E		++
C59/310W	24 (100% covered)	+	C59/310E	16 (100% covered)	+
59M	20	+	BFE	16 (50% covered)	++++

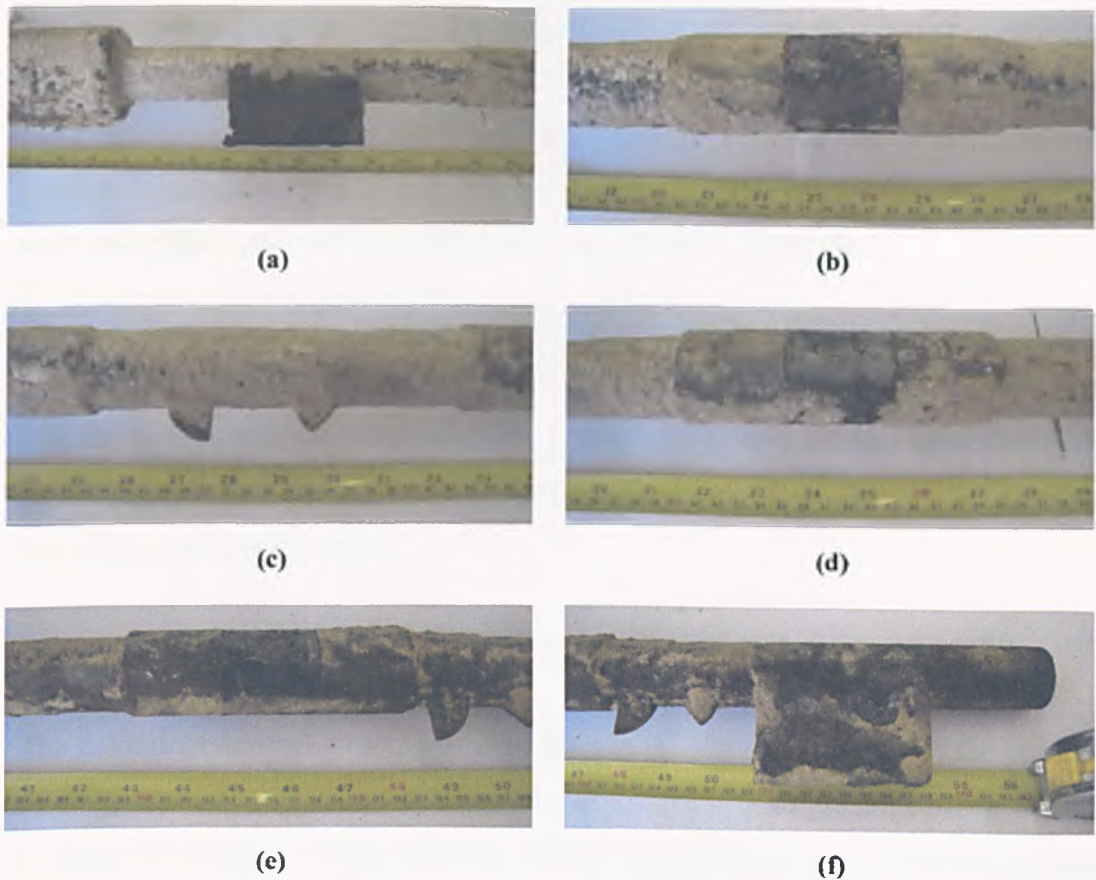


Figure 5.9 Probe No.2 after the test: (a) linchW and baffle wall – front, (b) wall/front, (c) linchM1 and coated coupons – front, (d) middle/front, (e) end/front, (f) linchE, coated coupons, baffle end - front

b. Characteristics of Deposits

Deposits on probe No.2 were generally composed of 4 types of particles: yellow fine powder, yellow flakes (larger sizes), brown/black particles, and condensed deposits. The first two types were the main compositions of deposit collected from probe No.1 and they are the main constituents of the thick deposits on the top side of this probe. Flakes and brown/black particles were occasionally detected inside the body of these thick deposits. The condensed deposit was in the form of a thin film appearing adjacent to the metal surface or corrosion products. It was the initial layer of deposit formed when the probe was first placed into the furnace. From the modelling work, the temperatures of the metal surface were relatively low, varying from 397 – 474°C. These temperatures induce the condensation of liquid aerosols to take place instantly; after that, particles of different sizes of were accumulated.

The particulates found in the 2nd pass of the furnace are generally larger in size than those found in the 1st pass. The reason is that the lower temperature and the longer residence time in the flue gas allows more particles to form, and in the same time more accumulation of these small particles. Therefore, the deposits from probe No.2 were more likely to crumble than the packed deposit on probe No.1.

There was no evidence of molten salts or melted deposits on this probe although its deposits were thicker than for probe No.1. This is because the temperature on the deposit surface may be lower than its melting point. This finding agrees with the modelling results suggesting that the maximum surface temperature of deposit on this probe can be only 616°C.

c. Corrosion Products of Alloy 59, 556, and 625

The colours of corrosion products formed on each alloy were similar to the previous findings. Corrosion products of alloy 59 and 625 were dark greenish brown and the corrosion products of alloy 556 were black. Spallation of the un-protective oxide layers was not commonly found because of the lower operating temperature.

The thickness of alloy rings was measured by using a vernier calliper in order to make a preliminary evaluation of the corrosion damage. The changes (%) in the thickness of each alloy ring are shown in Table 5.9. The measurement was carried out both for the top side and the bottom side. Unfortunately, the results do not provide conclusive evidence about the effect of particle deposition. The thickness of the rings seems to increase at the end section of the probe due to the additional thickness of the oxide layers. In general, these results support previous findings suggesting that alloy 556 experienced the most damage, followed by alloy 59. However, there were a lot of possible errors during the thickness measurement because: (1) the thin film could not be removed from the metal surface and (2) the alloy rings distorted by the heat during the cutting, or when they were taken apart.

d. Corrosion of Coated Coupons

The coated coupons were entirely covered with corrosion under the deposit when the probe was taken out. After the thick deposits were removed and coupons were cut

out from the probe, it was found that there were thin oxide films formed on the metal surfaces. The coupons were in a good condition. There is no chip, broken structure, or spallation detected. Coatings proved to be an efficient way to protect the alloy from this corrosive environment. Both alloy 59 and alloy 310 showed no severe corrosion damage.

Table 5.9 Changes (%) in thickness of metal rings after deposits and spalled corrosion products were removed.

Material	59			556			625		
	W	M	E	W	M	E	W	M	E
Top side (%)	-2.32	-2.70	+1.60	-6.40	-5.79	+0.19	-2.48	+1.79	+1.49
Bottom side (%)	-1.45	-0.15	+0.42	-6.70	-6.90	-6.74	-0.57	+0.99	+4.72
Average (%)	-1.89	-1.43	+1.01	-6.55	-6.34	-3.28	-1.52	+1.39	+3.10

e. Corrosion of Baffles

It was noted that the wall-section baffle was fully covered by the deposits. Only the bottom of the end-section baffle was covered by the deposits. They were as severely corroded as the baffle on probe No.1. Spallation was commonly detected, especially at the edges. The baffle-wall was very thin and had chipped. Its spalled corrosion products were easily detached and fell off. This proves that the deposits increase corrosion damage significantly (hot corrosion). There was no evidence that these baffles can reduce or prevent the corrosion of the 1 inch tube in the area where they were welded. Instead, it retains the deposit and probably increases the risk of hot corrosion in that area.

5.5 Physical Characteristics of Other Combustion Residues

Samples of combustion residues collected from various locations inside the furnace are shown in Figure 5.10. The descriptions in the following section present the average particle sizes in term of 'volume mean diameter'. These values were taken from the previous experiment (Phongphiphat, 2006) in which samples of combustion residues from a similar waste to energy plant were analysed.

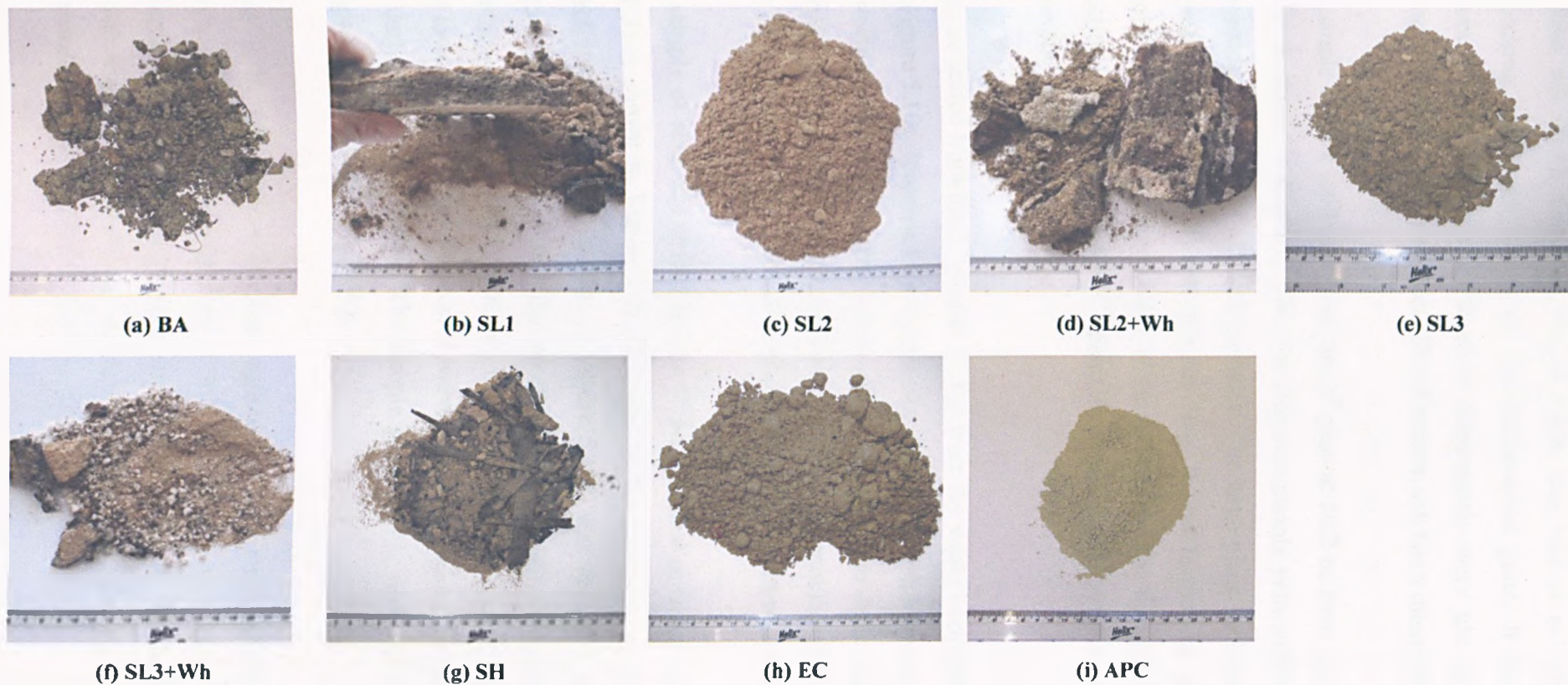


Figure 5.10 Combustion residues collected from the furnace: (a) BA: bottom ash, (b) SL1: slag from the 1st pass at 10.2m from the waste burning bed, (c) SL2: slag from the 1st pass at 25.1m from the waste burning bed, (d) SL2+Wh: white deposit from the 1st pass at 25.1m from the waste burning bed, (e) SL3: slag from the 1st pass at 28.7m from the waste burning bed, (f) SL3+Wh: white deposit from the 1st pass at 28.7m from the waste burning bed, (g) SH: fouling from the superheater tube in the 2nd pass, (h) EC: deposits collected from the economizer, (i) APC: air pollution control residues

Bottom ash (BA), shown in Figure 5.10a, was wet as collected because of the quenching after being burnt on the incineration grate. It consisted of the un-combustible materials and the main components were glasses, pieces of metal, ceramic and gravels. More than 85% of bottom ash has a diameter larger than 1 mm.

A sample of slag collected from the 1st pass at 10.2 m from the waste burning bed (SL1) is shown in Figure 5.10b. The slag was mainly yellowish brown powder with a considerable amount of black particles. The large piece in this picture is a fraction of refractory that was fused with the slag. It was formed by the condensation of liquid aerosols on the hot surface of the refractory. The flue gas temperatures at this location are higher than 850°C (plant data) and the waterwall directly receives heat from the flame.

Slag collected from the 1st pass at 15.8 m from the waste burning bed (SL2) is shown in Figure 5.10c. It appears to be sand-like, fine yellowish brown powder. At the same collection point, a white precipitate (SL2+Wh) was also detected as shown in Figure 5.10d. This precipitate might be the result of the ammonia injection which was used for NO_x removal. This precipitate was white and semi-transparent.

A sample of slag collected from the 1st pass at 19.4 m from the waste burning bed (SL3) is shown in Figure 5.10e. Similar to the previous sampling point, a white precipitate (SL3+Wh), shown in Figure 5.10f, was found at this position. These samples were collected from the site of probe No.1 where the measured temperature was approximately 850°C. The colour of SL3 was darker than the deposits found in the lower section of the furnace. However, various colours varying from light yellow to dark brown were found. The sample of SL3+Wh was a white semi-transparent agglomerate similar to SL2+Wh.

Slag is in the form of packed agglomerates of small particles and condensed aerosols. The real particle size of this sample can be largely altered during the sampling and the sample preparation prior to analysis. Therefore, the particle size distribution of slag was not carried out. However, the particle size of SL3 is noticeably larger than that of SL1 and SL2.

Fouling material (SH) collected from a superheater tube is shown in Figure 5.10g. It was sampled from the 2nd pass of the furnace at 28.3 m from the waste burning bed. This is the top of the superheater tube bank and the experiment site for probe No.2. The temperatures in this area were measured to be in the range of 730 - 791°C. The sample collected was both deposit on the tube, and the corrosion products of superheater material. The deposit comprised brown, white and yellow particles. The corrosion products of steel 15Mo3 were black and brittle. The thickness of this spalled layer is in the range of 2 – 4 mm. The mean diameter of the superheater deposit is 181 µm from previous study.

Fly ash from the economiser (EC), shown in Figure 5.10h, was collected from the bunker installed at the connection of the 2nd and the 3rd pass. The flue gas temperature in this area was approximately 300°C. The bunker collects two sources of particles. First is the fly ash that was removed from the economiser by using the soot blower. Second is the heavy and large fly ash that falls into the bunker as it could not be transported further with the upward flow. The samples were dark brown in colour and generally contain heavy and/or large particles ($\approx 355 \mu\text{m}$). This fly ash is sent to a secure landfill site together with other air pollution control residues.

The air pollution control residue (APC), as shown in Figure 5.10i, was collected from the bag filter. This sample had a yellowish grey colour. It was a mixture of fly ash, lime and activated carbon. The particle size of this residue is the smallest, partly due to the presence of lime. The mean diameter of the APC is approximately 75 µm.

5.6 Elemental Composition of the Probe Deposits and Other Combustion Residues

5.6.1 Combustion Residues

The elemental compositions of combustion residues, expressed in mg/kg, are shown in Table 5.10. The major elements, contributing more than 1% by weight, are listed in Table 5.11. Alternatively, results expressed in term of 'mol/kg' are shown in Table 5.12.

These results are in the same range as reported by previous studies (Wiles, 1996; Li et al., 2004; Williams, 2005). The results show that the major constituents of the bottom ash were Ca, Al, Fe and P.

The waterwall slag collected from the level of 10.2 m (SL1), 15.8 m (SL2) and 19.4 m (SL3) from the waste burning bed were mainly composed of Cl, Ca, Na, S, K, Zn, Al, and Pb. White precipitates found in the slag were composed of a high concentration of K (15.10 – 19.20%) and Na (13.00 – 13.40%), and to a lesser extent S, Zn, Ca and Fe. These precipitates are probably oxides, chlorides, and other compounds of K and Na; however, further analysis for Cl and N is needed for a conclusion.

The main components of the superheater deposit (SH1 and SH2) are Cl, S, Fe, K, Ca, Na, Zn, and Al. It is obvious that the amounts of Cl, Zn, Ca and Pb were lower than those of the slag samples. The age of slag samples, which allow longer time for the accumulation of elements, might be the reason. The high amount of Fe detected was due to contamination from the Fe oxide layer on the tube surface.

Samples of slag and superheater deposit contained a high concentration of S, Cl and alkali metals, as expected. These elements were reported to potentially form compounds of molten salts which enhance the hot corrosion in the furnace. Other significant constituents are SO₃, HCl, soot and volatile metal compounds. These compounds also contributed largely to the corrosion as they (1) supply S and Cl to the metal surface and (2) create a local reducing atmosphere.

Fly ash from the economizer ash bunker (EC) was mainly composed of Ca and, to a lesser extent, Cl, S, Al, K, Na, C, H, Fe and Mg. The high concentrations of Ca and Al are contributed largely from the sediment of heavy particles that cannot be transported further with the gas stream. The high concentration of Fe was mainly due to the ferrous oxide scale particles detached from the superheater tube.

Table 5.10 Elemental composition of 10 samples of combustion residues (m/kg)

	BA	SL1	SL2	SL2+Wh	SL3	SL3+Wh	SH1	SH2	EC	APC
C	n.m.	n.m.	n.m.	n.m.	n.m.	n.m.	n.m.	n.m.	14,600	9,200
H	n.m.	n.m.	n.m.	n.m.	n.m.	n.m.	n.m.	n.m.	15,100	3,400
N	n.m.	n.m.	n.m.	n.m.	n.m.	n.m.	n.m.	n.m.	n.detect	n.detect
Cl	n.m.	n.m.	155,000	n.m.	138,000	n.m.	111,000	54,500	59,500	60,000
S	6350	22,200	53,500	10,500	91,700	21,000	26,000	75,700	35,000	148,000
P	12,900	9350	5550	1600	3760	1530	1090	4070	6850	2,200
Zn	3050	10,500	36,200	10,600	35,100	8160	10,900	20,200	7860	13,800
K	4430	7350	69,900	151,000	90,400	192,000	33,100	81,900	24,600	54,000
Na	9410	17,300	48,300	130,000	62,200	134,000	22,700	60,500	21,600	44,500
Mg	8000	9400	8050	2480	4940	2400	1410	5300	10,700	2850
Ca	152,000	128,000	147,000	48,200	10,400	54,000	28,500	98,000	197,000	197,000
Al	34,000	31,000	21,000	8500	15,800	7400	3600	12,900	29,000	5500
Si	2760	2780	1160	2390	3920	1530	1010	3040	760	6570
Ti	1510	1030	2680	857	1630	958	563	1760	2120	838
Fe	44,500	6140	7280	10,800	3690	5570	235,000	43,200	14,200	2130
Pb	1500	398	25,000	3600	55,000	3900	5500	6200	1800	6000
Cu	2400	160	950	720	1060	740	1600	1150	530	9200
Hg	<0.1	<0.1	<0.1	<0.1	<0.1	<0.1	<0.1	<0.1	<0.1	<0.1
Tl	0.2	0.1	6.3	0.8	9.2	1.0	1.3	0.9	1.2	1.9
V	22	197	21	26	23	17	10	36	37	6.2
Se	1.9	<1	6.3	2.8	5.5	1.9	3.5	8.0	7.5	4.2
Mn	760	480	817	278	460	210	3600	2200	1020	270
Sb	75	605	380	70	590	90	180	680	520	1020
Ni	120	84	100	8150	720	610	650	1200	78	17
Mo	8	7	12	580	68	85	750	410	24	8.8
Cr	82	187	185	1070	260	249	343	340	181	73
Co	75	22	28	15	18	11	33	26	36	10
Be	0.5	0.8	0.8	0.4	0.5	0.3	0.1	0.5	0.9	0.3
As	4.2	51	17	4.7	21	4.4	18	29	33	31
Ag	4.3	3.2	20	28	17	28	14	28	13	28
Ba	980	205	400	230	333	180	205	395	675	230
Cd	3.9	24	350	140	560	170	410	330	89	290
Sn	1840	240	290	54	500	75	86	520	300	1150
Sr	370	145	300	110	227	99	67	212	400	360
Li	38	12	21	16	27	10	11	33	18	24
Rb	8.6	9.2	200	210	250	240	79	160	53	100
La	7.4	11	9.9	3.5	5.5	2.9	1.7	6.9	12	4.3
Ce	18	15	14	5.5	7.3	4.2	2.3	9.6	18	5.3
Nd	5.8	6.2	5.6	2.9	2.9	2.1	1	4.1	8	3.1
W	1.7	1.2	3.5	1.4	3.3	1.8	3.1	2.6	3.3	2.8
others	712,764	751,186	415,243	607,754	415,248	564,719	511,558	524,948	555,252	544,023

Note: n.m. is 'not measured', n.detect is 'can not be detected (lower than detectable level)'.

Table 5.11 Major elemental composition (>1%) of 10 samples of combustion residues (wt.%)

	BA	SL1	SL2	SL2+Wh	SL3	SL3+Wh	SH1	SH2	EC	APC
C	n.m.	n.m.	n.m.	n.m.	n.m.	n.m.	n.m.	n.m.	1.46	
H	n.m.	n.m.	n.m.	n.m.	n.m.	n.m.	n.m.	n.m.	1.51	
Cl	n.m.	n.m.	15.50	n.m.	13.80	n.m.	11.10	5.45	5.95	6.00
S		2.22	5.35	1.05	9.17	2.10	2.60	7.57	3.50	14.80
P	1.29									
Zn		1.05	3.62	1.06	3.51		1.09	2.02		1.38
K			6.99	15.10	9.04	19.20	3.31	8.19	2.46	5.40
Na		1.73	4.83	13.00	6.22	13.40	2.27	6.05	2.16	4.45
Mg									1.07	
Ca	15.20	12.80	14.70	4.82	10.40	5.40	2.85	9.80	19.70	19.70
Al	3.40	3.10	2.10		1.58			1.29	2.90	
Fe	4.45			1.08			23.50	4.32	1.42	
Pb			2.50		5.50					

Note: n.m. is 'not measured', n.detect is 'can not be detected (lower than detectable level)'.

Table 5.12 Major molecular composition of 10 samples of combustion residues ($\times 10^{-3}$ mol/kg)

	BA	SL1	SL2	SL2+Wh	SL3	SL3+Wh	SH1	SH2	EC	APC
C	n.m.	n.m.	n.m.	n.m.	n.m.	n.m.	n.m.	n.m.	1216	766
H	n.m.	n.m.	n.m.	n.m.	n.m.	n.m.	n.m.	n.m.	14,950	3366
Cl	n.m.	n.m.	4372	n.m.	3893	n.m.	3131	1537	1678	1693
S	198	692	1669	328	2402	655	811	2361	1092	4616
P	417	302	179		116			131	221	
Zn		161	553	162	555	125	167	309	120	211
K	113	188	1788	3862	2246	4910	847	2095	629	1381
Na	409	753	2101	5655	2706	5829	987	2632	940	1936
Mg	329	387	331	102	217			218	440	117
Ca	3792	3194	3668	1203	2323	1347	711	2445	4915	4915
Al	1260	1149	778	315	704	274	133	478	1075	204
Si								108		234
Fe	797	110	130	193		100	4208	774	254	
Pb			121		232					
Ni				139						

Note: n.m. is 'not measured'.

Air pollution control (APC) residues have a high concentration of Ca, S, Cl, K, Na, Zn, C and heavy metals such as Pb and As. This is largely a result of activated carbon and lime injection. Partitioning behavior of elements in the furnace was observed. Less volatile elements such as Fe and Al were mostly found in the bottom

ash whereas more volatile elements such as Cd, Pb and As were detected more in the air pollution control residues.

Pb concentration in these combustion residues was very high (up to 5.5% in wall slag at the position of probe No.1). The deposition and corrosion process can be affected by the presence of heavy metals. Heavy metals, in the form of chlorides and sulphates, can interact with alkali chloride or alkali sulphates. The consequent formation of liquid phases with even lower melting points compared to the pure salts significantly accelerates the deposition and corrosion processes (Arvelakis and Frandsen, 2005).

The other main constituents in all combustion residues, which were not analysed in this study, are O and Si due to the limitation of the instrument (results of Si were reported but they were not accurate). Wiles (1996) reported the range of Si concentration to be 9.1 – 31 % for the bottom ash, 9.5 – 21 % for fly ash and 3.6 – 12 % for APC residues.

Nitrogen was not detected in the samples from economizer ash (EC) and APC residues after being analysed by “Perkin Elmer 2400 CHN Analyzer” (for carbon, hydrogen and nitrogen as described in section 4.3.1). Similarly, N was not found in the samples of probe deposit (section 5.6.2) and corrosion products (section 5.6.3).

The common inorganic compounds in fly ash collected from waste to energy plants, reported by other studies (Vassilev and Braekman-Danheux, 1999; Williams, 2005) are summarized in Table 5.13. The high contents of chloride salts, alkali oxides and soluble matter contents in the ash are due to the use of high amounts of salty foods and plastic materials during incineration. For the bottom ash, a great amount of hexahedral crystals α -SiO₂ (fuel component), CaCO₃, and CaSO₄ are often detected (Li et al., 2004).

Table 5.13 The typical compounds found in fly ash collected from waste to energy plants (Vassilev and Braekman-Danheux, 1999; Williams, 2005)

Types of Compounds	Examples of Compounds
Potassium and Sodium	NaCl, K ₂ ZnCl ₄ , K ₂ PbO ₄ , KCl, K ₂ H ₂ P ₂ O ₅ , Na ₂ SO ₄ , K ₂ SO ₄
Silica, Silicate, Aluminosilicate	SiO ₂ , CaSiO ₃ , Al ₂ SiO ₅ , CaAl ₂ SiO ₆ , Ca ₃ Al ₆ Si ₂ O ₁₆ , NaAlSiO ₃ , KAlSi ₃ O ₈ , 3Al ₂ O ₃ ·2SiO ₂ , MgAl ₂ O ₄ , Al ₂ O ₃
Calcium	CaAl ₄ O ₇ , CaSO ₄ , CaCO ₃ , CaO, Ca(OH) ₂
Lead	Pb ₃ SiO ₇ , Pb ₃ O ₂ SO ₄ , Pb ₃ Sb ₂ O ₇
Cadmium	CdSO ₄ , Cd ₅ (AsO ₄) ₃ Cl
Zinc	K ₂ ZnCl ₄ , ZnCl ₂ , ZnSO ₄
Iron and Titanium	Fe ₂ O ₃ , FeO, TiO ₂
Other compounds	CuCl ₂ , Pb ₃ PO ₄ , SnO ₂

5.6.2 Deposit on Probes

The elemental compositions of the deposits on probe No.1, expressed in mg/kg, are shown in Table 5.14. The major elements, contributing more than 1% are listed in Table 5.15. Results expressed in 'mol/kg' are shown in Table 5.16. Results of furnace wall slag at the same position (SL3, SL3+Wh) are also presented for comparison.

Table 5.17 - Table 5.19 present the results of elemental composition, in terms of mg/kg, percentage of major elements, and mol/kg for probe No.2. Results for superheater deposits (SH1, SH2) are also given in the last two columns for comparison.

For both probes, the elemental compositions for deposit samples were relatively similar to the elemental composition of the wall slag in the surrounding area. The major elements found in probe deposits are Ca, Cl, S, K, Na, and Al.

Table 5.14 Elemental composition of deposit collected from probe No.1 (mg/kg)

	2inch (h387)	2inch (h769)	Wall (556W)	Middle (556M)	End (59E)	End (BF-E)	SL3	SL3+Wh
C	n.m.	n.m.	n.detect	n.detect	n.m.	3900	n.m.	n.m.
H	n.m.	n.m.	11,800	5,500	n.m.	n.detect	n.m.	n.m.
N	n.m.	n.m.	n.detect	n.detect	n.m.	n.detect	n.m.	n.m.
Cl	144,500	n.m.	159,900	273,100	n.m.	90,900	138,000	n.m.
S	57,400	50,500	50,800	53,700	42,400	49,300	91,700	21,000
P	5590	7150	4750	5400	5220	7800	3760	1530
Zn	7840	4690	5930	8330	10,200	4590	35,100	8160
K	52,500	20,400	83,200	90,900	85,500	32,200	90,400	192,000
Na	50,400	21,100	66,200	67,000	66,000	30,900	62,200	134,000
Mg	8240	11,600	7250	8230	7950	12,000	4940	2400
Ca	187,000	236,000	176,000	181,000	146,000	224,000	10,400	54,000
Al	30,900	22,000	13,700	15,700	17,300	23,700	15,800	7400
Si	2740	1800	2350	2400	1730	2600	3920	1530
Ti	2300	3400	2330	2620	2030	3460	1630	958
Fe	5380	6410	4460	4640	7500	7420	3690	5570
Pb	2200	177	1430	1110	2300	290	55,000	3900
Cu	800	320	850	920	890	510	1060	740
Hg	<0.1	<0.1	<0.1	<0.1	<0.1	<0.1	<0.1	<0.1
Tl	0.3	<0.1	0.7	0.5	0.9	0.1	9.2	1.0
V	36	32	17	17	41	37	23	17
Se	8.5	5.5	10	12	5.7	5.7	5.5	1.9
Mn	740	1030	620	741	847	1030	460	210
Sb	320	390	240	280	240	280	590	90
Ni	2400	92	460	94	22,700	840	720	610
Mo	290	23	87.5	32.5	3890	742	68	85
Cr	690	402	523	375	4790	2700	260	249
Co	28	34	300	34	701	38	18	11
Be	0.1	0.4	0.2	0.2	0.4	0.6	0.5	0.3
As	12	16	12	12	9	17	21	4.4
Ag	28	13	48	52	45	19	17	28
Ba	630	749	859	662	728	550	333	180
Cd	190	34	215	210	230	48	560	170
Sn	260	290	210	250	210	250	500	75
Sr	326	440	370	410	285	330	227	99
Li	16	9.6	15	17	19	10	27	10
Rb	88	37	150	160	140	58	250	240
La	8.8	11	6.6	6.8	9.1	12	5.5	2.9
Ce	12	16	10	11	13	17	7.3	4.2
Nd	4.9	6.8	4.6	4.7	5.6	7.7	2.9	2.1
W	6.3	12	72	12	110	17	3.3	1.8
Others	436,115	610,810	404,819	276,056	569,960	499,421	415,248	564,719

Note: n.m. is 'not measured', n.detect is 'can not be detected (lower than detectable level)'

Table 5.15 Major elemental composition (>1%) of the deposit collected from probe No.1 (wt.%)

	2inch (h387)	2inch (h769)	Wall (556W)	Middle (556M)	End (59E)	End (BF-E)	SL3	SL3+Wh
H	n.m.	n.m.	1.18		n.m.	n.detect	n.m.	n.m.
Cl	14.45	n.m.	15.99	27.31	n.m.	9.09	13.8	n.m.
S	5.74	5.05	5.08	5.37	4.24	4.93	9.17	2.10
Zn					1.02		3.51	
K	5.25	2.04	8.32	9.09	8.55	3.22	9.04	19.2
Na	5.04	2.11	6.62	6.90	6.6	3.09	6.22	13.4
Mg		1.16				1.2		
Ca	18.70	23.60	17.6	18.1	14.6	22.4	1.04	5.40
Al	3.09	2.20	1.37	1.57	1.73	2.37	1.58	
Pb							5.50	
Ni					2.27			

Note: n.m. is 'not measured', n.detect is 'can not be detected (lower than detectable level)'

Table 5.16 Major molecular composition of deposit collected from probe No.1 ($\times 10^{-3}$ mol/kg)

	2inch (h387)	2inch (h769)	Wall (556W)	Middle (556M)	End (59E)	End (BF-E)	SL3	SL3+Wh
C	n.m.	n.m.	n.detect	n.detect	n.m.	325	n.m.	n.m.
H	n.m.	n.m.	11,683	5446	n.m.	n.detect	n.m.	n.m.
Cl	4076	n.m.	4511	7704	n.m.	2564	3893	n.m.
S	1790	1575	1585	1678	1323	1538	2402	655
P	180	231	153	174	169	252	116	
Zn	120			127	156		555	125
K	1343	522	2128	2325	2187	824	2246	4910
Na	2192	918	2880	2914	2871	1344	2706	5829
Mg	339	477	298	339	327	494	217	
Ca	4666	5888	4391	4516	3643	5589	2323	1347
Al	1145	815	508	582	641	878	704	274
Fe		115			134	133		100
Pb							232	
Ni					387			

Note: n.m. is 'not measured', n.detect is 'can not be detected (lower than detectable level)'

Table 5.17 Elemental composition of deposit collected from probe No.2 (mg/kg)

	Wall (556W)	Middle (556M)	End 1 (556E)	End 2 (556E)	SH1	SH2
C	n.detect	n.detect	n.detect	n.detect	n.m.	n.m.
H	3900	3300	4100	n.detect	n.m.	n.m.
N	n.detect	n.detect	n.detect	n.detect	n.m.	n.m.
Cl	127,200	199,800	186,500	232,600	111,000	54,500
S	60,000	65,000	61,000	71,000	26,000	75,700
P	4970	3840	4060	2550	1090	4070
Zn	5100	7570	8080	6610	10,900	20,200
K	49,200	87,000	84,500	114,000	33,100	81,900
Na	43,400	64,800	63,000	86,000	22,700	60,500
Mg	7840	6050	6380	4110	1410	5300
Ca	201,000	165,000	168,000	138,000	28,500	98,000
Al	18,000	14,000	16,000	10,000	3,600	12,900
Si	5840	3150	5060	2410	1010	3040
Ti	2390	2090	2120	1450	563	1760
Fe	6440	5150	5870	3280	235,000	43,200
Pb	980	1100	1320	1070	5500	6200
Cu	578	922	935	758	1600	1150
Hg	0.1	<0.1	<0.1	0.1	<0.1	<0.1
Tl	0.5	0.6	0.7	0.7	1.3	0.9
V	45	37	40	26	10	36
Se	8.2	8.7	6.2	7.6	3.5	8.0
Mn	692	562	599	354	3600	2200
Sb	360	280	280	180	180	680
Ni	300	80	1060	90	650	1200
Mo	38	22	150	53	750	410
Cr	320	266	613	222	343	340
Co	25	20	83	17	33	26
Be	0.5	0.3	0.4	0.2	0.1	0.5
As	22	17	19	13	18	29
Ag	28	47	44	47	14	28
Ba	590	644	635	591	205	395
Cd	140	260	290	290	410	330
Sn	280	240	230	170	86	520
Sr	338	373	383	352	67	212
Li	17	23	21	24	11	33
Rb	100	180	170	220	79	160
La	8.9	7.6	7.1	4.7	1.7	6.9
Ce	13	10	10	6.9	2.3	9.6
Nd	5.6	4.7	4.4	3	1	4.1
W	14	11	26	9.9	3.1	2.6
Others	459,816	369,134	378,403	323,480	511,558	524,948

Note: n.m. is 'not measured', n.detect is 'can not be detected (lower than detectable level)'

Table 5.18 Major elemental composition (>1%) of the deposit collected from probe No.2 (wt.%)

	Wall (556W)	Middle (556M)	End 1 (556E)	End 2 (556E)	SH1	SH2
Cl	12.72	19.98	18.65	23.26	11.10	5.45
S	6.00	6.50	6.10	7.10	2.60	7.57
Zn					1.09	2.02
K	4.92	8.70	8.45	11.4	3.31	8.19
Na	4.34	6.48	6.30	8.60	2.27	6.05
Ca	20.10	16.50	16.80	13.80	2.85	9.80
Al	1.80	1.40	1.60	1.00		1.29
Fe					23.50	4.32

Note: n.m. is 'not measured', n.detect is 'can not be detected (lower than detectable level)'

Table 5.19 Major molecular composition of deposit collected from probe No.2 ($\times 10^{-3}$ mol/kg)

	Wall (556W)	Middle (556M)	End 1 (556E)	End 2 (556E)	SH1	SH2
C	n.detect	n.detect	n.detect	n.detect	n.m.	n.m.
H	3861	3267	4059	n.detect	n.m.	n.m.
Cl	3588	5636	5261	6561	3131	1537
S	1871	2027	1903	2215	811	2361
P	160	124	131			131
Zn		116	124	101	167	309
K	1258	2225	2161	2916	847	2095
Na	1888	2819	2740	3741	987	2632
Mg	323	249	263	169		218
Ca	5015	4117	4192	3443	711	2445
Al	667	519	593	371	133	478
Si	208	112	180			108
Fe	115		105		4208	774

Note: n.m. is 'not measured', n.detect is 'can not be detected (lower than detectable level)'

It was obvious that the Ca concentrations in the deposits were much more than that found in the slag. The percentage of Ca in the deposits accounts for 14.6 – 23.6% for probe No.1, and 13.8 – 20.1% for probe No.2 whereas there was less than 9.8% of Ca in the slag wall. This can be explained by the following. Ca is often present as small particles released from the waste burning bed. It is therefore easier to deposit on the probes that were placed in the flow rather than on the wall. The lower surface temperature of the probe also induces particle deposition by thermophoresis, and condensation of liquid aerosol. Certain elements (namely Zn, Pb and S) are present

in the wall slag at higher percentages than the amount present in the probe deposits. A possible reason for this could be that: (1) there is a large concentration of Ca on the probe, and (2) the wall slag is older deposit and hence has greater accumulation of particles containing these elements.

Some deposit samples were contaminated with corrosion products. Deposit collected from the end section (59E) was contaminated by the corrosion products of alloy 59, resulting in a high concentration of Ni. Samples of SH1 and SH2 were contaminated with corrosion products (Fe_xO_y) from the superheater.

In Cl-containing flue gases, high temperature corrosion of the superheater by chlorine is normally accelerated by oxidation and sulphidation. A high concentration of S in deposits (varying from 4.24 – 5.74% for probe No.1, and 6.0 – 7.1% for probe No.2) and Cl (9.09 – 27.31% for probe No.1, and 12.72 – 23.26% for probe No.2) can certainly lead to severe damage to the alloy.

Other elements such as Pb, Zn and Sn can also critically increase the damage chlorine corrosion (Uusitalo et al., 2004). Compounds of these elements, particularly the chlorides, generally have low melting temperatures. Therefore, molten-phase corrosion is triggered at a low temperature and subsequently the reaction rate of Cl-induced corrosion is increased.

5.6.3 Corrosion Products

This section presents the elemental composition of the corrosion products originating from four types of alloys: alloy 59, alloy 556, alloy 625 and austenitic stainless steel 316 (baffle). The elemental compositions in term of mg/kg are shown in Table 5.20.

The major elements (%) are listed in Table 5.21. Results expressed in 'mol/kg' are shown in Table 5.22. Most of the corrosion product samples were taken from sampling probe No.1 because the experiment using sampling probe No.2 did not yield enough corrosion products for this analysis.

Table 5.20 Elemental composition of corrosion products (mg/kg)

	Alloy 59		Alloy 556					Alloy 625		Alloy 316	
	59W	59E	556W	566M	556M	556E	556E	625W	625E	BF-E	BF-E
	(sp 1)	(sp 1)	(sp 1)	(sp 1)	(sp 2)	(sp 1)	(sp 2)	(sp 1)	(sp 1)	(sp 1)	(sp 2)
S	50,300	44,700	33,500	31,400	56,000	37,200	49,000	57,200	54,700	19,800	22,200
P	2330	2750	730	1400	1800	870	1020	1970	1900	235	141
Zn	23,300	13,000	20,300	18,800	29,500	14,200	14,900	24,200	14,000	4770	4520
K	81,200	97,100	84,800	75,100	70,800	107,000	83,200	92,900	107,000	36,400	38,000
Na	51,900	68,200	39,700	36,900	34,700	59,600	37,800	62,100	73,600	29,800	23,300
Mg	3290	4300	1260	2490	2080	1470	1010	3470	3600	250	70
Ca	100,000	98,900	53,500	71,600	65,500	44,400	46,400	94,600	87,100	15,100	14,500
Al	7800	10,000	3500	6500	14,000	3700	4800	8300	7500	430	415
Si	1620	2600	500	480	1730	630	1410	1050	1950	650	702
Ti	1130	1460	260	500	713	280	359	880	870	120	87.2
Fe	4800	4470	67,900	62,000	57,100	59,900	78,200	4460	28,800	152,000	149,000
Pb	34,500	9900	34,500	26,000	33,600	18,400	14,800	24,700	5700	580	1540
Cu	2160	1560	2480	2000	2400	2350	2100	1870	1380	550	443
Hg	<0.1	<0.1	<0.1	<0.1	0.6	<0.1	0.6	<0.1	<0.1	<0.1	<0.1
Tl	16	4.3	16	12	20	7.6	8.5	11	2.4	0.3	0.8
V	140	180	95	90	87	93	93	26	25	36	88
Se	5.5	2.9	6.1	6.4	6.4	<1	1.3	6.8	<1	<1	<1
Mn	497	517	2420	2400	2180	2270	2850	430	1530	4520	4080
Sb	300	170	120	130	260	61	100	280	180	28	30
Ni	67,300	83,600	51,500	53,300	39,700	53,300	50,300	70,500	71,900	13,500	1300
Mo	15,000	21,500	8780	8630	6160	9980	7880	9680	10,200	4580	760
Cr	17,600	15,700	34,800	32,300	24,800	28,900	25,300	13,500	13,800	6510	6330
Co	960	400	36,000	36,300	28,300	34,300	32,900	537	3510	210	94
Be	0.2	0.2	<0.1	0.2	<0.1	0.1	<0.1	0.1	0.1	<0.1	<0.1
As	10	4.4	6.7	9	16	5.6	7.6	6.1	4.5	21	6.4
Ag	33	46	30	35	38	45	49	37	41	14	14
Ba	707	744	410	602	342	356	244	621	626	143	137
Cd	1200	570	1350	1240	1200	1220	980	970	400	72	160
Sn	280	140	120	120	250	58	100	250	160	55	31
Sr	325	240	170	220	133	115	93	255	215	45	39
Li	19	21	11	13	12	14	10	23	19	5.5	4.9
Rb	250	180	260	260	270	260	250	260	180	59	85
La	4.4	5.1	27	24	23	26	35	3.6	5.2	0.3	0.2
Ce	5	6.4	1.6	4	4.1	1.9	2.3	5	4.4	0.3	0.2
Nd	1.8	2.6	0.9	1.4	1.8	0.8	1.1	2.1	1.9	0.2	0.2
W	250	92	1400	1900	3100	1800	3200	34	210	33	23
Ta					160		140				<1
Others	530,766	516,934	519,546	527,233	523,013	517,186	540,456	524,862	508,886	709,482	717,898

Table 5.21 Major elemental composition (>1%) of the corrosion products (wt.%)

	Alloy 59		Alloy 556					Alloy 625		Alloy 316	
	59W	59E	556W	566M	556M	556E	556E	625W	625E	BF-E	BF-E
	(sp 1)	(sp 1)	(sp 1)	(sp 1)	(sp 2)	(sp 1)	(sp 2)	(sp 1)	(sp 1)	(sp 1)	(sp 2)
S	5.03	4.47	3.35	3.14	5.60	3.72	4.90	5.72	5.47	1.98	2.22
Zn	2.33	1.30	2.03	1.88	2.95	1.42	1.49	2.42	1.40		
K	8.12	9.71	8.48	7.51	7.08	10.7	8.32	9.29	10.70	3.64	3.80
Na	5.19	6.82	3.97	3.69	3.47	5.96	3.78	6.21	7.36	2.98	2.33
Ca	10.00	9.89	5.35	7.16	6.55	4.44	4.65	9.46	8.71	1.51	1.45
Al		1.00			1.40						
Fe			6.79	6.20	5.71	5.99	7.82		2.88	1.52	1.49
Pb	3.45		3.45	2.60	3.36	1.84	1.48	2.47			
Ni	6.73	8.36	5.15	5.33	3.97	5.33	5.03	7.05	7.19	1.35	1.53
Mo	1.50	2.15							1.02		
Cr	1.76	1.57	3.48	3.23	2.48	2.89	2.53	1.35	1.38		
Co			3.60	3.63	2.83	3.43	3.29				

Table 5.22 Major molecular composition of corrosion products ($\times 10^{-3}$ mol/kg)

	Alloy 59		Alloy 556					Alloy 625		Alloy 316	
	59W	59E	556W	566M	556M	556E	556E	625W	625E	BF-E	BF-E
	(sp 1)	(sp 1)	(sp 1)	(sp 1)	(sp 2)	(sp 1)	(sp 2)	(sp 1)	(sp 1)	(sp 1)	(sp 2)
S	1569	1394	1045	979	1747	1160	1528	1784	1706	618	692
Zn	356	199	310	287	451	217	228	370	214		
K	2077	2483	2169	1921	1811	2737	2128	2376	2737	931	972
Na	2258	2967	1727	1605	1509	2592	1644	2701	3201	1296	1013
Mg	135	177		102				143	148		
Ca	2495	2468	1335	1786	1634	1108	1158	2360	2173	377	362
Al	289	371	130	241	519	137	178	308	278		
Fe			1216	1110	1023	1073	1400		516	2722	2668
Pb	167		167	125	162			119			
Ni	1147	1147	877	908	676	908	857	1201	1225	230	261
Mo	156	1424				104		101	106		
Cr	338		669	621	477	556	487	260	265	125	122
Co			611	616	480	582	558				

The results show that the corrosion products are comprised of (1) the deposit composition such as Ca, K, Na, S, Zn, Al, and Pb and (2) the elements of alloys such as Fe, Ni, Mo, Cr, and Co.

The percentage of Cd is significant in these corrosion products, accounting for 72 – 1350 mg/kg. However, the maximum concentration of Cd was only 290 mg/kg in the deposits covering the probes. Cd plays a vital role in hot corrosion since it can form compounds that have a low melting temperature.

Elements in the corrosion products of alloys varied depending on the major alloy composition. In general, alloys can withstand the corrosive environment when their composition species, such as Fe, Ni, Cr, Mo, V, Ti, and Al, form a passive or protective oxide layer. Other elements are also required in order to increase the corrosion resistance or to stabilize the alloy composition. Mo and N are added to the alloy to give high resistance to chloride pitting and crevice corrosion. Al, Nb, Ta, and Ti are added to prevent the grain boundary corrosion that results from the formation of Cr_3Cr_2 .

Alloy 59 and alloy 625 are nickel based alloys. Therefore a major component of their corrosion products is Ni (6.73–8.36% for alloy 59 and 7.05–7.19% for alloy 625). Other important components are Mo (1.5–2.15% for alloy 59, 0.97-1.02% for alloy 625) and Cr (1.76-1.57% for alloy 59, 1.35-1.38% for alloy 625). Possible compounds forming the protective oxide layer for alloy 59 and alloy 625 include NiO, Cr_2O_3 , MoO_2 . Other minor compounds consist of Al_2O_3 , SiO_2 and Nb_2O_5 (Kawahara, 2002).

The corrosion products of stainless steel 556 and stainless steel 316 are composed mainly of Fe (5.71-6.79% for alloy 556, and 1.49-1.52% for steel 316). Other major components include Ni (3.97-5.33% for alloy 556, 1.35-1.53% for steel 316), Cr (2.48-3.48% for alloy 556, 0.63-0.65% for steel 316) and Co (2.83-3.60% for alloy 556). The possible compounds forming a protective oxide layer for these stainless steels are Fe_2O_3 , Fe_3O_4 , Ni, and Cr_2O_3 (Kawahara, 2002). Other compounds such as $(\text{Fe,Cr})_2\text{O}_3$, FeCr_2O_4 , NiCr_2O_4 are reported to be main components in the external scale (Tsaur et al., 2005).

5.7 Phase Study by Using X-Ray Diffractometer

The results of phase analysis for the corrosion products from alloy 59, coated alloy 59, alloy 625, alloy 556 and coated stainless steel 310 are shown in Figure 5.11. There are 3 diffraction patterns for each alloy. The first graph (black colour) is the diffraction pattern of the substrate or the fresh alloy. The results of samples after being exposed in the furnace are shown in the second (red) and the third graphs (blue). The second graph is derived from the 'locked coupled' scan which gives the results for the deeper level of alloy (~25 μm from the surface). The third graph presents the results from the 'detector scan' mode operated at a glancing angle of 8° , which gives the results for the alloy surface (~2 μm from the surface).

Crystalline substances detected in corrosion products of these alloys are summarized in Table 5.23 together with their reference card numbers. The presence of substances is marked by a plus sign. The question mark indicates an uncertainty due to the inadequate amount or height of peaks. The last column lists the other possible substances. The presence of some of these compounds cannot be confirmed because their diffraction patterns are superseded by the other major substances.

In summary, substances detected in the corrosion products of alloy 59 and alloy 625 include NiO^* , $\text{NiCr}_2\text{O}_4^*$, Cr_2O_3 , CrO_2 , MoO_2^* and MoO_3^* (where * indicates compounds detected with a strong signal). For coated alloy 59; NiAl^* , Ni_2Al_3^* , NiAl_3 , $\theta\text{-Al}_2\text{O}_3$, $\alpha\text{-Al}_2\text{O}_3^*$, NiO^* , Cr_2O_3 , CrO_2 , MoO_2 , and MoO_3 were detected.

Compounds detected in the corrosion products of alloy 556 were Fe_2O_3^* , Fe_3O_4^* , FeO(OH) , NiO^* , $\text{NiCr}_2\text{O}_4^*$, Cr_2O_3 , and CrO_2 .

Finally, for the coated stainless steel 310, FeAl , Fe_3Al^* , NiAl^* , $\theta\text{-Al}_2\text{O}_3$, $\alpha\text{-Al}_2\text{O}_3^*$, Fe_2O_3^* , Fe_3O_4^* , FeO(OH) , NiO , Cr_2O_3 and CrO_2 were detected.

NiO was detected throughout the depth analysed (from the scale surface to the alloy substrate) where as other compounds were only detected near the substrate alloy (> 2 μm from the scale surface).

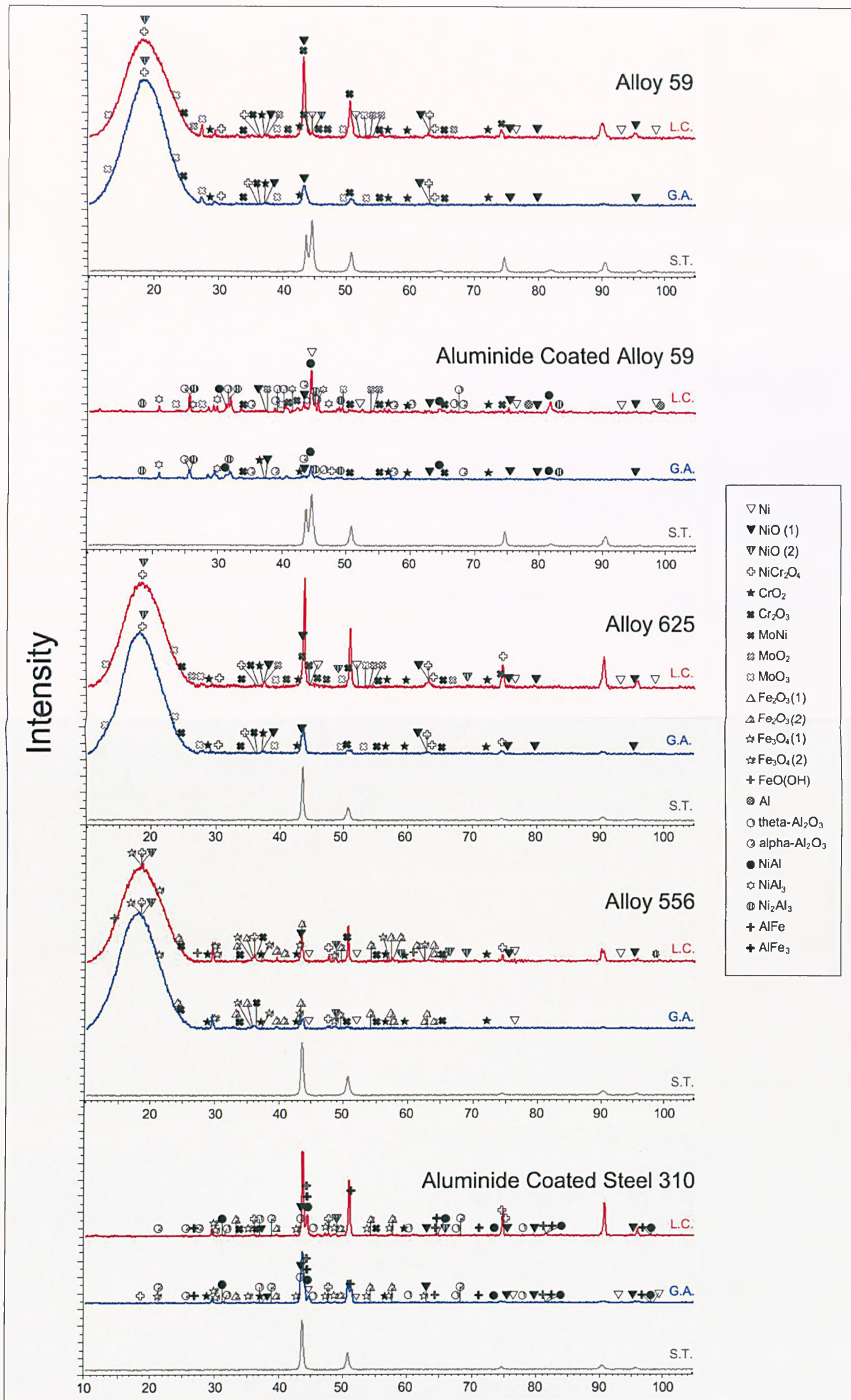


Figure 5.11 XRD analysis for alloy rings and aluminide coated alloys.

Table 5.23 Crystalline substances detected in the scale/corrosion products of alloy samples

Name		No.	Crystal Structure	59 (Ni-Cr-Mo)			C59 (Al)		625 (Ni-Cr-Mo)			556 (Fe-Ni-Cr-Co)			C310 (Fe-Cr-Ni)		
				LC	GA	ST	LC	GA	LC	GA	ST	LC	GA	ST	LC	GA	ST
AlNi	Al Ni	44-1188	Cubic	-	-	-	S	S	-	-	-	-	-	-	S	W	-
Al ₃ Ni	Al Ni	02-0416	Orthorhombic	-	-	-	W	-	-	-	-	-	-	-	-	-	-
Al ₃ Ni ₂	Al Ni	02-1265	Hexagonal	-	-	-	S	S	-	-	-	-	-	-	-	-	-
AlFe	Al Iron	33-0020	Cubic	-	-	-	-	-	-	-	-	-	-	-	W	W	-
AlFe ₃	Al Iron	06-0695	Cubic	-	-	-	-	-	-	-	-	-	-	-	S	W	-
δ-Al ₂ O ₃	Al oxide	46-1131	Tetragonal	-	-	-	-	-	-	-	-	-	-	-	?	-	-
θ-Al ₂ O ₃	Al oxide	11-0517	Monoclinic	-	-	-	W	?	-	-	-	-	-	-	W	W	-
α-Al ₂ O ₃	Al oxide	50-1496	Monoclinic	-	-	-	S	W	-	-	-	-	-	-	S	W	-
NiO	Ni Oxide	44-1159	Hexagonal	S	S	-	S	S	S	S	-	W	-	-	W	W	-
	Ni Oxide	85-1977	Hexagonal	S	S	-	-	-	S	S	-	S	W	-	W	-	-
NiCr ₂ O ₄	NiCrOx	85-0935	Tetragonal	S	W	-	-	-	W	W	-	S	W	-	W	W	-
Cr ₂ O ₃	Cr oxide	82-1484	Hexagonal	W	W	-	W	W	W	W	-	W	W	-	W	-	-
CrO ₂	Cr oxide	75-0078	Tetragonal	W	W	-	W	W	W	W	-	W	W	-	-	W	-
Fe ₃ O ₄ - 1	Magnetite	79-0416	Cubic	-	-	-	-	-	-	-	-	S	W	-	W	W	-
Fe ₃ O ₄ - 2	Magnetite	89-0951	Cubic	-	-	-	-	-	-	-	-	W	W	-	S	W	-
Fe ₂ O ₃ - 1	Maghemite, syn	39-1346	Cubic	-	-	-	-	-	-	-	-	W	?	-	-	-	-
Fe ₂ O ₃ - 2	Hematite, syn	33-0664	Hexagonal	-	-	-	-	-	-	-	-	S	S	-	S	W	-
Fe ₂ O ₃	Hematite, syn	39-0238	Cubic	-	-	-	-	-	-	-	-	?	-	-	-	-	-
B-Fe ₂ O ₃	Iron Ox beta	40-1139	Hexagonal	-	-	-	-	-	-	-	-	?	-	-	?	-	-
FeO(OH)	Lepidocrodite	74-1877	Orthorhombic	-	-	-	-	-	-	-	-	W	?	-	?	?	-
FeO(OH)	Goethite, syn	81-0462	Orthorhombic	-	-	-	-	-	-	-	-	-	-	-	?	?	-
MoO ₂	Mo oxide	73-1249	Monoclinic	S	?	-	W	-	S	?	-	-	-	-	-	-	-
MoO ₃	Molybdite, syn	35-0609	Orthorhombic	S	W	-	W	-	S	W	-	-	-	-	-	-	-
CoO	Co oxide	48-1719	Cubic	-	-	-	-	-	-	-	-	-	-	-	-	-	-
CoO	Co oxide	42-1300	Cubic	-	-	-	-	-	-	-	-	-	-	-	-	-	-
CoCr ₂ O ₄	Cochromite, syn	78-0711	Cubic	-	-	-	-	-	-	-	-	?	-	-	-	-	-
Ni	Nickel, syn	04-0850	Cubic	S	-	?	?	-	W	-	?	W	W	-	-	W	-
Mo-Ni	Mo nic	48-1745	Orthorhombic	S	?	-	W	?	W	?	-	-	-	-	-	-	-
Al	Al, syn	04-0787	Cubic	-	-	-	W	?	-	-	-	-	-	-	-	-	-

Note: 'S' indicates strong presence of signal, 'W' indicates weak presence of signal, and '?' indicates inadequate presence of signal of the diffraction pattern.

5.8 Phase Transformation Study of Deposits and Other Combustion Residues

Differential thermal analysis of combustion residues or probe deposits was conducted in order to find out the melting temperature of these samples. The results of DTA are shown in Figure 5.12. The numbers written in the graph are the temperatures at which the peaks occur. The samples that were analysed consist of (1) SL3 - wall slag collected near the position of probe No.1, (2) Deposit on probe No.1 – middle section, (3) SH - superheater deposit collected near the location of probe No.2, (4) Deposit on probe No.2 – middle section, (5) Deposit on probe No.2 – End section. These samples were heated in a furnace in the presence of air. A sample of superheater deposit was re-analysed in order to confirm the results but Argon gas was used instead of air.

The results show that these samples are composed of several compounds characterized by the broad, asymmetric melting peaks. A eutectic melt was detected as a small second peak present prior the tall peak at the melting temperature. This can be found in the results for probe No.1's deposit. There was a eutectic melt at 1321°C prior the melting peak at 1365°C.

In general, the trends of all results were similar, especially for the samples of SL3, deposit on probe No.1, and both samples of deposit on probe No.2. The first endothermic peak for these results, varied between 137 – 174°C, represents the evaporation of physical and hygroscopic water. Then, there are more endothermic peaks falling between 524 – 683°C. This temperature range can be interpreted as the melting temperature of eutectic mixtures in the ash or simply of the presence of low melting compounds. Compounds that have melting temperatures lower than 524 °C are, for example, PbCl_2 (501°C), $73\text{ZnCl}_2+27\text{PbCl}_2$ (300°C), $31\text{NaCl}+69\text{PbCl}_2$ (410°C), $21\text{KCl}+79\text{PbCl}_2$ (411°C) and $\text{K}_2\text{SO}_4+\text{Na}_2\text{SO}_4+\text{ZnSO}_4$ (384°C). These compounds are abundant in the deposit samples as shown from the elemental analysis and the SEM/EDS analysis. More details for melting temperatures of different species and binary mixtures are shown in Table 2.2 (page 16).

The graphs of SL3 and probe No.1's deposit start to decline from 683°C whereas the results for deposit on probe No.2 decrease from approximately 800 °C. This possibly expresses the collapse of the structure. They have an endothermic peak at the end of the experiment (1360°C for SL3, 1365°C for probe No.1's deposit, 1179°C for SH, 1234°C for SH(in Argon), 1308°C for probe No.2 DepMid, and 1123°C for probe No.2-DepEnd). These temperatures possibly are the melting temperatures of binary mixtures of compounds shown in Table 5.24, as well as the signs for sublimation, phase transition and chemical reactions.

Table 5.24 Common minerals in solid residues from MSW combustion and their melting temperatures

Minerals in solid residues from MSW combustion	Melting temperatures (°C)
KCl	771
NaCl	801
PbO	888
CaF ₂	1418
CaSO ₄	1460
Fe ₂ O ₃	1475-1565
CaSiO ₃	1540
Fe ₃ O ₄	1597
SiO ₂	1610
BaTiO ₃	1625
TiO ₂	1840
CaTiO ₃	1980

The slag sample may undergo a re-crystallization at 1129°C. Similarly, the deposit sample for probe No.2 may have re-crystallized around 809°C. Results for the superheater sample do not show a water evaporation peak. There is first endothermic peak at 272°C which could be a melting point of, for example, 48ZnCl₂+52KCl (254°C), 82ZnCl₂+18KCl (262°C), 39ZnCl₂+50KCl+11PbCl₂ (275°C) and ZnCl₂ (290°C). In the presence of argon, this sample shows a peak at 100°C for water evaporation. The wide endothermic peak with the highest point at 642°C might represent phase transition or crystallization.

In summary, compounds in these deposit samples start to melt in the temperature range of 524 – 683°C. At a higher temperature, samples experience further melting, structural damage, phase transition, re-crystallization and maybe sublimation.

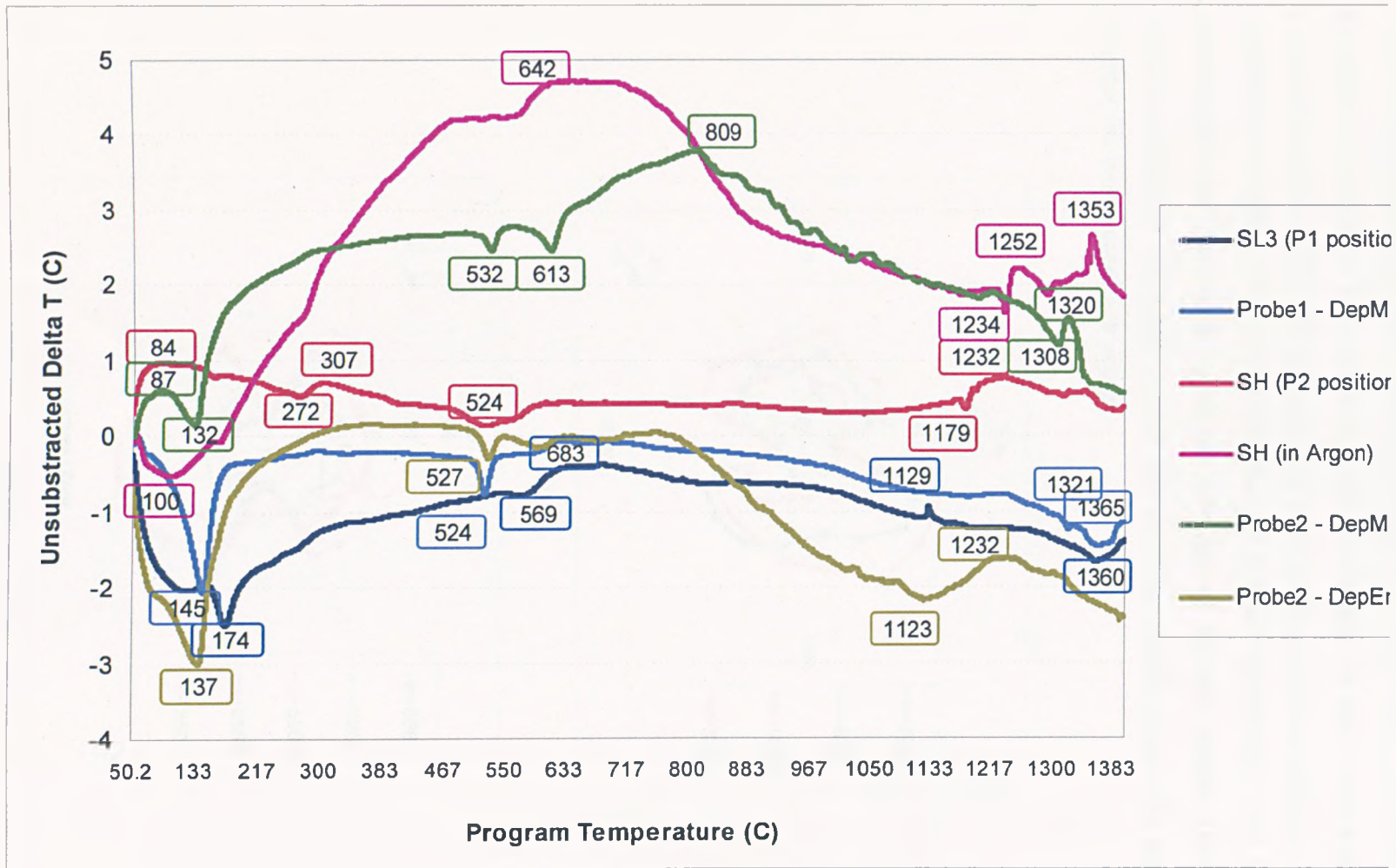
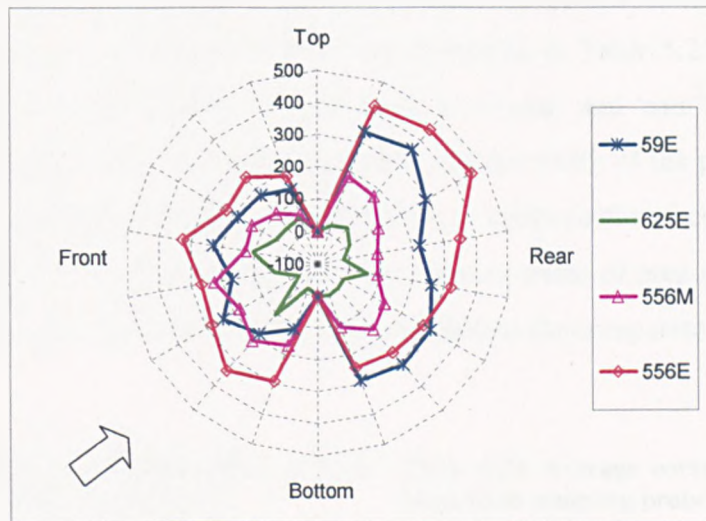


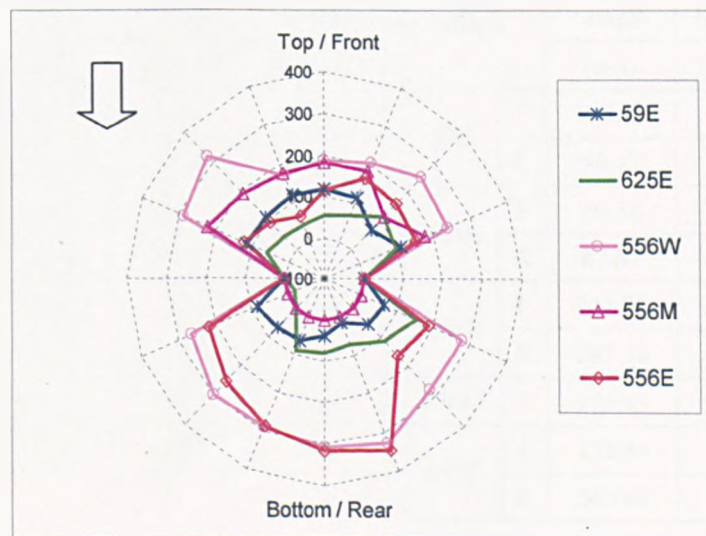
Figure 5.12 The results of Differential Thermal Analysis (DTA) for samples of combustion residues and probe deposits.

5.9 Corrosion Rates of Metal Alloy Samples

Corroded lengths for different segments on the alloy rings were measured by using an optical microscope. The results of corroded length (in μm) were then plotted against the position on the alloy by using a circle graph as shown in Figure 5.13. The position on the graph directly signifies the real position on the ring when looked at from the end, and the arrow shows the direction of flue gas stream. The distance from the center to the graph means the corroded length; hence the longer the distance, the worse corrosion occurs.



(a)



(b)

Figure 5.13 Corroded length (μm) of alloy rings from the sampling probes: (a) sampling probe No.1, (b) sampling probe No.2

The results for both probes are not plotted in a full circle because the samples of the alloy rings were cut into half; front side and rear side, during the disassembling. Thus, measurements close to the cut edge were not carried out. The reason is to avoid errors due to the alloy expansion as a result of cutting.

The effects of deposit on the corrosion rate can be investigated by using Figure 5.13. The results reveal that the area covered with the deposit becomes less corroded compared to the side that is exposed to the flue gas. However, the results for 556M do not comply with this statement.

The results for the cross-sectional corroded length (μm) and corrosion rate of alloy rings from probe No.1 and probe No.2 are presented in Table 5.25 and Table 5.26. The corrosion rates are present in both units: 'mm/year' and 'mm²/year'. The latter unit was calculated from the corroded length and the width of the particular location in which the length occurs. The average values of cross-sectional corroded area were then used to find the corrosion rate of alloy rings in terms of area per unit time. The corrosion rates (mm/year) for both probes are plotted for comparison in Figure 5.14.

Table 5.25 Average corrosion rates of alloy rings from sampling probe No.1

Alloy Rings		Average Corroded Length	Corrosion Rate (Length)	Corrosion Rate (Area)
		(μm)	(mm/yr)	(mm ² /yr)
59E	F	178.75	2.04	239
	R	293.62	3.34	387
625E	F	41.27	0.47	53
	R	14.89	0.17	19
556M	F	150.33	1.71	189
	R	131.99	1.50	176
556E	F	267.76	3.05	354
	R	343.60	3.91	456

Table 5.26 Average corrosion rates of alloy rings from sampling probe No.2

Alloy Rings		Average Corroded Length	Corrosion Rate (Length)	Corrosion Rate (Area)
		(μm)	(mm/yr)	(mm ² /yr)
59E	F	104.43	1.13	132
	R	59.17	0.64	75
625E	F	69.38	0.75	86
	R	67.87	0.73	86
556W	F	242.28	2.62	300
	R	287.18	3.10	355
556M	F	175.43	1.89	220
556E	F	123.86	1.34	155
	R	240.69	2.60	304

Corrosion Rate (mm/year) for probe No.1

Corrosion Rate (mm/year) for probe No.2

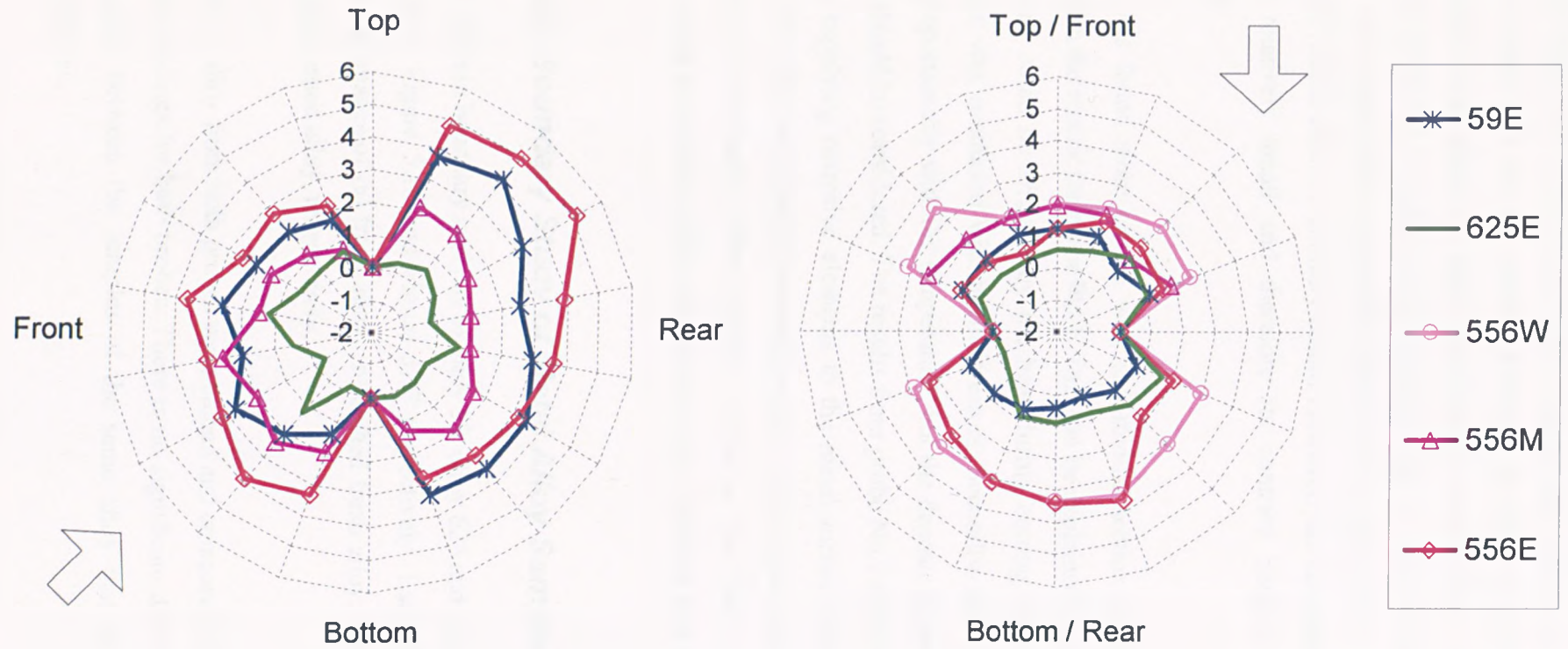


Figure 5.14 Comparison of corrosion rate of alloy rings from the sampling probes (mm/year)
 (Note: Arrows represent the direction of flue gas stream)

The results from this measurement and calculations reveal that the corrosion resistance of alloy 625 was the greatest followed by alloy 59 and alloy 556. The alloys suffered more under the local conditions for probe No.1. On average, the operation of probe No.1 increases the corrosion rate in alloy 59 and alloy 556 by 204% and 77% respectively compared to the results for probe No.2. This is not valid for alloy 625 which shows a contrary result. However, the corroded values of alloy 625 were relatively small and therefore its contrary number should not be convincing.

Corrosion was found more on the wall and middle section of probe No.2. This disagrees with the results for probe No.1. This can be explained in two ways. Firstly, the alloy ring could be affected by the heat during cutting. Hence the thickness measurement was conducted with intrinsic errors. Secondly, the corrosion damage increases proportionally with the temperature, but the deposit thickness was another factor that should be considered. The results from probe No.2 show that a thick layer of deposit, supplying corrosive elements to the metal surface through cracks, can overcome the effect of reduced temperature and initiate more corrosion damage. These cracks result mainly from thermal stress, as the thick layer of deposit generates a large temperature difference between the waterwall side and hot gas side.

5.10 Grain Boundary Study of Metal Alloy Samples

The results of grain boundary analysis of alloy 59, alloy 625 and alloy 556 are shown in Figure 5.15, Figure 5.16 and Figure 5.17 respectively. Each figure shows the cross-sectional images of (a) fresh alloy, (b) etched fresh alloy, (c) tested alloy and (d) – (f) etched tested alloy, respectively.

The samples of alloy from both probes were etched and compared. The image results show similar findings for both probes. There is no significant difference detected in the comparison between the samples of the same alloy that are located at the different positions.

The grain arrangement of alloy 59 (Figure 5.15) is composed mainly of a series of large, equiaxed grains, containing numerous twin boundaries. The grain size varies from 5 – 300 μm . Corrosion took place both uniformly on the surface and along the grain boundary.

The grains of alloy 625 (Figure 5.16) were small and uniform. A typical grain structure has long rectangular/stripes in between the grains, similar to alloy 59. Grain sizes vary from 5 to 20 μm . The corrosion structure occurring in this alloy is similar to that of alloy 59. It is clear that pitting occurs along the grain boundary, in addition to the uniform surface corrosion. It is concluded that alloy 59 and alloy 625 are susceptible to the grain boundary corrosion attack.

Grain sizes for alloy 556 (Figure 5.17) were generally bigger than that of other materials. The major feature is a long rectangular shape. The grain size varied widely. Grains with a size smaller than 10 μm were detected, and they could be as large as 400 μm . The corrosion took place equally and randomly on the surface. Corrosion or cracking on the grain boundary was not detected.

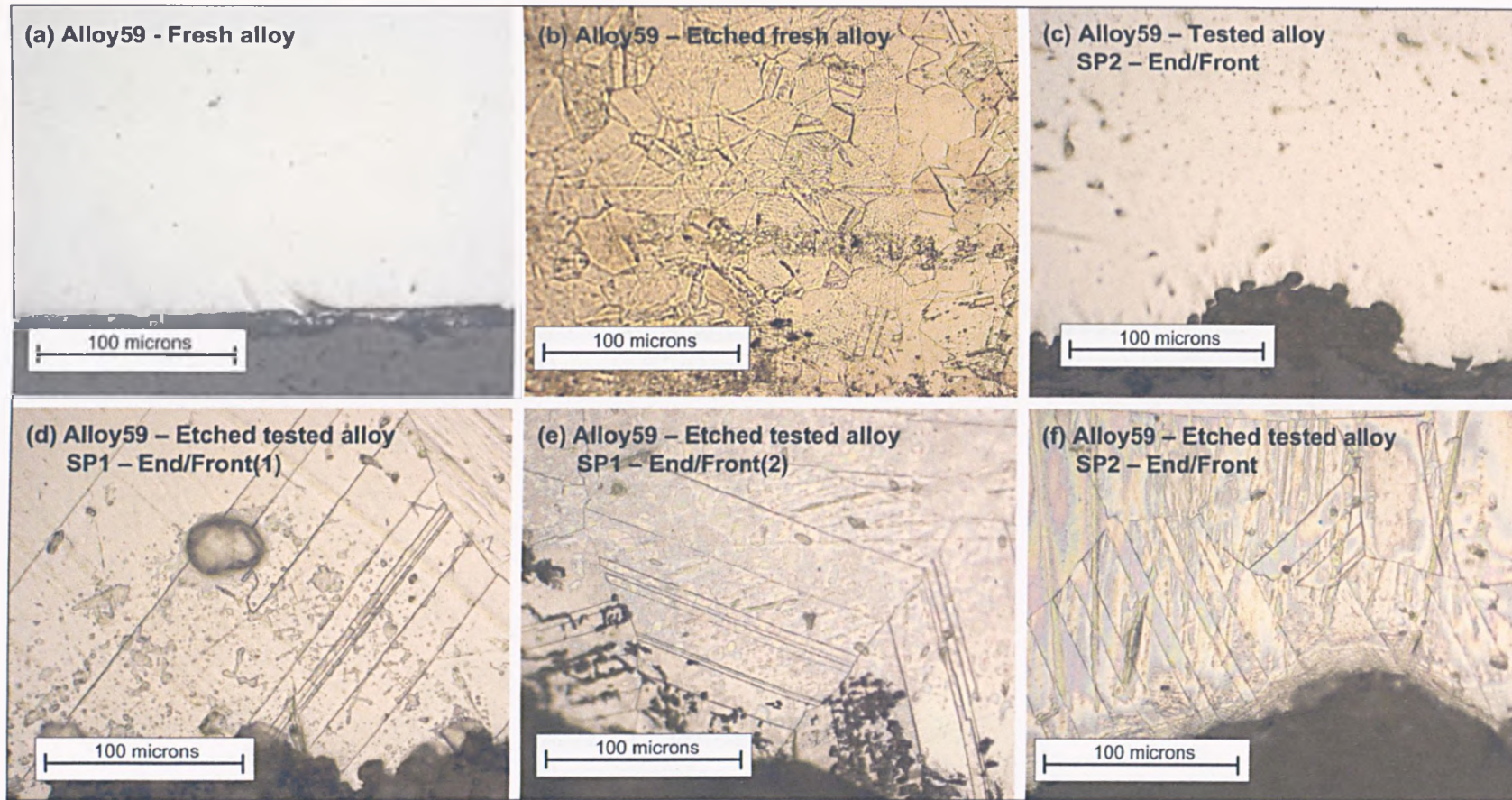


Figure 5.15 Cross-sectional images of alloy 59 and its grain boundary structure.

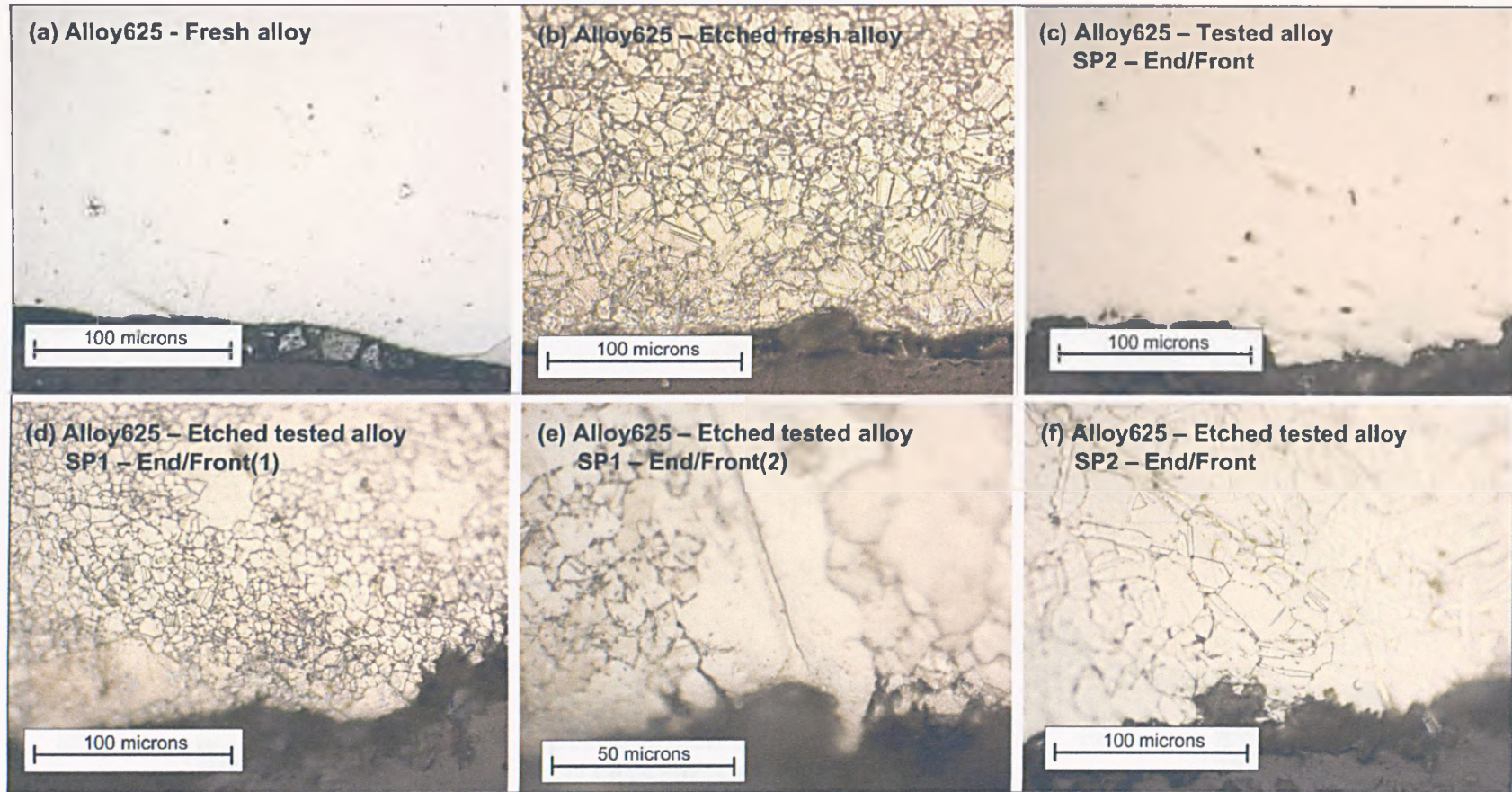


Figure 5.16 Cross-sectional images of alloy 625 and its grain boundary structure.

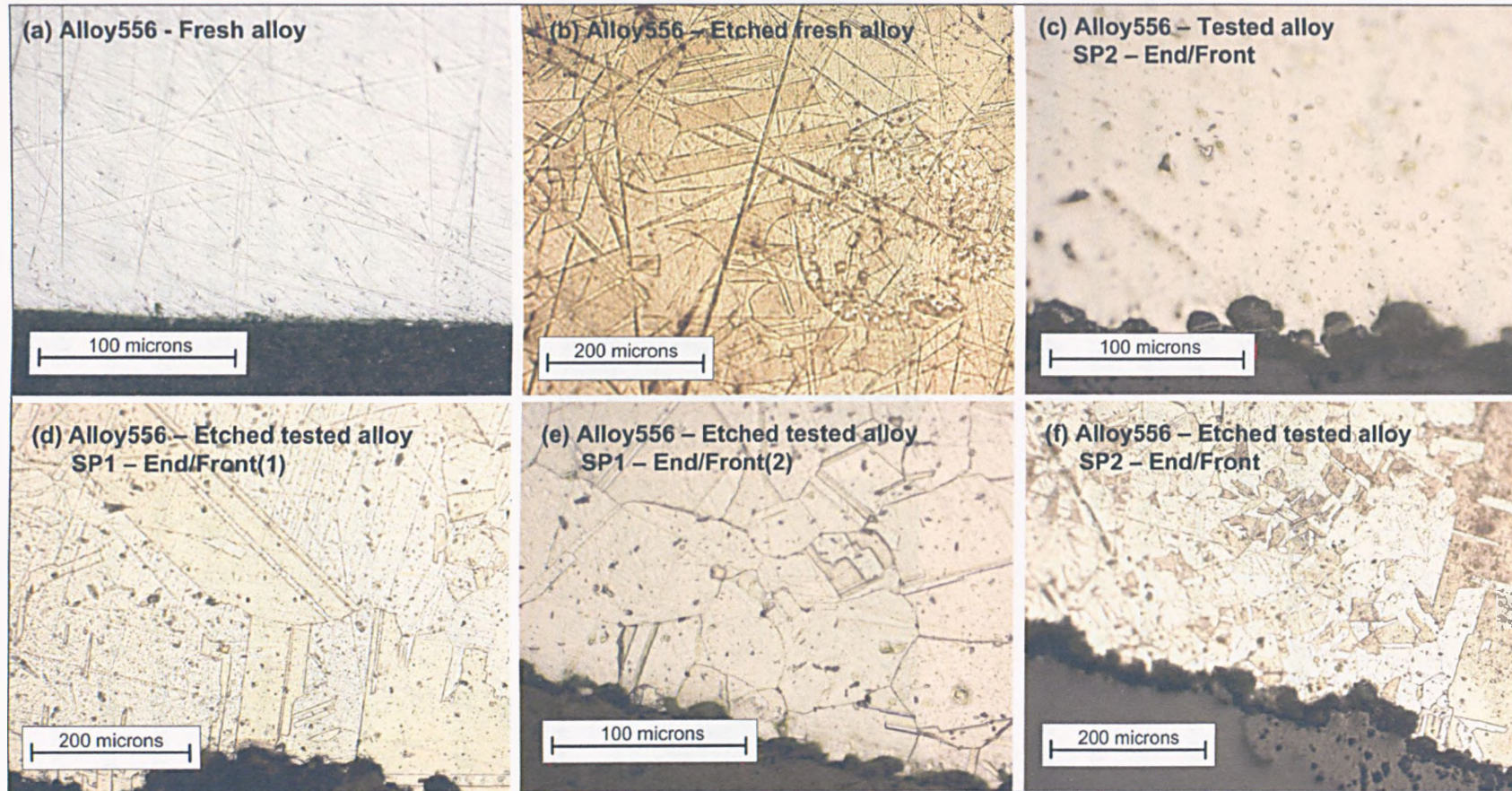


Figure 5.17 Cross-sectional images of alloy 556 and its grain boundary structure.

5.11 Morphology and Elemental Composition of Corrosion Products and Alloy Samples

5.11.1 Results for Alloy 59

SEM cross-sectional images created by back scattered electrons from alloy 59 are shown in Figure 5.18. The sample was taken from the ring at the end section of probe No.1. It was clear that this alloy experienced severe corrosion. Both deep pits and wide crevices, as shown in these figures, were detected in this sample. The depth of the pit as shown in Figure 5.18b was up to 40 μm . The point scan carried out at the bottom of the crevices revealed that Pb, S, Cl, and K were the main constituents. Other elements include Ca, Zn and As.

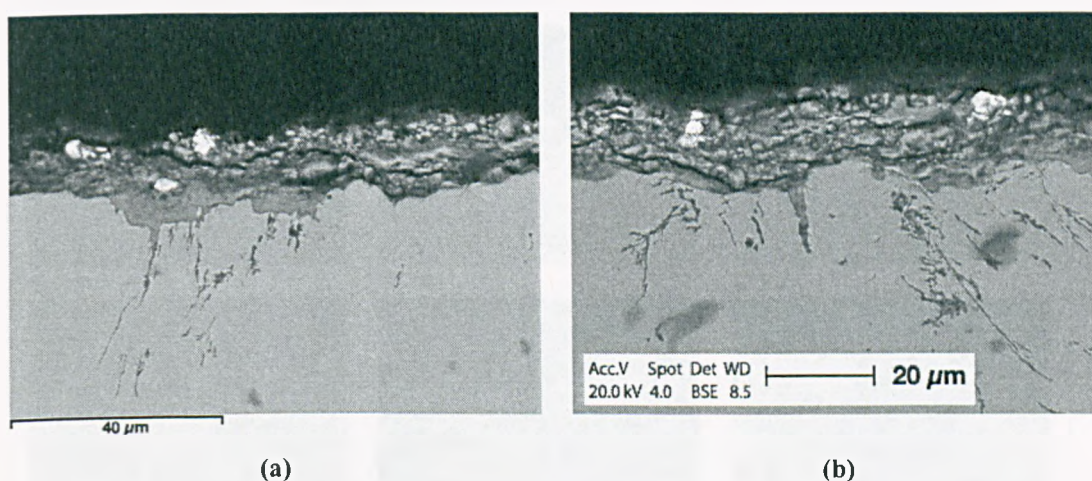


Figure 5.18 Back scattered electron image of alloy 59: SP1 - end/top

A thick layer of deposit coupled with corrosion products was analysed as shown in Figure 5.19. The results agree with the elemental composition previously discussed. The scale layer, a combination of deposit and corrosion products, was mainly: (1) compounds of alkali metals, Pb, As and Zn with O and Cl; (2) oxides of substrate alloy elements; and (3) other components such as SiO_2 , compounds of Al, and C particles. The long black threads present in Figure 5.19 were the resin that was formed under pressure by passing through the pores inside the corrosion products. It takes place right after the sample was discharged from the vacuum impregnation process during sample preparation.

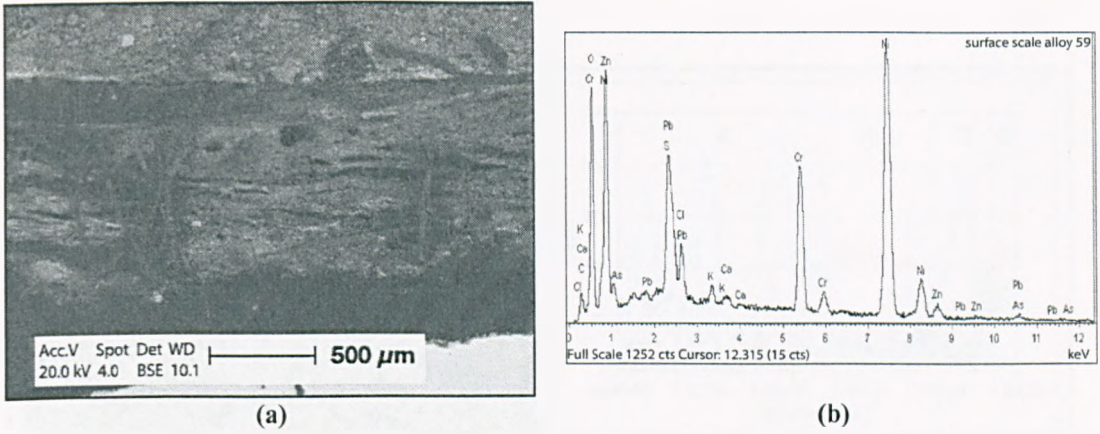


Figure 5.19 Corrosion products of alloy 59: SP1 – end/top: (a) back scattered electron image, (b) elemental composition results

The position shown in Figure 5.18 was analysed for its elemental map. The results are shown in Figure 5.20.

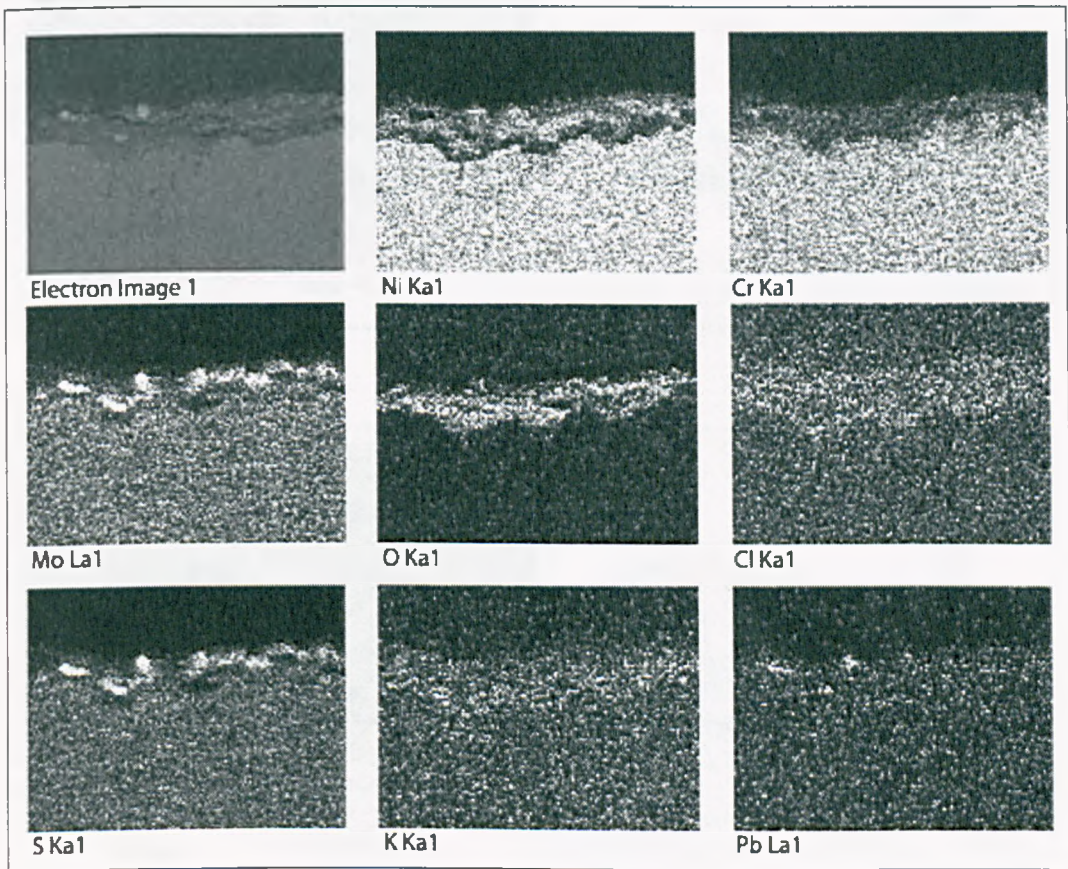
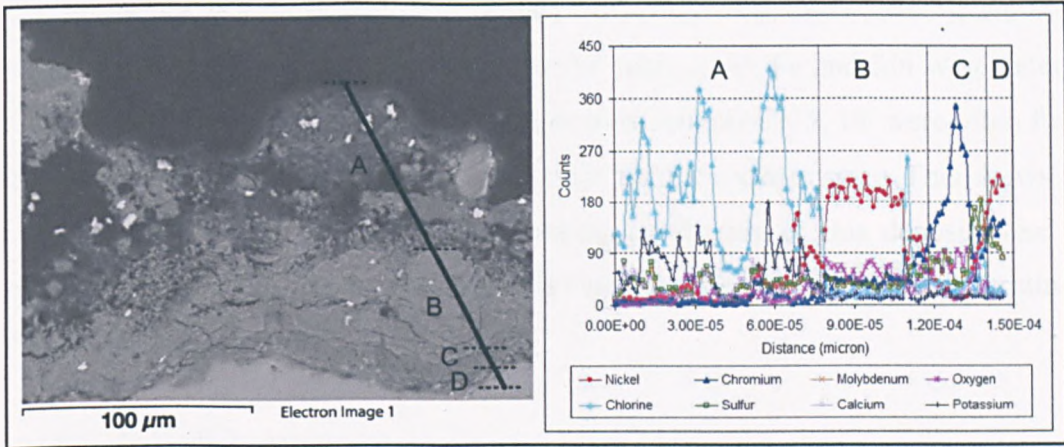
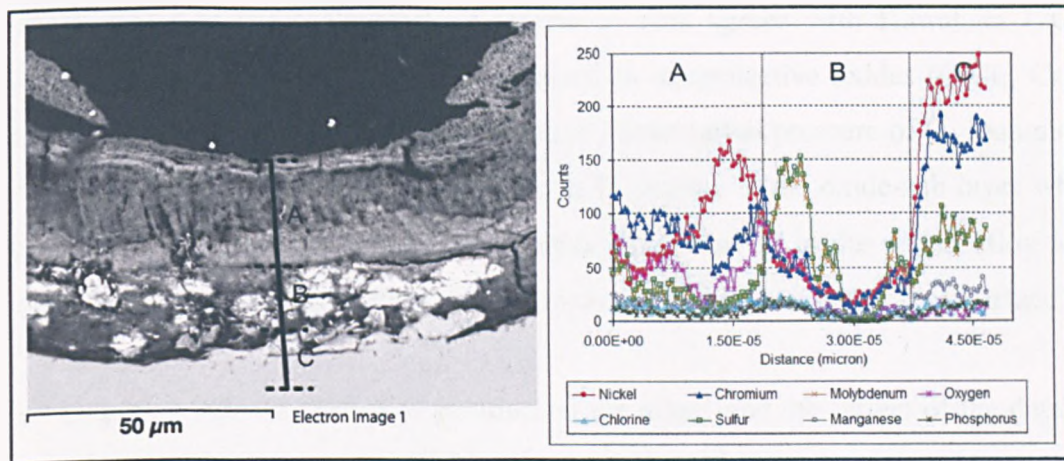


Figure 5.20 Elemental mapping of alloy 59 and its corrosion products: SP1 – end/top

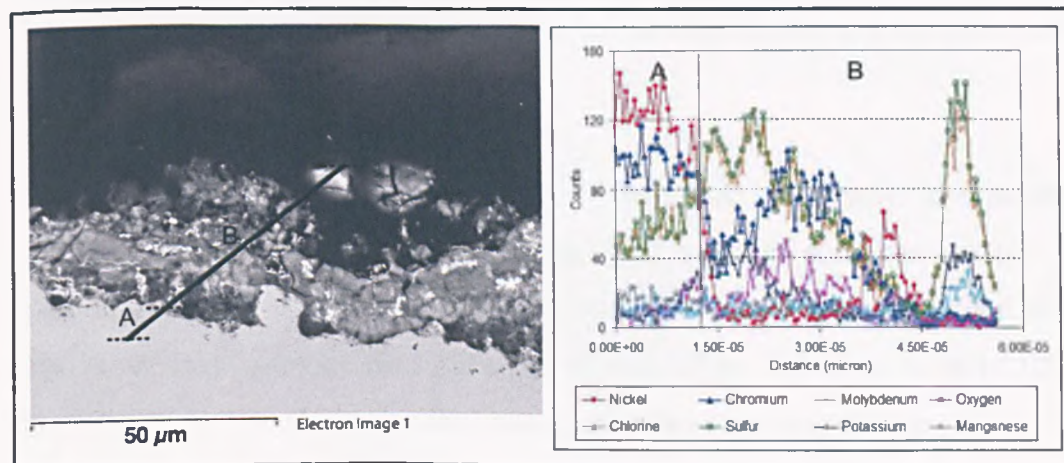
The composition of corrosion products were investigated by using the line scan technique. The results are shown in Figure 5.21.



(a)



(b)



(c)

Figure 5.21 Line scan results of alloy 59: (a) SP1 – end/bottom, (b) SP2 – end/top, (c) SP2 – end/bottom

Figure 5.21 show that the corrosion products of alloy 59 consist mainly of oxides of Ni, Cr and Mo that are in the forms of NiO, NiCr₂O₄, CrO₂, Cr₂O₃, MoO₂, and MoO₃ (analysed by XRD). Minor alloy constituents such as Al, Fe and Mn were detected but at a less quantity. Elements from the deposit such as Cl, S, Pb were often found at the interface between the corrosion product and the metal surface. This shows that the oxide layers of Ni, Cr, and Mo existing on the top of this deposit were not protective. Thus, there is no evidence of a constant protective oxide layer forming at the metal surface.

Layer of nickel oxide was detected at the outer side of scale (depleted at the sub-layer). The oxides of molybdenum followed by oxides of chromium were commonly found closer to the scale/substrate interface. This agrees with Kawahara (2002) stating that chlorides of Cr and Mo oxidized to un-protective oxides (CrCl₂, CrCl₃, MoCl₃ → Cr₂O₃, MoO₂) more readily and at lower partial pressure of O₂ than nickel (NiCl₂ → NiO). It is noted that NiO seems to deplete at the oxide-sub layer where Cr₂O₃ or CrO₂ were abundant. One explanation is that Cr in the parent alloy were oxidised preferentially and form protective oxides layer close to the alloy surface.

Investigation into the 'effect of position on the alloy' and the 'effect of the deposit' revealed that the end section of this alloy experienced more corrosion damage than the wall section. For example in probe No.2, the depths of pits on the end section ring were up to 100 µm whereas the depths on the wall section ring were less than 50 µm.

The side of the alloy being exposed to hot gas corroded uniformly. In contrast, the side of the alloy under deposits was attacked by local corrosion notably from chlorides of heavy metals. Pits detected under the deposits were larger and deeper. This is obvious for probe No.1. The pits of alloy under deposit were up to 100 µm depth while the pits of alloy on the opposite side were less than 20 µm.

5.11.2 Results for the Coated Coupon of Alloy 59

The elemental maps of the end-section coated alloy 59 and its corrosion products are shown in Figure 5.22 and Figure 5.23.

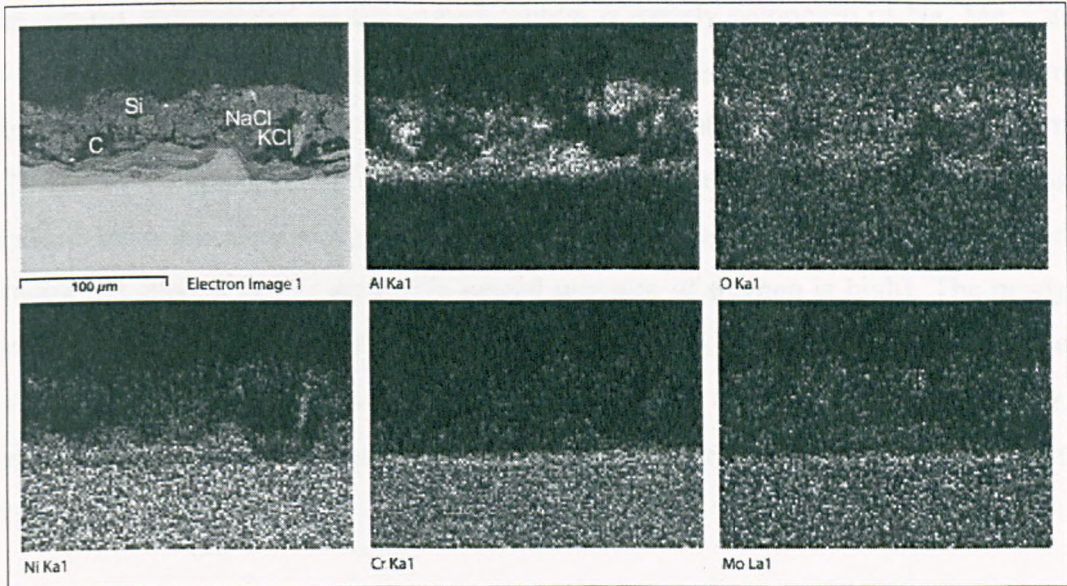


Figure 5.22 Elemental mapping of coated alloy 59 and its corrosion products: SP2 - end/top

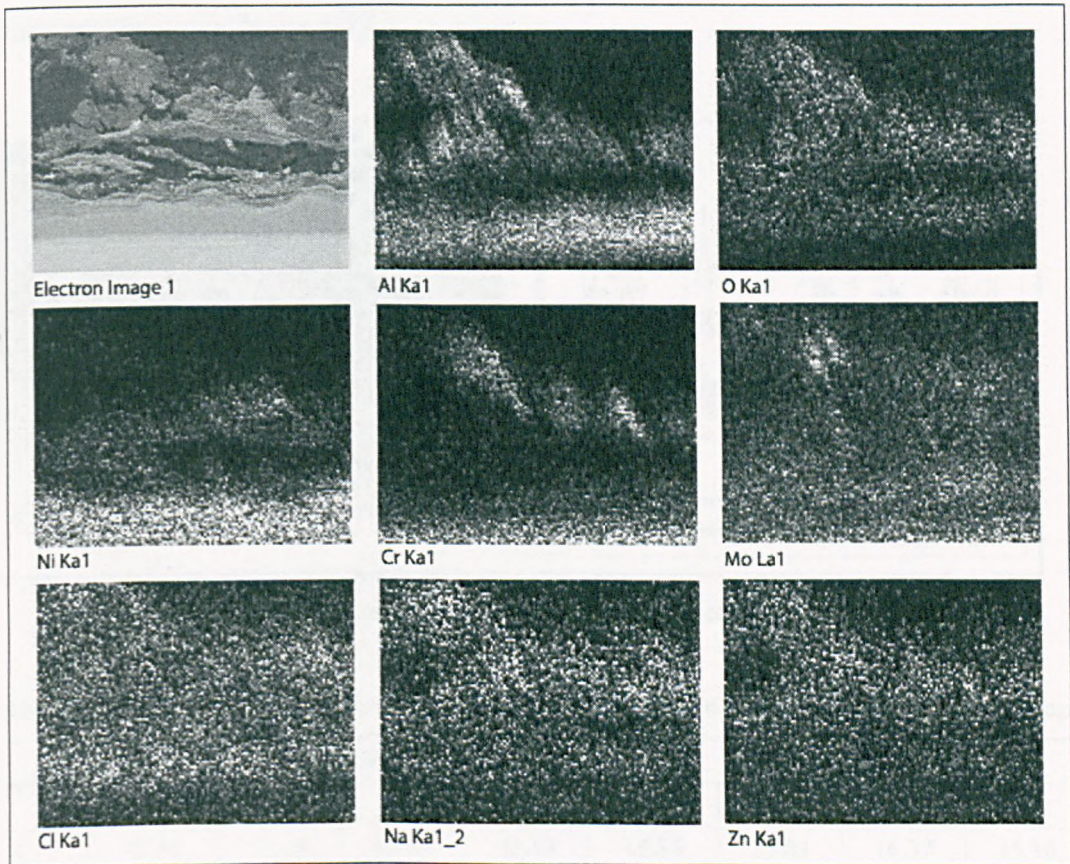


Figure 5.23 Elemental mapping of coated alloy 59 and its corrosion products: SP2 - wall/top

Figure 5.22 and Figure 5.23 show that the scale layers consist of: (1) deposit layers; (2) un-protective oxide layers of Al, Ni, Cr, and Mo as Al_2O_3 , NiO , Cr_2O_3 , CrO_2 , MoO_2 and MoO_3 ; and (3) a layer of coating present next to the alloy interface.

The deposit accumulated on the coated coupon is mainly composed of Na, Mg, Ca, K, Cl, Si, and S. Round particles having sizes that varied from 20 – 100 μm were often detected. They are the condensed droplets of liquid CaCl₂ and ZnCl₂. Figure 5.23 shows the presence of chromium oxides and molybdenum oxides. Cr was depleted from the alloy substrate. The evaporated CrCl₂ was oxidized as it passed through the deposit layer (where the partial pressure of oxygen is high). The newly formed Cr₂O₃ (un-protective) was therefore detected on the top of the deposit. The amount of MoO₂/MoO₃ oxide seems to be more than the amount of Cr₂O₃. However, one should note that the signal results for Mo can be interfered with the signal results for S.

Results from line scan analysis are shown in Figure 5.24 and Figure 5.25. The coating site from Figure 5.24 was also analysed by the point scan technique and the results are shown in Table 5.27.

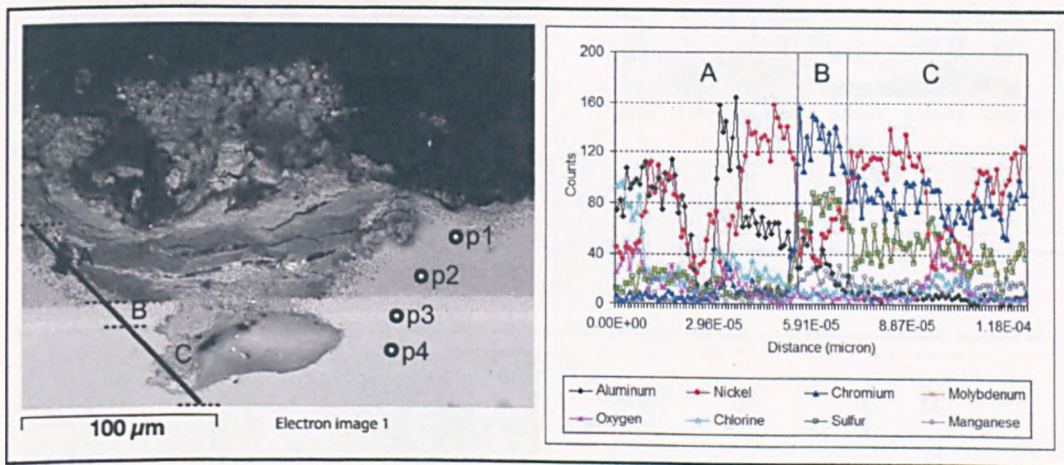
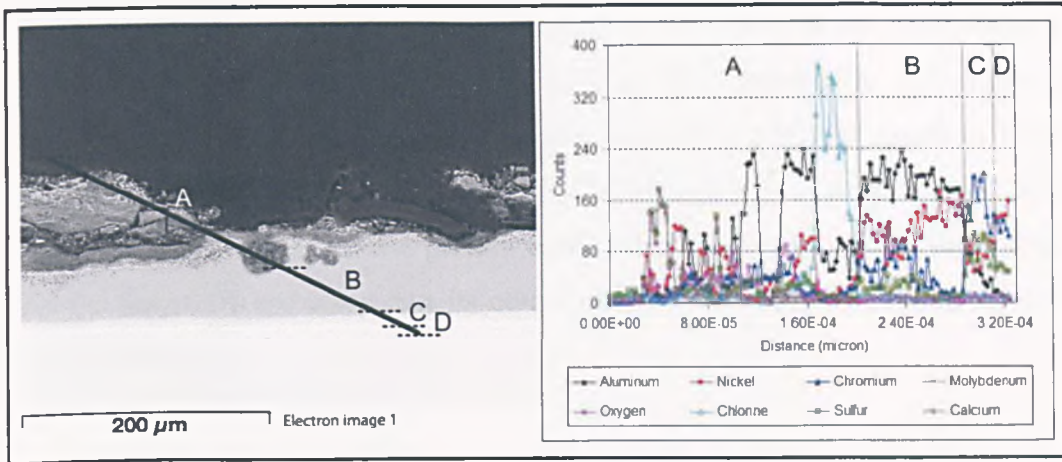


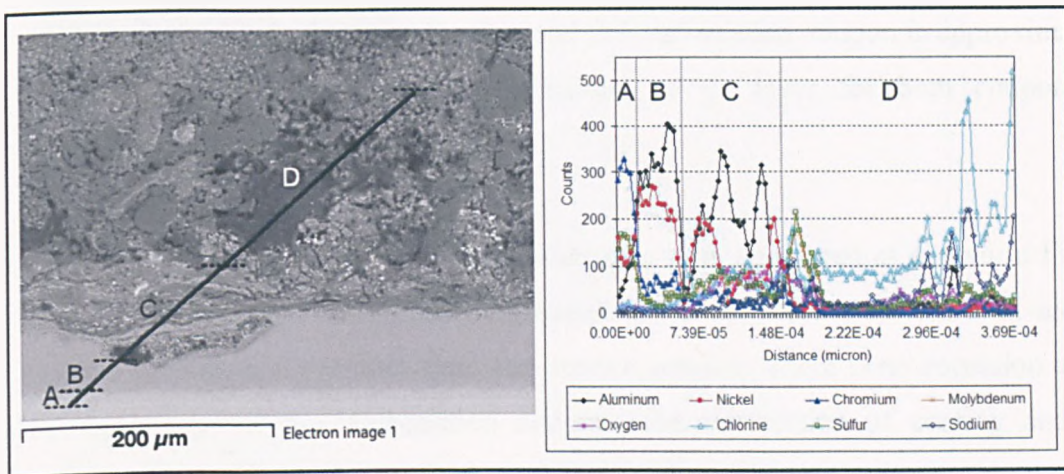
Figure 5.24 Results of line scan and point scanning for coated alloy 59: SP2 - end/top

Table 5.27 Elemental composition results of corrosion products of coated alloy 59: SP2 - end/top

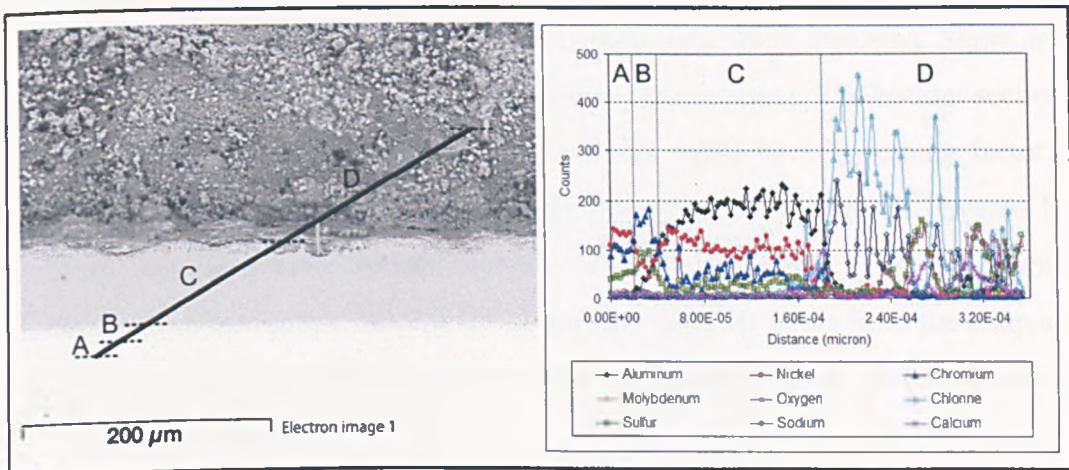
Element	Atomic%				Weight%			
	P1	P2	P3	P4	P1	P2	P3	P4
C	45.31	53.26	49.61	47.53	18.83	23.83	16.37	16.18
Al	28.54	22.25	2.08	-	26.65	22.37	1.54	-
Ni	20.03	22.91	21.02	29.74	40.69	50.11	33.90	49.48
Cr	3.95	1.20	19.16	13.09	7.11	2.32	27.37	19.29
Fe	0.33	-	0.57	0.54	0.64	-	0.87	0.86
Mo	1.83	0.38	7.57	4.45	6.09	1.37	19.95	12.09
O				4.65				2.11



(a)



(b)



(c)

Figure 5.25 Line scan results of coated alloy 59: (a) SP2 - end/top, (b) & (c) SP2 - wall/top

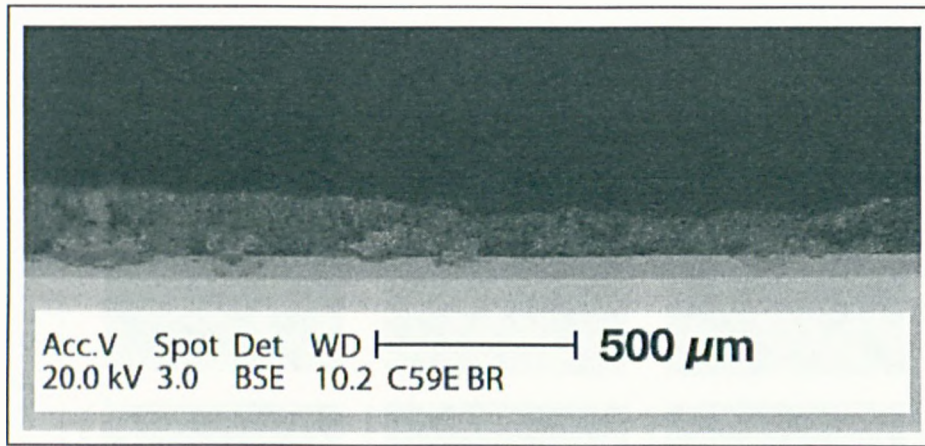
The coating layer is comprised mainly of Al and Ni that were fused to form Ni-Al intermetallic layer during the heating process. Figure 5.24 and the results from Table 5.27 show that the atomic ratios of Ni to Al at this intermetallic layer varied from 1:1.0 (close to the substrate) to 1:1.4 (top part). A ratio of Ni:Al equals to 1:2.9 was detected in the wall-section coupons. NiAl, NiAl₃ and Ni₂Al₃ were detected by XRD analysis. Cr and Mo were also present in the intermetallic layer but at the less extent. Mn is present in the alloy, but its contribution in the protective oxide layer is not clearly shown.

Figure 5.25 clearly shows 2 different layer of coating above the substrate: (1) a layer of aluminum and nickel and (2) a thin layer Cr next to the substrate. The thickness of Al-Ni layer of the End-section coupon and the wall-section coupon is approximately 60 and 70 μm respectively. The thickness of Cr layer for both coupons is approximately 10 – 12 μm .

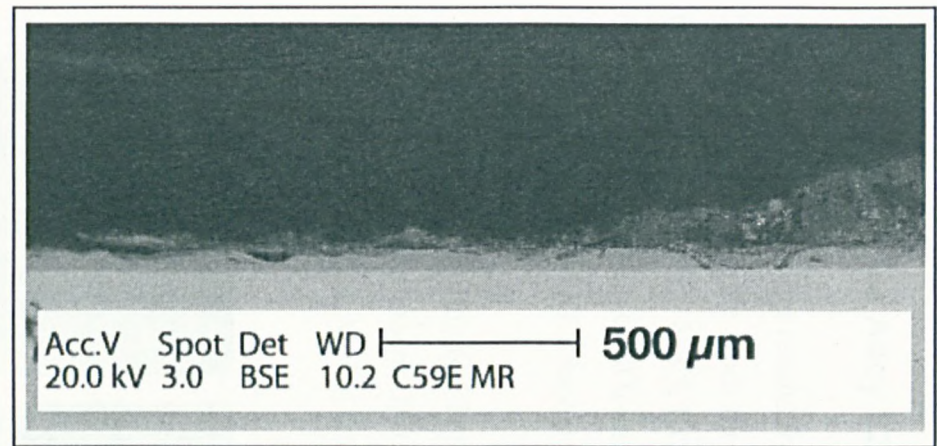
Images of coated alloy 59 at different locations were compared as shown in Figure 5.26. The temperature difference significantly affects the corrosion. The wall-section coupon became less corroded than end-section coupon. There is no corrosion at the substrate level at the wall-section coupon. The destruction of coating and the corrosion of substrate alloy were widespread in the end-section coupon.

Surprisingly, the top sections of coated coupons were more damaged. Some areas of coating on the top section were broken due to the corrosion. The bottom section was found to have a uniform coating. Heat transfer could be a governing factor; with better heat transfer at the bottom section. However, they were all covered by the deposit and the contact surface with the tube was too small to cause a significant thermal gradient change. So, this difference was unlikely come from the temperature. Another explanation is that the top sections of the coupons are more exposed to the deposit and its elements.

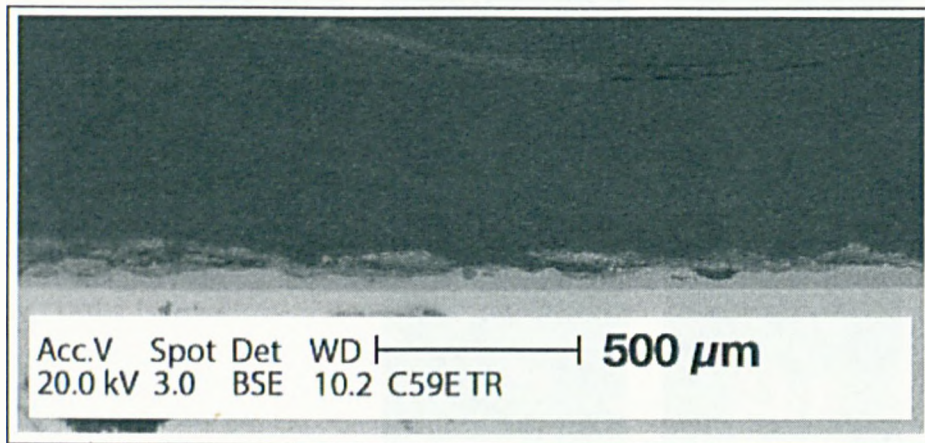
In summary, the aluminum pack coating on alloy 59 significantly improves the corrosion resistance of this alloy.



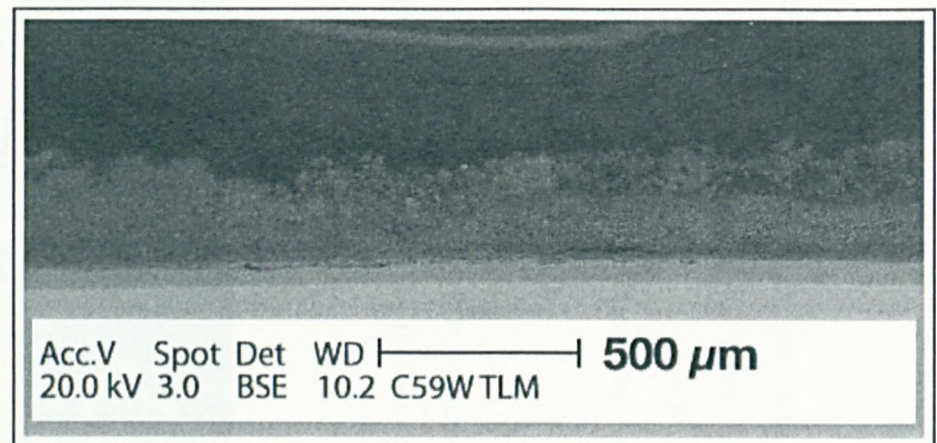
(a)



(b)



(c)



(d)

Figure 5.26 Coated alloy 59: (a) SP2 - end/bottom, (b) SP2 - end/middle, (c) SP2 - end/top, (d) SP2 - wall/top

5.11.3 Results for Alloy 625

The elemental mapping results for the sample of alloy 625 are shown in Figure 5.27. These are for a sample from the end section of probe No.1. Figure 5.27 shows the thick deposit including NaCl, KCl and CaCl₂. Silicon particles were found especially on the metal interface. CaSO₄ and CaCl₂ were commonly detected on the upper layer of deposit; NaCl and KCl deposit first.

The oxide layer for alloy 625 is similar to that for alloy 59. It is composed mainly of Ni, Cr and to a less extent, Mo. XRD analysis showed that these oxides are NiO, NiCr₂O₄, Cr₂O₃, CrO₂, MoO₂, and MoO₃.

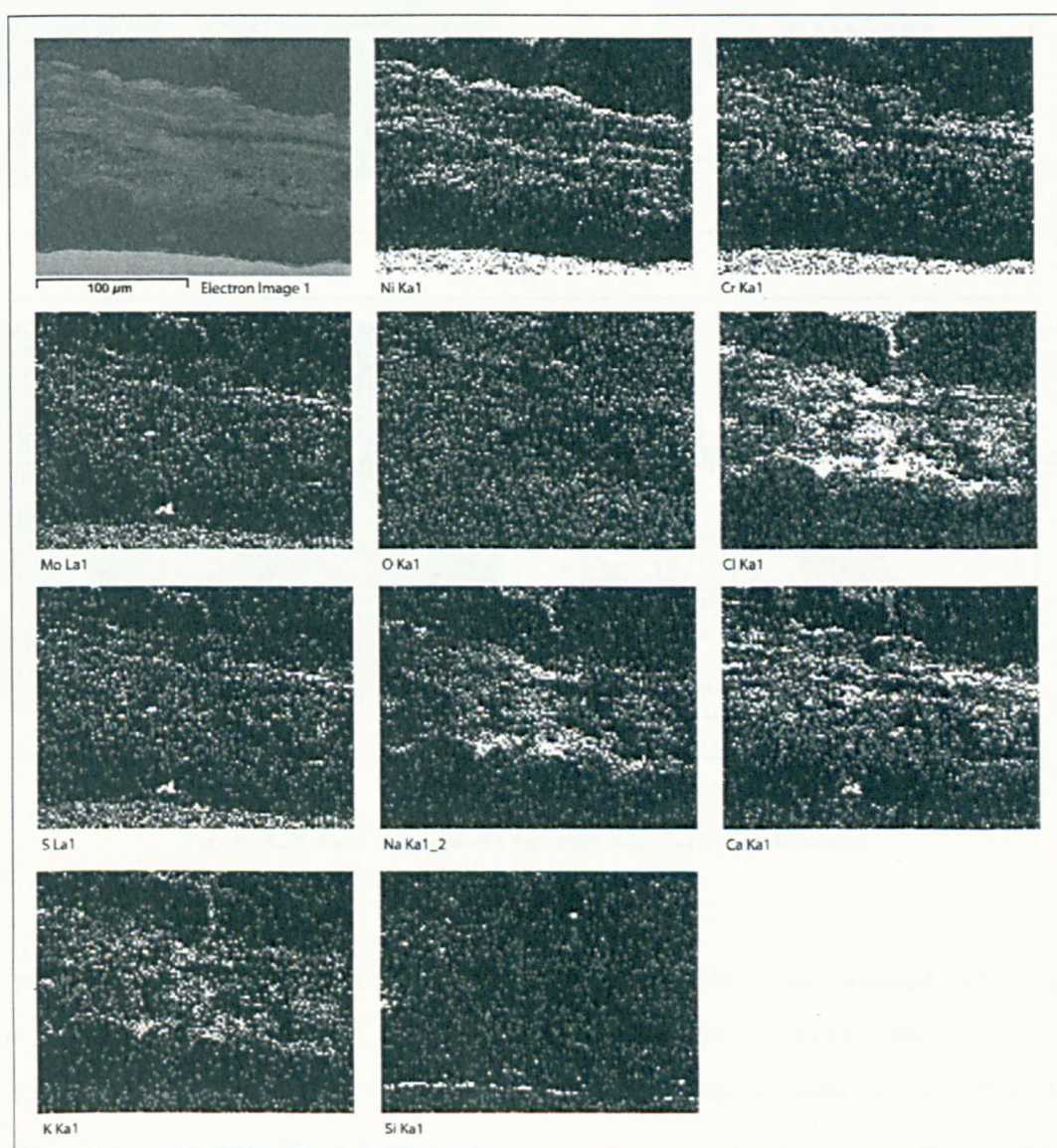
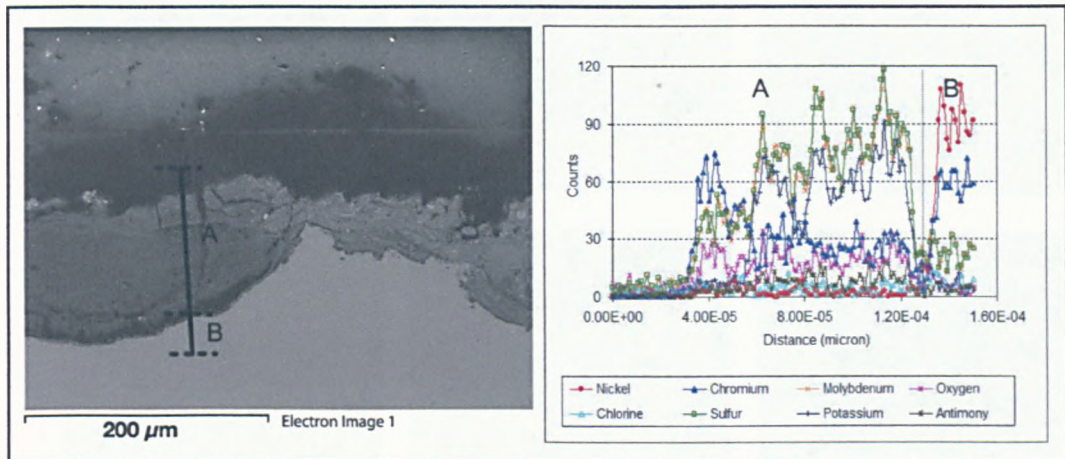
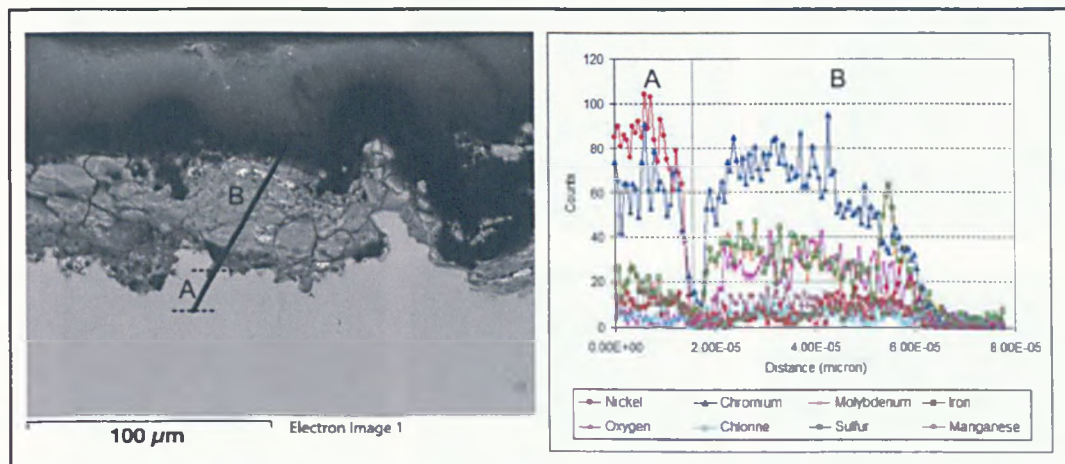


Figure 5.27 Elemental mapping of alloy 625 and its corrosion products: SPI – end/top

The samples from probe No.2 were analysed by the line scan technique and the results are shown in Figure 5.28. These results show that CrCl_2 and MoCl_2 are readily oxidized at the low partial pressure of oxygen (compared to NiCl_2) following their volatilization. However, the layer of NiO was not often found. It might have been in the upper layer of the deposit and therefore was detached from this sample. Furthermore, deposit on probe No.2 contained higher amount of S and C than deposit on probe No.1.



(a)



(b)

Figure 5.28 Line scan results for alloy 625: SP2 – end/bottom

It was found that the areas covered by the deposit and the areas exposed to the hot gas have a similar structure. The corroded areas were relatively smooth as the corrosion takes place uniformly. The deep pits or crevices as seen in alloy 59 were detected but they were less common.

5.11.4 Results for Alloy 556

The elemental mapping results for alloy 556 are shown in Figure 5.29. Point scan results for the End-ring of probe No.1 are shown in Figure 5.30 and Table 5.28 - Table 5.29. The samples of alloy 556 were also analysed by the line scan technique and the results are shown in Figure 5.31.

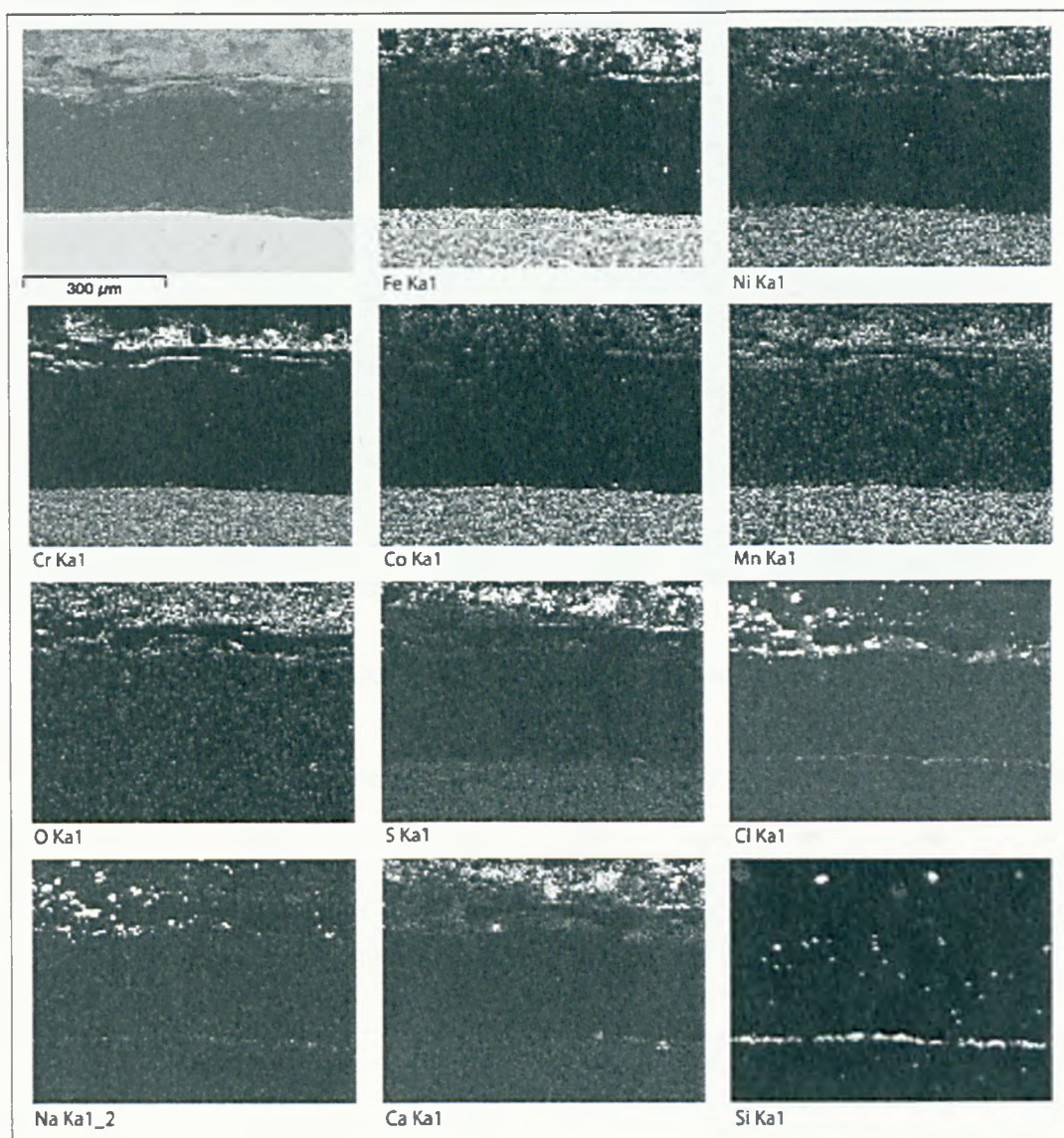


Figure 5.29 Elemental mapping of alloy 556 and its corrosion products: SP1 – end/top

The structure of the alloy 556 surface is different from that of other alloys. It looks relatively smooth which means that the corrosion form is uniform corrosion. Hence, the results do not show deep pits or crevices.

The point analysis (Figure 5.30 and Table 5.28 - Table 5.29) shows that the deposit adjacent to the metal surface contains a large amount of Pb and Zn compounds. They were mixed into the oxide layer; hence corrosion damage due to heavy metal chlorine compounds can be dominant. C was also one of the major constituents in the deposit.

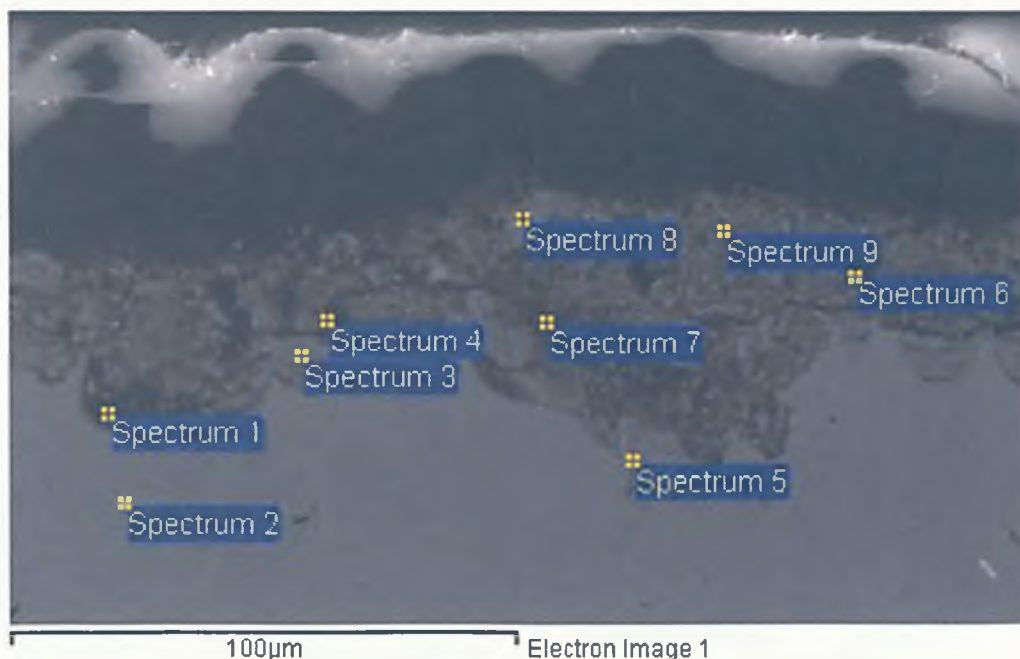


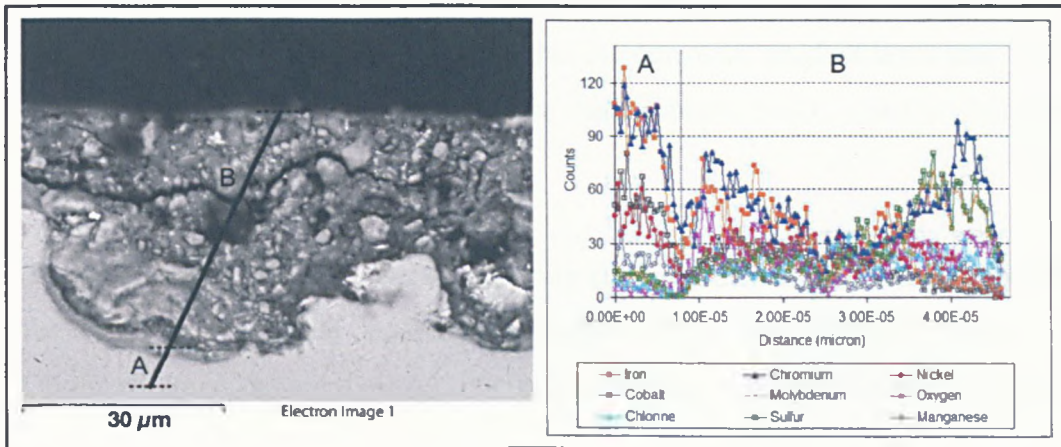
Figure 5.30 Point scan results for alloy 556 and its corrosion products: SP1 – end/top

Table 5.28 Elemental composition results for point scan of alloy 556: SP1 - end/top (atomic%)

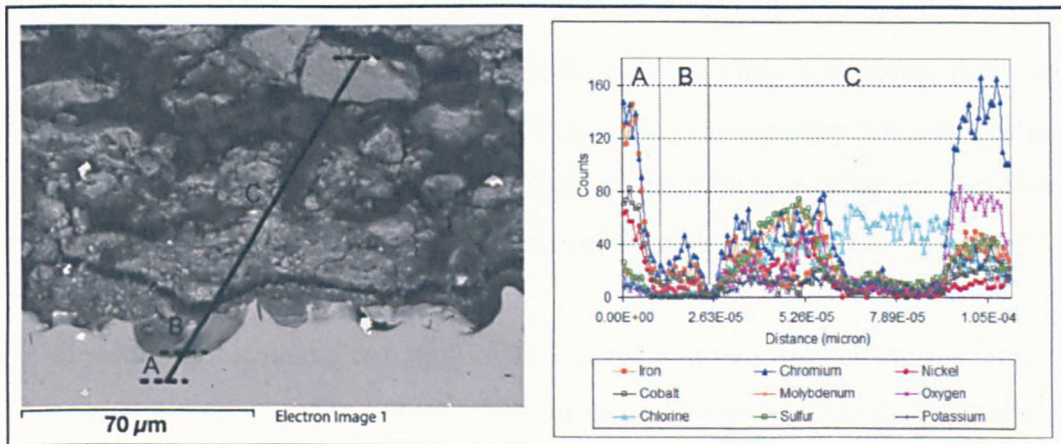
Element	sp1	sp2	sp3	sp4	sp5	sp6	sp7	sp8	sp9
Fe	2.32	31.16	6.14	1.79	18.28	5.84	3.35	7.56	7.43
Cr	2.28	25.32	15.07	3.02	22.09	3.80	2.87	4.18	6.54
Ni	1.69	20.51	6.19	1.86	13.85	3.53	2.13	4.27	4.66
Co	1.59	18.41	7.77	3.35	11.95	2.15	1.89	4.76	2.70
Mo					2.23				
C	71.83			67.54		41.39	58.35	61.05	20.15
O	17.91		61.02	21.35	21.05	37.79	28.37	13.16	47.86
Cl	0.54		2.08	0.69	6.41	2.47	1.57	2.68	4.56
S	0.25	1.82		0.23		0.53		0.79	0.82
Pb			1.32			0.64	0.43		0.92
Zn						0.51	0.27		0.95
Ca	0.20				1.50	0.47	0.44	0.69	0.99
K				0.16	1.19	0.35	0.20	0.42	1.02
Na						0.54			1.09
Si	1.38								
Mn		1.32						0.45	
W		1.46	0.40		1.45		0.13		0.33

3Table 5.29 Elemental composition results for point scan of alloy 556: SP1 - end/top (weight%)

Element	sp1	sp2	sp3	sp4	sp5	sp6	sp7	sp8	sp9
Fe	7.78	30.30	10.25	5.70	21.11	14.36	9.65	18.34	14.81
Cr	7.12	22.92	23.42	8.96	23.74	8.68	7.69	9.43	12.14
Ni	5.97	20.96	10.86	6.23	16.80	9.11	6.44	10.87	9.77
Co	5.63	18.88	13.69	11.26	14.56	5.58	5.76	12.18	5.68
Mo					4.41				
C	51.83			46.22		21.87	36.12	31.84	8.65
O	17.22		29.18	19.46	6.96	26.59	23.39	9.14	27.35
Cl	1.15		2.21	1.38	4.70	3.85	2.86	4.12	5.77
S	0.48	1.02		0.43		0.74		1.10	0.94
Pb			8.16			5.79	4.63		6.78
Zn						1.46	0.91		2.23
Ca	0.49				1.25	0.82	0.90	1.20	1.41
K				0.36	0.96	0.61	0.40	0.71	1.42
Na						0.55			0.89
Si	2.32								
Mn		1.26						1.06	
W		4.67	2.22		5.52		1.26		2.16



(a)



(b)

Figure 5.31 Line scan results for alloy 556: SP2 – end/top

Figure 5.29 - Figure 5.31 show that the oxidation products of this alloy are oxides of Fe, Cr, Ni and Co. The losses of these metals are characterized by the presence of their oxides on the deposit surface. Crystalline phase detected on the surface of tested alloy 556 were Fe_2O_3 , Fe_3O_4 , $\text{FeO}(\text{OH})$, NiO , NiCr_2O_4 , Cr_2O_3 , and CrO_2 . These oxides were detected in the corrosion products which also contain a significant amount of S and Cl. In general, oxides of Cr/Fe were found next to the substrate while oxides of Co/Ni were detected at the outer scale layer.

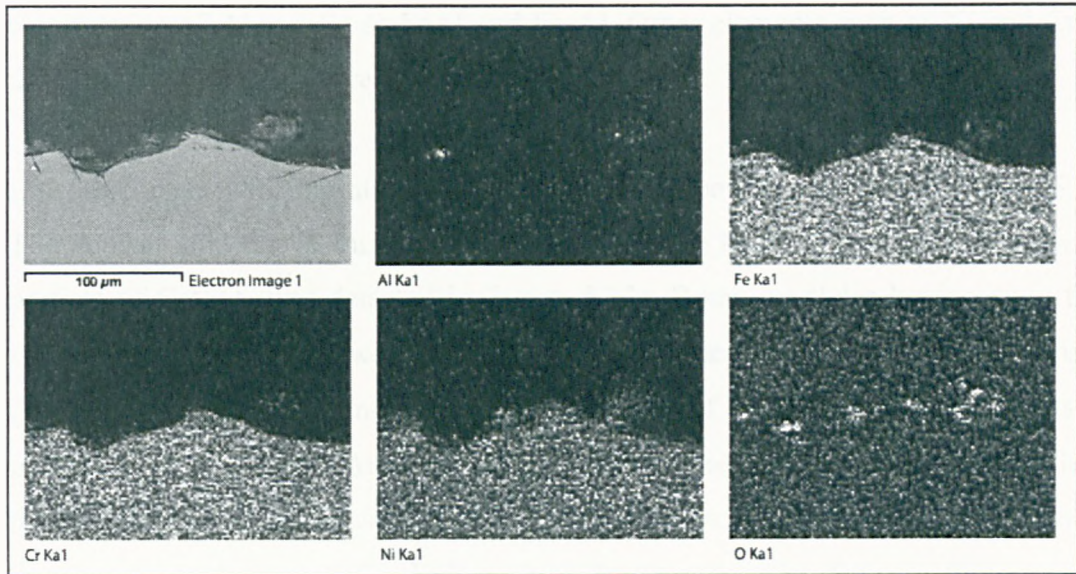
Kawahara (2002) concluded that the ability of oxides for prevent the penetration of corrosive deposits are in the following order: $\text{SiO}_2 > \text{Al}_2\text{O}_3 > \text{Cr}_2\text{O}_3 > \text{Fe}_3\text{O}_4 > \text{Fe}_2\text{O}_3$. The stabilities of chlorides of elements are in the following order: $\text{Cr} > \text{Fe} > \text{Ni} \approx \text{Mo}$ at temperature 500 °C. Thus, alloy 556 is more susceptible to corrosion in the chlorine-bearing gas, compared to the nickel based alloy. Kawahara (2002) also suggest that the stabilities of oxides of elements are in the following order: $\text{Cr} > \text{Mo} \approx \text{Fe} > \text{Ni}$ at 500 °C. This pointed out that the corrosion product layer may form by the compounds in this order: NiO (from the topmost), Fe_2O_3 / Fe_3O_4 / MoO_2 , and Cr_2O_3 (close to the metal interface).

The corrosion at different locations in this alloy was investigated. It was found that the areas covered by the deposit were rough as shown in Figure 5.30 - Figure 5.31. On the contrary, the areas exposed to the hot gas have a smooth corroded surface.

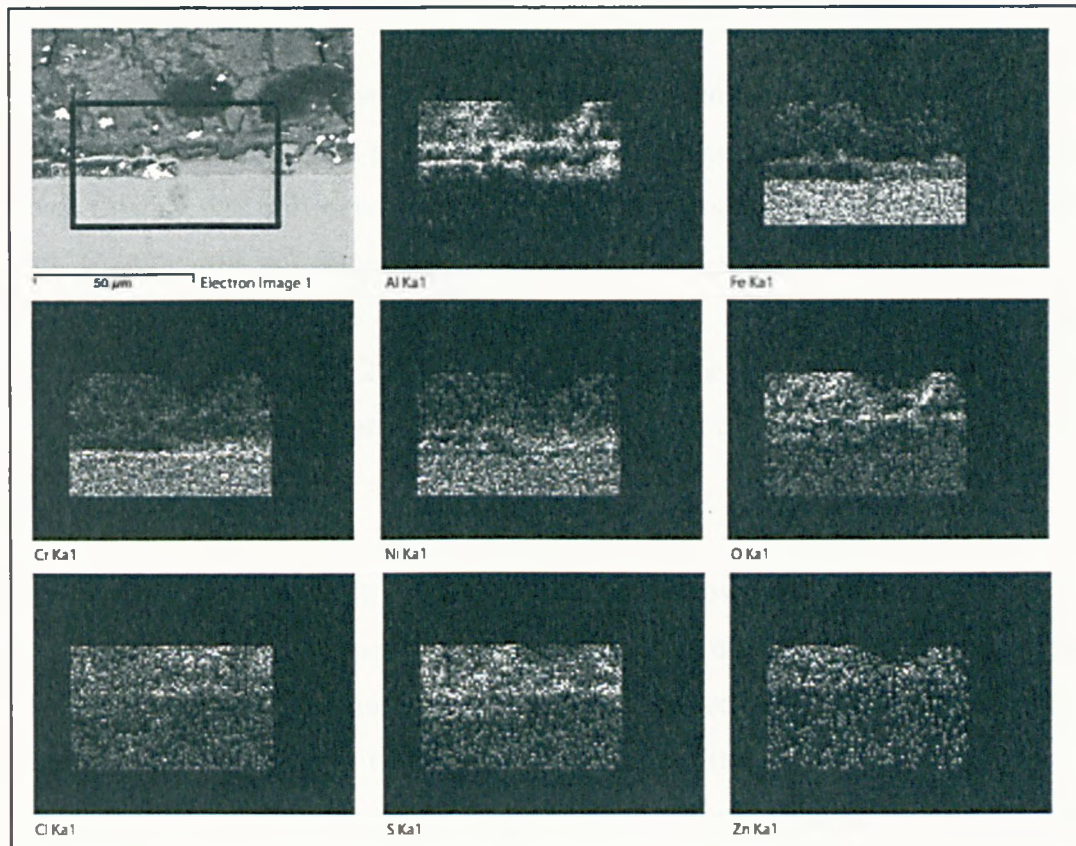
5.11.5 Results for the Coated Coupons of Alloy 310

Stainless steel 310 has a similar composition to the alloy 556 except that steel 310 does not contain Co (18% for alloy 556) and Mo (3% for alloy 556). It was used in this study in order to evaluate the affects of aluminide coating on the corrosion resistance of stainless steels, compared to exotic superalloy 556.

The results of elemental mapping of the coated coupons are shown in Figure 5.32a for the end-section and in Figure 5.32b for the wall-section coupon. The coating was barely detected at the end-section (Figure 5.32a), but was present in the wall-section with an average thickness of 3 - 8 μm . Figure 5.32b shows the area where the coating layer is broken.



(a)



(b)

Figure 5.32 Elemental mapping of coated steel310 and its corrosion products: (a) SP2 – end/top, (b) SP2 – wall/middle

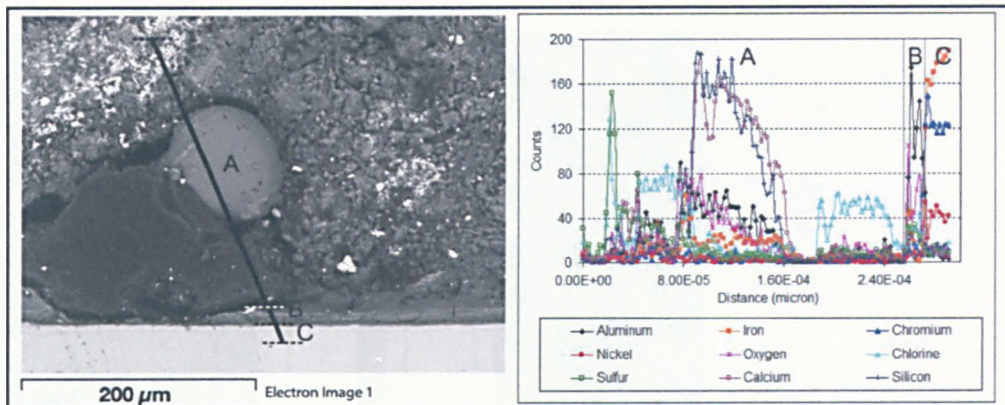
Oxides of Fe, Cr, Ni and Al were detected in the corrosion products. XRD analysis showed that the main composition in the corrosion products were $\theta - \text{Al}_2\text{O}_3$, $\alpha - \text{Al}_2\text{O}_3$, Fe_2O_3 , Fe_3O_4 , $\text{FeO}(\text{OH})$, NiO , Cr_2O_3 and CrO_2 . The coating layer was a

combination of Al and Fe as FeAl and Fe₃Al. Other elements such as Ni and Cr in the inter-metallic layer were also detected.

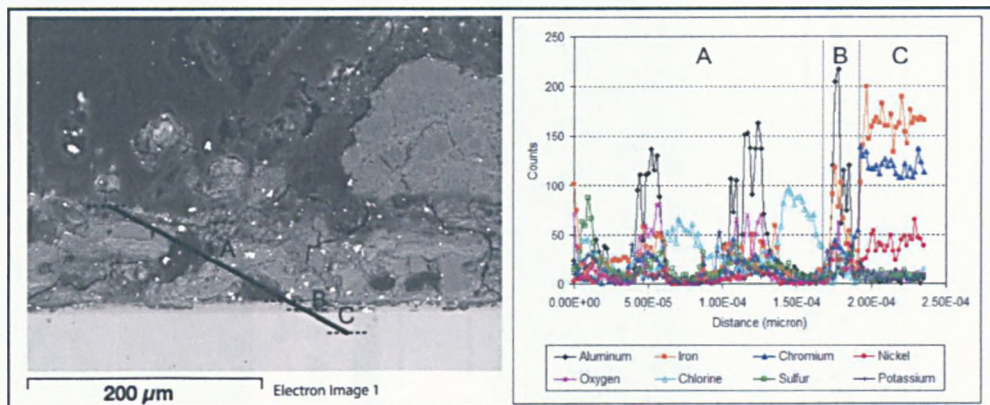
Line scan results for the aluminide coated 310 coupons are shown in Figure 5.33. The deposit adjacent to this coupon contains a large amount of alkali chlorides. A particle of CaSiO₄ was detected in Figure 5.33s. Round particles having sizes that varied from 20 – 100 µm were often detected in the deposit. They are the condensed droplets of liquid CaCl₂ ZnCl₂ SiO₂ or compounds of Si, Ca, Al, and O. Chunks of particle are often carbon. An aluminide coating is present in Figure 5.33b which is at the middle left side of the coupon. Figure 5.33c shows a thin layer of coatings under the deposit containing NaCl, KCl and CaCl₂. Figure 5.33d shows a thin layer of aluminum oxides covered under a thick layer of chlorine compounds.

Figure 5.34 shows a corrosion layer on the various positions of the coupons. It was noted that the coating was generally consumed and corrosion reached the substrate level. Coating was only detected in the wall-section coupon at the bottom and middle part. Coating was not found on the top part of wall-section coupon and the entire End-section coupon. This is due to the difference in temperature as previously described in section 5.10.2. The causes are also the quality of the coating itself (FeAl₃) or the non-homogenous nature of the deposit causing different rates of local corrosion

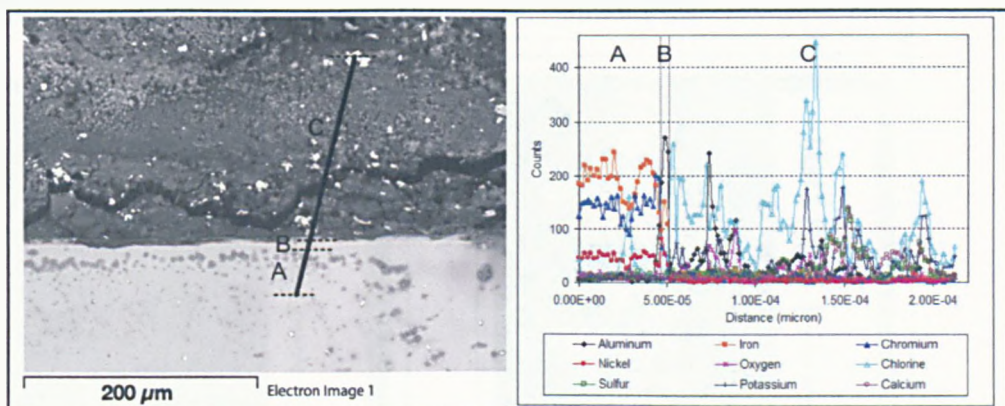
In summary, the aluminide pack coating does improve the corrosion resistance of stainless steel. Coated coupon of stainless steel 310 proves that the aluminide coating can provide a good corrosion resistance. The coated coupons had less suffered from the corrosion compared to the higher grade material (alloy556) and a stainless steel 316 which was entirely corroded. The presence of some coating (original thickness of 40 – 50 µm) also showed that FeAl and Fe₃Al can provide a greater corrosion resistance than nickel-based alloy 59 and alloy 625 (corroded lengths were 59.17 – 104.43 µm). However, the aluminide coating on stainless steel 310 does not perform as well as a similar coating on nickel-based alloy59.



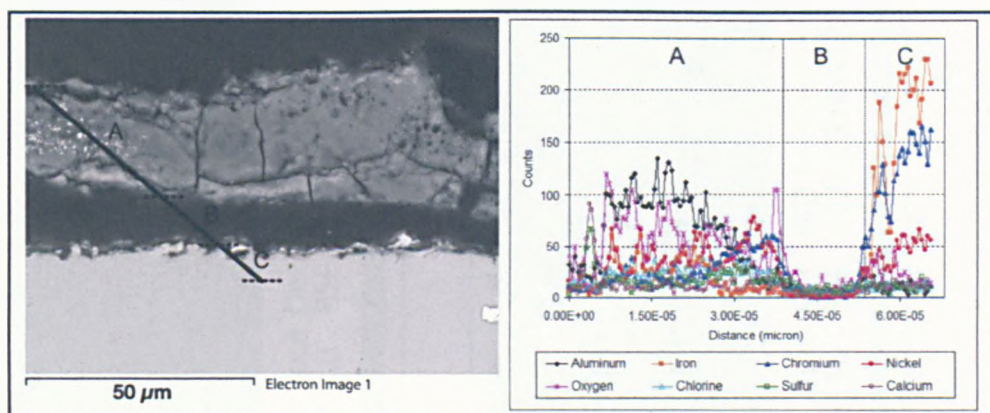
(a)



(b)

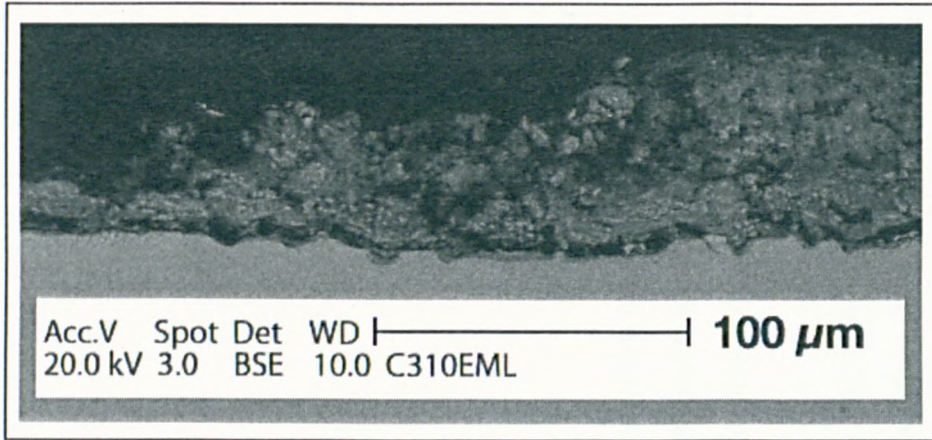


(c)

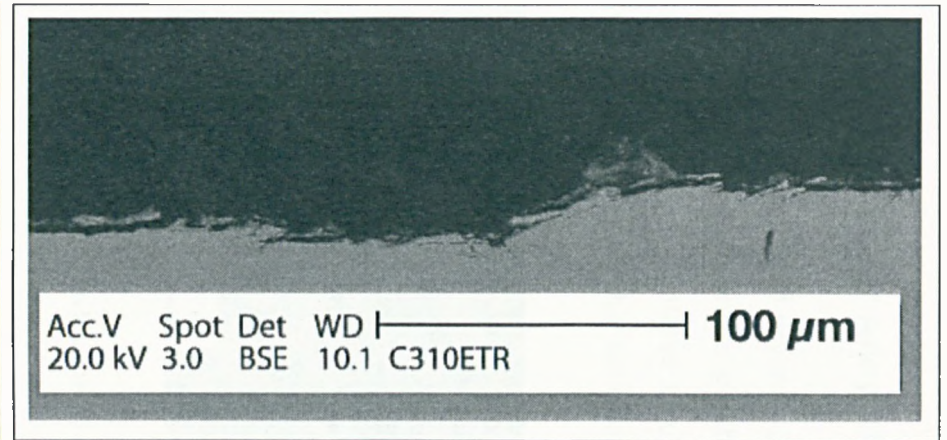


(d)

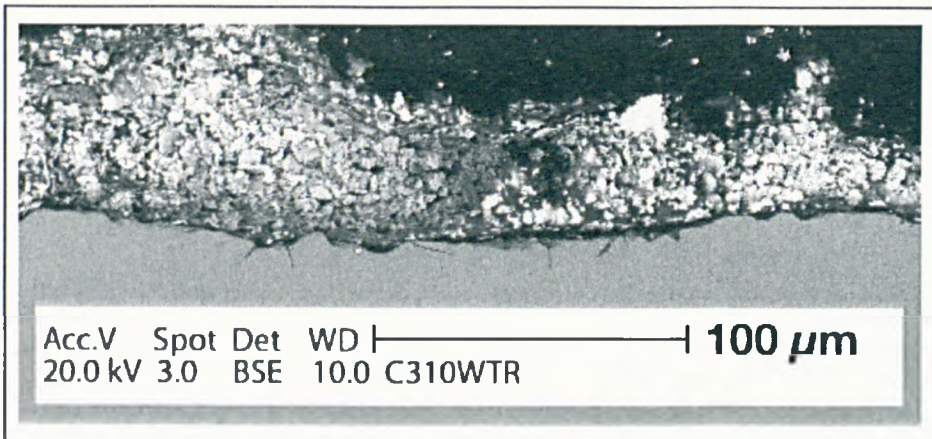
Figure 5.33 Line scan results of coated steel 310: (a) & (b) SP2 – wall/middle, (c) SP2 – wall/bottom, (d) SP2 – end/middle



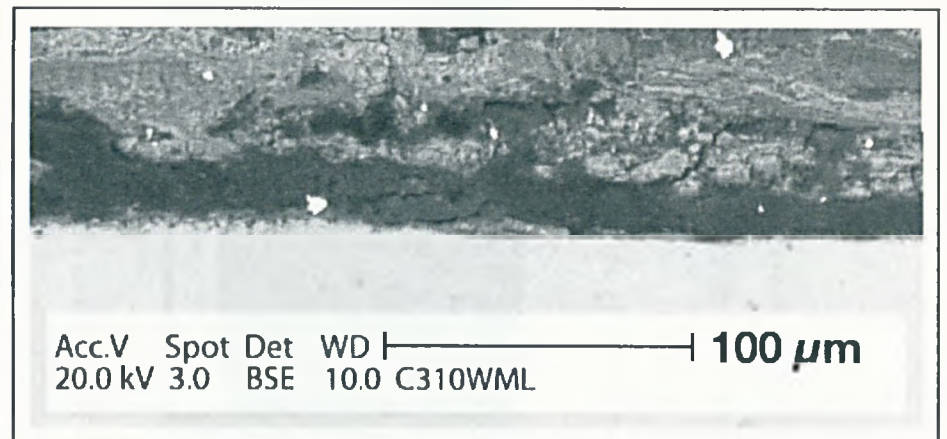
(a)



(b)



(c)



(d)

Figure 5.34 Coated steel 310: (a) end/middle, (b) end/bottom, (c) wall/top, (d) wall/middle

5.11.6 Results for Alloy 316 (Baffle)

Baffles were corroded severely as can be seen from Figure 5.35. The first picture is the secondary electron image showing the general structure. The second picture is taken using back scattered electrons in which the colour is varied by the atomic weight. It is obvious that the alloy 316 corroded both inside and on the surface.

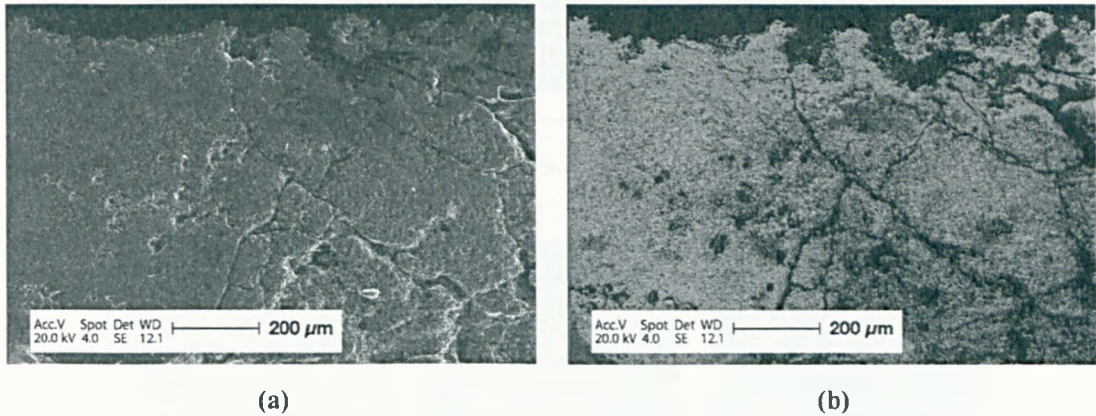
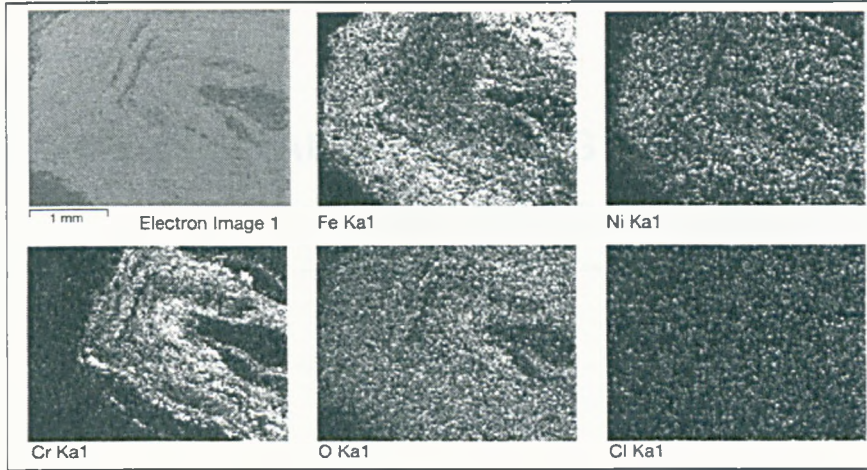


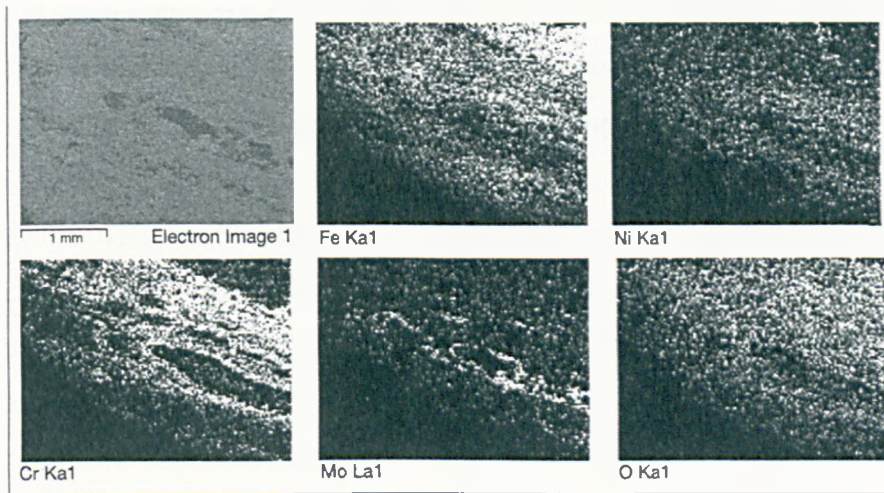
Figure 5.35 Backscattered electron images for stainless steel 316: SP1 - wall

The results of elemental mapping of the baffle sample from the end section of probe No.1 are shown in Figure 5.36.

It is found that major constituents of stainless steel 316 including Fe, Ni, Cr and Mo were removed from the substrate. After they passed through the deposit, they were oxidized at the position where the partial pressure oxygen was sufficient and formed Fe_3O_4 , Cr_2O_3 and NiO .



(a)



(b)

Figure 5.36 Elemental mapping results for alloy 316: SP1 – end

CHAPTER 6

3-DIMENSIONAL MODELLING OF THE FURNACE AND THE SAMPLING PROBES

6.1 Overview

Mathematical modelling using FLUENT code was carried out in order to simulate the flow characteristics and heat transfer inside the furnace and the region around the air cooled sampling probes. The CFD work consisted mainly of 3-dimensional models of the furnace, sampling probe No. 1, and sampling probe No. 2.

The furnace model simulated the flow characteristic of combustion gaseous products that were released from the waste burning bed. The results, including gas temperature, gas properties, flow velocity and direction, at “probes’ locations” were subsequently used as inlet boundary conditions for the sampling probe models. Sampling probes were modelled both with and without the accumulation of deposits.

Results from these modelling works were then used to discuss the following topics:

- a. Effects of combustion gas characteristics on the deposition of particles and the temperatures of probes,
- b. Effects of alloy composition on the heat transfer of sampling probes, and hence the corrosion behaviour of materials,
- c. Effects of particle deposition on the heat transfer and the temperature of the sampling probes,
- d. The temperature gradient across the sampling probes and deposit layers,
- e. The performance of the flow diverted sacrificial baffles.

Additional investigations into the effect of particle size on the particle trajectories and use of “sacrificial baffles” were carried out by conducting 2 – dimensional modelling of the sampling probes.

The details of mathematical modelling approaches and related equations used in this study are given in the next section. The following sections present the results obtained from CFD modelling of the furnace, sampling probes No.1 & No.2 as well as 2-D models of the probes. Finally, mathematical modelling results are compared and discussed using some of the experimental data obtained from this study.

6.2 FLUENT code modelling

The mathematical modelling codes used in this study were the FLIC bed modelling code and FLUENT computational fluid dynamics code. FLIC code simulated the processes in the waste burning bed. It provided information on the velocity, temperature and chemical composition of the combustion gaseous products that are released from the waste bed. These results were then implemented as the input boundary conditions in the FLUENT code. Combustion gaseous products in the freeboard region and the convective pass of the furnace were simulated using FLUENT. The principal equations used in the simulations by FLUENT code are summarized in Table 6.1.

All models in this study were solved with the assumption of a “steady state”. For the viscous model, the standard $k - \varepsilon$ turbulence model equations were applied with the standard wall functions. Radiation was calculated by the Discrete Ordinate model (DO). Species transport modelling calculated 7 chemical species: O₂, CO₂, H₂O, CH₄, CO, H₂, and N₂. The density of gases was calculated using the incompressible ideal gas law. The reaction of the mixture was calculated using the finite-rate and eddy dissipation models.

Table 6.1 Principal equations used in FLUENT code for the furnace and sampling probe models (Goddard, 2006)

Name	Equation
Conservation of mass	$\frac{\partial \rho}{\partial \tau} + \nabla \cdot (\rho \vec{v}) = S_m$
Conservation of momentum	$\frac{\partial}{\partial t} (\rho \vec{v}) + \nabla \cdot (\rho \vec{v} \vec{v}) = -\nabla p + \nabla \cdot (\vec{\tau}) + \rho \vec{g} + \vec{F}$
Transport Equations for the standard $k - \varepsilon$ model	$\frac{\partial}{\partial t} (\rho k) = \frac{\partial}{\partial x_i} (\rho k u_i) = \frac{\partial}{\partial x_j} \left[\left(\mu + \frac{\mu_t}{\sigma_k} \right) \frac{\partial k}{\partial x_j} \right] + G_k + G_b - \rho \varepsilon - Y_M + S_k$ $\frac{\partial}{\partial t} (\rho \varepsilon) = \frac{\partial}{\partial x_i} (\rho \varepsilon u_i) = \frac{\partial}{\partial x_j} \left[\left(\mu + \frac{\mu_t}{\sigma_\varepsilon} \right) \frac{\partial \varepsilon}{\partial x_j} \right] + C_{1\varepsilon} \frac{\varepsilon}{k} (G_k + C_{3\varepsilon} G_b) - C_{2\varepsilon} \rho \frac{\varepsilon^2}{k} + S_\varepsilon$
Energy Equation	$\frac{\partial}{\partial t} (\rho E) + \nabla \cdot (\vec{v} (\rho E + p)) = \nabla \cdot \left(k_{eff} \nabla T - \sum_j h_j \vec{J}_j + (\vec{\tau}_{eff} \cdot \vec{v}) \right) + S_h$
Discrete ordinates radiation model	$\nabla \cdot (I(\vec{r}, \vec{s}) \vec{s}) + (a + \sigma_s) I(\vec{r}, \vec{s}) = a n^2 \frac{\sigma T^4}{\pi} + \frac{\sigma_s}{4\pi} \int_0^{4\pi} I(\vec{r}, \vec{s}') \Phi(\vec{s} \cdot \vec{s}') d\Omega'$
Chemical species transport	$\frac{\partial}{\partial t} (\rho Y_i) + \nabla \cdot (\rho \vec{v} Y_i) = -\nabla \cdot \vec{J}_i + R_i + S_i$
Chemical reactions of combustion	$CH_4 + \frac{3}{2} O_2 \rightarrow CO + 2H_2O \quad R_{CH_4} = 5.012 \times 10^{11} \exp\left(-\frac{2 \times 10^8}{RT}\right) C_{CH_4}^{0.7} C_{O_2}^{0.8}$ $CO + \frac{1}{2} O_2 \rightarrow CO_2 \quad R_{CO} = 2.239 \times 10^{12} \exp\left(-\frac{1.7 \times 10^8}{RT}\right) C_{CO} C_{O_2}^{0.25} C_{H_2O}^{0.5}$ $CO_2 \rightarrow CO + \frac{1}{2} O_2 \quad R_{CO_2} = 5.0 \times 10^8 \exp\left(-\frac{1.7 \times 10^8}{RT}\right) C_{CO_2}$ $H_2 + \frac{1}{2} O_2 \rightarrow H_2O \quad R_{H_2} = 3.123 \times 10^{16} \exp\left(-\frac{1.7 \times 10^8}{RT}\right) C_{H_2}^{0.5} C_{O_2}^{1.4}$

6.3 Three-dimensional modelling of the furnace

6.3.1 Model description

The geometry and the calculation units (mesh) of the model were first created by the GAMBIT software before it was exported to FLUENT software for further mathematical modelling work. The geometry of the model in GAMBIT was based on the design drawings of the waste to energy plant. The schematic diagram of the furnace model (side view) created by GAMBIT software is shown in the Figure 6.1.

The cross-sectional dimensions of the furnace are $4.9 \times 11 \text{ m}^2$ for the first pass, and $4.4 \times 11 \text{ m}^2$ for the second pass. The over-fire air is supplied to the furnace via the front and rear nozzles. The front over-fire air system consists of $35 \times 70 \text{ mm}$ diameter nozzles, whereas the rear over-fire air system consists of $33 \times 60 \text{ mm}$ diameter nozzles. In the second pass, there are 2 sets of pendent superheater (as shown in Figure 6.1). Each set is composed of 36 panels located in parallel throughout the cross sectional area of the furnace. In this design, the number of superheater panels is almost equal to the number of over-fire air nozzles. Therefore, only a slice of furnace was modelled and it was assumed to be representative of the whole furnace. The geometry which was modelled had a width of 0.3 m and consisted of a rear over-fire air nozzle, a front over-fire air nozzle, and a pair of superheater panels. The isometric view of the model is shown in Figure 6.2.

The model begins at the free board region adjacent to the waste burning bed. This was the main inlet where the combustion gaseous products entered the domain. Other inlets include the front and rear over-fire air nozzles. The end of this model, or the domain's outlet, was located in the second pass under the superheater panels. The locations of the sampling probes are also presented in Figure 6.2. The sampling probe No. 1 was placed in the first pass at the position 28.70 m from ground. The location of the sampling probe No. 2 was at the position 25.85 m from ground.

6.3.2 Input data

FLIC code computed the velocity, temperature and chemical composition of the combustion gaseous products primarily by using the data of plant's operating conditions and the fuel properties. The total air amount supplied to the furnace was $105,000 \text{ Nm}^3/\text{h}$ which was divided into $65,872 \text{ Nm}^3/\text{h}$ of the under-fire air supply, $22,383 \text{ Nm}^3/\text{h}$ of the front over-fire air supply and $16,745 \text{ Nm}^3/\text{h}$ of the rear over-fire air supply. The waste was fed into the furnace at the rate of 30 ton/h or 8.33 kg/s. The calorific value of MSW was assumed to be 8600 kJ/kg. The chemical compositions of the typical MSW in UK were shown in Table 6.2 and Table 6.3.

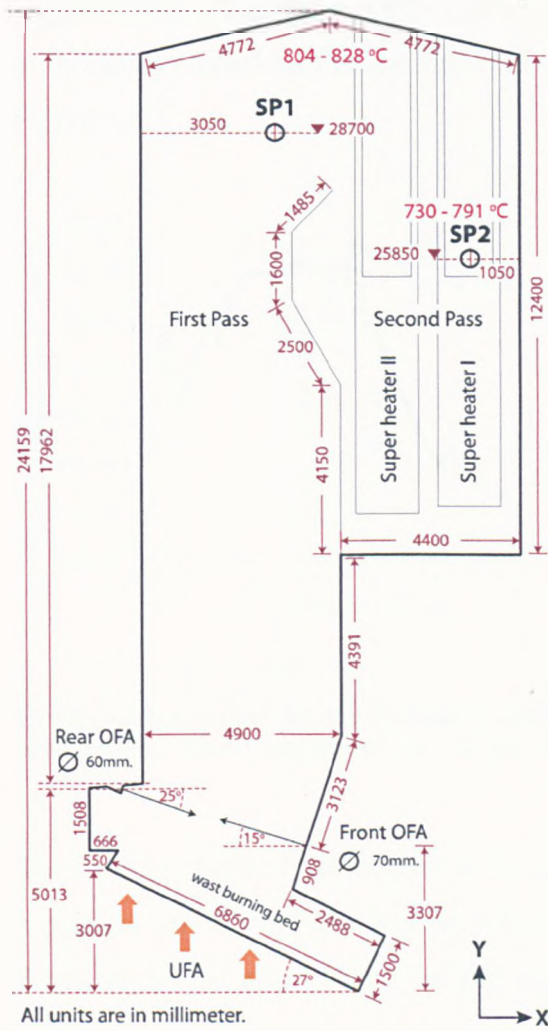


Figure 6.1 Schematic diagram (side view) and dimension of the furnace model

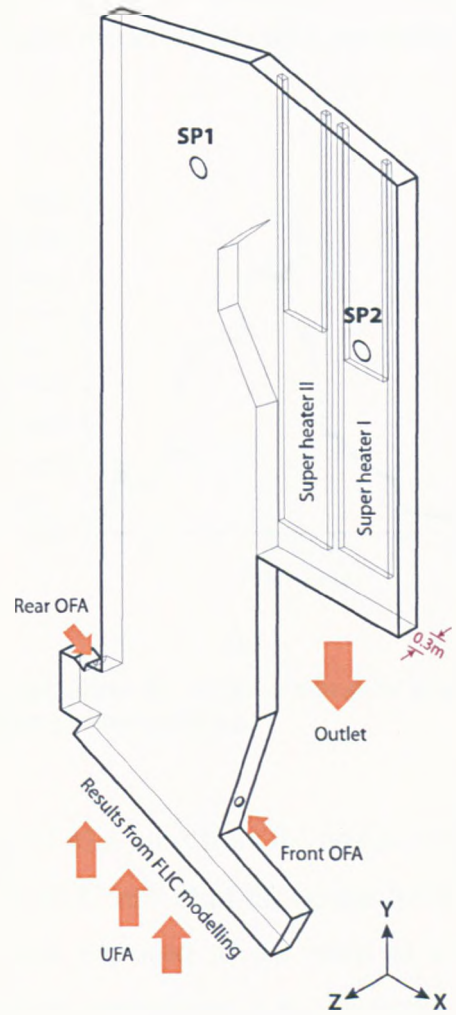


Figure 6.2 Isometric view of the furnace model.

Table 6.2 The chemical composition (by wt%) of the typical MSW in UK

Elemental analysis	%wt
Carbon	21.50
Hydrogen	3.00
Oxygen	16.90
Nitrogen	0.50

Table 6.3 The proximate analysis results of the typical MSW in UK

Proximate Analysis	%wt
Combustibles	41.40
Moisture H ₂ O	31.00
Ash	27.60

The results of FLIC modelling were subsequently input into the FLUENT modelling as the boundary conditions of the main inlet. Results of the temperature and velocity of the gases plotted against the length of the furnace model's main inlet are shown in Figure 6.3.

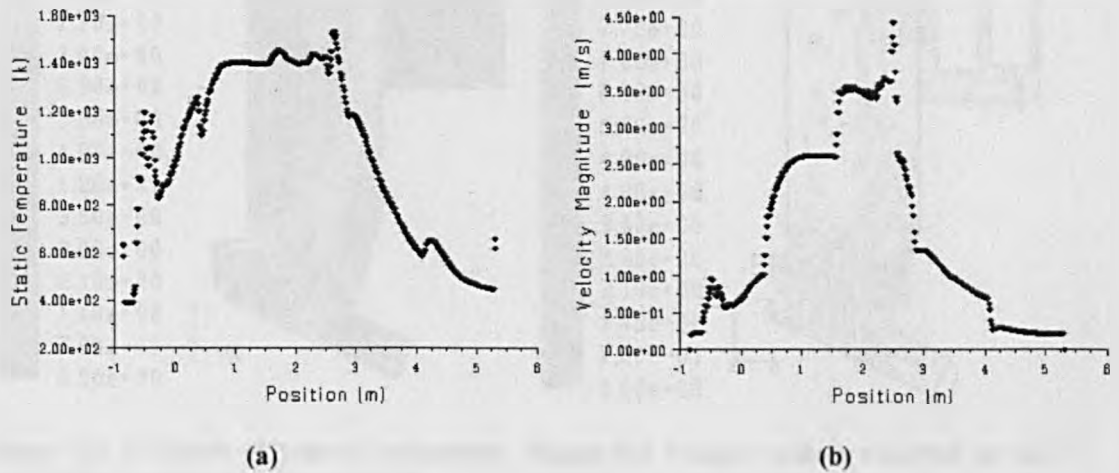


Figure 6.3 Input data for the furnace model: (a) temperature (K) of the combustion gaseous products, (b) velocity magnitude (m/s) of the combustion gaseous products.

The front over-fire air jet was set at the velocity of 45.60 m/s from the nozzle having a diameter of 70 mm. The rear jet velocity was 49.73 m/s from the nozzle having a diameter of 60 mm. This over-fire supply was provided to the plant at room temperature. For the calculation purpose, the room temperature was assumed to be 288 K (15°C).

6.3.3 Results: Velocity

The results for velocity profile and direction of the combustion gas stream in the furnace model are shown in Figure 6.4 and Figure 6.5 respectively. The velocity of the gas stream is the highest around the over-fire air jets. It then decreased to be lower than 10 m/s half way up the first pass. The average velocity at the outlet after the flow passed through the superheater panels was 2.73 m/s. The over-fire air supplies played a vital role in the stream flow. The high velocity of these jets created turbulent regions in the furnace. From this modelling, the angle of over-fire air nozzles created some vortexes preventing a well-circulating flow in the furnace.

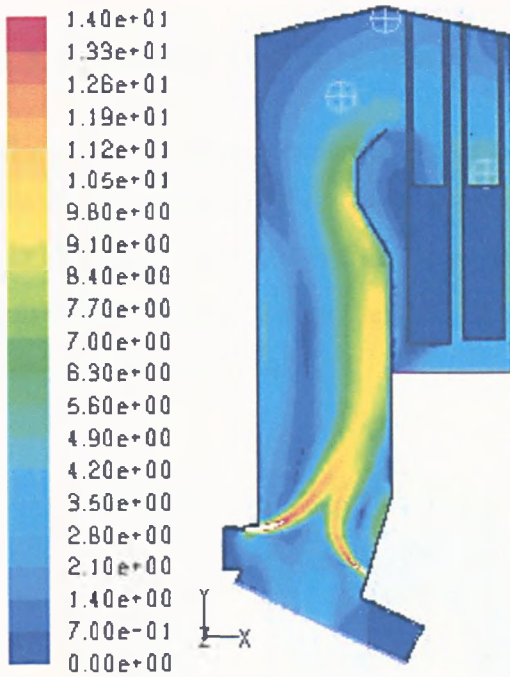


Figure 6.4 Contours of velocity magnitude (m/s) of the gases in the furnace model

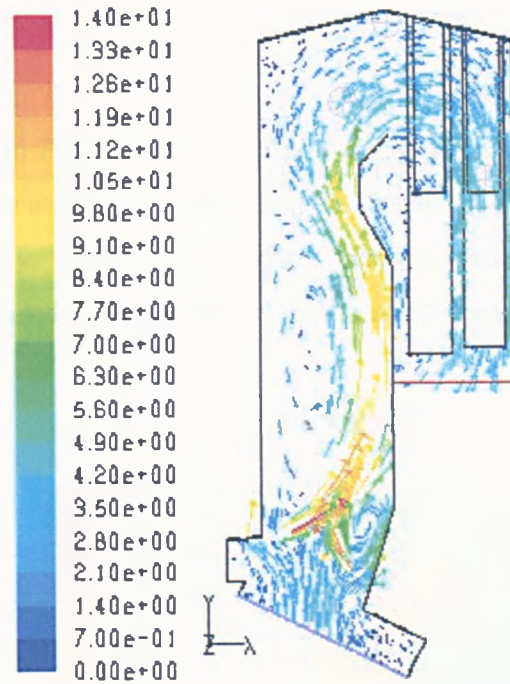


Figure 6.5 Velocity vectors coloured by the velocity magnitude (m/s) of the gases in the furnace model

The velocity vectors showed that the flow around sampling probe No.1 had an inclined angle while the flow direction around sampling probe No.2 was relatively straight from the top.

The results of gas velocity calculated based on the area-weighted average showed that the resultant velocity of the gases at the position of probe No.1 was 3.05 m/s. The velocity in the X and Y directions were 2.02 m/s and 2.28 m/s, respectively. This resulted in the flow angle of -138.4° to the Y-axis. The resultant gas velocity at the position of probe No.2 was 4.83 m/s. The velocity in the X and Y direction were 0.41 and -4.81 m/s, respectively. This resulted in the flow angle of -4.83° to the Y-axis. The negative values of the velocity showed that the gas stream was flowing downward. The path lines of gases coloured by the residence time are shown in Figure 6.6. The residence time in the furnace from the point where secondary air is injected to the point where the temperature falls below 850°C is at least 2 seconds as required.

6.3.4 Results: Temperature

The gas temperature result was presented in Figure 6.7. The area-weighted average calculation showed that the gas temperature at the probe No.1 and No. 2 was 1144 K (871°C) and 990 K (717°C) respectively. As the hot gases passed through superheater panels, the temperature decreased, which resulted in the gases leaving the outlet at 859 K (586 °C).

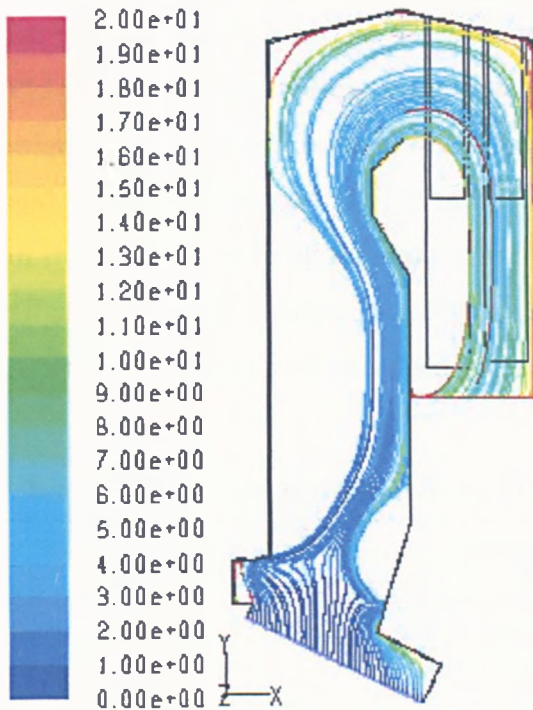


Figure 6.6 Path lines coloured by the residence time (s) of the gases in the furnace model

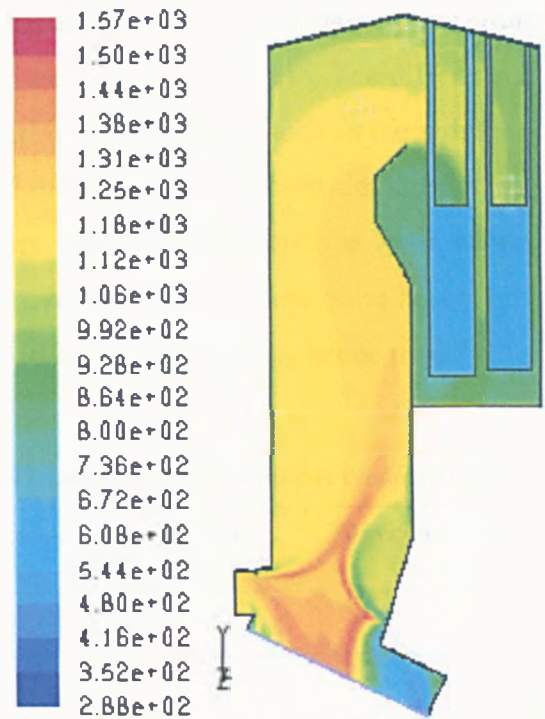


Figure 6.7 Contours of temperature (K) of the gases in the furnace model

6.3.5 Results: Chemical species of gases

Mole fractions of CO₂, O₂, H₂O, CH₄, CO, H₂, and N₂ are presented in Figure 6.8. The mole fraction of the CO₂ and O₂ were 0.1032 and 0.0692 respectively at the outlet. When considered in mass fraction ratios, CO₂ and O₂ contributed to the gas stream 15.89 wt% and 7.73 wt% respectively. O₂ was depleted on top of the waste burning bed since it was used for the oxidation reaction. However, the O₂ concentration reached 6% before the gas stream travelled past sampling probe No.1.

The locations of the sampling probes were therefore in the oxidizing environment. Methane (CH₄) and carbon monoxide (CO) were burnt out almost completely just above the burning bed. The outlet, therefore, contained mainly O₂, CO₂, H₂O (10.95 wt%) and N₂ (65.42 wt%).

6.3.6 Validity of the modelling results

The results from this furnace model were then compared with the values recorded online by plant operators. The results of gas temperature in Celsius, gas velocity and the oxygen content in the gas stream are summarized in Table 6.4. The results from FLUENT modelling corresponded relatively well to the real values. The differences might come from various parameters assumed in the modelling such as the radiation and the material properties. The radiation of the wall and the absorption coefficient of the gaseous combustion products were very important parameters as these values affect the overall furnace temperature. However, the results were quite acceptable and were subsequently used as the boundary input for the sampling probe models.

Table 6.4 Comparison of results from the FLUENT modelling and the on-line recorded values

Results	Temperature (°C)	Velocity (m/s)	Oxygen content (% wt)
Real measurement – roof probe	804 – 828		
Model – at the roof probe	769	1.26	6.55
Real measurement – 1st pass	754 – 813		8.38 – 8.77
Model – at the probe No.1	871	3.05	6.69
Real measurement – 2nd pass	730 – 791	≈ 5	
Model – at the probe No.2	717	4.83	6.68

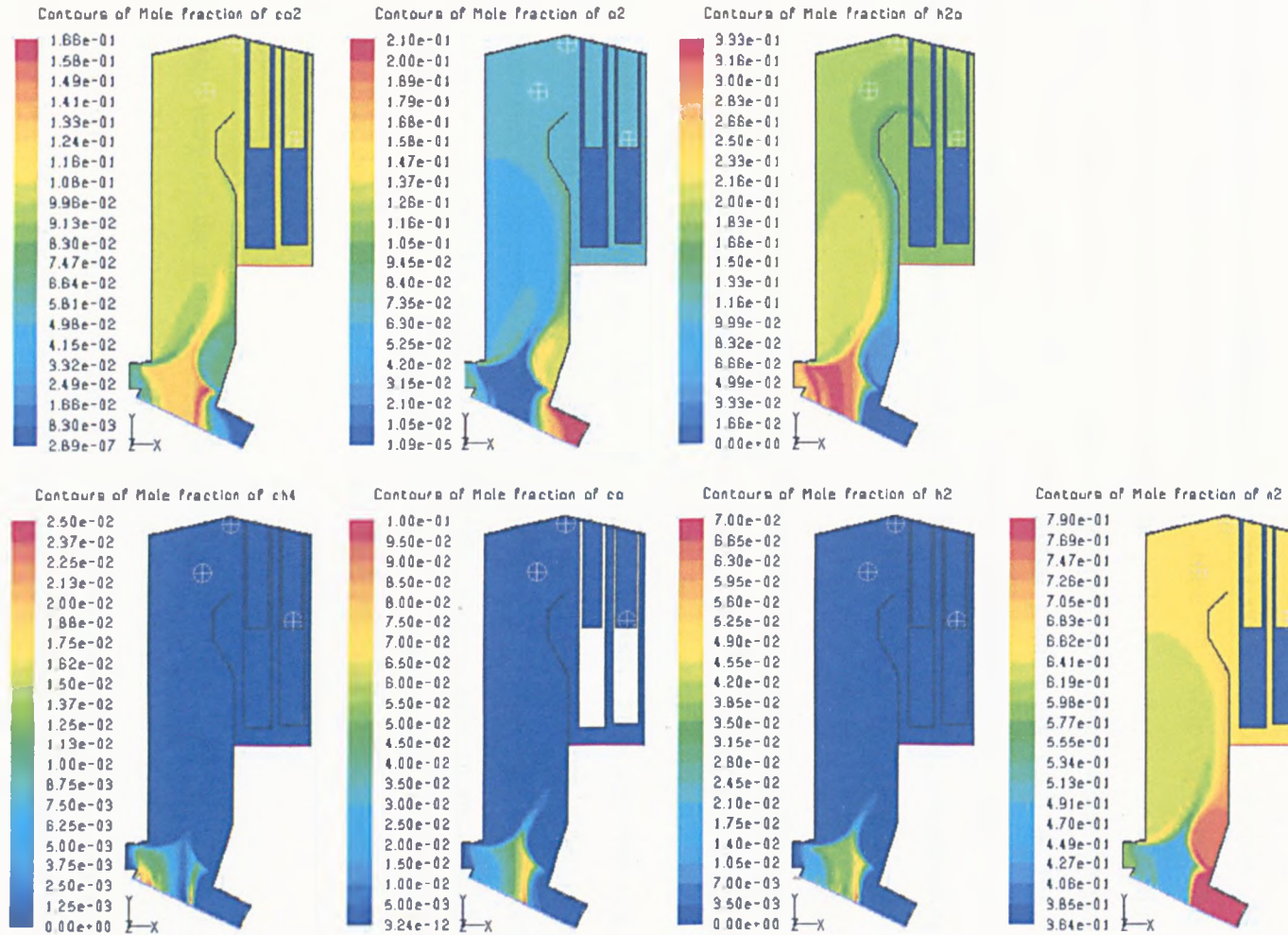


Figure 6.8 Contours of mole fractions of chemical species presented in the furnace model

6.4 Three-dimensional modelling of the sampling probe No.1

6.4.1 Model description

The modelling work of the sampling probe No.1 consisted of 2 models; 'sampling probe No.1 without deposits' and 'sampling probe No.1 with deposits'. The former model was carried out in order to simulate the probe just after it was just placed into the furnace while the latter one simulated the probe conditions when the probe was taken out. Both models used the same initial parameters such as the domain geometry, inlet conditions, and material properties. However, the deposit information and its properties were applied only in the model of the sampling probe with deposits.

The geometry of both models was based on the drawing of the probe presented in section 4.2.4. The information on particle deposit was based on the conditions of the real sampling probe after it was exposed in the furnace for 769 hours. The deposits were not found to cover the surface of the probe evenly. This was observed during the removal and disassembly of the probe. There was a thick layer of deposit only on the front side of the probe where the flow attacked. The deposits in the GAMBIT model were designed by using the experimental findings plus an assumed thin layer of uniform deposit (2 mm thickness) covering on the entire probe surface. The details of the deposit location, angle and the thickness used in this model are listed in Table 6.5.

The geometry of the model 'sampling probe No.1 with deposits' created by the software GAMBIT is shown in Figure 6.9. In both models, the probe was located in a domain with a dimension of $250 \times 250 \times 2,000$ mm. Since the flow direction had an angle of -138.4° (to the Y-axis) at the probe, the inlet of combustion gases to the domain was defined in 2 planes. Therefore, there were 2 outlet planes. The probe was located asymmetrically located in the domain to provide an efficient grid assignment. Details of the probe dimension, fabrication and materials were presented in the section 4.2.4.

Table 6.5 Details of deposit thickness and their locations in the model ‘sampling probe No.1’

Location of deposits on the probe	Position from wall (m)	Thickness of deposits (mm)	Angle of deposit (based on the Y-axis)
2 inch tube	0.165 – 0.315	18	-120° to 30°
1 inch tube – wall	0.315 – 0.525	14	
3 alloy rings – wall	0.525 – 0.650	12	
1 inch tube – middle 1	0.650 – 0.805		
3 alloy rings – middle	0.805 – 0.934	8	-105° to 20°
1 inch tube – middle 2	0.934 – 1.089		
3 alloy rings – end	1.089 – 1.214	6	-90° to 0°
1 inch tube – end	1.214 – 1.432		
Baffle – wall	0.390 – 0.465	2	-
Baffle – end	1.289 – 1.364		

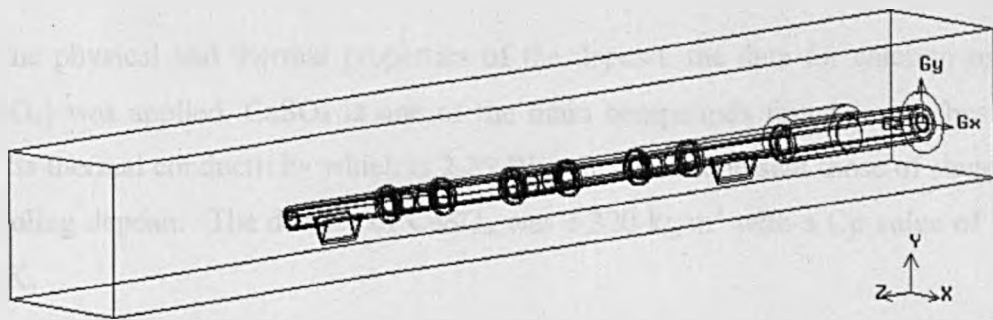


Figure 6.9 Isometric view of the model ‘sampling probe No.1 with deposit’ created by GAMBIT software

6.4.2 Input data

The input data of combustion gases to the probe domain was previously obtained from the furnace model. The velocity inlet of the hot gases was assigned to the models as components in the X and Y directions. The velocities in the X and Y direction were 2.07 m/s and 2.29 m/s, respectively. This resulted in a total velocity of 3.08 m/s. The temperature of the hot gases was 1145 K (872°C). The flow rate of the air jet supplied into the probe and the amount of air supplied to cool down the surrounding base area of the probe were taken from the actual measurement. The throughput and velocity of the air jet supplied into the probe was 1320 ft³/h or 20.5 m/s. The air supplied to cool the base area had a velocity of 5 m/s. The inlet temperature of these air supplies was assumed to be 288 K (15°C).

Since the probes were constructed from different materials, the properties of the probe materials were required in the sampling probe models in order to calculate the heat transfer between the furnace and the air-cooled probes. Five types of metals were used in the fabrication of this probe and their properties are listed in Table 6.6. The physical and thermal properties of these materials at 773 K (500°C) were used in all probe models.

Table 6.6 Physical and thermal properties of probe materials at 773 K (500°C)

Properties	Alloy 59	Alloy 556	Alloy 625	Steel 316	15Mo3
Density (kg/m ³)	8,600	8,230	8,440	8,000	7,817
Cp (j/kg-K)	459	538	527	500	683
Thermal conductivity (W/m-K)	18.6	20.8	16.9	21.5	38.3

For the physical and thermal properties of the deposit, the data for calcium oxide (CaSO₄) was applied. CaSO₄ is one of the main compounds found in combustion ash. Its thermal conductivity which is 2.25 W/m-K could represent those of slagging or fouling deposit. The density of CaSO₄ was 3,320 kg/m³ with a Cp value of 738 j/kg-K.

6.4.3 Results: Velocity

The results of velocity magnitude of the gases in models of sampling probe No.1 are shown in Figure 6.10. The velocity of the air inside the tube increased as it flowed through the probe. Area-weighted average calculations indicated that the velocity of the air increased from 20.5 m/s at entry to 37.6 m/s at the outlet of the probe, in the model of the sampling probe with deposits. An even higher outlet velocity of air, 38.9 m/s, was found in the model of the sampling probe without deposits due to the higher temperature.

Velocity vectors coloured by the velocity magnitude of the hot gas stream are shown in Figure 6.11. Two planes of cross section presented in this figure were positioned at the baffle - end (1.33 m from the wall), and at alloy 556 - middle section (0.88 m from the wall). As the hot gas passed the tube its velocity increased from 3.08 m/s to

as high as 5.6 m/s. High velocity flow attacking at front side of the probe (area facing the hot gas stream) resulted in a higher amount of deposit accumulated on this area. This result of modelling agreed with the experimental results. There were areas around the rear of the probe in which a vortex occurred. This could possibly lead to the accumulation of the small particles on the rear side of the probe, due to the Thermophoresis process.

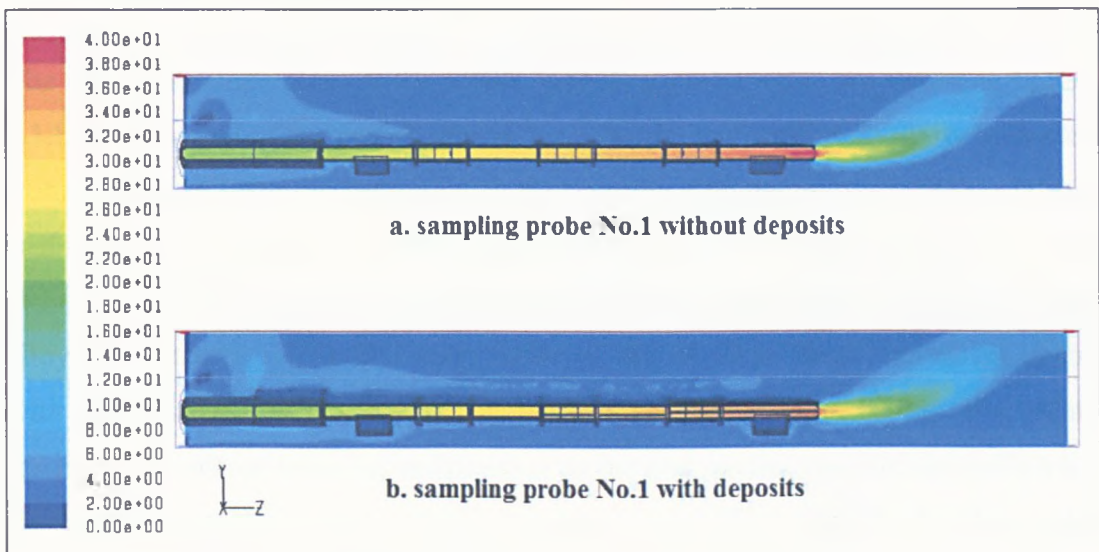


Figure 6.10 Contours of velocity magnitude (m/s) of the model 'sampling probe No.1'

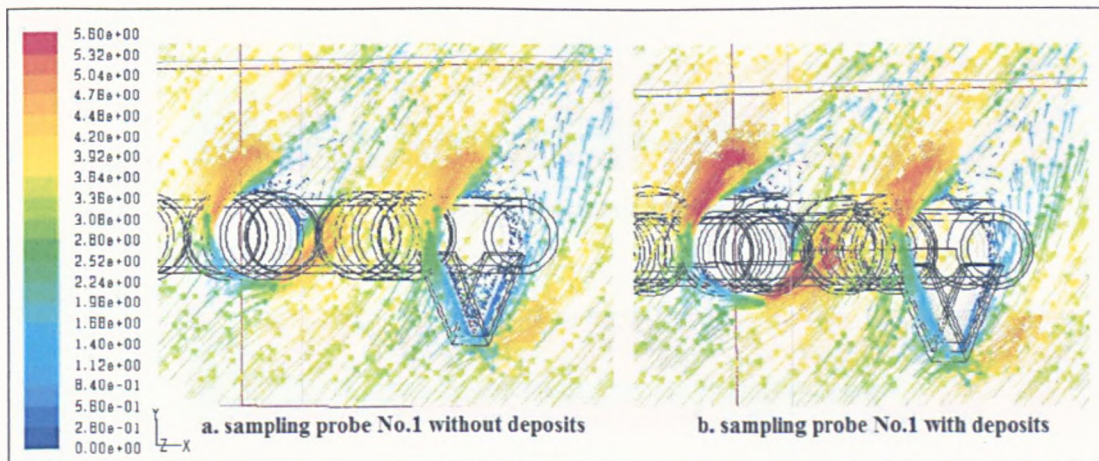


Figure 6.11 Velocity vector, coloured by the velocity magnitude (m/s) of the flow across the model 'sampling probe No.1'

Installation of sacrificial baffles could prevent the direct attack of hot gases by diverting their flow. However, an almost stagnant flow that occurred in the closed areas of the baffles also resulted in the accumulation of deposit. The flow and the

entrained particles could be trapped within the triangular volume between the baffle and the main tube. As the accumulation of deposit increases, the surface temperature of this deposit layer increases. This could intensify the corrosion damage due to molten salts deposit. A build-up of a thick deposit layer and the stagnant flow could also create a more reducing environment at the probe – deposit interface region.

6.4.4 Results: Temperature

The results of temperature of the model ‘sampling probe No.1’ are shown in Figure 6.12. In the model of the probe without deposits, the temperature of air jet increased from 288 K (15°C) at the beginning of the probe to a temperature of 490 K (217°C) at the end of the probe due to the heat transferred from the combustion gases. The deposit accumulation on the probe resulted in lower temperatures of the air jet and alloy temperatures. The outlet temperature of the air jet in the model of the probe with deposits was 424 K (151°C). The temperature difference of the air flow inside the probe calculated from the wall section to the end section was 115 K (115°C) for the model ‘sampling probe without deposits’, and 102 K (102°C) for the model ‘sampling probe with deposits’.

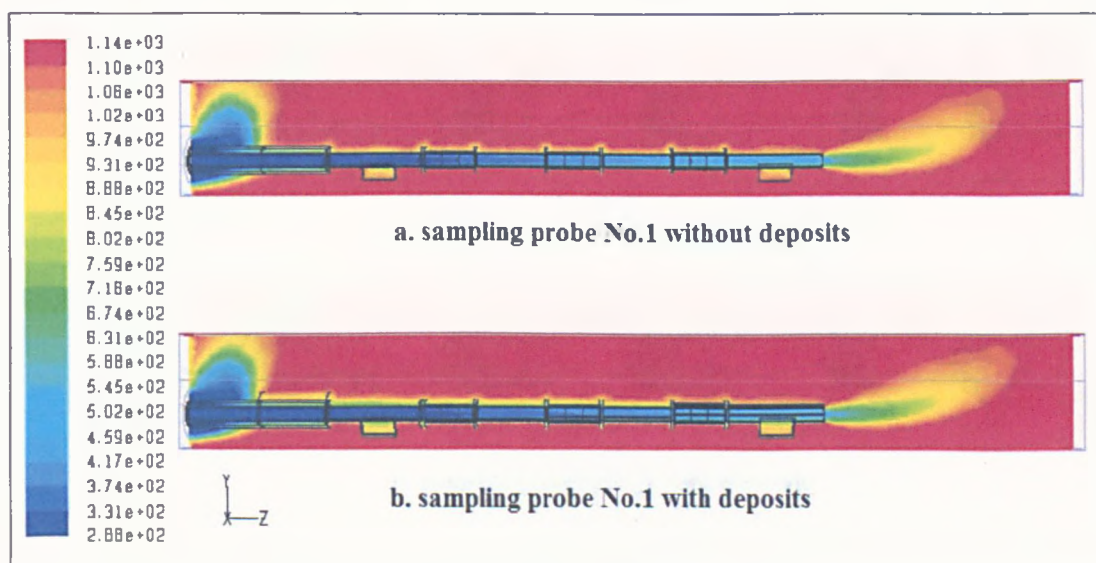


Figure 6.12 Contours of temperature (K) of the model ‘sampling probe No.1’

The temperatures of the air inside the probes at the 556-wall section (0.59 m from the wall), 556-middle section (0.88 m from the wall) and 556-end section (1.16 m

from the wall) compared with experimental data measured by thermocouples are shown in Table 6.7. In general, the results obtained from FLUENT modelling were slightly lower than the recorded temperature even though the input temperature of the hot gas was 1145 K (872°C) which is significantly higher than the actual temperature at this location. One reason could be that the real deposit had a greater thermal conductivity value compared to 0.5 W/m-K used in the modelling. The temperature contours at the cross sections at 0.59 m (556W), 0.88 m (556M), 1.16 m (556E), and 1.33 m (Baffle E) from the wall are shown in Figure 6.13.

Table 6.7 Temperature (K/°C) of the air jet inside sampling probe No.1

Position of the air jet	Wall section (0.59 m)	Middle sect (0.88 m)	End section (1.16 m)	Outlet (1.43 m)
Actual Temperature (measured by thermocouples)	367 K	395 K	448 K	NA
	(94°C)	(122°C)	(175°C)	NA
Sampling probe No.1 without deposits	326 K	384 K	441 K	490 K
	(53°C)	(111°C)	(168°C)	(217°C)
Sampling probe No.1 with deposits	322 K	373 K	424 K	470 K
	(49°C)	(100°C)	(151°C)	(197°C)

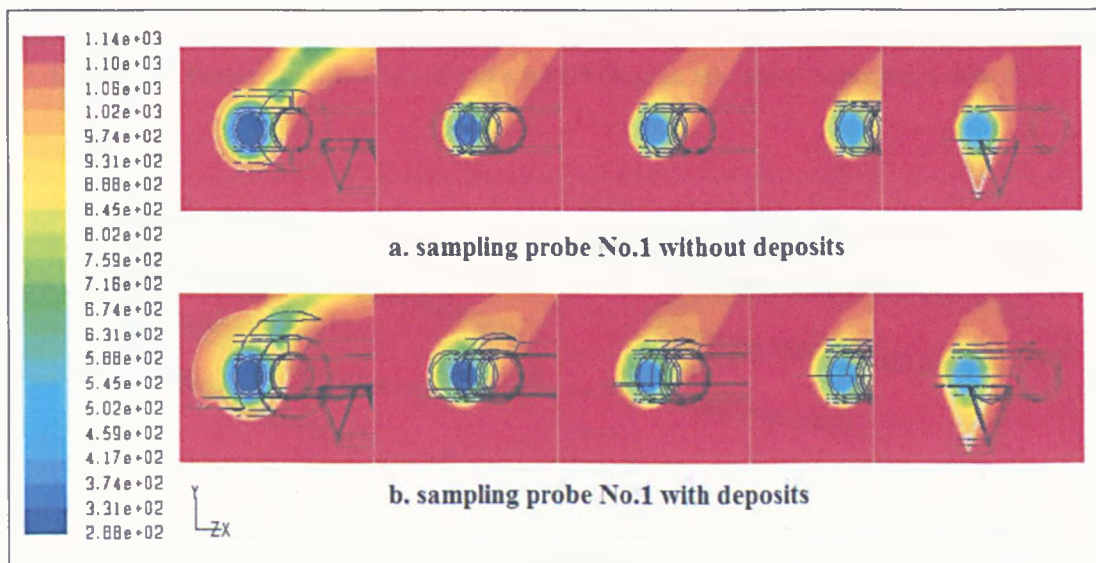


Figure 6.13 Contours of temperature (K) of the model 'sampling probe No.1' at various cross-sections

The temperatures at the surface of the alloy rings varied depending on its position and its thermal conductivity. The surface temperatures of alloy 59 rings at the wall,

middle, and end section are plotted against X-direction as shown in Figure 6.14. The negative X-positions represent the front side of the probe where the combustion gases attacked directly, while the positive X-positions represent the rear side of the probe. The letter 'F' represents the front half of the alloy ring where the combustion gases directly attack whereas the letter 'R' represents the rear half of the ring.

Similarly, the surface temperature of alloy 556 rings and 625 rings are shown in Figure 6.15 and Figure 6.16 respectively. The average values of alloy surface temperatures as shown in Figure 6.14 - Figure 6.16 are presented in Table 6.8 (in K) and Table 6.9 (in °C).

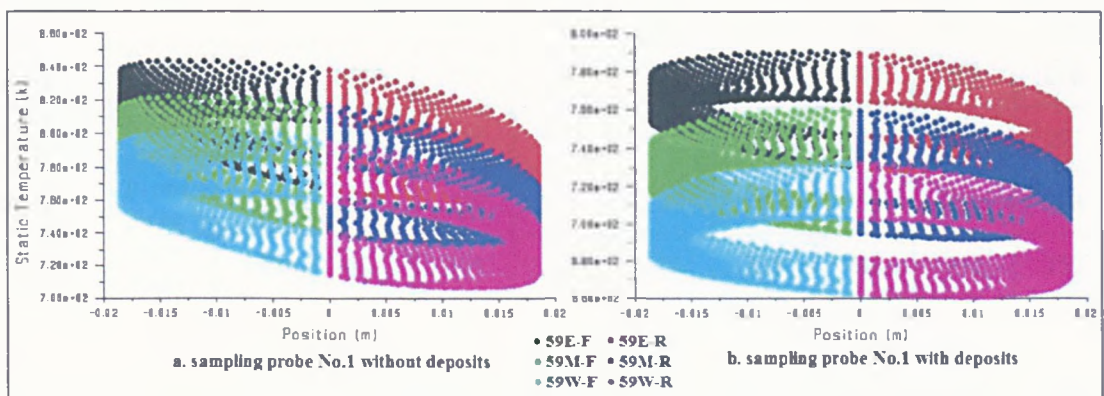


Figure 6.14 Surface temperature (K) of alloy 59 rings in the model 'sampling probe No.1'

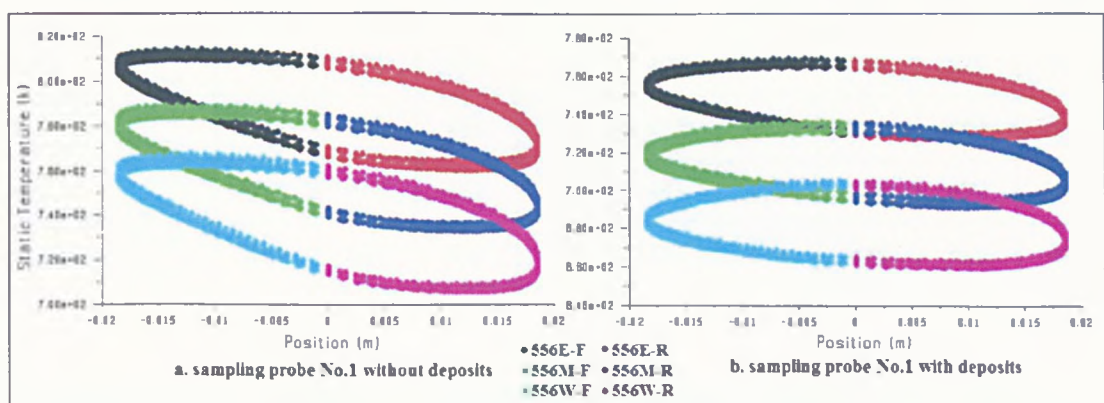


Figure 6.15 Surface temperature (K) of alloy 556 rings in the model 'sampling probe No.1'

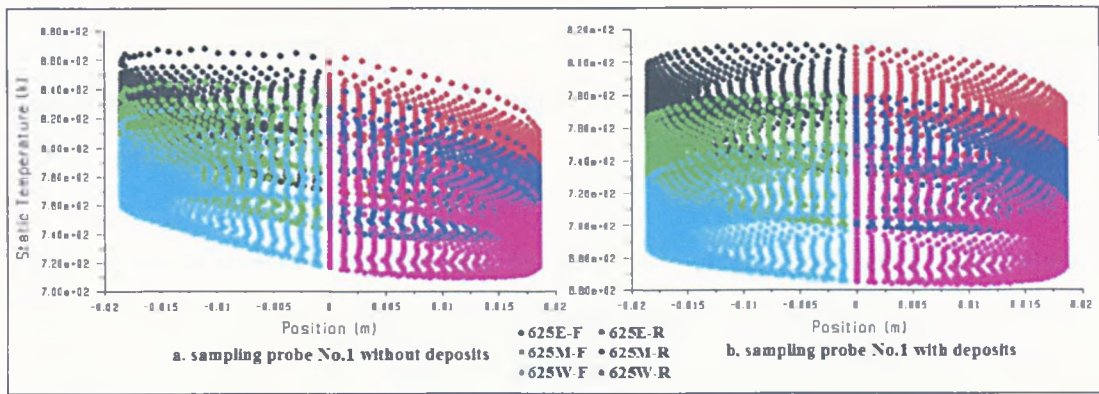


Figure 6.16 Surface temperature (K) of alloy 625 rings in the model 'sampling probe No.1'

Table 6.8 The average values of alloy surface temperatures from model 'sampling probe No.1' (K)

Models	Alloys	Wall section (0.59 m)			Middle section (0.88 m)			End section (1.16 m)		
		59	556	625	59	556	625	59	556	625
SP1 without deposit	Front piece	762	749	769	783	772	792	807	798	816
	Rear piece	735	725	741	758	750	766	784	777	792
SP1 with deposit	Front piece	692	683	700	724	716	735	759	752	768
	Rear piece	686	677	693	715	708	725	748	742	757

Table 6.9 The average values of alloy surface temperatures from model 'sampling probe No.1' (°C)

Models	Alloys	Wall section (0.59 m)			Middle section (0.88 m)			End section (1.16 m)		
		59	556	625	59	556	625	59	556	625
SP1 without deposit	Front piece	489	476	496	510	499	519	534	525	543
	Rear piece	462	452	468	485	477	493	511	504	519
SP1 with deposit	Front piece	419	410	427	451	443	462	486	479	495
	Rear piece	413	404	420	442	435	452	475	469	484

Results show that the surface temperatures of alloy rings located at the end side of the probe were clearly higher than those located next to the air supply. In the model of the probe without deposits, the average temperature increases from the wall section to the end section for alloy 59, alloy 556, and alloy 625 were 47 K(°C), 50 K(°C), and 49 K(°C) respectively. The existence of deposits resulted in greater

temperature differences. In the model of the probe with deposits, the average temperature increases for alloy 59, alloy 556, and alloy 625 were 64 K($^{\circ}$ C), 67 K($^{\circ}$ C), and 66 K($^{\circ}$ C) respectively.

At the same distances from the wall, the front side of the rings had a higher surface temperature compared to the rear side due to their direct exposure to the hot gas stream. The average percentages of temperatures difference for rings of alloy 59, alloy 556, and alloy 625 were 3.32%, 3.05%, and 3.35% respectively. Deposits covering these alloy rings reduced the direct contact of the alloys to the hot gas stream. Hence, the temperature differences between the front and rear side of the rings were minimized. The differences for alloy 59, alloy 556, and alloy 625 were 1.17%, 1.13%, and 1.28% respectively.

Alloy 625 had the highest surface temperatures followed by alloy 59, and alloy 556 had the lowest surface temperatures. This corresponded with the fact that alloy 556 had the highest thermal conductivity followed by alloy 59 and alloy 625. The higher thermal conductivity could lead to a greater heat transfer rate. Furthermore, the high surface temperatures of alloy 556 and alloy 625 could be the result of heat transfer from the brace rings which were installed next to the rings of alloy 625 and alloy 59.

Surface temperatures of the deposit at various locations, which is divided into a thick top part and a thin bottom part, are presented in Figure 6.17. The average surface temperatures of the deposit at various locations are summarized in Table 6.10. The surface temperatures of the deposit depended on the thickness of the deposit layer and the position on the probe. The top part of the deposit had a higher surface temperature compared to the bottom part. The deposit temperatures were found to vary from 904 – 953 K (631 – 680 $^{\circ}$ C) for the top part, and 762 – 815 K (489 – 542 $^{\circ}$ C) for the bottom part.

The deposit on the 2inch tube had a maximum thickness of 18 mm and its top part had a surface temperature of 1042 K (769 $^{\circ}$ C). This was supported by the experimental results since the deposit on the 2 inch tube was found to have melted. The temperatures of the deposit on the baffles were also very high being at 912 – 964

K (639 – 691°C). The reason was that the baffles had a very low contact area for heat transfer with the main probe.

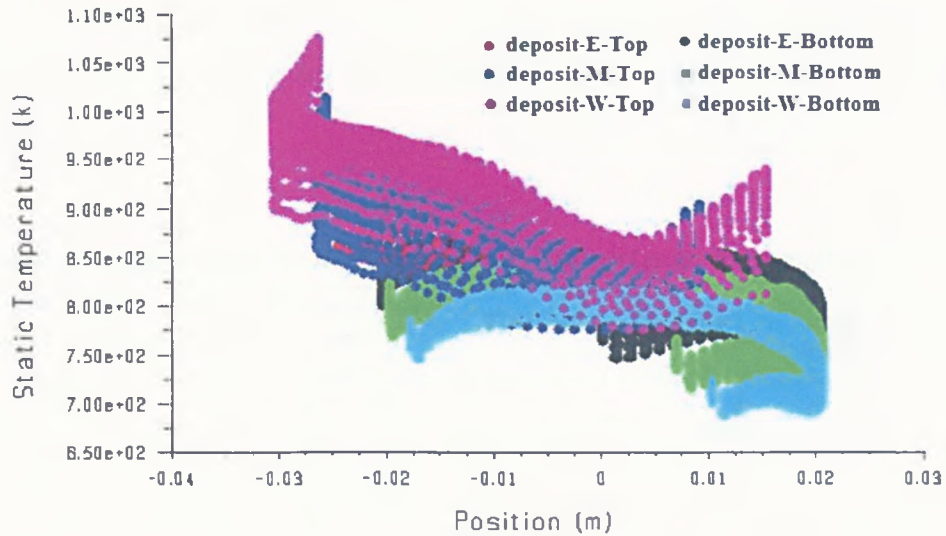


Figure 6.17 Surface temperatures (K) of deposits in the model 'sampling probe No.1'

Table 6.10 The average values of deposit surface temperatures from the model 'sampling probe No.1'

Deposit Temperature		2inch tube	Baffle Wall	Wall section	Middle section	End section	Baffle End
K	Top	1042	912	953	914	904	964
	Bottom	940		762	787	815	
°C	Top	769	639	680	641	631	691
	Bottom	667		489	514	542	

6.5 Three-dimensional modelling of the sampling probe No.2

6.5.1 Model description

The modelling work for sampling probe No.2 consisted of 2 models; 'sampling probe No.2 without deposits' and 'sampling probe No.2 with deposits'. The concept of modelling was similar to the modelling of sampling probe No.1 which was discussed in section 6.4.1. The geometry of both models was based on the drawing of the probe presented in section 4.2.4. The information on particle deposit was based on the conditions of the real sampling probe after it was exposed in the furnace for 811 hours. The deposits were found to cover only the top part of the sampling

probe where the hot gas stream attacked. The deposits in the GAMBIT model were designed by using the experimental findings plus an assumed thin layer of uniform deposit (having a thickness of 1 mm) covering the entire probe surface. The details of deposit location, angle and the thickness used in this model are summarized in Table 6.11.

Table 6.11 Details of deposit thickness and their locations in model 'sampling probe No.2'

Location on the probe	Distance from wall (m)	Thickness of deposits (mm)	Angle of deposit (based on the Y-axis)
2 inch tube	165 – 315	37	-90° to 90°
1 inch tube – wall	315 – 531		
3 alloy rings – wall	531 – 651	24	
1 inch tube – middle 1	651 – 811		
3 alloy rings – middle	811 – 932	20	
1 inch tube – middle 2	932 – 1092		
3 alloy rings – end	1092 – 1213	18	-60° to 60°
1 inch tube – end	1213 – 1432		
Baffle – wall	385 – 460	1	-
Baffle – end	1293 – 1368		

The geometry of the model 'sampling probe No.2 with deposits' created by the software GAMBIT is shown in Table 6.19. In the models, the probe was located in a domain having a dimension of 150 × 250 × 2000 mm. Since the flow direction had an angle of 4.83° (to the Y-axis) to the probe, 2 planes were appointed as inlets of combustion gas. Hence, there were 2 outlet planes. Details of the probe dimensions were presented in Chapter 5, Experimental methodology.

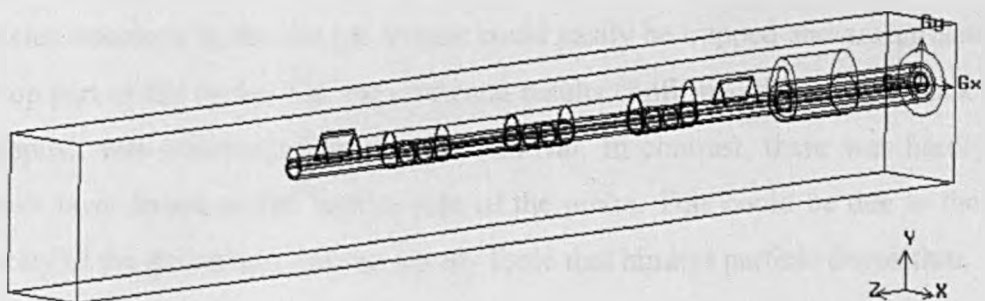


Figure 6.18 Isometric view of the model 'sampling probe No.2 with deposits' created by GAMBIT software

6.5.2 Input data

The input data for the combustion gases was previously derived from the furnace model. The velocities in the X and Y directions were 0.40 m/s and -4.81 m/s, respectively. This resulted in a total velocity of 4.82 m/s. The temperature of the hot gases was 989 K (716°C). Other input data including air supplies and material properties in this model were similar to the model 'probe No.1'. The velocity of the air flow supplied into the probe was 20.5 m/s. The air used for cooling the base area had a velocity of 5 m/s. The temperature of these air supplies were assumed to be at 288 K (15°C). The physical and thermal properties of probe materials were listed in Table 6.6. The physical and thermal properties of deposit were assumed to be equal to that of CaSO₄. The thermal conductivity was therefore 0.5 W/m-K with density being 2960 kg/m³ and Cp of 856 j/kg-K.

6.5.3 Results: Velocity

The results of velocity magnitude of the gases in models of sampling probe No.2 are shown in Table 6.20. In the model of the sampling probe with deposit, the area weighted average velocity of the air inside the probe increased from 20.5 m/s at entry to 36.4 m/s at the outlet of the probe. An outlet velocity of 36.6 m/s was found in the model of the sampling probe without deposit.

The velocity vectors coloured by the velocity magnitude of the hot gas stream are shown in Figure 6.20. Two planes of cross section presented in this figure were at the position of the baffle - end (1.33 m from the wall) and alloy 556 - middle section (0.87 m from the wall). The velocity of the hot gas increased from 4.82 m/s to as high as 8.0 m/s as it was passed the tube. According to the flow directions, the particles entrained in the hot gas stream could easily be trapped and accumulated on the top part of the probe. The experimental results confirmed this since a thick layer of deposit was observed during probe removal. In contrast, there was hardly any deposit layer found on the bottom side of the probe. This could be due to the high velocity of the gas stream and the gravity force that hinders particle deposition.

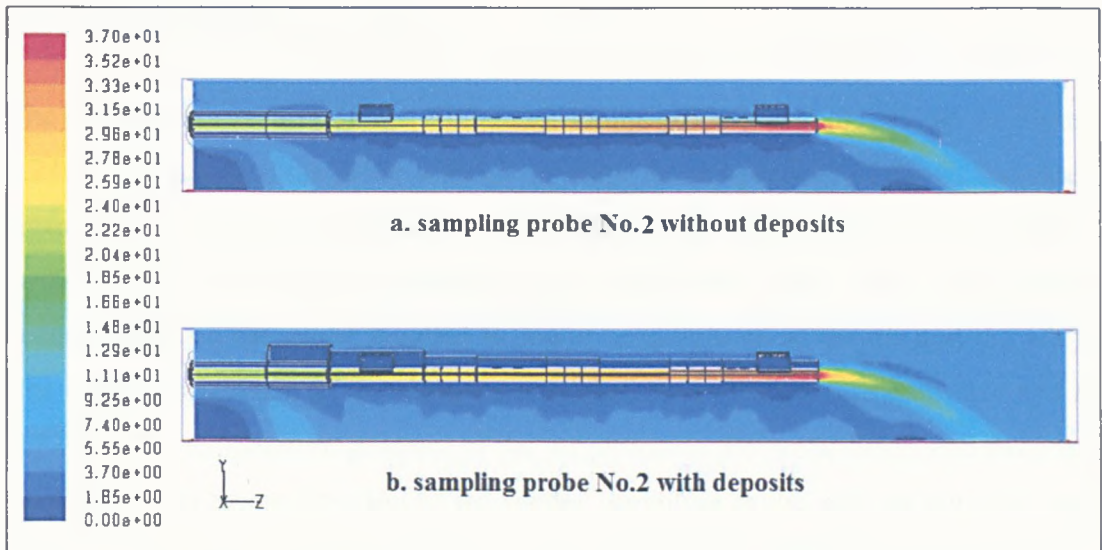


Figure 6.19 Contours of velocity magnitude (m/s) of the model 'sampling probe No.2'

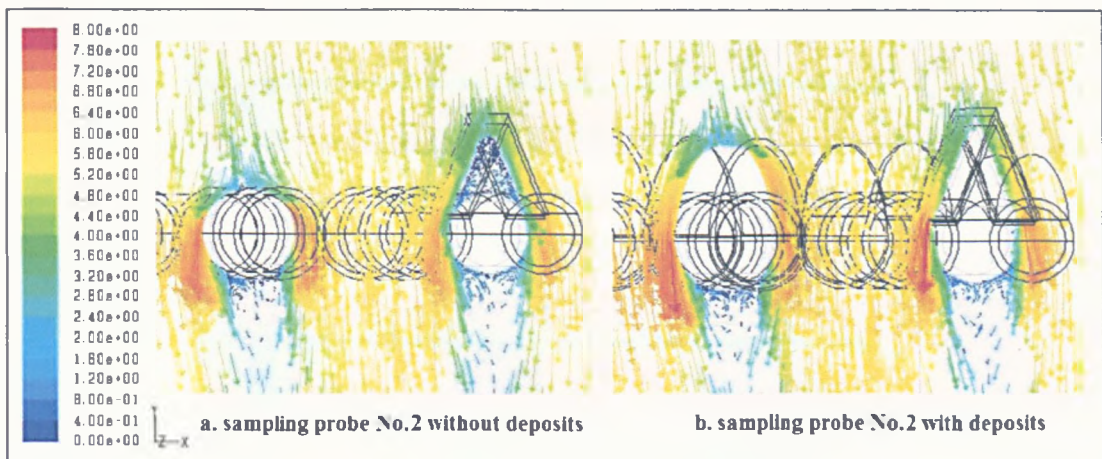


Figure 6.20 Velocity vector, coloured by the velocity magnitude (m/s) of the flow across the model 'sampling probe No.2'

From the modelling results, the installation of sacrificial baffles could divert the flow and prevent direct attack from hot gases and entrained particles on the tube. However, in the experimental probe, some deposit was found in the triangular volume between the baffle and the main tube but to a lesser extent compared to probe No.1. Therefore, sacrificial baffles with this design might be a useful device to prevent erosion but could magnify the deposit-induced corrosions on the tube surface located behind the baffles.

6.5.4 Results: Temperature

The temperature results of the model 'sampling probe No.2' are shown in Figure 6.21. In the model of the probe without deposits, the temperature of the air increased from 288 K (15°C) at the beginning of the probe to a temperature of 459 K (186°C) at the end of the probe. Similar to the results for probe No.1, the deposit accumulation on the probe resulted in lower temperatures of the air and the alloy. The outlet temperature of the air in the model of the probe with deposits was 445 K (172°C). The temperature gradient of the air jet inside the probe calculated from the wall section to the end section of the model 'sampling probe without deposits' and the model 'sampling probe with deposits' were 99 K (°C) and 88 K (°C) respectively.

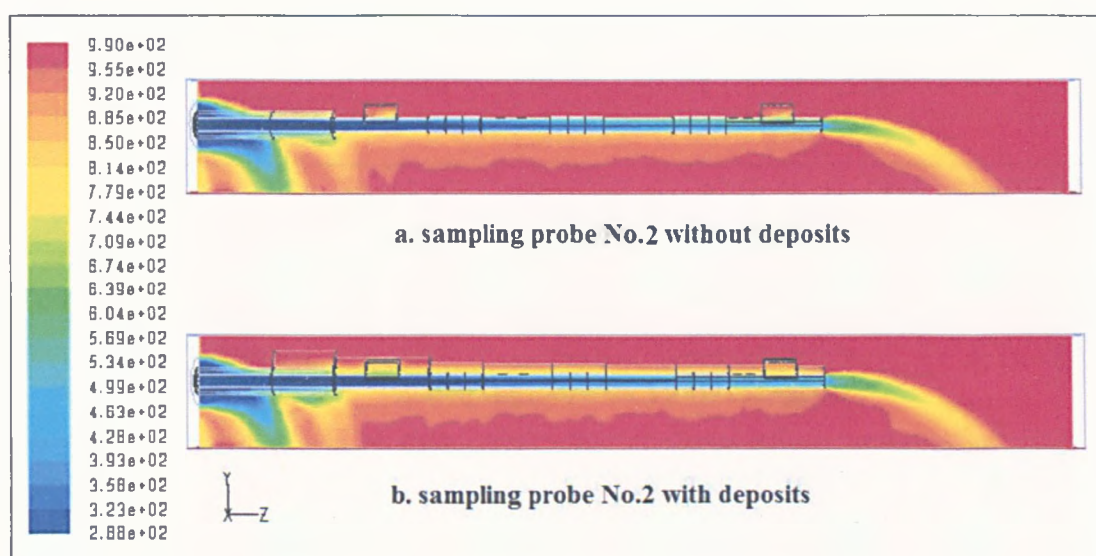


Figure 6.21 Contour of temperature (K) of the model 'sampling probe No.2'

The calculated temperatures of the air inside the probe at the 556-wall section (0.59 m from the wall), 556-middle section (0.87 m from the wall) and 556-end section (1.15 m from the wall) and experimental data measured by thermocouples are shown in Table 6.12. It was found that the results obtained from FLUENT modelling were higher than the recorded temperatures especially at the end section where the temperature difference was up to 75 K (°C). This was primarily due to the lower initial temperature of the hot gas in the modelling. The temperature used for modelling was 989 K (716°C) whereas the actual combustion gases temperature ranged from 1003 – 1064 K (730 – 791°C). Another reason could be that the actual

deposit had a greater thermal conductivity value than the one used in the modelling (0.5 W/m-K).

Table 6.12 Temperature (K/°C) of the air jet inside the model ‘sampling probe No.2’

Position of the air jet	Wall section (0.59 m)	Middle sect (0.87 m)	End section (1.15 m)	Outlet (1.43 m)
Actual Temperature	390 K	383 K	477 K	NA
	(117°C)	(110°C)	(204°C)	NA
Sampling probe No.2 without deposits	316 K	366 K	415 K	459 K
	(43°C)	(93°C)	(142°C)	(186°C)
Sampling probe No.2 with deposits	314 K	359 K	402 K	445 K
	(41°C)	(86°C)	(129°C)	(171°C)

The temperature contours for the cross sections at 0.59 m (556W), 0.87 m (556M), 1.15 m (556E), and 1.33 m (baffle E) from the wall are shown in Figure 6.22.

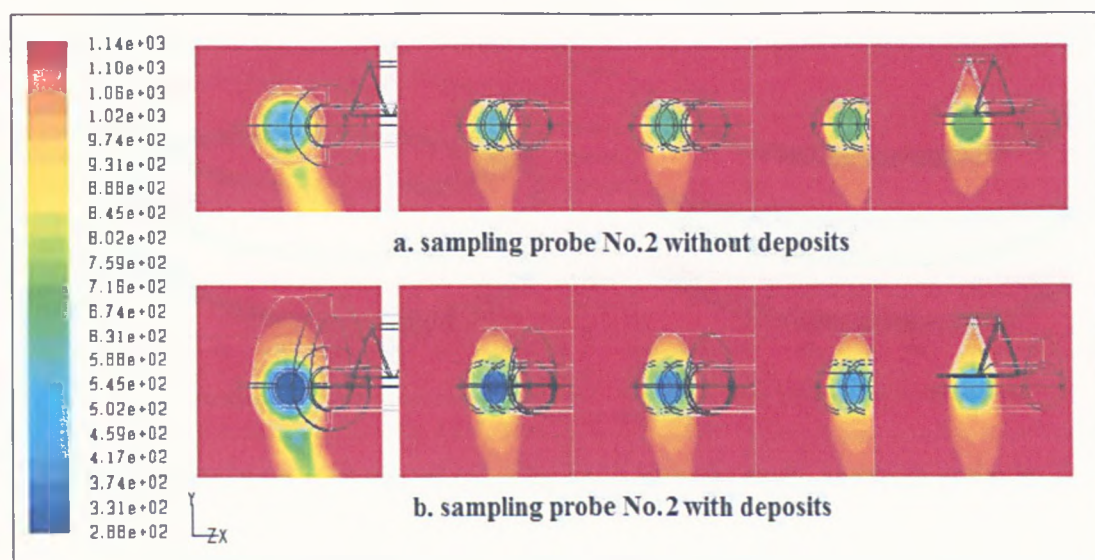


Figure 6.22 Contour of temperature (K) of the model ‘sampling probe No.2’ at various cross-sections

As discussed previously, the surface temperatures of an alloy ring varied depending on its position, its thermal conductivity, and the thickness of covering deposits. The surface temperatures of alloy 59 rings at the wall, middle, and end section are plotted against X-direction as shown in Figure 6.23. The negative X-positions represented the front side of the probe where the combustion gases directly attacked, while the positive X-positions represented the rear side of the probe. The letter ‘T’ represented the top half of the alloy ring where the combustion gases directly attacked whereas

the letter 'B' represented the bottom half of the ring. Similarly, the surface temperature of alloy 556 rings and 625 rings are shown in Figure 6.24 and Figure 6.25 respectively. The average values of alloy surface temperatures as shown in Figure 6.23 – Figure 6.25 are presented in Table 6.13 (in K) and Table 6.14 (in °C).

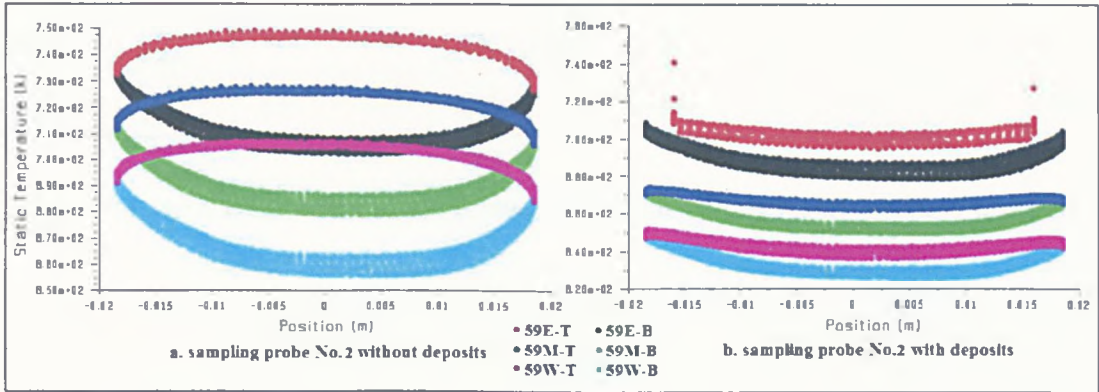


Figure 6.23 Surface temperature (K) of alloy 59 rings in the model 'sampling probe No.2'

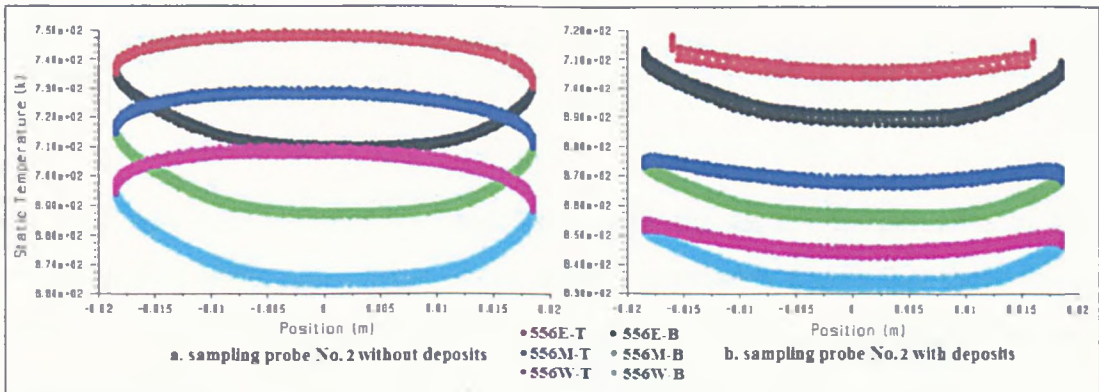


Figure 6.24 Surface temperature (K) of alloy 556 rings in the model 'sampling probe No.2'

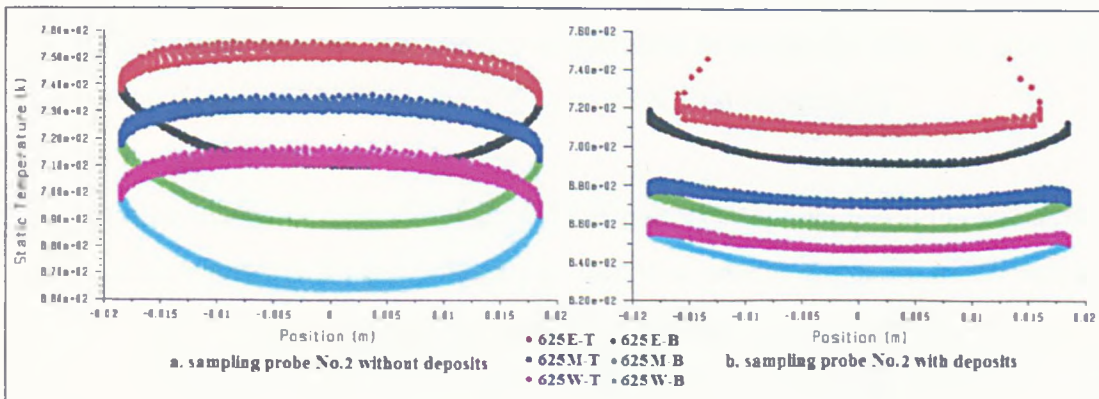


Figure 6.25 Surface temperature (K) of alloy 625 rings in the model 'sampling probe No.2'

Table 6.13 The average values of alloy surface temperatures from model 'sampling probe No.2' (K)

Models	Alloys	Wall section (0.59 m)			Middle section (0.87 m)			End section (1.15 m)		
		59	556	625	59	556	625	59	556	625
SP2 without deposit	Top piece	700	703	707	721	723	726	741	743	747
	Bottom piece	670	675	677	693	697	698	714	719	720
SP2 with deposit	Top piece	644	648	651	667	671	674	703	708	713
	Bottom piece	636	640	643	659	662	665	691	697	700

Table 6.14 The average values of alloy surface temperatures from model 'sampling probe No.2' (°C)

Models	Alloys	Wall section (0.59 m)			Middle section (0.87 m)			End section (1.15 m)		
		59	556	625	59	556	625	59	556	625
SP2 without deposit	Top piece	427	430	434	448	450	453	468	470	474
	Bottom piece	397	402	404	420	424	425	441	446	447
SP2 with deposit	Top piece	371	375	378	394	398	401	430	435	440
	Bottom piece	363	367	370	386	389	392	418	424	427

From Figure 6.23 - Figure 6.25 and Table 6.13, the surface temperatures of alloy rings located at the end section of the probe were clearly higher than those located next to the air supply. In the model of the probe without deposits, the average temperature increases of alloy rings from the wall section to the end section for alloy 59, alloy 556 and alloy 625 were 43 K (°C), 42 K (°C), and 42 K (°C) respectively. The higher temperature changes were found in the presence of deposits. In the model of the probe with deposits, the average temperature increases for alloy 59, alloy 556 and alloy 625 were 57 K (°C), 59 K (°C), and 59 K (°C) respectively.

At the same distances from the wall, the top part of the rings had a higher surface temperature compared to the bottom part due to a greater exposure to the hot gas stream. The average percentages of temperature differences were 2.80% for alloy 59, 2.40% for alloy 556, and 2.69% for alloy 625. These temperature differences were lower in the model of the sampling probe with deposits where the percentages of temperature difference for alloy 59, alloy 556, and alloy 625 were 1.41%, 1.34%, and 1.47% respectively

Alloy 625 had the highest surface temperature followed by alloy 556 and alloy 59 respectively. Alloy 556, despite it having the highest thermal conductivity (20.8 W/m K) did not consistently have the lowest surface temperature compared to the other alloys (18.6 W/m K for alloy 59, and 16.9 W/m K for alloy 625). These results were different from the results for the model of probe No.1. One reason could be that the sampling probe No.2 did not have brace rings installed next to alloy 59 and alloy 625. Therefore the surface temperature of the alloy rings mainly depended on the heat transfer to the cool air flow and was not affected by the heat of brace rings. Consequently, rings of alloy 59 located closer to the wall compared to those of alloy 556 and alloy 625 could have lower surface temperatures.

Surface temperatures of deposits at various positions which are divided into a thick top part and a thin bottom part are presented in Figure 6.26. The average surface temperatures of deposits at various locations are summarized in Table 6.15.

The deposits on the metal rings were found to vary from 762 – 953 K (489 – 680°C). These results were supported by the actual deposit layer detected after 811 hours of exposure. The deposit on probe No.2 was composed of small grain particles and there was no sign of a melted area.

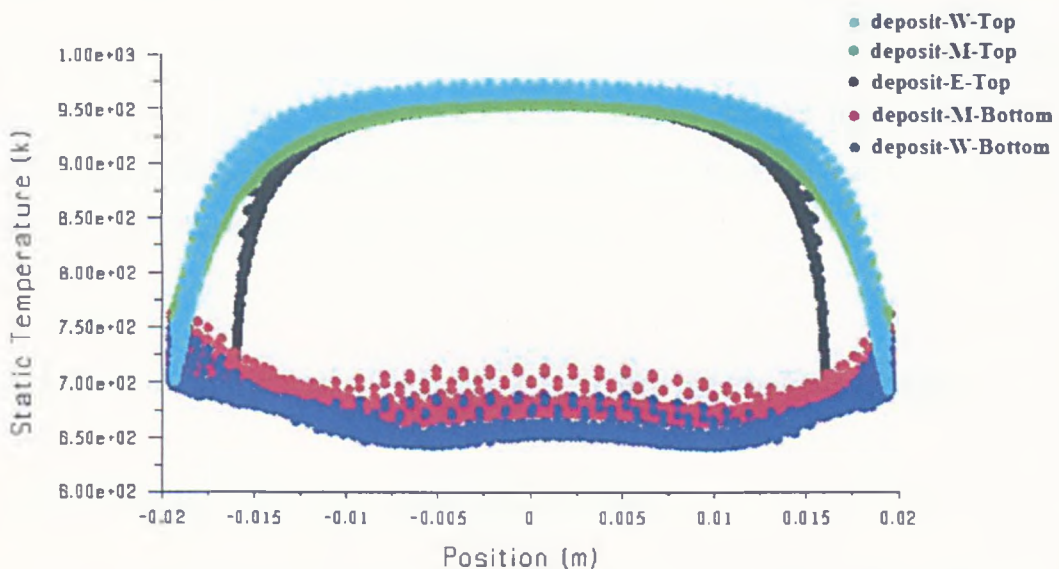


Figure 6.26 Surface temperatures (K) of deposits in model 'sampling probe No.2'

Table 6.15 The average values of deposit surface temperatures from model ‘sampling probe No.2’

Deposit Temperature		2inch tube	Baffle Wall	Wall section	Middle section	End section	Baffle End
K	Top	951	879	871	869	889	885
	Bottom	809		673	692	NA	
°C	Top	678	606	598	596	616	612
	Bottom	536		400	419	NA	

The surface temperatures of the deposits depended on the thickness of the deposit layer and its position on the probe. In general, the top part of the deposits had a higher surface temperature being at 904 – 953 K (631 – 680°C) compared to the bottom part which had a temperature range of 762 – 815 K (489 – 542°C). However, the deposits located closer to the wall did not had a lower surface temperature compared to the one located further from the wall. This means that the thickness of the deposits was more significant than the locations of deposits on the probe.

The highest surface temperature was found to be 951 K (678°C) on the 2inch tube. The surface temperatures of deposits on the baffles were also very high ranging from 879 to 885 K (606 – 612°C). This was due to the small contact area for heat transfer of the baffles with the main probe.

The coated coupons, located at 0.72 m and 1.25 m from the wall, were covered by the deposits according to the experimental findings. Results from this modelling work indicated that the deposits at 0.72 m and 1.25 m from wall had a temperature of 871 K (598°C) and 894 K (621°C) respectively.

6.6 Two-dimensional modelling of the sampling probe

6.6.1 Effects of welded sacrificial baffles

The effects of the baffle installation by welding it to the tube surface were further investigated in 2D modelling. The baffle is used to prevent particles from depositing on the tube surface and it was considered for use as a protection for corrosion.

However, the installation of the baffle by welding it to the tube is suspected to induce more corrosion since the contact area from welding had a higher temperature compared to the rest of the outer tube surface. The temperature of the baffle itself should be very high since there was no source of heat transfer by cooler fluid, also due to the surface area contacting the tube being too small. Therefore, this modelling was used to show the temperature difference between the tube surface and the area where the baffle was attached. The input information for this modelling was the same as that for the sampling probe No.1 model. The temperature difference results are summarized in Table 6.16.

Table 6.16 Average temperatures on surface of tube equipped with a baffle in 2-D modelling (K)

Material Temperature	Alloy 59	Alloy 556	Alloy 625
Temperature of exposed surface	791	826	790
Temperature of area contacted to baffle	805	838	803
Temperature at the baffle surface	942	943	941
Temperature of surface area behind the baffle	567	583	566
% temperature increase at the welding	1.77	1.45	1.64

The results show that the average surface temperature of the alloy tube was lower than the average temperature of the surface contacted by the baffle. The velocity vectors and temperature contours are shown in Figure 6.27 and Figure 6.28 respectively.

In summary, when baffle was welded to the tube surface, the baffle itself could induce more damage to the tube surface where it was attached. This was due to the higher temperature at the contact region. Therefore, although the baffle is useful in diverting particles from accumulating on the tube, the method of installation has to be carefully considered.

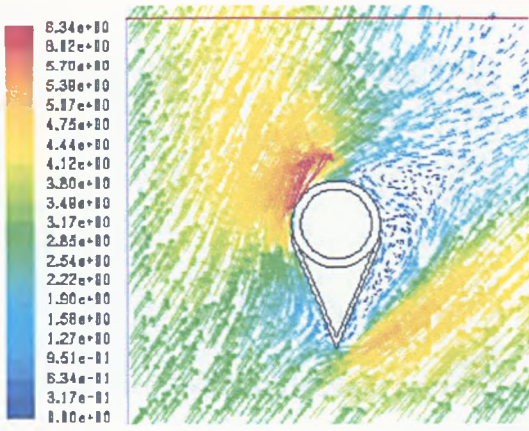


Figure 6.27 Velocity vectors of the flow passing the baffle for 2-D modelling

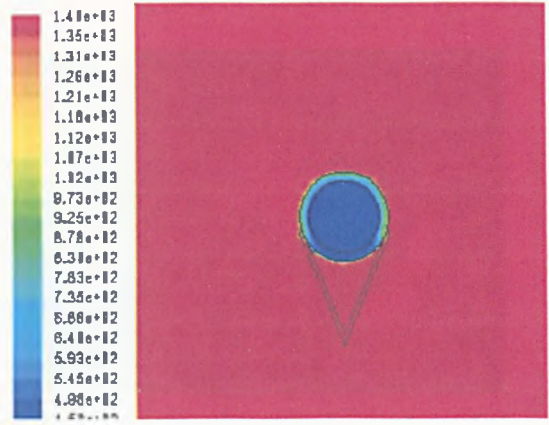


Figure 6.28 Temperature contour of the tube and connected baffle for 2-D modelling

6.6.2 Effects of the particle size on the particle trajectory

The discrete particle model was used in FLUENT to investigate the trajectory of particles as they pass across the sampling probe equipped with a baffle. Three different particles sizes were studied: 1 μm , 10 μm and 100 μm . These particles were also assumed to be CaO which was inert. All particles were assumed to be spherical with a uniform diameter. The model was based on the assumption that particles travelled at an initial velocity equal to the gas stream with a particle loading of 0.01 kg/s. For the simulation of turbulent dispersion, the discrete random walk model was used for stochastic tracking. The input data for the hot gas stream was the same as for 3D modelling for sampling probe No.1.

The particle tracks coloured by the residence time in the system and the velocity magnitude for particles with different diameters (1 μm , 10 μm and 100 μm) are shown in Figure 6.29 – Figure 6.34.

The results show that particles with a smaller diameter spend a longer time when travelling through the system compared to particles with a larger diameter. The vortex that occurs in the flow field increases the residence time of the particles. Smaller particles tended to stay at the back of the baffle where the velocity of the flow is the lowest.

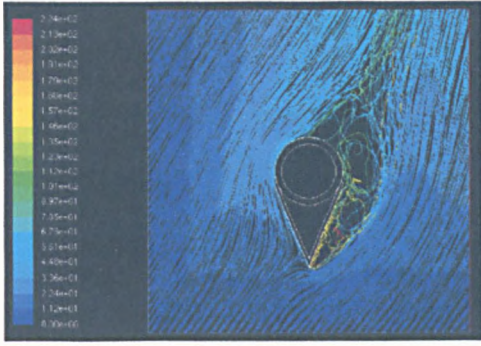


Figure 6.29 Particle tracks coloured by particle residence time: particles with diameter of 1 μm

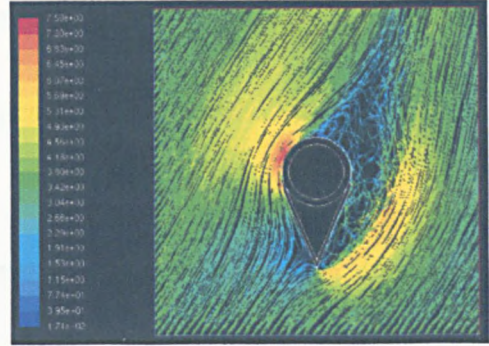


Figure 6.30 Particle tracks coloured by velocity magnitude: particles with diameter of 1 μm

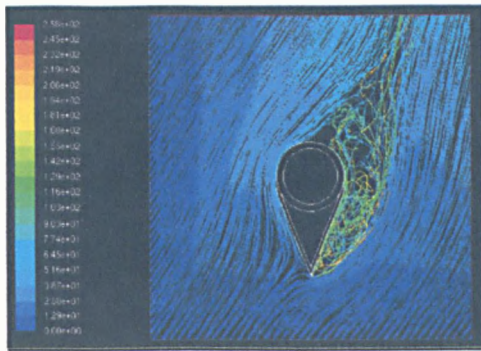


Figure 6.31 Particle tracks coloured by particle residence time: particles with diameter of 10 μm

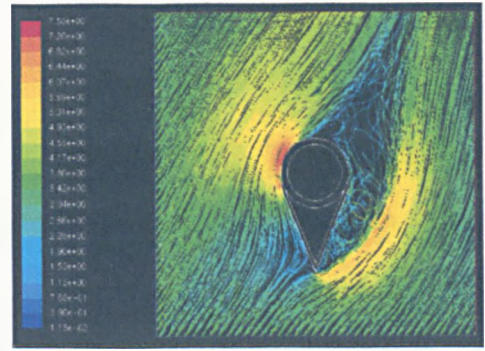


Figure 6.32 Particle tracks coloured by velocity magnitude: particles with diameter of 10 μm

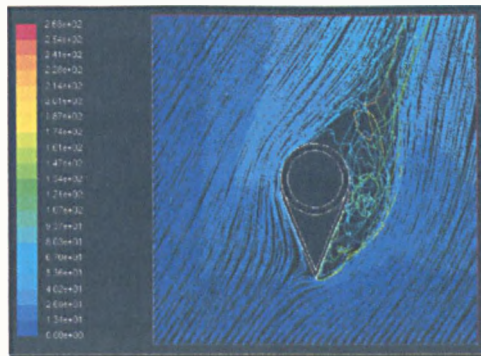


Figure 6.33 Particle tracks coloured by particle residence time: particles with diameter of 100 μm

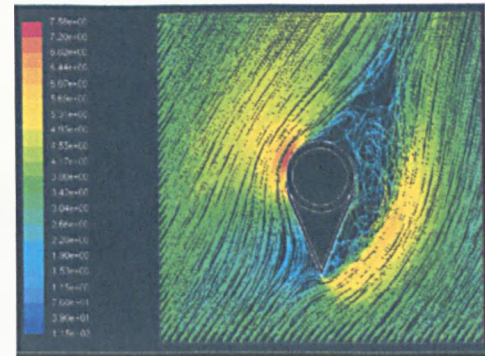


Figure 6.34 Particle tracks coloured by velocity magnitude: particles with diameter of 100 μm

6.7 Summary of the results from sampling probe models

The results for air temperature at different locations for both models are presented in Table 6.17 (for K) and Table 18 (for °C).

Table 6.17 Average temperatures of the air at different locations – comparison of 2 models (K)

Location	Sampling probe No.1		Sampling probe No.2	
	Without deposits	With deposits	Without deposits	With deposit
Wall section	326	322	316	314
Middle section	384	373	366	359
End section	441	424	415	402

Table 6.18 Average temperatures of the air at different locations – comparison of 2 models (°C)

Location	Sampling probe No.1		Sampling probe No.2	
	Without deposits	With deposits	Without deposits	With deposit
Wall section	53	49	43	41
Middle section	111	100	93	86
End section	168	151	142	129

The results for the surface temperatures of metal alloys at different locations on the probes are shown in Table 6.19 (for K) and Table 6.20 (for °C).

Table 6.19 Temperatures of the metal surface at different locations—comparison of 2 models (K)

Location	Sampling probe No.1		Sampling probe No.2	
	Without deposits	With deposits	Without deposits	With deposit
Wall section	725 – 769	677 – 700	670 – 707	636 – 651
Middle section	750 – 792	708 – 735	693 – 726	659 – 674
End section	777 – 816	742 – 768	714 – 747	691 – 713

Table 6.20 Temperatures of the metal surface at different locations—comparison of 2 models(°C)

Location	Sampling probe No.1		Sampling probe No.2	
	Without deposits	With deposits	Without deposits	With deposit
Wall section	452 – 496	404 – 427	397 – 434	363 – 378
Middle section	477 – 519	435 – 462	420 – 453	386 – 401
End section	504 – 543	469 – 495	441 – 474	418 – 440

The surface temperatures of deposits at different locations on the probes are presented in Table 6.21 (for K) and Table 6.22 (for °C).

Table 6.21 Surface temperatures of the deposits at different locations – comparison of 2 models (K)

Location	Sampling probe No.1	Sampling probe No.2
Wall section	762 – 953	673 – 871
Middle section	787 – 914	692 – 869
End section	815 – 904	889

Table 6.22 Surface temperatures of the deposits at different locations – comparison of 2 models (°C)

Location	Sampling probe No.1	Sampling probe No.2
Wall section	489 – 680	400 – 598
Middle section	514 – 641	429 – 596
End section	542 – 631	616

FLUENT code modelling work was successfully conducted and the results can be used to help explain the factors affecting corrosion of the heat exchanger material in a waste to energy plant. The effects of combustion gas characteristics on the deposition of particles and the temperatures of probes were demonstrated. The individual heat transfer ability of different alloys was shown to depend mainly on their thermal conductivity properties. However, the surface temperature of alloys depends on (1) their thermal conductivity, (2) nearby materials, (3) positions on the sampling probe, and (4) the existence of deposits.

In summary, the air-cooled sampling probe No.1 and probe No.2 could provide suitable temperature conditions for this study with an average air temperature of 192 K(°C) and 164 K(°C) respectively. The accumulation of deposit, typically having a thermal conductivity less than 5 W/m-K, significantly decreased the temperature of the heat exchanger tube.

The surface temperatures of alloys for the model ‘probe No.1 without deposits’ were varied from 725 to 816 K (452 – 543°C). These surface temperatures were reduced

to 677 – 768 K (404 – 495°C) when the probe was modelled with the particle deposition. Similarly, the surface temperatures of alloy rings in the model ‘probe No.2 without deposits’ ranged from 670 – 747 K (397 – 474°C) whereas lower values, 636 – 713 K (363 – 440°C), were found in the model ‘probe No.2 with deposits’.

The surface temperature of the deposits could be as high as 953 K (680°C) and 889 K (616°C) for probe No.1 and probe No.2 respectively. These temperatures were higher than the melting points of various eutectic Alkali-Chloride compounds. Therefore, the sampling probes could suffer from deposit-induced corrosions.

Finally, sacrificial baffles could be used for diverting the flow and therefore protect the materials from erosion and corrosion. However, welding the baffle directly on the material surface increased the surface temperature, and could lead to severe local corrosion. Therefore a better design of the baffles is necessary to optimise the stagnant conditions of particle-laden flow.

CHAPTER 7

OVERALL DISCUSSION

The research for this PhD study, including the experiments, the analytical work and the mathematical modelling, was carried out successfully. The results from the mathematical modelling correspond with the information received from the experiments. The results of the experiments extensively explain the factors affecting the high temperature corrosion in the furnace. The investigation into the performance of different types of material and the corrosion control methods yielded satisfactory findings.

This chapter brings these results together to present an overall discussion about the high temperature corrosion in the waste to energy plant.

7.1 Flue Gas Characteristics in the Superheater Areas

The mathematical simulation by using FLIC and FLUENT codes showed that the chemical composition of the flue gas at the position of probe No.1 and the gas composition at the end of the superheater panels were similar. The average flue gas composition are 16.1% CO₂, 7.7% O₂, 11.2% H₂O, 65.0% N₂ by weight, or 10.3% CO₂, 6.8% O₂, 17.7% H₂O, 65.1% N₂ as mole fraction. The average temperature of flue gas at the position of probe No.1 is 871°C and reduces to 586°C.

The condition in the furnace is therefore an oxidizing environment; high in O₂ and CO₂ which are favorable conditions for high temperature corrosion. The presence of steam is known to accelerate the active corrosion. Although the simulation did not consider the concentration of Cl and S in the gas phase, their presence was confirmed in the deposit characterization.

7.2 Characterization of the Combustion Residues and the Probe Deposits

The elemental composition of the combustion residues and deposit found in this study was in the same range as in previous studies (Wiles, 1996; Li et al., 2004; Williams, 2005). The partitioning behavior of metal elements in the furnace was observed. The distribution mechanisms of metals governed by the volatilisation-condensation theory and also the particle formation are explained in articles in the literature (Couch, 1994; Delay et al., 2001; Obernberger and Brunner, 2005). The high boiling point elements such as Al, Ba, Be, Ca, Co, Fe, K, Mg, Si, Sr, Ti were found mainly in the fly ash matrix or the bottom ash. Low boiling point elements such as As, Cd, Cu, Ga, Pb, Sb, Zn and Se are often in the gas phase. They are detected on the fly ash surface as they condense while the gas streams cool down, or when these elements have enough partial pressure.

The presence of chlorides (HCl and Cl₂) and SO₂ in the combustion gas stream and the volatilized metals can lead to the formation of metal chloride or metal sulphate compounds. These particles can either condense directly on the surface of the heat exchanger and the waterwall or condense on the fly ash matrix. The deposit collected from the waterwall surface (1st pass) and the superheater area therefore contained a high concentration of these metal chlorides and metal sulphates.

The high concentration of S (up to 9.17% in the waterwall slag, up to 7.57% in the superheater deposit) and Cl (up to 15.50% in the waterwall slag, up to 11.10% in the superheater deposit) in these deposits indicates a very corrosive environment on the heat exchanger surfaces. Study has shown that alkali chlorides were more corrosive and play a more serious role in hot corrosion compared to sulphate compounds (Tsaour et al., 2005b). The discovery of Pb and Zn in the slag (up to 5.5% for Pb, and 3.6% for Zn) and in the superheater deposit (up to 0.6% for Pb, and 2.0% for Zn) indicates that hot corrosion due to the molten salts on the superheater tubes possibly occurred. The chlorides of Pb and Zn (PbCl₂ and ZnCl₂) can form binary mixtures with other species especially alkali metals creating compounds with lower melting temperatures.

The superheater deposit was contaminated by a higher concentration of Fe. The porous un-protective oxide layer on the superheater tube in this plant was found to be very thick and brittle. The thickness of this spalled layer is in a range of 2 – 4 mm. It confirmed that a serious corrosion problem occurs due to the present use of steel 15Mo3. The deposit from the economiser area contains a similar range of Cl and S but a lower concentration of heavy metals. The corrosion on the economiser is not serious because the gas temperature entering the economiser section is about 310°C. Superheater tubes located in areas with gas temperatures of 730 - 791°C were more prone to high temperature corrosion, especially in the form of hot corrosion.

The elemental compositions of deposits on the sampling probes were similar to the characteristics of the deposit collected from the surroundings. The major elements in the probes' deposit are Cl, S, K, Na, Al and Ca. These elements were also found in the corrosion products of alloys where Zn and Pb were present in a significant amount. SEM micrographs reveal that compounds containing Zn, Pb and Cl were present at the metal/oxide layer interface and in the crevices or pits. They contribute significantly to the corrosion of the tested alloys.

The concentrations of Cl in the probes' deposits were generally higher than in the surrounding deposits (up to 27.31% in probe No.1, and up to 23.26% in probe No.2). This is due to the lower surface temperature of probes compared to the water walls or the operating superheater tubes. The surface temperature of the sampling probe No.1 and probe No.2 ranged from 404 – 495°C and 363 – 440°C respectively. This induces more condensation of gas phases, and also increases the particle deposition by thermophoresis.

These deposits were analysed by DTA and the results showed that the deposit on the superheater possibly had a melting temperature at 272°C. However, the melting temperatures of these deposits generally fall in the range of 524 – 683°C. These results were almost in the same range as another study that reports melting temperatures of 484 – 555°C (Kawahara, 2002). Since the surface temperatures of the deposits were calculated to be 489 – 680°C for probe No.1 and 400 – 616°C for probe No.2, the sampling probes were likely to experience liquid phase corrosion, or hot corrosion.

7.3 Effects of Gas Stream Characteristics, Deposition and Alloy Temperatures

7.3.1 Gas Stream Characteristics and Deposition

The direction of the gas stream and the arrangement of the heat exchanger tubes are among the most important factors determining the particle deposition on the tubes. Other major factors include the characteristics of the fuels, fly ash and aerosols, the operating conditions of the furnace and the conditions of the heat transfer surface (Wang and Harb, 1997; Coulson et al., 1999; Joller et al., 2007).

The structure and the thickness of the deposit on both probes corresponded to the direction of gas stream. On the front side of the probe (directly facing the flow) lies the thickest portion of the deposits. The particles on this side have various sizes and types. The spherical particles of CaSiO_2 and CaCl_2 having diameters of 50 – 100 μm were frequently detected under the SEM at about 100 μm from the alloy surface. The main mechanisms governing particle deposition on this side of the probe are the inertia-controlled transport and the gravity effects (for the situation of probe No.2). The rear side of the probe was covered by a thin layer of deposit, which consisted of only fine particles. These particles are transported to the probe surface mainly by the eddy turbulence.

For both sides of the probe, the deposit at the deposit/scale interface was present as a layer of dense fine particles. These particles firmly attach to the scale and are present in the mix matrix with porous oxide layer. This suggests that the preliminary mechanisms of deposition involve the condensation of aerosols on the cold surface all around the probe. This mechanism is not limited to any side of the probe.

The temperatures of both the gas stream and the alloys play a vital role in particle deposition. The particles found in the deposit of probe No.2 consist of particles having a wide size range. As the flue gas travels from the position of probe No.1, the particles are formed through various mechanisms such as; ash condensation, agglomeration, and solidification promoted by the reducing temperature and longer residence time. The temperature of the gas stream cools down from 871°C

(modelling result) at the position of probe No.1 to 717°C (modelling result) at the position of probe No.2. Furthermore, the lower surface temperature of probe No.2 (363 – 440°C from modelling) compared to that of probe No.1 (404 – 495°C from modelling) enhances the liquid aerosol condensation. This can result in a sticky surface of the deposit, which can further trap a larger amount of particles.

7.3.2 Deposit and Alloy Temperatures

The temperature of the alloy has a significant effect on its corrosion. The metal temperature not only influences the accumulation of deposits, but also significantly affects the rate of corrosion reactions. Deposit accumulation on the other hand can reduce the alloy temperatures.

a. Comparison of results for the same ring: with and without deposit

The probe areas covered by the deposit were found to have a thicker layer of scale of corrosion products compared to the opposite side. The corrosion products on the rear side (thin deposit) probably fell off as it is a spalled porous layer. Corrosion rate measurements show that the alloy on the rear side of the probe (covered by a thin layer of deposit) was more corroded.

The build-up of deposit increases the possibility of molten material formation, which leads to severe corrosion of alloys. On the other hand, a thick layer of deposit can protect the alloy surface from further active oxidation and prevent the volatilization of metal chloride. Once a reducing condition is formed, the corrosion rate will be parabolic with time (Nielsen et al., 2000). Furthermore, the thickness of deposit can reduce the surface temperature of areas which it covers. Therefore, the rear side of the probe where deposit is barely present has a higher rate of corrosion reactions.

b. Comparison of results for two sampling probes: at different positions in the furnace

The deposit on probe No.2 was generally thicker (16 – 40 mm) than the deposit on probe No.1 (7 – 35 mm) and the corrosion rates for probe No.2 accounting for 0.64 – 3.10 mm/yr was lower than the rates of probe No.1 which was 0.17 – 3.91 mm/yr.

The morphology of corroded areas from probe No.1 is rougher and contains more pits and crevices than the alloy surface of probe No.2. The average surface temperatures of alloy on probe No.1 and probe No.2 were calculated from modelling work to be 448°C and 397°C respectively. This yields a temperature difference of approximately 50°C.

These results showed that the particle deposition does not cause severe corrosion as long as the temperature of the alloy and the deposits do not exceed their melting points. Additionally, the thicker layer of deposit provides the lower surface temperatures for the alloys. Hence, the corrosion rates in probe No.2 were lower.

c. Comparison of results for the same probe: wall, middle and end section

The results of corrosion rate measurements and the morphology study revealed that the alloys at the end section of probe No.1 had higher corrosion rates compared to the wall section. This is due to the higher temperature of the alloy, and the lower amount of deposit at the end section. The temperature difference between alloys at the end and wall section is approximately 66°C (modelling result). The average deposit thickness at the wall and the end section were 12 and 6 mm respectively.

The effect of deposit thickness may exceed the effect of temperature at the lower operating temperature. This is proved by the results for probe No.2 showing higher corrosion rates in the wall section (2.62 – 3.10 mm/yr) for alloy 556 compared to the end section (1.34 – 2.60 mm/yr). The temperature difference between alloys at the end and wall section is approximately 58°C (modelling result). The average deposit thickness at the wall and the end section were 24 and 16 mm respectively. In this case increasing the thickness of the deposit layer intensifies the partial pressure of the corrosive substances at the deposit/metal interface, which results in a higher corrosion rate.

7.4 Effects of Heat Transfer Materials (Alloy 59, 556 and 625)

7.4.1 Morphology of the Corroded Areas

The morphology of the corroded areas on alloy 59 and alloy 625 are similar. The localized corrosion, such as deep pits and crevices, is frequently noticed especially in probe No.1. The severity of corrosion is slightly higher in alloy 59. The depth of the pits in alloy 59 was up to 100 μm , while the maximum depth of the pits in alloy 625 was only 50 μm . Some pits were detected occurring along the grain boundary. Therefore, the most important corrosion modes of these alloys are the intergranular corrosion, crevice corrosion and pitting corrosion.

The form of corrosion in high alloyed steel 556 is generally uniform. The corroded areas were relatively smooth compared to the Ni-based alloy. No deep pits were detected. The depth of crevices was less than 10 micron.

7.4.2 Corrosion Rates

The experiment using the sampling probes shows that the Ni-based alloys (alloy 59, and alloy 625) have a lower corrosion rate than the high alloyed steel (alloy 556). The corrosion rates of alloy 625 are slightly lower than that of alloy 59.

The summary of the results is as follows:

In the flue gas temperature range of 754 – 813°C (calculated metal temperature range of 404 – 495°C) and the exposure time of 769 hours, the average corrosion rates of alloy 59, alloy 556, and alloy 625 are 2.69, 3.48 and 0.32 mm/yr, respectively.

At the flue gas temperature range of 730 – 791°C (calculated metal temperature range of 363 – 440°C) and the exposure time of 811 hours, the average corrosion rates of alloy 59, alloy 556, and alloy 625 are 0.88, 1.97 and 0.74 mm/yr, respectively.

As a caution, one should note that the very low corrosion rates measured for alloy 625 from the test of sampling probe No.1 had errors. The errors are due to (1) the

cutting which distorted and expanded the alloy cross sectional area and (2) the alloys' arrangement in the resin during the sample preparation.

7.4.3 Overall Performance for Corrosion Resistance

Alloy 556 is the Fe-Ni-Cr-Co alloy. It has an effective resistance to sulphidizing, carburizing, and Cl-bearing environments at high temperatures. It also has a good oxidation resistance, good fabricability and outstanding high-temperature strength. It has been tested to resist hot corrosion from molten salts, and molten zinc (Mankins et al., 1990). Its corrosion behavior is uniform. Pits and crevice are not detected. However, when it is compared with the Ni-based alloys 59 and 625 in the test environment, its composition containing mainly Fe is a disadvantage. The loss of metal in alloy 556 is noticeably higher than Ni-based alloys.

Both alloy 59 and alloy 625 are Ni-Cr-Mo alloys. Alloy 625 also contains Nb that reacts with Mo to provide the high strength. This type of alloy can resist various corrosive environments and has an excellent resistance to pitting and crevice corrosion (Mankins et al., 1990). The superior performance of alloy 625 compared to alloy 59 may be the result of the lack of Nb, Ta and Ti in alloy 59. These elements help to protect the loss of Cr through intergranular corrosion.

In summary, alloy 556 is inferior to Ni-based alloys in term of corrosion rates, but the evidence of localized corrosion in the Ni-based alloys raises some concern. The corroded depth of alloy 556 into the substrate was up to 344 μm , while the deepest pit detected in alloy 59 was less than 80 μm . Therefore, it can be concluded that the corrosion resistance of alloys are in the order alloy 625 > alloy 59 > alloy 556 under the conditions of this study. In the real application of alloy 59 and alloy 625 as superheater tube materials, the failure of the superheater tube may arise from the undetectable cracks along the grain boundary or the pits which cannot be pre-calculated. On the other hand, engineers may be able to predict its corrosion rate and hence can change the material according to duration of use.

The findings suggest that Ni-based alloy materials are more resistant to the general corrosion in this environment, but they are prone to the localized corrosion notably

from Cl attack. Therefore, the investigation into alternative corrosion control methods such as the use of sacrificial baffles and coating are necessary.

7.4.4 Corrosion Products and Corrosion Mechanisms

a. Corrosion Products of Ni-Based Alloy 59 and 625

The corrosion products of alloy 59 and alloy 625 are composed mainly of NiO, NiCr₂O₄, Cr₂O₃, CrO₂, MoO₂, and MoO₃. Other possible oxides reported from previous studies include Nb₂O₅ (Kawahara, 2002), Fe(Cr, Al)₂O₄, CoCr₂O₄, CoO, SiO₂, TiO₂ (Zhao et al., 2005).

It was noted that the XRD analysis for every alloy sample did not give a clear result of Cr₂O₃. However, its presence was confirmed by the results from the SEM analysis, elemental composition analysis and other literatures. The reason why Cr₂O₃ is not clearly detected might be that Cr was present in a deeper level, and also present in a small amount (1.57 – 1.76 % for alloy 59, 2.48 – 3.48% for alloy 556, and 1.35 – 1.38% for alloy 625) compared to Fe or Ni. Also, Cr₂O₃ is situated

b. Corrosion Products of High Alloyed Steel 556

The thickness of the corrosion products plays a vital role in heat transfer. The corrosion products of alloy 556 were the thickest among the three alloys (up to 2.5 mm for the probe No.1, and 2.0 mm for the probe No.2). This spalling layer is highly porous and detachable. Therefore, superheater tubes made from this type of material can significantly cause the plant to loose the efficiency.

XRD analysis showed that the black corrosion products of alloy 556 comprised Fe₂O₃, Fe₃O₄, FeO(OH), NiO, NiCr₂O₄, Cr₂O₃, and CrO₂. Other possible compounds reported by other studies include K₂Fe₂O₄, ZnCr₂O₄, K₂CrO₄, CrO₄, CrO₂Cl₂ (Li et al., 2003), Cr₃C₂ (Tawancy and Abbas, 1992), FeO(OH), FeO, MoO₃ (Tsaour et al., 2005a), and SiO₂ (Kawahara, 2002).

c. Corrosion Mechanisms

This study does not deeply investigate the high temperature corrosion mechanisms of alloys. However, the results of corrosion product characterization correspond well with the previous studies and therefore the existing models can be used to explain the corrosion process of alloys in this study.

The models of corrosion mechanisms, governing reactions, and thermodynamic consideration are widely discussed elsewhere (Nielsen et al., 2000; Zahs et al., 2000; Ishitsuka and Nose, 2002; Kawahara, 2002). The mechanisms of high temperature corrosion in the presence of the Cl-bearing gas and the deposit having low melting temperatures are summarized as follows:

1. Formation of a protective oxide layer (which is often un-continuous) due to simultaneous contact with oxygen and other corrosive gases,
2. The presence of free Cl and S at the metal surface either derived from the gas phases or the particle deposition,
3. The formation of metal chlorides (such as FeCl_2 , MFe_2Cl_8 when M is divalent metal, CrCl_2 , NiCl_2) which subsequently volatilize through the initial oxide layer,
4. The oxidization of metal chlorides into metal oxides (such as Fe_2O_3 , Fe_3O_4 , Cr_2O_3 , NiO) which is formed as a porous layer in between or on the top of the deposit layer. The oxidization takes place at the position where the partial pressure of oxygen is enough for the reactions. These oxides easily disintegrate and hence the components loose their constituents.
5. The release of free Cl as a product of oxidation which can penetrate through the scale to further oxidize/reduce the metal.

The ability of oxides to prevent the penetration of corrosive deposits are in the following order: $\text{SiO}_2 > \text{Al}_2\text{O}_3 > \text{Cr}_2\text{O}_3 > \text{Fe}_3\text{O}_4 > \text{Fe}_2\text{O}_3$ (Kawahara, 2002). Nevertheless, the stabilities of chlorides of elements are in the following order: $\text{Cr} > \text{Fe} > \text{Ni} \approx \text{Mo}$ at temperature 500 °C. Thus, alloy 556 is more susceptible to corrosion in the Cl-bearing gas, compared to the Ni-based alloy.

Kawahara (2002) also suggests that the stabilities of oxides of elements are in the following order: $\text{Cr} > \text{Mo} \approx \text{Fe} > \text{Ni}$ at 500 °C. This indicates that the corrosion product layer may form by the compounds in this order: NiO (from the topmost), $\text{Fe}_2\text{O}_3 / \text{Fe}_3\text{O}_4 / \text{MoO}_2$, and Cr_2O_3 (close to the metal interface) The thermodynamic equilibrium diagram calculated for the temperature range of 730 – 813 °C will offer a better understanding of the corrosion in this study's conditions.

7.5 Corrosion control by aluminum pack cementation

The aluminide coating significantly improved the corrosion resistance for the selected materials. The coated coupons were mounted at the top of the probe and they were totally covered under the deposit, having a surrounding temperature of (values from mathematical modelling) approximately 487 °C for the end section, and 502 °C for the wall section. After 811 hours of furnace exposure, they were found to be in a better condition than the substrate alloys which were tested at a temperature range of 363 – 440 °C.

The temperature has an influence on the corrosion of coupons especially on the coated alloy 59. The coupons in the end part of the probe are more corroded than the ones at the wall section. There is a tendency for more severity on the top part of coupons, which was not directly contacted with the air-cooled probe. A greater access to the various oxidants in the covering deposits may be one of the reasons.

The degradation of the aluminide coating is triggered by the oxidation/chloridation of aluminized compounds, which results in the formation of interconnecting voids in the coating layer. These voids allow further penetration of molten deposit to the substrate (Tsaur et al., 2005a). Once the aluminide coating is broken, the corrosion mechanisms on the substrate carry on as previously discussed.

7.5.1 Aluminide Coating on Alloy 59

The aluminide coating on alloy 59 after furnace exposure was detected over the entire coupons. The end-section coupon suffered severe corrosion. Its coating was thin and corrosion at the substrate level was widely detected. The coatings on the

wall-section coupon and the lower part of the end-section coupon were corroded to a less extent. There was no significant sign of corrosion at the substrate level of the wall-section coupon. The average thickness of coating was approximately 60 μm .

XRD analysis carried out on the coated alloy 59 coupons show the following compounds: NiAl, NiAl₃, Ni₂Al₃, θ - Al₂O₃, α - Al₂O₃, NiO, Cr₂O₃, CrO₂, MoO₂ and MoO₃. Other possible compounds could be similar to those of alloy 59 as well as Mo₃Al₈ (Houngninou et al., 2004).

The aluminide coating on Ni-based alloys proved to be the most efficient method to prevent high temperature corrosion in the furnace of the WTE plant. The performance of this coating can be enhanced by pre-oxidation prior to the exposure to the corrosive gases. Further investigation into the price and the strength of this material are recommended in order to apply it in the field.

7.5.2 Aluminide Coating on Stainless Steel 310

The coating on the hottest area, i.e. end-section coupon, was mostly oxidized as soon as the test was completed. It was noted that the thickness of the coating on the wall-section coupons was reduced to 10 μm from original thickness 40 – 50 μm .

Crystalline phases on the coated stainless steel 310, detected by XRD analysis, consisted of FeAl, Fe₃Al, NiAl, θ - Al₂O₃, α - Al₂O₃, Fe₂O₃, Fe₃O₄, FeO(OH), NiO, Cr₂O₃ and CrO₂. Other possible compounds could be Fe₂Al₅, FeAl₃Si₃, ferrite, austenite (Tsaur et al., 2005a), FeAl₃, (FeCr)Al, (FeCr)₃Al, (Fe₂Cr)Al, Ni₂Al₃ (Houngninou et al., 2004), Al₇₈Fe₂₄, AlFeO₃ and Ni₃Al (Sharafi and Farhang, 2006).

The aluminide layer on this material was more severely degraded compared to the aluminide coating on alloy 59. This result agrees with the previous study in the laboratory furnace showing that AlFe₃ is not suitable in the Cl bearing oxidizing environment (Tsaur et al., 2005a). Nevertheless, an aluminide coating on steel has a greater resistance to high temperature corrosion compared to the Ni-based alloy 59 and 625. Therefore, it can be a promising alternative material to withstand this corrosive condition. Its advantages include the high temperature strength of the

substrate (steel 310), low cost, low density, and good fabricability. However, the disadvantages of using AlFe_3 at the temperatures higher than 500°C should be noted (Houngninou et al., 2004).

7.6 Corrosion control by using sacrificial baffles

The modelling work shows that baffles can divert the particles from the probe preventing deposition and erosion corrosion. On the contrary, the design of these baffles, which were attached to the tube, was found to be not beneficial under real operation. It generated pockets and recesses for deposit accumulation, and subsequently hot corrosion to take place. The mathematical modelling must consider the condensation of aerosols and use more accurate particle loads in order to achieve a better simulation of this baffle model. A different design, where the baffle is not attached to the tube, is required to optimize the stagnant conditions of particle-laden flow.

The baffles made from austenitic stainless steel 316 were found to be corroded severely. The entire pieces of the baffles were oxidized. This concurs with the fact that the austenitic stainless steel cannot withstand the corrosive conditions in this high temperature furnace. Another important factor increasing its corrosion is the temperature. The baffles did not have enough surface area for heat transfer to the air cooled probes, therefore they are detrimentally influenced by the temperature of the surrounding deposits.

The welding regions that connected the baffles with the probes were oxidized to be thick spalled layers. This agrees with the modelling results showing the higher temperature at the welding points. This finding raises concern about the use of sacrificial baffles in the industry. The welding points possibly become the source of localized corrosion which potentially punctures the superheater tube.

7.7 Problems and Errors

The main problem that emerged in the mathematical work was largely due to the limited memory resource of the program. Simulation of the probe models, especially of the baffle part and the coating specimen, required a very fine mesh that can easily overwhelm the capacity of the program. Therefore, a coarser model was created and the simulation of baffles and coating coupons were avoided in the large probe models. This can result in errors in the calculations, especially for the heat transfer. The results of temperatures in the modelling are possibly lower than the actual temperatures.

The problems and errors during the sample analysis principally come from the (1) transportation of the probes after the experiment, (2) the dismantling of the probes and (3) the cutting of the samples. During these processes the deposit and corrosion products were greatly disturbed. Corrosion products were cracked, spalled off and were affected by the humidity. Cutting caused expansion and distortion of the samples. The solution to these problems may be to use a better design of probe where the samples can be taken from the probe with the minimum damage. Another suggestion is the prompt sample preparation in order to preserve the genuine sample conditions acquired from the furnace exposure.

CHAPTER 8 CONCLUSIONS AND RECOMMENDATIONS FOR FUTURE WORK

8.1 CONCLUSIONS

The study of high temperature corrosion in WTE plants is presented in this PhD thesis. The study project, which consists of; literature reviews, experiments in a UK WTE plant, analytical work and the associated mathematical modelling, was carried out successfully.

The results give a comprehensive understanding about the significance and mechanisms of factors governing the process. The investigation into the performance of proposed corrosion control methods (use of new high grade alloys, aluminide coating, and sacrificial baffles) yielded satisfactory findings. Results from the mathematical modelling correspond with the plant information and explained the experimental results very well. All results pointed out that high temperature corrosion and hot corrosion took place in probes No.1, and to a less extent in probe No.2. The following conclusions can be drawn from this study:

8.1.1 Conditions of Flue Gas at the Sampling Points

1. The average flue gas compositions at the sampling points are 65.1% N₂, 17.7% H₂O, 10.3% CO₂, and 6.8% O₂ by mole. The average temperatures of the flue gas at the sampling point of probe No.1 and probe No.2 were 871°C (754 – 813°C by plant's thermocouple probe), and 717°C (730 – 791°C by plant's thermocouple probe) respectively. Therefore, the sampling points were at a high temperature oxidizing condition.
2. At the position of probe No.1, the velocity vectors of flue gas in the X and Y directions were 2.02 m/s and 2.28 m/s respectively. This resulted in a total velocity of 3.05 m/s with a flow angle of -138.40° to the Y-axis.

3. At the position of probe No.2, the velocity vectors of flue gas in the X and Y directions were 0.41 m/s and -4.81 m/s respectively. This resulted in a total velocity of 4.83 m/s with a flow angle of -4.83° to the Y-axis.

8.1.2 Temperatures of Sampling Probes

1. The temperatures of air inside the probe calculated by modelling are lower than the experimental results. At the end section, the differences are 8.79% for probe No.1 and 22.76% for probe No.2. Therefore, the actual surface temperatures of the alloys are higher than the model-derived values being used in this study.
2. For model probe No.1 with deposits, the surface temperature of the alloys increase from 404 – 427°C at wall section to 469 - 495°C at end section resulting in an average temperature difference of 66°C.
3. For probe No.2, surface temperatures of alloys increase from 363 – 378°C at wall section to 418 - 440°C at end section resulting in an average temperature difference of 58°C.
4. The surface temperatures of alloys are in the following order: 625 > 59 > 556. This is due to their thermal conductivity values (556 > 59 > 625).
5. The accumulation of deposit significantly decreased the temperature of the heat exchanger tube. Models of the probe without deposits shows increases in temperature of 50°C for probe No.1 and 39°C for probe No.2.
6. The surface temperatures of deposits are in range of 489 – 680°C for probe No.1 and 400 – 616°C for probe No.2.

8.1.3 Characterization of Deposits

1. The deposit collected from the waterwall surface (1st pass) and the superheater areas contains a high concentration of alkali metals (K, Na and Ca), heavy metals (Pb and Zn), Cl and S.
2. Deposit from the economizer area, having a lower temperature, contains a similar range of Cl and S but a lower level of heavy metals.
3. Deposit on the sampling probes had a similar elemental composition to the

deposits from the surroundings. The major elements are Cl, S, K, Na, Al and Ca. Elements such as Zn, Pb and Cl were detected in significant amounts in the corrosion products, at the interface of metal/oxide layer, and in crevices or pits.

4. DTA results showed that the deposit from the superheater possibly has a melting temperature at 272°C. However, the melting temperatures of deposits from probes and superheaters generally fall in the range of 524 – 683°C.

8.1.4 Corrosion Products

1. Corrosion products of these alloys are porous and spalled. The thickness of the corrosion products is directly proportional to the thickness of deposit and the alloy temperature. Alloy 556 has a thicker deposit layer than others.
2. Corrosion products of alloy 59 and alloy 625 are composed mainly of NiO, NiCr₂O₄, Cr₂O₃, CrO₂, MoO₂, and MoO₃. The thickness of corrosion products was up to 1 mm for alloy 59, and 0.5 mm for alloy 625.
3. Corrosion products of alloy 556 comprised Fe₂O₃, Fe₃O₄, FeO(OH), NiO, NiCr₂O₄, Cr₂O₃, and CrO₂. The thickness of corrosion products was up to 2 mm.

8.1.5 Effects of Flue Gas Characteristics, Deposition and Alloy Temperatures

1. The structure and the thickness of the deposit on both probes corresponds with the direction of the gas stream. The front side of the probe (directly facing the flow) has the thickest portion of the deposits.
2. The temperature of both the gas stream and the alloy play a vital role in particle deposition. Lower temperatures result in deposition of particles with a wider size range. This is due to the increases in particle formation, thermophoretic transportation, and aerosol condensation on the colder surface.
3. For probe No.1, the average corrosion rates of alloy 59, alloy 556, and alloy 625 are 2.69, 3.48 and 0.32 mm/yr. For probe No.2, the average corrosion rates of alloy 59, alloy 556, and alloy 625 are 0.88, 1.97 and 0.74 mm/yr.
4. The surface temperature of the alloy has a greater influence on the rates of

corrosion than the thickness of deposits.

5. The side of the probe covered under a thick layer of deposit has a lower corrosion rate compared to the side covering by a thin film. The reasons are (1) the thick deposit protects the alloy surface from further active oxidation and prevents the volatilization of metal chlorides and (2) it reduces the surface temperature by acting as a thermal barrier between the hot gas and the metal substrate.

8.1.6 Effects of Heat Transfer Materials

1. The Ni-based alloys (alloy 59 and alloy 625) have a lower corrosion rate than the high alloyed steel (alloy 556). The corrosion rates of alloy 625 are slightly lower than that of alloy 59.
2. The Ni-based alloys are more resistant to the uniform corrosion in this environment, but they are prone to the localized corrosion notably from metal chlorides. Alloy 556 has a higher resistance against pitting and crevice corrosion but its uniform corrosion causes deeper loss of alloy material (up to 344 μm) than alloy 59 (up to 100 μm).
3. The superior performance of alloy 625 compared to alloy 59 may be the result of the lack of niobium, tantalum and titanium in alloy 59. These elements help to protect the loss of Cr through intergranular corrosion.

8.1.7 Corrosion Control by Aluminide Pack Cementation

1. The aluminized coating significantly improved the corrosion resistance for the selected materials - despite being tested under a higher surrounding temperature (surface temperature ranges from modeling results are 363 – 440°C for the alloy rings and 487 - 502°C for the coated coupons).
2. The order of corrosion resistance of materials is as follows: coated alloy 59 > coated steel 310 > alloy 625 > alloy 59 > alloy 556 > steel 316.
3. Temperature significantly affects the corrosion of the coating in the same way as it does for un-coated samples. As the temperature increases, the undamaged

coating region becomes thinner and local penetration to the substrate increases. Penetration of coatings and corrosion of the substrate were detected in the end section coupons (where the temperatures of deposit and coupons were the highest and fluxing hot corrosion by molten salts could occur).

4. Crystalline phases detected from the aluminide coated alloy 59 (after exposure) consist of NiAl, NiAl₃, Ni₂Al₃, θ - Al₂O₃, α - Al₂O₃, NiO, Cr₂O₃, CrO₂, MoO₂ and MoO₃. The thickness of the aluminide coating on alloy 59 was approximately 60 μ m for almost the entire coupon.
5. Crystalline phases detected on the aluminide coated steel 310 consist of FeAl, Fe₃Al, NiAl, θ - Al₂O₃, α - Al₂O₃, Fe₂O₃, Fe₃O₄, NiO, NiCr₂O₄, Cr₂O₃ and CrO₂. The coating layer thickness was variable. It was detected only at the wall section coupons and with a thickness of 10 μ m.

8.1.8 Corrosion Control by Using Sacrificial Baffles

1. This design of baffle generated traps for particle deposition (and subsequently hot corrosion) to take place.
2. The mathematical modelling must consider the condensation of aerosols and use accurate particle loads in order to achieve a better simulation of the baffle model.
3. Welding the baffle directly on the tube increased the surface temperature and led to severe local corrosion. The welding points were oxidized into a thick spalled layer. A better design of the baffles is necessary.
4. Austenitic stainless steel 316 was found to be ineffective as a baffle material and corroded severely since it cannot withstand the corrosive conditions in this high temperature furnace

8.2 RECOMMENDATIONS FOR FUTURE WORK

1. Further investigation into the performance of different types of coatings is recommended. There are many types of coatings available to prevent the high temperature corrosion of metal. However, there are only limited studies showing the result of tests of these coatings in the real operating conditions of WTE

plants. Examples for coatings that can be tested include the aluminide coating with the addition of Zr or Si, and chromized coatings.

2. These coatings could be oxidized by pure oxygen prior to the flue gas exposure. This will help the coating to form a protective oxide layer that is dense and continuous. The pre-oxidized coatings will have a greater corrosion resistance than the coatings oxidized in the mixed-oxidant conditions, especially in the presence of alkali metal, heavy metals, S and Cl.
3. Different designs of baffle should be investigated. It should not be connected by welding with the heat exchanger tubes or with a minimum contact. Further investigations into other grades of low-cost stainless steel with better corrosion resistant properties (such as 310), or of aluminized steels should be carried out.
4. The feasibility study of the applications of these corrosion control techniques (high grade alloys, coatings, and baffles) should be conducted. Various aspects including the strength of material, the capital cost and the maintenance cost, the reliability, and the accessibility of technology should be considered. This will give a better outlook for their industrial application.
5. The mathematical modelling results can be improved by using a finer mesh. It is better to dissect a large scale and complicated model into several sub-models. The output data from the large model will be the input for the smaller models having a finer mesh.
6. Different designs of sampling probe (that can be more easily dis-assembled after environmental exposure) are encouraged, in order to (1) avoid or minimize the cutting of alloy samples, and (2) prevent the breaking or spallation of the layer of deposit and corrosion products.

REFERENCES

- AK Steel (2000). *316/316L stainless steel (UNS S31600/S31603). Product Data Sheet*. Ohio: AK Steel Corporation.
http://www.aksteel.com/pdf/markets_products/stainless/austenitic/316_316L_Data_Sheet.pdf. [Accessed 5 July 2007].
- Arvelakis, S. & Frandsen, F.J. (2005). "Study on analysis and characterization methods for ash material from incineration plants". *Fuel*, 84 (14-15), pp. 1725-1738.
- Baxter, L.L., Miles, T.R., Jenkins, B.M., Milne, T., Dayton, D., Bryers, R.W. & Oden, L.L. (1998). "The behavior of inorganic material in biomass-fired power boilers: field and laboratory experiences". *Fuel Processing Technology*, 54 (1-3), pp. 47-78.
- Bernath, P., Sinquefield, S.A., Baxter, L.L., Sclipa, G., Rohlfing, C.M. & Barfield, M. (1998). "In situ analysis of ash deposits from black liquor combustion". *Vibrational Spectroscopy*, 16 (2), pp. 95-103.
- Callister, W.D. (2007). *Materials Science and Engineering: An Introduction*. 7th edn., pp. 621-664. New York: John Wiley & Sons, Inc. ISBN: 9780471736967.
- Couch, G. (1994). *Understanding Slagging and Fouling in PF Combustion*. IEA Coal Research. Report No. IEACR/72. ISBN: 9789290292401.
- Coulson, J.M., Richardson, J.F., Backhurst, J.R. & Harker, J.H. (1999). *Coulson and Richardson's Chemical Engineering: Fluid Flow, Heat transfer and Mass Transfer*. 6th edn., Vol. 1, pp. 379-570. Oxford : Elsevier Butterworth-Heinemann. ISBN: 9780750644440.
- Delay, I., Swithenbank, J. & Argent, B.B. (2001). "Prediction of the distribution of alkali and trace elements between the condensed and gaseous phases generated during clinical waste incineration". *Journal of Alloys and Compounds*, 320 (2), pp. 282-295.
- E-Pipe Co.Ltd. (2007). *DIN 17175-79 seamless steel tubes for elevated temperatures (DIN17175-79). Pipe/Tube Standard Data*. E-Pipe Co.,Ltd. <http://www.e-pipe.co.kr/eng/DIN/17175.htm>. [Accessed 21 December 2007].
- European Communities (2007). *Renewables Make the Difference*. Belgium: Office for Official Publications of the European Communities.
http://ec.europa.eu/energy/climate_actions/doc/brochure/2008_res_brochure_en.pdf. [Accessed 20 December 2007]. ISBN: 9789279063619.
- Fichera, M., Leonardi, R. & Farina, C.A. (1987). "Fuel ash corrosion and its prevention with MgO addition". *Electrochimica Acta*, 32 (6), pp. 955-960.

- Frandsen, F.J. (2005). "Utilizing biomass and waste for power production - A decade of contributing to the understanding, interpretation and analysis of deposits and corrosion products". *Fuel*, 84 (10), pp. 1277-1294.
- Goddard, C.D. (2006). *Mathematical Modelling of a Waste-to-Energy Plant*. Doctor of Philosophy Thesis, Department of Chemical and Process Engineering, The University of Sheffield.
- Goldstein, I.J. (1974). "Metallography - A practical tool for correlating the structures and properties of materials". In: ASTM (ed.), *ASTM Special Technical Publication No.557*, pp. 86. ASTM.
- Grabke, H.J. (1991). "Fundamental mechanisms of the attack of chlorine HCl and chlorides on steels and high Temperature alloys in the temperature range 400 to 900°C". In: Bryers, R.W. (ed.), *Incinerating Municipal and Industrial Waste: Fireside problems and prospects for improvement*, pp. 161 - 176. New York: Hemisphere Pub. Corp. ISBN: 9781560321453.
- Hansen, L.A., Nielsen, H.P., Frandsen, F.J., Dam-Johansen, K., Horlyck, S. & Karlsson, A. (2000). "Influence of deposit formation on corrosion at a straw-fired boiler". *Fuel Processing Technology*, 64 (1-3), pp. 189-209.
- Haynes International Inc. (1998a). *Haynes 556 alloy (H-3013E). High Temperature Alloys*. Haynes International. <http://www.inkosas.cz/haynes/hay556.pdf>. [Accessed 7 July 2007].
- Haynes International Inc. (1998b). *Haynes 625 alloy (H-3073C). High Temperature Alloys*. Haynes International. <http://www.inkosas.cz/haynes/hay625.pdf>. [Accessed 7 July 2007].
- Ho, K. & Doane, E.P. (2002). "Current evidence concerning coal chlorine content and fireside corrosion in coal-fired PC and fluidized bed boilers". *Fuel and Energy Abstracts*, 43 (3), pp. 203-204.
- Holman, J.P. (2001). *Heat Transfer, McGraw-Hill Series in Mechanical Engineering*. 9th edn., pp. 511-574. New York: McGraw-Hill Higher Education. ISBN: 9780071122306.
- Houngninou, C., Chevalier, S. & Larpin, J.P. (2004). "Synthesis and characterisation of pack cemented aluminide coatings on metals". *Applied Surface Science*, 236 (1-4), pp. 256-269.
- Ilander, A. & Vaisanen, A. (2007). "An ultrasound-assisted digestion method for the determination of toxic element concentrations in ash samples by inductively coupled plasma optical emission spectrometry". *Analytica Chimica Acta*, 602 (2), pp. 195-201.
- Incropera, F.P. & De Witt, D.P. (1990). *Introduction to Heat Transfer*. 2nd edn., pp. 597-652. New York: John Wiley & Sons. ISBN: 9780471612476.
- Ishitsuka, T. & Nose, K. (2002). "Stability of protective oxide films in waste incineration environment - Solubility measurement of oxides in molten chlorides". *Corrosion Science*, 44 (2), pp. 247-263.
- Joller, M., Brunner, T. & Obernberger, I. (2007). "Modeling of aerosol formation during biomass combustion for various furnace and boiler types". *Fuel Processing Technology*, 88 (11-12), pp. 1136-1147.

- Juzon, P., Ziemnicka, M., Chevalier, S., Przybylski, K. & Larpin, J.P. (2007). "Improving Fe₃Al alloy resistance against high temperature oxidation by pack cementation process". *Applied Surface Science*, 253 (11), pp. 4928-4934.
- Kaer, S.K., Rosendahl, L.A. & Baxter, L.L. (2006). "Towards a CFD-based mechanistic deposit formation model for straw-fired boilers". *Fuel*, 85 (5-6), pp. 833-848.
- Kawahara, Y. (2002). "High temperature corrosion mechanisms and effect of alloying elements for materials used in waste incineration environment". *Corrosion Science*, 44 (2), pp. 223-245.
- Klasen, T. & Gorner, K. (2000). "The Use of CFD for the Prediction of Problem Areas Inside a Waste Incinerator with Regards to Slagging, Fouling and Corrosion". *5th European Conference on Industrial Boilers and Furnaces (INFUB)*, 11 - 14 April 2000. Porto, Portugal. ISBN: 9728034040.
- Lai, G.Y. (1990). *High Temperature Corrosion of Engineering Alloys*. pp. 1-4. Ohio: ASM International. ISBN: 9780871704115.
- Levenspiel, O. (1972). *Chemical Reaction Engineering*. pp. 1-40. New York: John Wiley & Sons. ISBN: 9780471530190.
- Li, L., Duan, Y., Cao, Y., Chu, P., Carty, R. & Pan, W.P. (2007). "Field corrosion tests for a low chromium steel carried out at superheater area of a utility boiler with three coals containing different chlorine contents". *Fuel Processing Technology*, 88 (4), pp. 387-392.
- Li, M., Xiang, J., Hu, S., Sun, L.S., Su, S., Li, P.S. & Sun, X.X. (2004). "Characterization of solid residues from municipal solid waste incinerator". *Fuel*, 83 (10), pp. 1397-1405.
- Li, Y.S., Niu, Y. & Wu, W.T. (2003). "Accelerated corrosion of pure Fe, Ni, Cr and several Fe-based alloys induced by ZnCl₂-KCl at 450°C in oxidizing environment". *Materials Science and Engineering A*, 345 (1-2), pp. 64-71.
- Mankins, W.L., Lamb, S. & Inco Alloys International Inc. (1990). "Nickel and nickel alloys ". In: International, A. (ed.), *Metals Handbook*, Vol. 2, pp. 428-445. Ohio: ASM International. ISBN: 9780871703781.
- Martin GmbH (2007). *Reverse-acting grate. Technologies*. The MARTIN System for Thermal Waste Treatment.
http://www.martingmbh.de/index_en.php?level=2&CatID=6.24&inhalt_id=20. [Accessed 20 December 2007].
- McKendry, P. (2002). "Energy production from biomass (part 2): Conversion technologies". *Bioresource Technology*, 83 (1), pp. 47-54.
- Meadowcroft, D.B. (1987). "High temperature corrosion of alloys and coatings in oil- and coal-fired boilers". *Materials Science and Engineering*, 88, pp. 313-320.
- Michelsen, H.P., Frandsen, F., Dam Johansen, K. & Larsen, O.H. (1998). "Deposition and high temperature corrosion in a 10 MW straw fired boiler". *Fuel Processing Technology*, 54 (1-3), pp. 95-108.

- Mohanty, B.P. & Shores, D.A. (2004). "Role of chlorides in hot corrosion of a cast Fe-Cr-Ni alloy. Part I: Experimental studies". *Corrosion Science*, 46 (12), pp. 2893-2907.
- NACE International (2002). *Corrosion Costs and Preventive Strategies in the United States. The National Association of Corrosion Engineers* [Online]. http://www.nace.org/nace/content/publicaffairs/cost_corr_pres/cost_corrosion_files/frame.htm. [Accessed January 2008].
- Natesan, K. (1993). "Applications of coatings in coal-fired energy systems". *Surface and Coatings Technology*, 56 (3), pp. 185-197.
- Nielsen, H.P., Frandsen, F.J. & Johansen, K.D. (1999). "Lab-scale Investigations of high-temperature corrosion phenomena in straw-fired boilers". *Energy & Fuels*, 13, pp. 1114-1121.
- Nielsen, H.P., Frandsen, F.J., Johansen, K.D. & Baxter, L.L. (2000). "The implications of chlorine-associated corrosion on the operation of biomass-fired boilers". *Progress in Energy and Combustion Science*, 26, pp. 283-298.
- Obernberger, I. & Brunner, T. (2005). "Fly ash and aerosol formation in biomass combustion processes - An Introduction". In: Obernberger, I. & Brunner, T. (eds.), *Aerosol in Biomass Combustion: Formation, characterisation, behaviour, analysis, emissions, health effects.*, Vol. 6, pp. 1 - 11. Medienfabrik Graz, Steiermarkische Landesdruckerei GmbH. ISBN: 9783950198027.
- Office of Public Sector Information (2008). *UK Legislation (1987 - 2008). National Archives* [Online]. <http://www.opsi.gov.uk/>. [Accessed 4 March 2008].
- Oksa, M. (2006). "Material Endurance in Waste Incineration - On-line Monitoring". *Workshop "Research in the Waste Area - Towards the FP7"*, 31 January 2006. Vtt Technical Research Centre of Finland, Brussels. http://www.vtt.fi/palvelut/cluster7/topic7_3/energia_taso3_item5_WI.jsp. [Accessed December 2007].
- Persson, K., Brostrom, M., Carlsson, J., Nordin, A. & Backman, R. (2007). "High temperature corrosion in a 65 MW waste to energy plant". *Fuel Processing Technology*, 88 (11-12), pp. 1178-1182.
- Pettit, F.S. & Goward, G.W. (1983a). "Gas turbine applications". In: Lang, E. (ed.), *Coatings for High Temperature Application*, pp. 341 - 359. Essex: Applied Science Publishers Ltd. ISBN: 9780853342212.
- Pettit, F.S. & Goward, G.W. (1983b). "Oxidation - corrosion - erosion mechanisms of environmental degradation of high temperature materials". In: Lang, E. (ed.), *Coatings for High Temperature Applications*, pp. 1 - 32. Essex: Applied Science Publishers Ltd. ISBN: 9780853342212.
- Phongphiphat, A. (2006). *Micropollutant Emissions from Burning Beds of Biomass and Waste*. Master Degree Thesis, Department of Chemical and Process Engineering The University of Sheffield.
- Poole, D., Argent, B.B., Sharifi, V.N. & Swithenbank, J. (2008). "Prediction of the distribution of alkali and trace elements between the condensed and gaseous phases in a municipal solid waste incinerator". *Fuel*, 87 (7), pp. 1318-1333.

- Rademakers, P., Hesselings, W. & Wetering, J.v.d. (2002). *Review on Corrosion in Waste Incinerators, and Possible Effect of Bromine*. TNO Industrial Technology. Report No. I02/01333/RAD CEF-12.
- Rafaja, D., Dopita, M., Masimov, M., Klemm, V., Wendt, N. & Lengauer, W. (2008). "Analysis of local composition gradients in the hard-phase grains of cermets using a combination of X-ray diffraction and electron microscopy". *International Journal of Refractory Metals and Hard Materials*, 26 (3), pp. 263-275.
- Ryu, C., Yang, Y.B., Khor, A., Yates, N.E., Sharifi, V.N. & Swithenbank, J. (2006). "Effect of fuel properties on biomass combustion: Part I. experiments - fuel type, equivalence ratio and particle size". *Fuel*, 85 (7-8), pp. 1039-1046.
- Sandmeyer Steel Company (2007a). *Alloy 310/310S spec sheet (UNS S31000/UNS S31008). 300 Series Heat Resistant Stainless Steel*. Sandmeter Steel Company. <http://www.sandmeyersteel.com/310-310S.html>. [Accessed 5 July 2007].
- Sandmeyer Steel Company (2007b). *Alloy 316/316L spec sheet (UNS S31600/S31603). 300 Series Austenitic Stainless Steel*. Sandmeter Steel Company. <http://www.sandmeyersteel.com/316-316L.html>. [Accessed 5 July 2007].
- Schutze, M., Malessa, M., Rohr, V. & Weber, T. (2006). "Development of coatings for protection in specific high temperature environments". *Surface and Coatings Technology*, 201 (7), pp. 3872-3879.
- Schweitzer, P.A. (2007). *Fundamentals of Metallic Corrosion: Atmospheric and Media Corrosion of Metals*. 2nd edn., pp. 1-66. Florida: CRS Press (Taylor & Francis Group). ISBN: 9780849382437.
- Sharafi, S. & Farhang, M.R. (2006). "Effect of aluminizing on surface microstructure of an HH309 stainless steel". *Surface and Coatings Technology*, 200 (16-17), pp. 5048-5051.
- Sidhu, T.S., Agrawal, R.D. & Prakash, S. (2005). "Hot corrosion of some superalloys and role of high-velocity oxy-fuel spray coatings - A review". *Surface and Coatings Technology*, 198 (1-3), pp. 441-446.
- Singh, P.M. & Anaya, A. (2007). "Effect of wood species on corrosion behavior of carbon steel and stainless steels in black liquors". *Corrosion Science*, 49 (2), pp. 497-509.
- Sinnott, R.K., Coulson, J.M. & Richardson, J.F. (2005). *Coulson and Richardson's Chemical Engineering: Chemical Engineering Design 4th edn.*, Vol. 6, pp. 634-793. Oxford : Elsevier Butterworth-Heinemann. ISBN: 9780750665384.
- Spirax-Sarco Limited (2007). *Superheated Steam Region - Steam Table*. <http://www.spiraxsarco.com/resources/steam-tables/superheated-steam.asp>. [Accessed 21 December 2007].
- Srikanth, S., Ravikumar, B., Das, S.K., Gopalakrishna, K., Nandakumar, K. & Vijayan, P. (2003). "Analysis of failures in boiler tubes due to fireside corrosion in a waste heat recovery boiler". *Engineering Failure Analysis*, 10 (1), pp. 59-66.

- Stringer, J. (1986). "Role of coatings in energy-producing systems: An overview". In: Streiff, R., Stringer, J., Krutenat, R.C. & Caillet, M. (eds.), *The First International Symposium on High Temperature Corrosion of Materials and Coatings for Energy Systems and Turboengines*, Vol. 1, 7 - 11 July. Elsevier Applied Science Publishers Ltd., Marseille, France. ISBN: 9781851661077.
- Swithenbank, J., Nasserzadeh, V., Wasantakorn, A., Lee, P.H. & Swithenbank, C. (2000). "Future integrated waste, energy and pollution management (WEP) systems exploit pyrotechnology". *Process Safety and Environmental Protection*, 78 (5), pp. 383-398.
- Swithenbank, J., Sharifi, V.N., Yang, Y.B., Ryu, C., Poole, D., Goddard, C. & Gan, S. (2005). "Tracking micro-pollutants from cradle to grave". *9th International Congress on Combustion By-Products and Their Health Effects*, 12 - 15 June. Arizona, USA. <http://www.lsu.edu/piccongress/>.
- Tawancy, H.M. & Abbas, N.M. (1992). "Mechanism of carburization of high - temperature Alloys". *Journal of Materials Science*, 27, pp. 1061 - 1069.
- ThyssenKrupp VDM (2002a). *Nicrofer 5923 hMo - alloy 59 (according to ASTM). Corrosion-Resistant Alloy*. A company of ThyssenKrupp Stainless. http://www.thyssenkrupp-vdm-fareast.com/media/down_datasheets/nicrofer_5923hmo_e.pdf. [Accessed 5 December 2007].
- ThyssenKrupp VDM (2002b). *Nicrofer 6020 hMo - alloy 625 (according to ASTM). Corrosion-Resistant Alloy*. A company of ThyssenKrupp Stainless. http://thyssenkruppvdm.de/pdf/Nicrofer6020hMo_d.pdf. [Accessed 5 December 2007].
- Tsaur, C.C., Rock, J.C. & Chang, Y.Y. (2005a). "The effect of NaCl deposit and thermal cycle on an aluminide layer coated on 310 stainless steel". *Materials Chemistry and Physics*, 91 (2-3), pp. 330-337.
- Tsaur, C.C., Rock, J.C., Wang, C.J. & Su, Y.H. (2005b). "The hot corrosion of 310 stainless steel with pre-coated NaCl/Na₂SO₄ mixtures at 750°C". *Materials Chemistry and Physics*, 89 (2-3), pp. 445-453.
- Uusitalo, M.A., Vuoristo, P.M.J. & Mantyla, T.A. (2004). "High temperature corrosion of coatings and boiler steels below chlorine-containing salt deposits". *Corrosion Science*, 46 (6), pp. 1311-1331.
- Van Beek, M.C., Rindt, C.C.M., Wijers, J.G. & Van Steenhoven, A.A. (2001). "Analysis of fouling in refuse waste incinerators". *Heat transfer engineering*, 22 (1), pp. 22-31.
- Vassilev, S.V. & Braekman-Danheux, C. (1999). "Characterization of refuse-derived char from municipal solid waste: 2. Occurrence, abundance and source of trace elements". *Fuel Processing Technology*, 59 (2-3), pp. 135-161.
- Vencl, A., Ivljanin, B. & Dojcinovic, M. (2004). "Testing of the Mechanical Properties for 15Mo3 Steel". *3rd Youth Symposium on Experimental Solid Mechanics*. Porretta Terma, Italy. <http://www.yesem.ing.unibo.it/yesem2004/Abstracts/Vencl.pdf>. [Accessed 5 July 2007].

- Wall, T.F., Bhattacharya, S.P., Baxter, L.L., Richards, G. & Harb, J.N. (1995). "The character of ash deposits and the thermal performance of furnaces". *Fuel Processing Technology*, 44 (1-3), pp. 143-153.
- Wallinder, I.O., Goidanich, S., Herting, G., Bahar, B. & Midander, K. (2008). *Environmental and Health Aspects of Corrosion-Induced Metal Release From Metals and Alloys*. KTH Royal Institute of Technology, Stockholm [Online]. <http://www.corrosionscience.se/research.php?gid=5>. [Accessed March 2008].
- Wang, C.J. & Pan, J.Y. (2003). "Corrosion of carbon steel with NaCl coating in an atmosphere produced by burning emulsified diesel oil". *Materials Chemistry and Physics*, 82 (3), pp. 965-973.
- Wang, H. & Harb, J.N. (1997). "Modeling of ash deposition in large-scale combustion facilities burning pulverized coal". *Progress in Energy and Combustion Science*, 23 (3), pp. 267-282.
- Wiles, C.C. (1996). "Municipal solid waste combustion ash: State-of-the-knowledge". *Journal of Hazardous Materials*, 47 (1-3), pp. 325-344.
- Williams, P.T. (2005). *Waste Treatment and Disposal*. 2nd edn., pp. 245-324. West Sussex: John Wiley & Sons Ltd. ISBN: 9780470849125.
- Yang, Y.B., Ryu, C., Khor, A., Yates, N.E., Sharifi, V.N. & Swithenbank, J. (2005). "Effect of fuel properties on biomass combustion. Part II. modelling approach - identification of the controlling factors". *Fuel*, 84 (16), pp. 2116-2130.
- Yin, R.C., Al Refaie, A.A., Al Yami, B. & Bairamov, A.K. (2005). "High temperature corrosion of a thermowell in an incineration plant". *Engineering Failure Analysis*, 12 (3), pp. 413-419.
- Zahs, A., Spiegel, M. & Grabke, H.J. (2000). "Chloridation and oxidation of iron, chromium, nickel and their alloys in chloridizing and oxidizing atmospheres at 400-700°C". *Corrosion Science*, 42 (6), pp. 1093-1122.
- Zbogar, A., Frandsen, F.J., Jensen, P.A. & Glarborg, P. (2005). "Heat transfer in ash deposits: A modelling tool-box". *Progress in Energy and Combustion Science*, 31 (5-6), pp. 371-421.
- Zhao, S., Xie, X., Smith, G.D. & Patel, S.J. (2005). "The corrosion of INCONEL alloy 740 in simulated environments for pulverized coal-fired boiler". *Materials Chemistry and Physics*, 90 (2-3), pp. 275-281.
-

APPENDIX A

CHEMICAL COMPOSITION OF VARIOUS ENGINEERING ALLOYS

Table A1 Chemical composition (wt%) of material commonly used in the fabrication of superheater tubes. (The values of maximum steam temperature are subjected to the application in straw-fired boilers)

Alloy	C	Cr	Fe	Mn	Mo	Ni	Nb	V	Others	Max. steam temp.	Ref.
ST35.8	0.2		Bal	0.6					P, S, Si: trace		[1]
15Mo3	0.12-0.20		Bal.	0.40-0.90	0.25-0.35				P, S: ≤0.035, Si: 0.10-0.35	< 450 °C [2]	[3]
13CrMo44	0.13	1.00	Bal.		0.50						[2]
10CrMo910	0.10	2.25	Bal.	0.50	1.00						[2]
HCM2S	0.06	2.25	Bal.		0.30		0.05	0.25	N, B: trace, W: 1.60		[2]
P91	0.10	9.00	Bal.		1.00		0.07	0.23	N: trace		[2]
NF616	0.10	9.00	Bal.		0.50		0.06	0.20	N,B: trace, W: 1.80		[2]
X20CrMoV121	0.2	11.2	Bal	0.5	1.0	0.5		Trace	P, S, Si: trace	< 470 °C [2]	[1]
HCM12	0.10	12.00			1.00		0.05	0.25	W: 1.00		[2]
Esshete1250	0.1	15.0	Bal	6.3	1.0	9.5	Trace	Trace	B: Trace		[1]
C-276	≤0.010	14.5 16.5	4.0 7.0	≤1.0	15.0 17.0	Bal		≤0.35	Co: ≤2.5, P: ≤0.025, S: ≤0.010, Si: ≤0.08, W: 3.0 – 4.5		[4]
X3CrNiMoN 1713	0.03	17.00	Bal.		2.25	13.00			N: trace		[2]
TP347H FG	0.07	18.00	Bal.			10.00	1.00			< 540 °C	[2]
AISI 347FG	0.07	18.0	Bal.	2.0		12.0	Nb+Ta: ≤1.2	≤0.5	Si: <0.75		[5]

Table A1 (continue) Chemical composition (wt%) of material commonly used in the fabrication of superheater tubes. (The values of maximum steam temperature are subjected to the application in straw-fired boilers)

Alloy	C	Cr	Fe	Mn	Mo	Ni	Nb	V	Others	Max. steam temp.	Ref.
Super304H	0.10	18.00	Bal.			9.00	0.40		N: trace, Cu: 3.0		[2]
NF709	0.07	20.00	Bal.		1.50	25.00	0.25		Ti: 0.05		[2]
625	≤0.10	20.0 23.0	≤5.0	≤0.50	8.0 10.0	Bal (>58.0)	Nb+Ta: 3.15-4.15		Al: ≤0.40, Co: ≤1.0, P: ≤0.015, S: ≤0.015, Si: ≤0.50, Ti: ≤0.40		[6]
556	0.10	22	Bal. (>31.0)	1.0	3	20			Al: 0.2, Co: 18.0, La: 0.02, N: 0.2, Si: 0.4, Ta: 0.6, W:2.5, Zr: 0.02		[7]
59	≤0.01	22.0 24.0	≤1.5	≤0.5	15.0 16.5	Bal.			Al: 0.1 – 0.4, Co: ≤0.3, P: ≤0.015, S: ≤0.005, Si: ≤0.10		[8]
HR3C	0.06	25.00	Bal.			20.00	0.40		N: trace		[2]
HR6W		23.00	Bal.		1.00	43.00	0.20		Ti: 0.10, W: 6.00		[2]
Sanicro28	0.02	27.0	Bal	1.7	3.5	31.0			Cu: Trace		[1]

Note:

1. Persson, K., et al., *High temperature corrosion in a 65 MW waste to energy plant*. Fuel Processing Technology, 2007. 88(11-12): p. 1178-1182.
2. Nielsen, H.P., et al., *The Implications of Chlorine-Associated Corrosion on the Operation of Biomass-Fired Boilers*. Progres in Energy and Combustion Science, 2000. 26: p. 283 - 298.
3. E-Pipe Co.Ltd. *DIN 17175-79 Seamless Steel Tubes for Elevated Tempeartures (DIN17175-79)*. Pipe/Tube Standard Data 2007 [cited 2007 21 December]; Available from: <http://www.e-pipe.co.kr/eng/DIN/17175.htm>.
4. Mankins, W.L., S. Lamb, and Inco Alloys International Inc., *Nickel and Nickel Alloys* 1998, Huntington, West Virginia.
5. Nielsen, H.P., F.J. Frandsen, and K.D. Johansen, *Lab-Scale Investigations of High-Temperature Corrosion Phenomena in Straw-Fired Biolers*. Energy & Fuels, 1999. 13: p. 1114-1121.
6. ThyssenKrupp VDM, *Nicrofer 6020 hMo - alloy 625 (according to ASTM)*. June 2002 ed. Corrosion-resistant alloy. Vol. 4018. 2002: A company of ThyssenKrupp Stainless.
7. Haynes International Inc., *Haynes 625 alloy High - Temperature Alloys* Vol. H-3073C. 1998: Haynes Internation.
8. ThyssenKrupp VDM, *Nicrofer 5923 hMo - alloy 59 (according to ASTM)*. March 2002 ed. Corrosion-resistant alloy. Vol. 4030. 2002: A company of ThyssenKrupp Stainless.

APPENDIX B

CALCULATION FOR HEAT TRANSFER AND SURFACE TEMPERATURE

B.1 CALCULATION OF THE SUPERHEATER TUBE

B.1.1 Parameter and Data Used for Calculation

Properties of steam leaving the superheater tube

Pressure (46 bar) at the outlet	4600	kPa
Actual temperature (395 C) at the outlet	668.15	K
Velocity of steam (u)	32	m/s

From superheated steam table

Saturation temperature (at 46 bar, 395 C)	533.31	K
Therefore, average temperature for calculation	600.73	K

Properties of superheated steam at 600.73 K

Density	18.99	kg/m ³
Viscosity	2.11E-05	kg/ms
Thermal conductivity	4.61E-02	W/mK
Specific heat capacity at constant pressure	2768.04	J/kgK

Properties of Superheater Tube

Carbon steel DIN17175, 15Mo3 (Inconel59 overlay was not considered)

Outside diameter	0.0380	m
Thickness	0.0063	m
Inside diameter	0.0254	m

Properties of carbon steel at 610 K (from trials)

Thermal conductivity	43.67	W/mK
Specific heat capacity at constant pressure	587.85	J/kgK

(Trials: Firstly, the average temperature of the superheater tube was unknown. Hence, the properties of tube material (depending on the temperature) were assumed for the initial calculation. Results of tube surface temperature obtained from the first calculation would then be used for acquiring material properties in the next calculation. Few trials were carried out in order to achieve the nearest values of surface temperature in which the properties could be referred)

Properties of Hot Combustion Gas

Temperature (850 C)	1123.15	K
Velocity normal to tube	5	m/s
Using properties of N ₂ at 1 atm, 1123.15 K (assumed properties)		
Density	0.30	kg/m ³
Viscosity	4.28E-05	kg/ms
Thermal conductivity	7.13E-02	W/mK
Specific heat capacity at constant pressure	1190.94	J/kgK
Pr	0.72	

B.1.2 Forced convection heat transfer coefficient inside a tube

$$\begin{aligned} \text{Re} &= \text{Reynolds number} \\ &= \rho u d_e / \mu = \frac{18.99 \times 32 \times 0.0254}{2.11 \times 10^{-5}} = 7.33\text{E}+05 \\ \text{Pr} &= \text{Prandtl number} \\ &= C_p \mu / k = \frac{2768.04 \times 2.11 \times 10^{-5}}{4.61 \times 10^{-2}} = 1.27 \end{aligned}$$

Use equation by Gnielinski (1976)

$$Nu = 0.0214(\text{Re}^{0.8} - 100)\text{Pr}^{0.4} \quad \text{for } 0.5 < \text{Pr} < 1.5 \text{ and } 10^4 < \text{Re} < 5 \times 10^6$$

$$\begin{aligned} Nu &= 0.0214 * ((7.33 \times 10^5)^{0.8} - 100) \times (1.27)^{0.4} = 1155.32 \\ h_i &= \text{heat transfer coefficient} = \frac{Nu \times k}{d} \\ h_i &= \frac{945.90 \times 4.61 \times 10^{-2}}{0.0254} = 2097.60 \quad \text{W/m}^2\text{K} \end{aligned}$$

Use heat transfer factor (j_h)

$$\begin{aligned} \frac{h \times d}{k} &= j_h \text{Re} \text{Pr}^{0.33} \left(\frac{\mu}{\mu_w}\right)^{0.14} \\ j_h &= 0.002 \quad (\text{from Sinnott et al (2005) [1]}) \\ h_i &= \frac{0.002 \times 7.33 \times 10^5 \times 1.27^{0.33} \times 4.61 \times 10^{-2}}{0.0254} = 2877.70 \quad \text{W/m}^2\text{K} \end{aligned}$$

Use equation by Butterworth (1977)

$$\begin{aligned} \frac{h}{\rho u C_p} &= St = E \text{Re}^{-0.205} \text{Pr}^{-0.505} \quad \text{when } E = 0.0225 \exp(-0.025(\ln \text{Pr})^2) \text{ for } 10^4 < \text{Re} \\ E &= 0.0225 \exp(-0.0225(\ln(1.27)^2)) = 0.0225 \\ St &= 0.0225 \times (5.71 \times 10^5)^{-0.205} (1.27)^{-0.505} = 0.0013 \\ h_i &= 0.0013 \times 18.99 \times 25 \times 2768.04 = 2109.92 \quad \text{W/m}^2\text{K} \end{aligned}$$

Use lowest value for calculation, therefore $h_i = 2097.60 \text{ W/m}^2\text{K}$

B.1.3 Forced convection heat transfer coefficient outside a tube

$$\begin{aligned}
 \text{Re} &= \text{Reynolds number} \\
 &= \rho u d / \mu = \frac{0.30 \times 5 \times 0.038}{4.28 \times 10^{-5}} = 1.33\text{E}+03 \\
 \text{Pr} &= \text{Prandtl number} \\
 &= C_p \mu / k = \frac{1190.94 \times 4.28 \times 10^{-5}}{7.13 \times 10^{-2}} = 0.72
 \end{aligned}$$

Use equation by Knudsen and Katz (1958)

$$\begin{aligned}
 \text{Nu} &= \frac{hd}{k} = C \text{Re}^n \text{Pr}^{1/3} \text{ where } C = 0.683 \text{ and } n = 0.466; \text{ for gas with } \text{Pr} = 0.72 \\
 \text{Nu} &= 0.683 \times (1.33 \times 10^3)^{0.466} \times 0.72^{1/3} = 17.45 \\
 h_o &= \frac{17.45 \times 7.13 \times 10^{-2}}{0.0380} = 32.77 \text{ W/m}^2\text{K}
 \end{aligned}$$

Use equation by Churchill and Bernstein (1977)

$$\begin{aligned}
 \text{Nu} &= 0.3 + \frac{0.62 \text{Re}^{0.5} \text{Pr}^{1/3}}{(1 + (0.4/\text{Pr})^{2/3})^{1/4}} \left(1 + \left(\frac{\text{Re}}{282000}\right)^{5/8}\right)^{4/5} \text{ for } 10^2 < \text{Re} < 10^7; \text{RePr} > 0.2 \\
 \text{Nu} &= 0.3 + \frac{0.62 \times (1.33 \times 10^3)^{0.5} \times 0.72^{1/3}}{(1 + (0.4/0.72)^{2/3})^{1/4}} \times \left(1 + \left(\frac{1.33 \times 10^3}{282000}\right)^{5/8}\right)^{4/5} \\
 &= 23.98 \\
 h_o &= \frac{23.98 \times 7.13 \times 10^{-2}}{0.0380} = 48.60 \text{ W/m}^2\text{K}
 \end{aligned}$$

Use lowest value for calculation, therefore $h_o = 32.77 \text{ W/m}^2\text{K}$

B.1.4 Conduction heat transfer coefficient

$$h_s = \frac{2k}{d_o \ln(d_o/d_i)} = \frac{2 \times 43.67}{0.038 \times \ln(0.038/0.0254)} = 5705.59 \text{ W/m}^2\text{K}$$

B.1.5 The overall heat transfer coefficient and surface temperature

$$U = \frac{1}{\frac{1}{h_i} + \frac{1}{h_s} + \frac{1}{h_o}} = \frac{1}{\frac{1}{2097.60} + \frac{1}{5705.59} + \frac{1}{32.77}} = 32.08 \text{ W/m}^2\text{K}$$

$$\begin{aligned}
 \text{Heat transfer per area} &= q/A = U(\Delta T) \\
 &= 32.08 \times (1123.15 - 600.73) = 16760.89 \text{ W/m}^2
 \end{aligned}$$

Since

$$q/A = h_i \times (T_{wall-in} - T_{steam}) = h_s \times (T_{wall-out} - T_{wall-in}) = h_o \times (T_{air} - T_{wall-out})$$

$$\text{Temperature of inner wall } (T_{wall-in}) = \frac{16760.89}{2097.60} + 600.73 = 608.72 \text{ K}$$

$$\text{Temperature of outer wall } (T_{wall-out}) = 1123.15 - \frac{16760.89}{32.08} = 611.66 \text{ K}$$

$$\text{Average temperature of the wall} = 610.19 \text{ K}$$

B.1.6 Results summary

Convection (Inside probe) heat transfer coefficient (h_i)	=	2097.60	W/m ² K
Convection (Outside probe) heat transfer coefficient (h_o)	=	32.77	W/m ² K
Conduction heat transfer coefficient (h_s)	=	5705.59	W/m ² K
Overall heat transfer coefficient (U)	=	32.08	W/m ² K
Heat transfer (q/A)	=	16760.89	W/m ²
Surface wall temperature of superheater tube	=	611.66	K

B.2 CALCULATION OF THE SAMPLING PROBE

B.2.1 Parameter and Data Used for Calculation

Properties of compressed air

Pressure (4.5 bar)		450	kPa
Flow rate of compressed air (37.38 m ³ /h) or		1.038E-02	m ³ /s
Velocity of compressed air		20.5	m/s
Air temperature at probe inlet		288.15	K
Average temperature for calculation (from trials)		350.00	K
Properties of superheated steam at 350.00 K, 4.5 bar			
Density	$= \frac{P}{RT} = \frac{10 \times 1.0132 \times 10^5}{287 \times 350}$	4.54	kg/m ³
Viscosity		2.08E-05	kg/ms
Thermal conductivity		3.00E-02	W/mK
Specific heat capacity at constant pressure		1009.00	J/kgK
Pr		0.70	

Properties of sampling probe material- Alloy Inconel 625

Outside diameter		0.0318	m
Thickness		0.0064	m
Inside diameter		0.0254	m

Probe length	1.5	m
Properties of Inconel 625 at 430 K (from trials)		
Thermal conductivity	12.54	W/mK
Specific heat capacity at constant pressure	455.66	J/kgK

Properties of hot combustion gas were same as the calculation for sampling probe.

B.2.2 Forced convection heat transfer coefficient inside a tube

$$\begin{aligned}
 \text{Re} &= \text{Reynolds number} \\
 &= \rho u d_e / \mu = \frac{4.54 \times 20.5 \times 0.0254}{2.08 \times 10^{-5}} = 1.13\text{E}+05 \\
 \text{Pr} &= \text{Prandtl number} \\
 &= C_p \mu / k = \frac{1009 \times 2.08 \times 10^{-5}}{3.00 \times 10^{-2}} = 0.700
 \end{aligned}$$

Use equation by Gnielinski (1976)

$$Nu = 0.0214(\text{Re}^{0.8} - 100)\text{Pr}^{0.4} \text{ for } 0.5 < \text{Pr} < 1.5 \text{ and } 10^4 < \text{Re} < 5 \times 10^6$$

$$\begin{aligned}
 \text{Nu} &= 0.0214 * ((1.13 \times 10^5)^{0.8} - 100) \times (0.7)^{0.4} = 220.63 \\
 h_i &= \text{heat transfer coefficient} = \frac{\text{Nu} \times k}{d} \\
 h_i &= \frac{220.63 \times 3.00 \times 10^{-2}}{0.0254} = 260.59 \text{ W/m}^2\text{K}
 \end{aligned}$$

B.2.3 Forced convection heat transfer coefficient outside a tube

$$\begin{aligned}
 \text{Re} &= \text{Reynolds number} \\
 &= \rho u d / \mu = \frac{0.30 \times 5 \times 0.0318}{4.28 \times 10^{-5}} = 1.11\text{E}+03 \\
 \text{Pr} &= \text{Prandtl number} \\
 &= C_p \mu / k = \frac{1190.94 \times 4.28 \times 10^{-5}}{7.13 \times 10^{-2}} = 0.72
 \end{aligned}$$

Use equation by Knudsen and Katz (1958)

$$Nu = \frac{hd}{k} = C \text{Re}^n \text{Pr}^{1/3} \text{ where } C = 0.683 \text{ and } n = 0.466; \text{ for gas with } \text{Pr} = 0.72$$

$$\begin{aligned}
 \text{Nu} &= 0.683 \times (1.11 \times 10^3)^{0.466} \times 0.72^{1/3} = 16.06 \\
 h_o &= \frac{16.06 \times 7.13 \times 10^{-2}}{0.0318} = 36.08 \text{ W/m}^2\text{K}
 \end{aligned}$$

B.2.4 The overall heat transfer coefficient

$$h_s = \frac{2k}{d_o \ln(d_o/d_i)} = \frac{2 \times 12.54}{0.0318 \times \ln(0.0318/0.0254)} = 3539.12 \text{ W/m}^2\text{K}$$

B.2.5 Surface temperature of superheater tube

$$U = \frac{1}{\frac{1}{h_i} + \frac{1}{h_s} + \frac{1}{h_o}} = \frac{1}{\frac{1}{260.59} + \frac{1}{3539.12} + \frac{1}{36.08}} = 31.41 \text{ W/m}^2\text{K}$$

$$\text{Since } mC_p(T_{air, probe, outlet} - T_{air, probe, inlet}) = UA(Thotgas - (\frac{T_{air, probe, outlet} + T_{air, probe, inlet}}{2}))$$

$$\text{Solve equation: } 1.308 \times 10^{-2} \times 1009 \times (T_{air, probe, outlet} - 288.15)$$

$$= 31.41 \times \pi \times 0.0254 \times 1.5 \times (1123.15 - (\frac{T_{air, probe, outlet} + 288.15}{2}))$$

$$T_{air, probe, outlet} = 379.08 \text{ K}$$

$$T_{air, average} = 333.61 \text{ K}$$

$$\begin{aligned} \text{Heat transfer per area } (q/A) &= UA(Thotgas - (\frac{T_{air, probe, outlet} + T_{air, probe, inlet}}{2})) \\ &= 24797.77 \text{ W/m}^2 \end{aligned}$$

Since

$$q/A = h_i \times (T_{wall-in} - T_{steam}) = h_s \times (T_{wall-out} - T_{wall-in}) = h_o \times (T_{air} - T_{wall-out})$$

$$\text{Temperature of inner wall } (T_{wall-in}) = \frac{24797.77}{260.59} + 333.61 = 428.77 \text{ K}$$

$$\text{Temperature of outer wall } (T_{wall-out}) = \frac{24797.77}{3539.12} + 428.77 = 435.78 \text{ K}$$

$$\text{Average temperature of the wall} = 432.28 \text{ K}$$

B.2.6 Results summary

$$\text{Convection (Inside probe) heat transfer coefficient } (h_i) = 260.59 \text{ W/m}^2\text{K}$$

$$\text{Convection (Outside probe) heat transfer coefficient } (h_o) = 36.08 \text{ W/m}^2\text{K}$$

$$\text{Conduction heat transfer coefficient } (h_s) = 3539.12 \text{ W/m}^2\text{K}$$

$$\text{Overall heat transfer coefficient } (U) = 31.41 \text{ W/m}^2\text{K}$$

$$\text{Heat transfer } (q/A) = 24797.77 \text{ W/m}^2$$

$$\text{Surface wall temperature of superheater tube} = 435.78 \text{ K}$$

APPENDIX C

CORROSION RATES MEASUREMENT

This section presents the results of corrosion rates measurement carried out by using an optical microscope. The discussion can be found in Chapter 5 (section 5.9). The following tables show the values of corrosion rate of each alloy rings in term of 'corroded area per unit length (mm²/mm)' and 'corroded length (mm)'.

C.1 Results for Sampling Probe No.1

59E Front	Area (mm ² /mm)	Length of corroded (mm)		
		Average	Min	Max
Bottom	120.04	116.37	74.39	157.03
Bot Side	181.48	182.88	124.20	223.33
Side Bot	240.72	237.98	184.28	317.70
Mid Bot	172.91	167.71	125.44	248.96
Mid Top	225.16	225.93	203.65	257.88
Side Top	186.20	184.37	166.18	202.41
Top Side	173.31	173.67	161.39	187.01
Top	142.02	141.09	121.20	173.34

59E Rear	Area (mm ² /mm)	Length of corroded (mm)		
		Average	Min	Max
Bottom	283.96	287.61	265.45	345.57
Bot Side	306.67	307.36	282.46	345.89
Side Bot	301.11	301.85	246.62	357.26
Mid Bot	257.76	259.51	224.54	289.84
Mid Top	219.81	219.83	185.80	254.31
Side Top	283.33	285.55	247.18	351.34
Top Side	362.85	358.77	312.85	401.41
Top	324.64	328.44	279.10	368.95

556E Front	Area (mm ² /mm)	Length of corroded (mm)		
		Average	Min	Max
Bottom	296.10	290.36	239.92	322.11
Bot Side	329.20	337.13	275.60	411.94
Side Bot	280.05	277.93	245.32	310.24
Mid Bot	266.18	266.55	240.37	312.08
Mid Top	326.41	321.37	256.21	407.04
Side Top	221.59	223.26	204.17	243.26
Top Side	237.24	240.04	207.47	290.80
Top	183.42	185.46	162.06	230.14

556E Rear	Area (mm ² /mm)	Length of corroded (mm)		
		Average	Min	Max
Bottom	247.81	243.84	207.88	278.99
Bot Side	256.27	258.02	234.74	290.85
Side Bot	276.94	277.43	235.54	320.08
Mid Bot	318.75	317.91	276.24	346.95
Mid Top	345.67	345.62	310.74	390.69
Side Top	450.49	450.29	413.77	480.55
Top Side	446.37	439.04	375.29	508.16
Top	416.16	416.62	384.63	472.51

556M Front	Area (mm ² /mm)	Length of corroded (mm)		
		Average	Min	Max
Bottom	215.56	169.70	135.07	217.88
Bot Side	176.00	213.45	166.61	278.18
Side Bot	223.25	175.48	149.53	212.97
Mid Bot	129.10	223.13	195.54	242.91
Mid Top	135.89	128.92	108.22	157.97
Side Top	102.21	134.45	101.04	158.80
Top Side	102.21	98.80	68.54	126.00
Top	59.12	58.73	38.84	104.96

556M Rear	Area (mm ² /mm)	Length of corroded (mm)		
		Average	Min	Max
Bottom	106.84	106.45	86.56	152.68
Bot Side	170.88	167.47	137.21	194.67
Side Bot	139.00	137.56	104.16	161.92
Mid Bot	87.61	87.43	66.72	116.47
Mid Top	87.69	87.57	71.99	107.34
Side Top	115.48	114.96	89.00	152.44
Top Side	172.36	170.24	123.41	234.98
Top	184.64	184.22	149.60	232.41

625E Front	Area (mm ² /mm)	Length of corroded (mm)		
		Average	Min	Max
Bottom	-25.25	-20.48	-112.70	66.82
Bot Side	106.94	107.33	-22.98	236.54
Side Bot	-33.64	-32.16	-74.86	57.58
Mid Bot	36.74	34.92	-72.51	106.01
Mid Top	101.63	103.01	45.75	143.96
Side Top	43.20	44.21	17.01	66.84
Top Side	40.85	41.30	6.41	87.03
Top	52.10	52.07	26.65	80.65

625E Rear	Area (mm ² /mm)	Length of corroded (mm)		
		Average	Min	Max
Bottom	8.35	3.76	-84.90	74.23
Bot Side	1.65	0.80	-47.43	93.09
Side Bot	-12.48	-7.47	-44.72	55.04
Mid Bot	50.28	56.71	22.01	107.14
Mid Top	-17.77	-17.08	-54.67	9.87
Side Top	14.93	13.99	-32.89	49.90
Top Side	42.66	43.61	13.11	98.11
Top	24.89	24.81	4.71	44.21

C.2 Results for Sampling Probe No.2

59E Top	Area (mm ² /mm)	Length of corroded (mm)		
		Average	Min	Max
Bottom	109.16	107.72	54.57	174.71
Bot Side	69.78	67.29	17.95	135.16
Side Bot	114.31	114.09	95.66	132.94
Mid Bot	113.55	116.65	90.80	184.47
Mid Top	107.28	108.17	78.49	137.42
Side Top	114.83	112.62	66.20	146.12
Top Side	109.16	107.72	54.57	174.71
Top	69.78	67.29	17.95	135.16

59E Bot	Area (mm ² /mm)	Length of corroded (mm)		
		Average	Min	Max
Bottom	66.09	65.57	39.68	81.62
Bot Side	55.71	56.42	31.61	100.85
Side Bot	18.80	17.01	-23.99	69.83
Mid Bot	61.43	63.18	-21.42	102.60
Mid Top	68.71	69.05	29.29	111.37
Side Top	87.01	83.81	65.53	119.65
Top Side	66.09	65.57	39.68	81.62
Top	55.71	56.42	31.61	100.85

59E Top	Area (mm ² /mm)	Length of corroded (mm)		
		Average	Min	Max
Bottom	148.58	147.13	105.57	219.31
Bot Side	155.65	157.82	121.81	198.64
Side Bot	163.87	163.36	143.18	194.66
Mid Bot	61.28	61.85	34.90	93.33
Mid Top	94.84	94.72	55.09	131.38
Side Top	117.86	118.27	94.67	148.17
Top Side	148.58	147.13	105.57	219.31
Top	155.65	157.82	121.81	198.64

556E Bot	Area (mm ² /mm)	Length of corroded (mm)		
		Average	Min	Max
Bottom	169.90	165.93	122.71	220.39
Bot Side	146.20	141.68	73.96	209.15
Side Bot	322.01	325.47	250.64	388.95
Mid Bot	268.35	269.28	242.97	295.45
Mid Top	234.53	232.65	178.31	283.50
Side Top	193.59	193.26	164.29	228.91
Top Side	169.90	165.93	122.71	220.39
Top	146.20	141.68	73.96	209.15

625E Top	Area (mm ² /mm)	Length of corroded (mm)		
		Average	Min	Max
Bottom	94.24	95.62	59.49	137.01
Bot Side	108.76	112.04	66.22	170.92
Side Bot	65.56	68.58	57.88	84.35
Mid Bot	37.48	39.21	-15.48	105.58
Mid Top	44.02	43.86	13.99	110.35
Side Top	60.29	56.95	1.40	147.59
Top Side	94.24	95.62	59.49	137.01
Top	108.76	112.04	66.22	170.92

625E Bot	Area (mm ² /mm)	Length of corroded (mm)		
		Average	Min	Max
Bottom	152.53	151.98	112.40	204.35
Bot Side	118.08	113.92	74.79	185.71
Side Bot	73.70	71.46	25.45	127.19
Mid Bot	84.52	87.07	54.71	153.67
Mid Top	2.38	1.08	-45.66	46.11
Side Top	-18.23	-18.27	-42.30	16.65
Top Side	152.53	151.98	112.40	204.35
Top	118.08	113.92	74.79	185.71

556W Top	Area (mm ² /mm)	Length of corroded (mm)		
		Average	Min	Max
Bottom	234.05	234.83	208.09	267.92
Bot Side	227.01	245.42	194.29	268.28
Side Bot	201.98	202.18	188.88	229.02
Mid Bot	167.34	167.68	160.86	176.83
Mid Top	319.46	317.41	263.43	363.43
Side Top	286.11	286.18	266.67	314.11
Top Side	234.05	234.83	208.09	267.92
Top	227.01	245.42	194.29	268.28

556W Bot	Area (mm ² /mm)	Length of corroded (mm)		
		Average	Min	Max
Bottom	270.24	274.35	235.01	340.47
Bot Side	275.10	275.73	251.61	317.17
Side Bot	302.46	326.44	297.39	359.47
Mid Bot	290.05	289.14	255.79	312.94
Mid Top	298.76	296.03	255.44	315.03
Side Top	262.02	261.41	217.72	284.41
Top Side	270.24	274.35	235.01	340.47
Top	275.10	275.73	251.61	317.17

556M Top	Area (mm ² /mm)	Length of corroded (mm)		
		Average	Min	Max
Bottom	175.00	173.90	126.32	227.25
Bot Side	111.18	109.59	82.59	129.21
Side Bot	181.89	182.19	167.22	195.08
Mid Bot	175.14	175.97	155.88	197.23
Mid Top	188.13	189.01	163.69	221.51
Side Top	220.77	221.90	171.29	281.49
Top Side	175.00	173.90	126.32	227.25
Top	111.18	109.59	82.59	129.21

APPENDIX D

LIST OF PUBLICATIONS AND PRESENTATIONS

1. Poster Presentations:

Phongphiphat, A., Ryu, C. K., Poole, D., Sharifi, V. N., Swithenbank, J., (2005), 'Characterization of Combustion Residues from Municipal Solid Waste Incinerators', presented at the 1st international *Conference on Persistent Organic Pollutants*', University of Birmingham, UK.

Phongphiphat, A., Ryu, C. K., Poole, D., Sharifi, V. N., Swithenbank, J., (2007), 'Characterization of Combustion Residues from Municipal Solid Waste Incinerators', *24-month poster Presentation, Department of Chemical & Process Engineering, Sheffield University.*

Phongphiphat, A., Leyland, A., Sharifi, V. N., Swithenbank, J., (2008), High temperature Corrosion in waste to energy plants, 6th International Waste Symposium, Torbay, UK

2. Journal Publications (Under Preparation):

Phongphiphat, A., Leyland, A., Sharifi, V. N., Swithenbank, J., (2008), 'High Temperature Corrosion Control for the Superheater Systems in a Waste-to-Energy Plant: Part I Corrosion Behaviors of Ni- & Fe-Based Alloys', To be submitted to the Journal '*Corrosion Science*'.

Phongphiphat, A., Leyland, A., Sharifi, V. N., Swithenbank, J., (2008), 'High Temperature Corrosion Control for the Superheater Systems in a Waste-to-Energy Plant: Part II Performance of Aluminide Coated Alloys and Baffles', To be submitted to the Journal '*Surface and Coatings Technology*'.

Phongphiphat, A., Ryu, C. K., Poole, D., Sharifi, V. N., Swithenbank, J., (2008), 'Characterisation of Ashes and Deposits from Municipal Waste Incineration', To be submitted to the Journal '*Fuel Processing Technology*'.

3. Oral Presentations:

Phongphiphat, A., Leyland, A., Sharifi, V. N., Swithenbank, J., (2007), 'High Temperature Corrosion in Waste-to-Energy Plants', 'Combustion & Incineration Research Group Meeting', Department of Chemical & Process Engineering, Sheffield University

Phongphiphat, A., Leyland, A., Sharifi, V. N., Swithenbank, J., (2008), 'High Temperature Corrosion in Waste-to-Energy Plants', 30-month PhD Presentation, Department of Chemical & Process Engineering, Sheffield University.

HIGH TEMPERATURE CORROSION CONTROL FOR THE SUPERHEATER SYSTEMS IN A WASTE-TO-ENERGY PLANT:

PART I CORROSION BEHAVIOURS OF NI- & FE-BASED ALLOYS

Awassada Phongphiphat^{1*}, Adrian Leyland², Vida N Sharifi¹, and Jim Swithenbank¹

¹Sheffield University Waste Incineration Center (SUWIC), Department of Chemical and Process Engineering,

²Department of Engineering Material, The University of Sheffield, UK.

ABSTRACT

High temperature corrosion and the control techniques for superheater in waste-to-energy processes were investigated in a 35MW UK plant. The experiment was carried out by placing two-air cooled sampling probes at different locations in the furnace in order to simulate the corrosion process taking place on the superheater tubes and also to collect the deposits of combustion residues. The probes were fabricated from 2 types of nickel-based alloys (alloy 59 and alloy 625), and an iron-based alloys (alloy 556). After approximately 800 hours of exposure to hot flue gas having temperature range of 730 – 813°C, each probe was carefully disassembled and analyzed. Our study showed that both 'temperature' and 'particle deposition' had great effects on the high temperature corrosion inside this plant. Damages due to hot corrosion were significantly magnified when the metal surface temperature range increased from 363 – 440°C to 404 – 495°C. Tests showed that sulphates and chlorides of alkali metals and heavy metals namely zinc, lead, and arsenic were the main contributors to the hot corrosion. In this particular environment, tubes made of nickel based alloys were found to have higher corrosion resistance than iron based alloys. However, nickel based alloys are more prone to the localized corrosion (creating deep pits and crevices) notably from metal chlorides. In addition, mathematical modelling using FLIC and FLUENT code was carried out in order to simulate the flow characteristics and heat transfer inside the furnace and the region around the air cooled sampling probes. Findings from the modelling agreed with the experimental results and were used to explain the experimental results.

1. INTRODUCTION

High temperature corrosion of heat exchanger material is the important factor that limits the efficiency of various energy systems (Jappe Frandsen 2005; Persson et al. 2007; Srikanth et al. 2003; Streiff et al. 1987). In combustion systems utilizing biomass and municipal solid waste, the steam temperatures are typically kept lower than 450°C in order to avoid the corrosion problems (Rapp et al. 1981). Increase in steam temperature for only 50°C can result in a significant increase of corrosion rate in a biomass power plant (Sidhu et al. 2005; Srikanth et al. 2003). The problems are more amplified by: (1) the use of fuels containing alkali metals, heavy metals, Cl and S; (2) the fluctuation of flue gas flow; (3) the high velocity, particle bearing flue gas, and finally (5) the deposit (combustion residues) accumulation (Ishitsuka and Nose 2002; Rapp et al. 1981; Srikanth et al.

2003; Swithenbank et al. 2000). In general, the overall plant efficiencies for the waste-to-energy plant are relatively low (e.g. 25 – 30%). Therefore, methods to prevent or control high temperature corrosion in these plants must be investigated in order to improve the plant efficiencies.

High temperature corrosion can be prevented by controlling the fluctuation in the furnace. CFD modelling is proved to be an effective tool for simulation and optimization of the flow conditions, heat transfer, and particle trajectory inside the furnace (Swithenbank et al. 2000). One of the corrosion control methods is to use the high graded alloys. However, this is not generally cost effective. The more popular approach is to use coatings such as the overlay coatings, and to implement the sacrificial baffles. Aluminide coating which forms protective oxide layer of Al_2O_3 and chromized coating (Cr_2O_3) were found to be effective in preventing the high temperature corrosion (He et al. 2002; Hounginou et al. 2004; Tsaur et al. 2005). The objectives of this research are to investigate (1) corrosion behaviours of three high temperature superalloys and (2) the performance of aluminide coating and sacrificial baffles in the furnace of a waste-to-energy plant. The results of work are presented separately in 2 papers. The answers for the first objective are presented in this paper.

2. METHODOLOGY

2.1 Experimental Sites

Two air cooled sampling probes namely probe No.1 (SP1) and probe No.2 (SP2) were fabricated for this experiment. They were installed in the furnace via existing furnace's viewing ports. A schematic diagram showing the probe locations is presented in Figure 1. Additionally, samples of combustion residues were collected from various locations and were subsequently analysed for their chemical composition.

2.2 Probe Fabrication

The main structure of the probes was made of a 1.5 m long tube of 1-inch alloy 625. Three identical sets of alloys rings welded onto the main tube at 0.59 m (W-section), 0.68 m (M-section) and 1.16 m (E-section) from the furnace wall. Each set of rings was composed of 3 individual rings made of 2 nickel-based alloys (alloy 59 and alloy 625) and an iron-based alloy (alloy 556). Triangular baffles (45°), made from stainless steel 316 sheets, were welded to the main tube according to the flow direction: on the bottom side for probe No.1 and on the top side for probe No.2. Four coupons of aluminide coated alloy were welded only on probe No.2. The design of probe No.2 and its components is showed in Figure 2. The chemical compositions of these materials are presented in Table 1. The wall-end of the main tube was mounted to the air compressor which fed air to the probe with the rate of $37.38 \text{ m}^3/\text{hr}$ ($1320 \text{ ft}^3/\text{hr}$) at 4.5 bars. The air flowed feely into the furnace at the other end. The temperatures of air inside the probe were measured by three thermocouple junctions and were recorded by a data logger. After approximately 800 hours of exposure to hot flue gas having temperature range of 730 – 813°C, each probe was carefully disassembled and analyzed.

2.3 Analytical Methods

Elemental analysis was conducted by using the "Spectro Genesis – Simultaneous Charged Coupled Device – Inductively Coupled Plasma (CCD-ICP) Spectrometer", "Perkin Elmer 2400 Elemental Analyzer for CHN Analysis" and standard titration method for chlorine. Crystalline phase was investigated by using "Siemens

D500 Reflection Diffractometer (Copper Radiation)" operated with $CuK_{\alpha 1}$ and $K_{\alpha 2}$ at 40 kV and 30 mA. The differential thermal analysis was carried out using a "Perkin Elmer - Differential Thermal Analyzer DTA7 (N538-1045)". Microstructure analysis were carried out by using "Environmental Scanning Electron Microscopy - Phillips XL30 ESEM-FEG" operated at 20 keV. Corrosion rates were analysed by "Reichert Jung - Polyvar Microscope". For grain boundary analysis, etchant No. 105 was used.

3. EXPERIMENTAL RESULTS AND DISCUSSION

3.1 Temperatures of the Sampling Probes

The average temperatures of the cooling air inside probe No.1 at the W, M, E-section were 93.63, 122.26 and 175.40 °C respectively. The values for probe No.2 were 117.16, 110.44 and 204.30 °C respectively. This resulted in an average temperature difference of 84.46 °C between W and E section. The temperatures profiles of both probes gradually decreased as time progressed as a result of deposit accumulation. The results agree with the modelling results, hence, the overall conclusions were drawn from both parts of the study.

3.2 Sampling Probes after the Furnace Exposures

After the probes were removed from the furnace, scale layers were detected on the probes. The scale is composed of (1) a thick layer of deposit on the topmost, (2) hard lamella layers of corrosion products or the unprotective oxide layer, and (3) a thin film of dense and powdery corrosion products at the scale-metal interface. The ranges of deposit thickness on the probes were 7 – 35 mm for probe No.1, and 16 – 40 mm for probe No.2. Molten deposit was detected in probe No.1 at the thickest deposit covering the 2 inch tube and on the baffles. This agrees with the modelling results. There was no evidence of molten deposits on probe No.2.

Contrarily, the amount of corrosion products increases with the temperature and also depends on the alloy types. For probe No.1, the thickness of corrosion products from alloy 59 and alloy 625 were less than 1 mm while the thickness of that from alloy 556 were up to 2.5 mm. For probe No.2, the corrosion products present only as a thin film. Corrosion products under the deposit layer were slightly thinner than those present on the flue gas-exposed side. The thickness of the corrosion products plays a vital role in heat transfer. The corrosion products of alloy 556 were highly porous and detachable, and were the thickest among the three alloys. Therefore, the superheater tubes made from this alloy 556 are prone to loose their efficiency.

3.3 Characterization of Combustion Residues and Probe Deposits

3.3.1 Combustion Residues

Samples of combustion residues were collected from various locations inside the furnace. The results showed that the major constituents of the bottom ash were Ca (15.2%), Al (3.4%), Fe (4.4%) and P (1.3%). Samples of wall slag and superheater fouling were composed mainly of Cl (5.45-15.50%), S (2.2-9.2%), Zn (1.0-3.6%), K (3.3-9.0%), Na (1.7-6.2%), Ca (2.8 – 14.7%), Al (1.3-3.1%) and Pb (2.5-5.5%). High concentration of Fe (4.3-23.5%) was detected in superheater fouling and economizer ash. It was derived from the iron oxide layers of the corroded tube surface. Fly ash from the economizer ash bunker was contributed largely from the sediment of heavy particle mainly of Ca (19.7%). The air pollution control residue was a mixture of fly ash, lime and

activated carbon. Thus, the major constituents were Ca (19.7%), S (14.8%), and Cl (6.0%). Other main constituent which were not analyzed in this study, are oxygen, and silicon. Wiles (1996) reported the range of Si concentration to be 9.1 – 31 % for the bottom ash, 9.5 – 21 % for fly ash and 3.6 – 12 % for APC residues. The common inorganic compounds in fly ash collected from waste to energy plants were reported by other studies (Vassilev and Braekman-Danheux 1999; Williams 2000).

3.3.2 Deposit on Probes

The major elements in deposit on both probes (shown in Table 2) were relatively similar to those of surrounding areas. The major elements found are Cl (9.1-27.3%), S (4.2-7.1%), K (2.0-11.4%), Na (2.1-8.6%), Al (1.0-3.1%) and Ca (14.6-23.6%). These elements combined with Pb (up to 0.23%), Zn (up to 1.02%) and Sn (up to 0.03%) potentially form low-melting point-compounds which induce the severe hot corrosion on the superheater tubes (Usitalo et al. 2004). Calcium was detected more in the probe deposits compared to slag samples, because the lower surface temperatures of the probes can induce more particle deposition.

These deposits were analysed by DTA and the results showed that the deposit from superheater possibly has a melting temperature at 272 °C. However, the melting temperatures of these deposits generally fall the range of 524 – 683 °C. This results were relatively in the same range as another study that reports the melting temperatures of 484 – 555 °C (Kawahara 2002).

3.3.3 Characterization of Detached Corrosion Products

The elemental compositions of the corrosion products detached from alloys are the combination of the deposit and the elements of alloys. The major component of corrosion products for alloy 59 and alloy 625 are Ni, Cr and Mo. Fe, Ni, Cr and Co were found abundant in the corrosion products of iron-based alloy 556. Considerable amounts of Zn (1.3-2.9%), Pb (up to 0.22%) and Cd (up to 0.13%) were noticed.

3.4 Corrosion Rates of Alloy Rings

The results of corroded length (in mm/year) plotted against the position on the alloy are shown in Figure 3. The position on the graph directly signifies the real positions on the ring when looked at from the end. The arrow shows the direction of flue gas flow which corresponds to the location of the thick deposit layer. The average corrosion rates are listed in Table.3 and Table.4. The results revealed that alloy 556 had the highest corrosion rate (up to 3.9 mm/yr) followed by alloy 59 (up to 3.3 mm/yr) and alloy 625 (up to 0.5 mm/yr). The area covered with the deposit becomes less corroded than the side exposed to the flue gas because (1) the thick layer of deposit protected the alloy surface from further active oxidation and prevent the volatilization of metal chloride, and (2) the thickness of deposit can reduce the surface temperature of areas in which it covers. Comparison of results from probe No.1 and probe No2 revealed that increase in metal temperature, approximately 50°C (from CFD modelling), results in the increase of corrosion rates.

3.5 Grain Boundary at the Corroded Area

Etched cross-section image showing the grain boundary at the corroded area of alloy 59, alloy 556, and alloy 625 are shown in Figure 4 respectively. The corrosion of alloy 59 and alloy 625 took place both in uniform mode and at the grain boundary. Pitting along the grain boundary of alloy 625 is more obvious but the deeper

pits were detected at the surface of alloy 59. For alloy 556, the corrosion took place uniformly on the surface. Cracking on the grain boundary was not detected.

3.6 Morphology of Corroded Areas by SEM

The morphology of corroded areas from probe No.1 is rougher and contains more pits and crevices than the alloy surface of probe No.2 due to the higher surface temperatures. For probe No.1, the bottom side of the alloy, despite being exposed to hot gas, corroded uniformly. The top side of the alloy, where deposit accumulated, was attacked by local corrosion notably chlorine and heavy metal related corrosion. For example, the average depth of pits of alloy 59 under deposit was up to 100 microns while it was less than 20 microns on the opposite side. The models of corrosion mechanisms, governing reactions, and thermodynamic consideration are widely discussed elsewhere (Ishitsuka and Nose 2002; Kawahara 2002; Nielsen et al. 2000; Zehs et al. 2000).

3.6.1 Results for Alloy 59

SEM cross-sectional images created by back scattered electrons from alloy 59 are shown in Figure 5 and Figure 6. It was clear that this alloy experienced severe corrosion. Both deep pits and wide crevices, as shown in these figures, were detected in this sample. The scale layer, a combination of deposit and corrosion products, was mainly: (1) compounds of alkali metals, Pb, As and Zn with S, O and Cl; (2) oxides of substrate alloy elements and (3) other components such as SiO_2 , compounds of Al, and C particles.

Elements from the deposit such as Cl, S, Pb were often found at the interface between the corrosion product/metal surface. This shows that the oxide layers of Ni, Cr, and Mo existing on the top of this deposit were not protective. There is no evidence of a constant protective oxide layer forming at the metal surface. Layer of nickel oxide was detected at the outer side of scale. The oxides of molybdenum followed by oxides of chromium were commonly found closer to the scale/substrate interface. This agrees with Kawahara (2002) stating that chlorines of Cr and Mo oxidized to un-protective oxides (CrCl_2 , CrCl_3 , $\text{MoCl}_3 \rightarrow \text{Cr}_2\text{O}_3$, MoO_2) more readily and at lower partial pressure of O_2 than nickel ($\text{NiCl}_2 \rightarrow \text{NiO}$).

3.6.2 Results for Alloy 625

The SEM results for alloy625 sample of are shown in Figure 7 - Figure 8. Analysis of the thick deposit shows that the very first layer of deposit (adjacent to the probe) were often composed of silicon particles, NaCl and KCl. The later deposits are CaCl_2 and other sulphates (CaSO_4). Layers of these salts were often detected in between the layer of nickel oxides and chromium/molybdenum oxides. The corrosion products of alloy 625 are similar to that of alloy59. Oxides of chromium and molybdenum are detected close to the alloy substrate whereas oxides of nickel were detected in the outer level.

The morphology of the corroded areas on alloy 59 and alloy 625 are similar. The localized corrosion such as the deep pits and crevices are frequently noticed especially in the probe No.1. However, the severity of corrosion is lower than in alloy 59. The superior performance of alloy 625 compared to alloy 59 may be the results of the lack of niobium, tantalum and titanium in alloy 59. These elements help to protect the loss of chromium through the intergranular corrosion.

Results of crystalline phase study by X-Ray Diffractometer for alloy 59 and alloy 625 are similar. The corrosion products detected on tested alloy surface consisted of NiO, NiCr₂O₄, Cr₂O₃, Cr₂O, MoO₂, MoO₃, Ni, and MoNi.

3.6.3 Results for Alloy 556

The elemental mapping results and line scan results for alloy 556 are shown in Figure 9 and Figure 10. Crystalline phase detected on the surface of tested alloy 556 were Fe₂O₃, Fe₃O₄, FeO(OH), NiO, Cr₂O₃, Cr₂O and Ni. Other elements found in the oxide layers also include cobalt. Scale of probe show very clear that the layer of Cr/Fe was close to the alloy whereas Co/Ni was found in outer scale.

The ability of oxides for prevent the penetration of corrosive deposits are in the following order: Fe₂O₃ >> Fe₃O₄ > Cr₂O₃ > Al₂O₃ > SiO₂ (Kawahara 2002). Therefore, the pits and crevice corrosion were less likely to occur on the high alloyed steel 556. Nevertheless, the stabilities of chlorides of elements are in the following order: Cr > Fe > Ni ≈ Mo at temperature 500 °C. Thus, alloy 556 is more susceptible to corrosion in the chlorine-bearing gas, compared to the nickel based alloy. Kawahara (2002) also suggest that the stabilities of oxides of elements are in the following order: Cr > Mo ≈ Fe > Ni at 500 °C. This pointed out that the corrosion product layer may form by the compounds in this order: NiO (from the topmost), Fe₂O₃ / Fe₃O₄ / MoO₂, and Cr₂O₃ (close to the metal interface).

4. MATHEMATICAL MODELLING

Mathematical modelling using FLIC and FLUENT code was carried out in order to simulate the flow characteristics and heat transfer inside the furnace and the region around the air cooled sampling probes.

The results for velocity vector and the temperature contour of combustion gas stream in the furnace model are shown in Figure 11 and Figure 12, respectively. The results from modelling corresponded relatively well to the values recorded by plant's probes as shown in Table 5. The simulation showed that the condition in the furnace is oxidizing (6.8% O₂) with the presence of steam (17.7% H₂O) which is favorable for the high temperature corrosions. The results for velocity vector and the temperature profile of the model 'sampling probe No.1' are shown in Figure 13 and Figure 14 respectively. Similar results for model 'sampling probe No.2' are shown in Figure 15 and Figure 16. The surface temperatures of alloy rings and deposit on the probes are summarized in Table 6. In summary, the surface temperatures for probe alloys were 404 – 495°C for probe No.1 and 363 – 440°C for probe No.2. The surface temperatures of the deposits could be as high as 680°C.

5. CONCLUSIONS

Nickel based alloys (alloy 59 and alloy 625) had lower corrosion rates which was 0.17 - 3.34 m/yr than the iron-based alloy (alloy 556) which was 1.34 – 3.91 m/yr. However, nickel based alloys are more prone to the localized corrosion notably from metal chlorides. Alloy 556 has a higher resistance against pits and crevices corrosion but its uniform corrosion cause deeper loss of alloy material (up to 344 microns) than alloy 59 (up to 80 microns). Therefore, it can be concluded that the corrosion resistance of alloys are in the order alloy 625 > alloy 59 > alloy 556 under the conditions of this study. In the real application of alloy 59 and alloy 625 as a superheater tube material, the failure of superheater tube may rise from the undetectable cracks along the grain

boundary or the pits which can not be pre-calculated. In contrary, engineers may be able to predict its corrosion rates and hence can change the material according to time.

Temperature and deposit has a great effect on the rates of corrosion. Results pointed out that probe No.1, having metal temperature range of 404 – 495°C, experienced severe deposit-induced corrosion or hot corrosion. The melting temperatures of deposits were found to be in the range of 524 – 683 °C. Therefore, deep pits and crevices were generally detected under deposit layer on probe No.1. Hot corrosion might take place on probe No.2 (363- 440°C) but at a very less extent. However, it was found that a thick layer of deposit could reduce the corrosion rates. The reasons are (1) it protects the alloy surface from further active oxidation and prevent the volatilization of metal chlorides and (2) it reduces the alloy surface temperatures

6. ACKNOWLEDGEMENT

The authors would like to thank UK Engineering and Physical Science Research Council (EPSRC) and the Royal Thai Government for their financial support for this work. We would like to thank UK Incineration industry for providing technical support for this work. We would like to thank Dr. Changkook Ryu, Dr. Yoa Bin Yang, Dr. Hailiang Du for their great contribution to this research.

7. REFERENCES

- He, J. L., et al. (2002), 'A comparative study of the cyclic thermal oxidation of PVD nickel aluminide coatings', *Surface and Coatings Technology*, 155 (1), 67-79.
- Houngninou, C., Chevalier, S., and Larpin, J. P. (2004), 'Synthesis and characterisation of pack cemented aluminide coatings on metals', *Applied Surface Science*, 236 (1-4), 256-69.
- Ishitsuka, Tetsuo and Nose, Koichi (2002), 'Stability of protective oxide films in waste incineration environment--solubility measurement of oxides in molten chlorides', *Corrosion Science*, 44 (2), 247-63.
- Jappe Frandsen, Flemming (2005), 'Utilizing biomass and waste for power production--a decade of contributing to the understanding, interpretation and analysis of deposits and corrosion products', *Fuel*, 84 (10), 1277-94.
- Kawahara, Yuuzou (2002), 'High temperature corrosion mechanisms and effect of alloying elements for materials used in waste incineration environment', *Corrosion Science*, 44 (2), 223-45.
- Nielsen, Hanne Philbert, et al. (2000), 'The Implications of Chlorine-Associated Corrosion on the Operation of Biomass-Fired Boilers', *Progress in Energy and Combustion Science*, 26, 283 - 98.
- Persson, Kristoffer, et al. (2007), 'High temperature corrosion in a 65 MW waste to energy plant', *Fuel Processing Technology*, 88 (11-12), 1178-82.
- Rapp, Robert A., et al. (1981), 'High temperature corrosion in energy systems', *Materials Science and Engineering*, 50 (1), 1-17.
- Sidhu, T. S., Agrawal, R. D., and Prakash, S. (2005), 'Hot corrosion of some superalloys and role of high-velocity oxy-fuel spray coatings--a review', *Surface and Coatings Technology*, 198 (1-3), 441-46.
- Srikanth, S., et al. (2003), 'Analysis of failures in boiler tubes due to fireside corrosion in a waste heat recovery boiler', *Engineering Failure Analysis*, 10 (1), 59-66.
- Streiff, Roland, et al. (1987), *High Temperature Corrosion of Materials and Coatings for Energy Systems and Turboengines* (1; Essex England: Elsevier Applied Science Publishers LTD).
- Swithenbank, J., et al. (2000), 'Future Integrated Waste, Energy and Pollution Management (WEP) Systems Exploit Pyrotechnology', *Process Safety and Environmental Protection*, 78 (5), 383-98.

- Tsaur, Charng-Cheng, Rock, James C., and Chang, Yo-Yu (2005), 'The effect of NaCl deposit and thermal cycle on an aluminide layer coated on 310 stainless steel', *Materials Chemistry and Physics*, 91 (2-3), 330-37.
- Uusitalo, M. A., Vuoristo, P. M. J., and Mantyla, T. A. (2004), 'High temperature corrosion of coatings and boiler steels below chlorine-containing salt deposits', *Corrosion Science*, 46 (6), 1311-31.
- Vassilev, Stanislav V. and Braekman-Danheux, Colette (1999), 'Characterization of refuse-derived char from municipal solid waste: 2. Occurrence, abundance and source of trace elements', *Fuel Processing Technology*, 59 (2-3), 135.
- Williams, Paul T. (2000), 'Pollutants from Incineration: An overview', *Incineration of Municipal Waste Course* (Department of Fuel and Energy, The University of Leeds).
- Zahs, Armin, Spiegel, Michael, and Grabke, Hans Jurgen (2000), 'Chloridation and oxidation of iron, chromium, nickel and their alloys in chloridizing and oxidizing atmospheres at 400-700[degree sign]C', *Corrosion Science*, 42 (6), 1093-122.

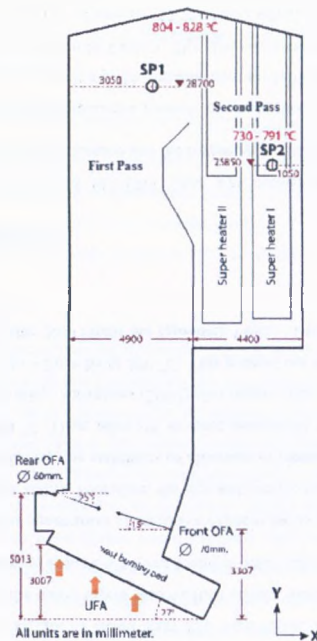


Figure 1 Schematic diagram of the furnace (side view) and locations of 2 sampling probes

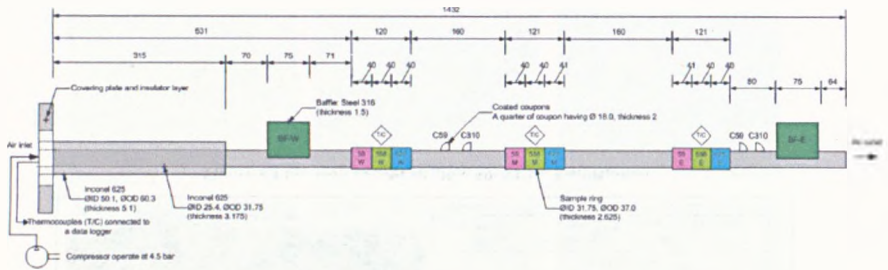


Figure 2 Drawing of the sampling probe No.2

Table 1 Typical chemical composition of metal alloy regarded in this study (% wt)

Alloy	Al	Co	Cr	Fe	Mn	Mo	Ni	Others
59	0.1 - 0.4	< 0.3	22 - 24	< 1.5	< 0.5	15-16.5	Bal.	
556	0.2	18	22	Bal	1.0	3	20	W, Ta, N, La, Zr
625	< 0.4	< 1.0	20 - 23	< 5.0	< 0.5	8 - 10	Bal	Nb+Ta
310	-	-	24 - 26	Bal.	< 2.0	-	19 - 22	
316	-	-	16 - 18	Bal.	< 2.0	2 - 3	10 - 14	

Table 2 Major elemental composition of the deposit collected from probe No.1 (%)

	Deposit from probe No.1 (%)						Deposit from probe No.2 (%)			
	2inch (hr387)	2inch (hr769)	Wall (556W)	Middle (556M)	End (59E)	End (BF-E)	Wall (556W)	Middle (556M)	End 1 (556E)	End 2 (556E)
Cl	14.45	n.m.	15.99	27.31	n.m.	9.09	12.72	19.98	18.65	23.26
S	5.74	5.05	5.08	5.37	4.24	4.93	6.00	6.50	6.10	7.10
Zn	0.78	0.47	0.59	0.83	1.02	0.46	0.51	0.76	0.81	0.66
K	5.25	2.04	8.32	9.09	8.55	3.22	4.92	8.70	8.45	11.40
Na	5.04	2.11	6.62	6.90	6.6	3.09	4.34	6.48	6.30	8.60
Ca	18.70	23.60	17.60	18.10	14.60	22.40	20.10	16.50	16.80	13.80
Al	3.09	2.20	1.37	1.57	1.73	2.37	1.80	1.40	1.60	1.00
Pb	0.22	0.02	0.14	0.11	0.23	0.03	0.10	0.11	0.13	0.11
Fe	0.54	0.64	0.45	0.46	0.75	0.74	0.64	0.52	0.59	0.33
Ni	0.24	0.00	0.05	0.00	2.27	0.08	0.03	0.00	0.11	0.00

Note: n.m. is 'not measured'

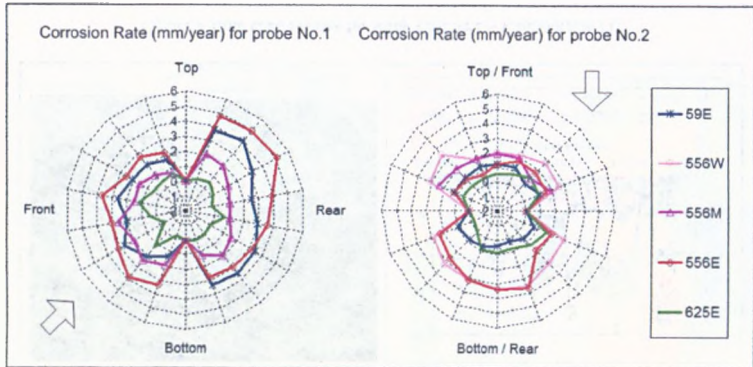


Figure 3 Corroded length (mm/year) of alloy rings from sampling probe No.1

Table.3 Average corrosion rates of alloy rings from sampling probe No.1

Alloy Rings		Average Corroded Length	Corrosion Rate (Length)	Corrosion Rate (Area)
		(μm)	(mm/yr)	(mm^2/yr)
59E	F	178.75	2.04	239
	R	293.62	3.34	387
556M	F	150.33	1.71	189
	R	131.99	1.50	176
556E	F	267.76	3.05	354
	R	343.60	3.91	456
625E	F	41.27	0.47	53
	R	14.89	0.17	19

Table.4 Average corrosion rates of alloy rings from sampling probe No.2

Alloy Rings		Average Corroded Length	Corrosion Rate (Length)	Corrosion Rate (Area)
		(μm)	(mm/yr)	(mm^2/yr)
59E	F	104.43	1.13	132
	R	59.17	0.64	75
556W	F	242.28	2.62	300
	R	287.18	3.10	355
556M	F	175.43	1.89	220
	R	123.86	1.34	155
556E	F	123.86	1.34	155
	R	240.69	2.60	304
625E	F	69.38	0.75	86
	R	67.87	0.73	86



Figure 4 Cross-sectional images of alloy 59 and its grain boundary structure.

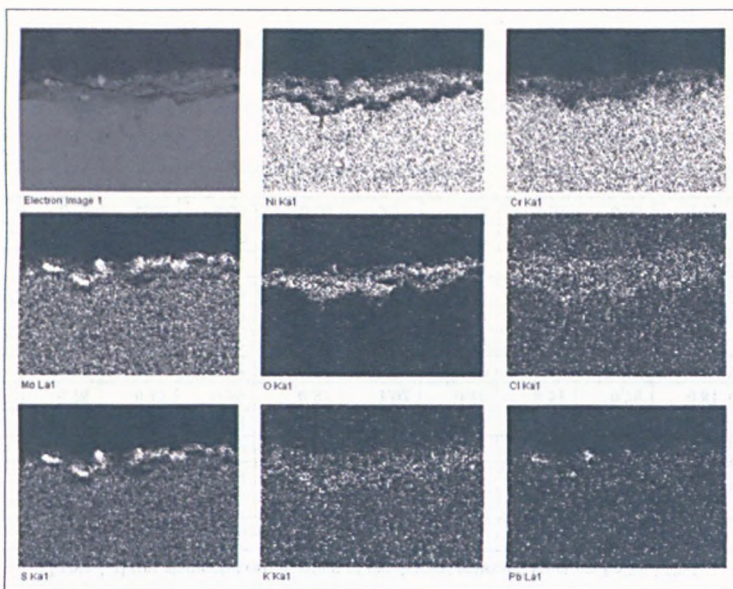


Figure 5 Elemental mapping of alloy 59 and its corrosion products: SP1 – End/Top

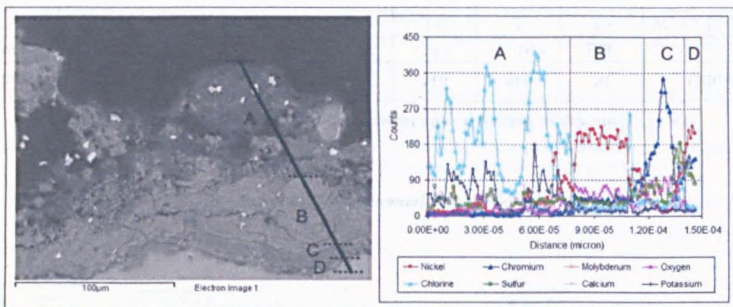


Figure 6 Line scan results of alloy 59: SP1 – End/Bottom

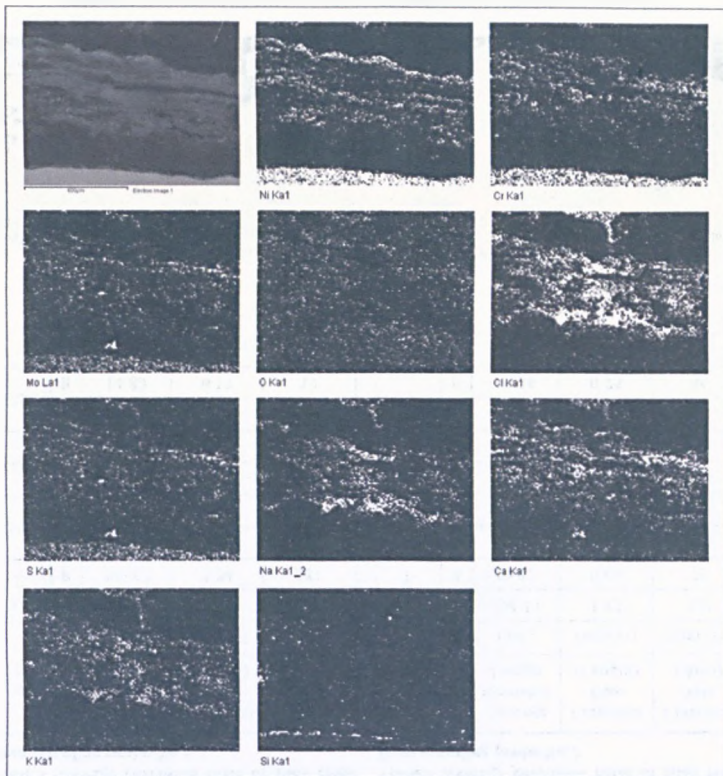


Figure 7 Elemental mapping of alloy 625 and its corrosion products: SP1 – End/Top

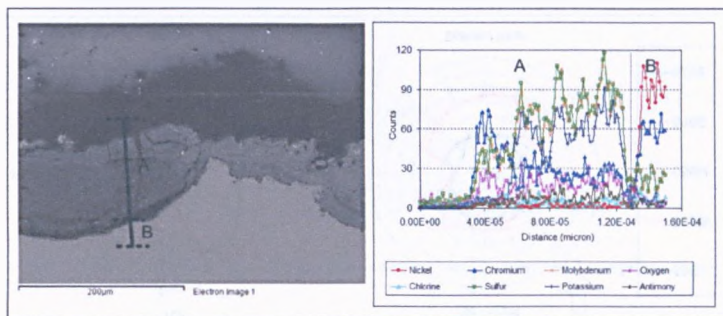


Figure 8 Line scan results for alloy 625: SP2 – End/Bottom (1)

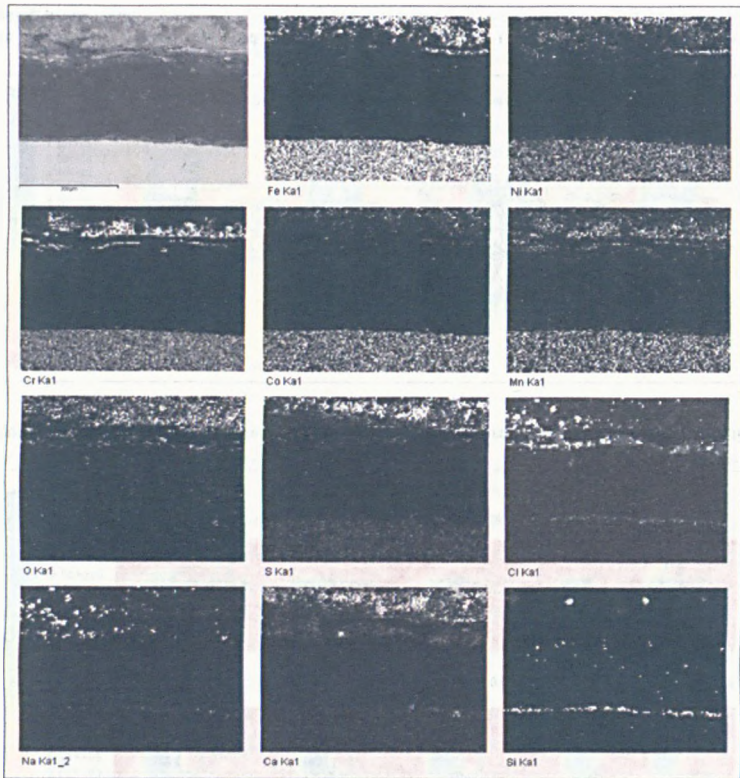


Figure 9 Elemental mapping of alloy 556 and its corrosion products: SP1 – End/Top

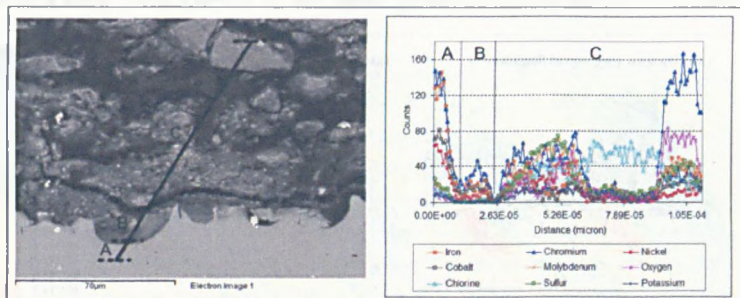


Figure 10 Line scan results for alloy 556: SP2 – End/Top (2)

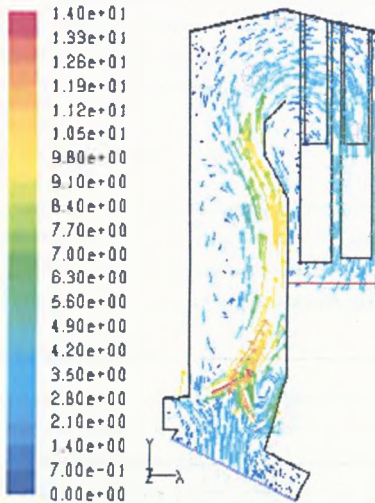


Figure 11 Velocity vectors coloured by the velocity magnitude (m/s) of the gases in the furnace model

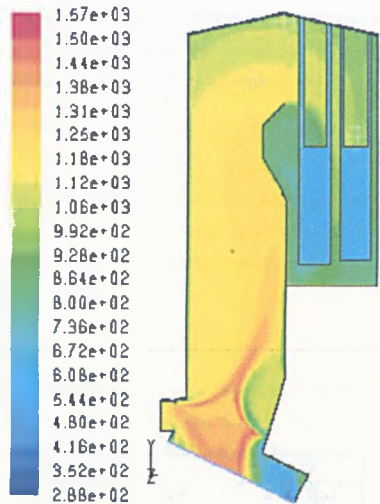


Figure 12 Contours of temperature (K) of the gases in the furnace model

Table 5 Comparison of results from the FLUENT modelling and the on-line recorded values

Results	Temperature (°C)	Velocity (m/s)	O ₂ content (wt%)
Real measurement – roof probe	804 – 828		
Model – at the roof probe	769.35	1.26	6.55
Real measurement – 1st pass	754 – 813		8.38 – 8.77
Model – at the probe No.1	871.31	3.05 (X =2.02, Y=2.28, θ = -138.4°)	6.69
Real measurement – 2nd pass	730 – 791	≈ 5	
Model – at the probe No.2	717.23	4.83 (X = 0.41, Y=-4.81, θ = 4.83°)	6.68

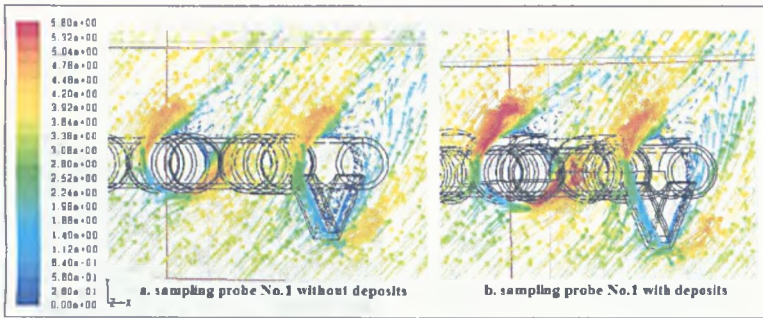


Figure 13 Velocity vector, coloured by the velocity magnitude (m/s) of the flow across the model 'sampling probe No.1'

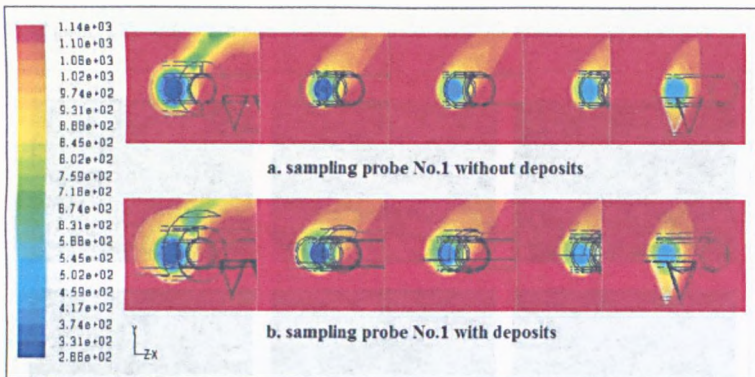


Figure 14 Contours of temperature (K) of the model 'sampling probe No.1' at various cross-sections

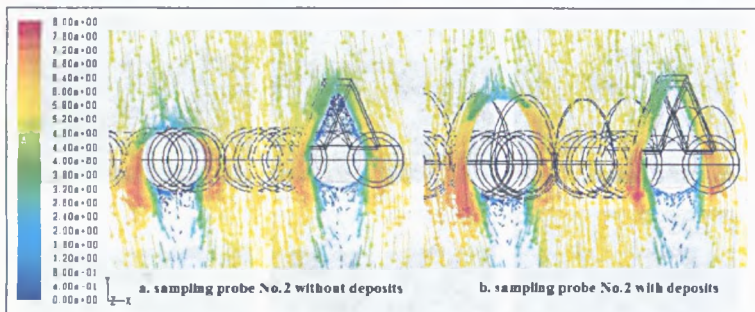


Figure 15 Velocity vector, coloured by the velocity magnitude (m/s) of the flow across the model 'sampling probe No.2'

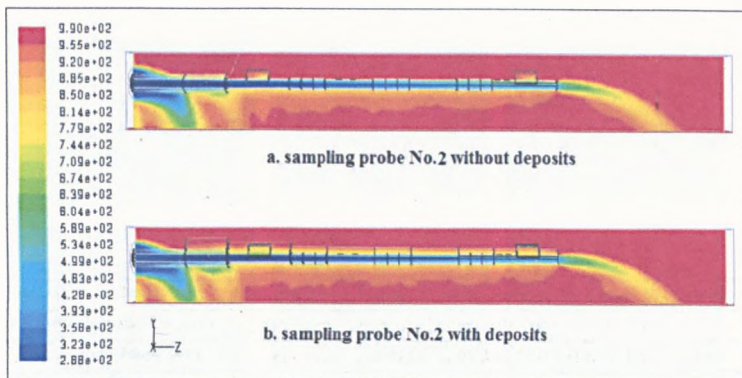


Figure 16 Contour of temperature (K) of the model 'sampling probe No.2'

Table 6 Surface temperature of metal and deposits at different locations on the sampling probes

Surface temperature (°C)	Location (section)	Sampling probe No.1		Sampling probe No.2	
		No deposits	With deposits	No deposits	With deposits
Metal surface temperature (°C)	0.59 m (W)	452 – 496	404 – 427	397 – 434	363 – 378
	0.87 m (M)	477 – 518	435 – 462	419 – 453	385 – 401
	1.15 m (E)	504 – 543	468 – 495	441 – 474	418 – 440
Deposit surface temperature (°C)	0.59 m (W)	n.a.	489 – 680	n.a.	399 – 598
	0.87 m (M)		514 – 641		419 – 596
	1.15 m (E)		542 – 631		615

HIGH TEMPERATURE CORROSION CONTROL FOR THE SUPERHEATER SYSTEMS IN A WASTE-TO-ENERGY PLANT:

PART II PERFORMANCE OF ALUMINIDE COATED ALLOYS AND BAFFLES

Awassada Phongphiphat¹*, Adrian Leyland², Vida N Sharifi¹, and Jim Swithenbank¹

¹Sheffield University Waste Incineration Center (SUWIC), Department of Chemical and Process Engineering,

²Department of Engineering Material, The University of Sheffield, UK.

ABSTRACT

In waste-to-energy plants, high temperature corrosion of heat exchanger materials is the important problem that limits the plant efficiency and it often leads to a high maintenance cost. To tackle the corrosion problem, one approach is to apply 'surface modification' on the superheater materials. This study investigates (1) the aluminide coating (Al_2O_3 former) which were found to be effective in preventing material against the high temperature corrosion and (2) the use of sacrificial baffle. An air-cooled sampling probe was placed in the furnace of a 35MW waste-to-energy plant in order to simulate the corrosion process taking place on the superheater tubes. It was fabricated from 5 different types of materials: (nickel-based alloy 59 and alloy 625, aluminide coated alloy 59, iron-based alloy 556, aluminide coated stainless steel 310 and stainless steel 316. After 800 hours of exposure to the flue gas having temperature range of 754 to 791°C, the probe was withdrawn. It was found that the order of corrosion resistance of tested materials is as follows: coated alloy 59 > coated steel 310 > alloy 625 > alloy 59 > alloy 556 > steel 316. The aluminized coating significantly improved the corrosion resistance for the selected materials despite being tested under the higher temperature. In contrary, this particular design of sacrificial baffle did not show its ability to be used as corrosion control equipment. Our study showed that 'aluminide coating' is a promising corrosion control technique for superheater materials in the waste-to-energy plants.

1. INTRODUCTION

Waste-to-energy plants are the most susceptible to severe corrosion than other types of energy systems due to the presence of deposit containing alkali metals, heavy metals (such as Pb, Zn and Cd), chlorine, and sulphur (Ishitsuka and Nose 2002; Rapp et al. 1981; Srikanth et al. 2003; Swithenbank et al. 2000). The existence of these elements leads to the formation of low melting points eutectic compounds (Hansen et al. 2000; Li et al. 2003). Liquid phase corrosion or hot corrosion is very likely to take place on the superheater tubes. This results in a high annual cost for the plant operators to repair and replace the superheater tubes. Therefore, reliable and cost effective methods to control the corrosion in these plants must be investigated. One of the promising methods is to use coatings such as the overlay coatings, and to implement the sacrificial baffles. Aluminide coating which forms protective oxide layer of Al_2O_3 and chromized coating (Cr_2O_3) were found to

be effective in preventing the high temperature corrosion (He et al. 2002; Houngninou et al. 2004; Tsaur et al. 2005). Aluminide coating on cheaper stainless steels may provide engineers with a high corrosion resistance material at an affordable price. Hence, the objective of this research is to investigate the corrosion behaviour of aluminide coated materials in the waste-to-energy plant. This paper presents the second part of study following the previous article (part I: corrosion behaviours of nickel-based and iron-based superalloys).

2. METHODOLOGY

Research work consisted of 2 parts: the experiments and the mathematical modelling. The experiment was performed by placing an air-cooled sampling probe in the furnace of a 35MW waste to energy plant for approximately 800 hours. The position of the probe was in the 2nd pass of the furnace just above the top of superheater panels where the temperature range of flue gases was 730 - 791°C.

2.1 Probe Fabrication

The main structure of the probe was made of a 1.5 m long tube of 1-inch alloy 625. Three identical sets of alloys rings welded onto the main tube at 0.59 m, 0.68 m and 1.16 m from the wall end. Each set of rings was composed of 3 individual rings made of 2 nickel-based alloys (alloy 59 and alloy 625) and an iron-based alloy (alloy 556). Triangular baffles (45°), made from stainless steel 316 sheets, were welded to the main tube at 0.42 m and 1.33 m from wall end. Four coupons of aluminide coated alloy coupons (ØOD 37.00 mm, Thickness 2 mm) were made of alloy 59 and stainless steel 310. Coupons of each alloy were welded to the main tube at 0.72 m (W-section) and 1.25 m (E-section) from wall. The aluminide pack cementation coating process was conducted by the Advanced Material Research Institute, School of Engineering, University of Northumbria at Newcastle. Firstly, coupons were ground up to 600 SiC grit finish. Then, they were heated in a ceramic crucible packed with aluminide chemicals in the furnace. For alloy 59, coupons were heated at a temperature of 1000 °C for 5 hours in the aluminide mixture composed of 15%Al + 3%NH₄Cl + 82%Al₂O₃ by weight. For stainless steel 310, coupons were heated at a temperature of 850 °C for 5 hours in the aluminide mixture composed of 4%Al + 2%AlCl₃ + 94% Al₂O₃ by weight. The chemical compositions of relevant materials are presented in Table I. Further details of the probe can be found in Part I.

The compressed air was fed to the probe with the rate of 37.38 m³/hr (1320 R³/hr) at 4.5 bars. The air flowed feely into the furnace at the other end. The temperatures of air inside the probe were measured by three thermocouple junctions and were recorded by a data logger.

2.2 Analytical Methods

Elemental analysis was conducted by using the "Spectro Genesis - Simultaneous Charged Coupled Device - Inductively Coupled Plasma (CCD-ICP) Spectrometer", "Perkin Elmer 2400 Elemental Analyzer for CHN Analysis" and standard titration method for chlorine. Crystalline phase was investigated by using "Siemens D500 Reflection Diffractometer (Copper Radiation)" operated with $CuK_{\alpha 1}$ and $K_{\alpha 2}$ at 40 kV and 30 mA. The differential thermal analysis was carried out using a "Perkin Elmer - Differential Thermal Analyzer DTA7 (N538-1045)". Microstructure analysis were carried out by using "Environmental Scanning Electron

Microscopy - Phillips XL30 ESEM-FEG" operated at 20 keV. Corrosion rates were analysed by "Reichert Jung - Polyvar Microscope". For grain boundary analysis, etchant No. 105 was used.

3. RESULTS AND DISCUSSION

3.1 Sampling Probes after the Furnace Exposures

After the probes were removed from the furnace, scale layers were detected on the probes. The scale is composed of (1) a thick layer of deposit on the topmost and (2) a thin film of corrosion products or the un-protective oxide layer on the alloy surface. The deposit thickness varied from 40 mm at the colder region (wall-end side) to 16 mm at the hotter region (outlet side). There was no evidence of molten deposits.

Visible corrosion products were barely detected on the wall and middle section of the probe. The corrosion products are thicker in the hotter end. Sections of the probe after deposit was removed are shown in Figure 1 - Figure 6. Corrosion products of alloy 556 were noticeably thicker than those of alloy 59 and alloy 625.

Baffles were totally covered under the deposit. The voids between baffles and the main tube were also filled with the yellow fine particles. The design of these baffles was found to be not beneficial under real operation. It granted a void for deposit accumulation, and subsequently hot corrosion to take place. Baffles, made of stainless steel 316, were severely corroded leaving brittle dark reddish brown corrosion products. The edges of baffles had chipped. Spallation of corrosion products were common at the edges welded to the main probe. There was no evidence that these baffles can reduce or prevent the corrosion of the 1 inch tube in the area where they were welded. Instead, it retains the deposit and increases the risk of hot corrosion in that area.

The coated coupons were also entirely by the deposit. After the thick deposits were removed, it was found that there was a very thin film of corrosion products randomly formed on the coupon surfaces. There was no chip, broken structure, or spallation detected. Both coated alloy 59, and coated stainless steel 310 were found to be in a better condition than substrate alloy (alloy 59) and its comparable materials (alloy 556, and steel 316).

3.2 Characterization of Combustion Residues and Probe Deposits

Samples of combustion residues were collected from various locations inside the furnace. The results showed that the major constituents of the bottom ash were Ca (15.2%), Al (3.4%), Fe (4.4%) and P (1.3%). Samples of wall slag and superheater fouling were composed mainly of Cl (5.45-15.50%), S (2.2-9.2%), Zn (1.0-3.6%), K (3.3-9.0%), Na (1.7-6.2%), Ca (2.8 - 14.7%), Al (1.3-3.1%) and Pb (2.5-5.5%). High concentration of Fe (4.3-23.5%) was detected in superheater fouling and economizer ash. It was derived from the iron oxide layers of the corroded tube surface. Fly ash from the economizer ash bunker was contributed largely from the sediment of heavy particle mainly of Ca (19.7%). The air pollution control residue was a mixture of fly ash, lime and activated carbon. Thus, the major constituents were Ca (19.7%), S (14.8%), and Cl (6.0%). Other main constituent which were not analyzed in this study, are oxygen, and silicon. Wiles (1996) reported the range of Si concentration to be 9.1 - 31 % for the bottom ash, 9.5 - 21 % for fly ash and 3.6 - 12 % for APC residues. The common inorganic compounds in fly ash collected from waste to energy plants were reported by other studies (Vassilev and Braekman-Danheux 1999; Williams 2000).

The elemental compositions of the deposit collected from the probe and superheater were shown in Table 2. The major elements in probe deposit were Cl (12.7-23.3 wt%), Ca (13.8-20.1 wt%), S (6.0-7.1 wt%), K (4.9-11.4 wt%), Na (4.3-8.6 wt%), Al (1.0-1.8 wt%) and Fe (0.3-0.64 wt%). Calcium and chlorine were detected more in the probe deposits compared to slag samples, because the lower surface temperatures of the probes can induce more particle deposition. Presence of heavy metals such as Zn (0.51-0.66 wt%), Pb (0.98-1.3 %), Cd (0.14-0.29 wt%) and Sn (0.17-0.28%) in the probe deposit and superheater deposit showed that low-melting point compounds may form, and hot corrosion may take place (Uusitalo et al. 2004)

DTA results showed that the deposit from superheater possibly has a first melting temperature at 272 °C. However, the melting temperatures of these deposits generally fall the range of 524 – 683 °C.

3.3 Corrosion Rates of Alloy Rings

Alloy rings (alloy 59, alloy 625 and alloy 556) were analysed for their corrosion rates. The measurement was taken at the cross-sectional surface of these rings. The results of corroded length for the exposure period (μm) and the predicted corrosion rate (mm/yr) are presented in Table 3. The results revealed that alloy 556 had the highest corrosion rate (1.3 – 2.6 mm/yr) followed by alloy 59 (0.6 – 1.1 cm/yr) and alloy 625 (0.7 – 0.8 m/yr).

3.4 Morphology of Corroded Areas by SEM & Crystalline Structure Analysis by XRD

3.4.1 Results for Aluminide Coated Alloy 59

The elemental map of the coated coupon of alloy 59 from W-section is shown in Figure 7 - Figure 8. Results of crystalline structure analysis are shown in Figure 9. It was found that the scale layers consist of: (1) deposit layers, (2) un-protective oxide layers of Al, Ni, Cr, and Mo as $\theta\text{-Al}_2\text{O}_3$, $\alpha\text{-Al}_2\text{O}_3$, NiO, Cr_2O_3 , NiCr_2O_4 , MoO_2 and MoO_3 , and (3) a layer of coating present next to the alloy interface. The coating layer is comprised mainly of Al and Ni that were fused to form Ni-Al intermetallic layer during the heating process. NiAl, NiAl₂ and Ni₂Al₃ were detected.

Figure 10 and Table 4 show that the atomic ratios of Ni to Al at this intermetallic layer varied from 1:1.0 (close to the substrate) to 1:1.4 (top part). A ratio of Ni:Al equals to 1:2.9 was detected in the Wall-section coupons. Cr and Mo were also present in the intermetallic layer but at the less extent. Mn is present in the alloy, but its contribution in the protective oxide layer is not clearly shown.

Figure 10 - Figure 11 clearly show 2 different layer of coating above the substrate: (1) a layer of aluminum and nickel and (2) a thin layer Cr next to the substrate. The thickness of Al-Ni layer of the End-section coupon and the Wall-section coupon is approximately 60 and 70 micron respectively. The thickness of Cr layer for both coupons is approximately 10 – 12 micron.

Images of coated alloy 59 at different locations were compared as shown in Figure 12 - Figure 15. The temperature difference significantly affects the corrosion. The wall-section coupon became less corroded than end-section coupon. There is no corrosion at the substrate level at the wall-section coupon. The destruction of coating and the corrosion of substrate alloy were widespread in the end-section coupon.

The aluminized coating on nickel based alloy is proved to be the most efficient method to prevent the high temperature corrosion in the furnace of waste-to-energy plant. The performance of this coating can be

enhanced by the pre-oxidation prior the exposure to the corrosive gases. Further investigation into the price and the strength of material are recommended in order to apply it in the field. However, the drawbacks of the NiAl which is the insufficient strength and creep resistance at the temperature above 1000 °C (Houngninou et al. 2004) should be carefully concerned.

3.4.2 Results for Aluminide Coated Stainless Steel 310

The results of elemental mapping of the coated coupons are shown in Figure 16. The coating was barely detected at the End-section but present in the Wall-section with an average thickness of 3 - 8 μm . Crystalline structure analysis, Figure 17, shows that the main composition in the corrosion products are $\theta - \text{Al}_2\text{O}_3$, $\alpha - \text{Al}_2\text{O}_3$, Fe_2O_3 , Fe_3O_4 , $\text{FeO}(\text{OH})$, NiO , Cr_2O_3 and CrO_2 . The coating layer was a combination of Al and Fe as FeAl and Fe_3Al .

Line scan results for the aluminide coated 310 coupons are shown in Figure 18 - Figure 20. The deposit adjacent to this coupon contains a large amount of alkali chlorides. A particle of CaSiO_4 was detected in Figure 18. Round particles having sizes that varied from 20 - 100 microns were often detected in the deposit. They are the condensed droplets of liquid CaCl_2 ZnCl_2 SiO_2 or compounds of Si, Ca, Al, and O. Figure 19 and Figure 20 shows a very thin layer of aluminide coating and layers of Al_2O_3 present among the deposit layer.

Figure 21 - Figure 24 show a corrosion layer on the various positions of the coupons. The coating was generally consumed and corrosion reached the substrate level. Coating was detected in the Wall-section coupon only at the bottom and middle part. It was not found on the top part of Wall-section coupon and the entire End-section coupon. This is due to the difference in temperature. The causes are also the quality of the coating itself (FeAl_3) or the non-homogenous nature of the deposit causing different rates of local corrosion

In summary, coated coupon of stainless steel 310 proves that the aluminide coating can provide a good corrosion resistance. The coated coupons had less suffered from the corrosion compared to the similar material, stainless steel 316, which was entirely corroded. However, the aluminide coating on stainless steel does not perform as well as the coating on nickel based alloy. This results agree with the previous study in the laboratory furnace showing that AlFe_3 is not suitable in the chlorine bearing oxidizing environment (Tsaour et al. 2005). Nevertheless, aluminized coating on steel has a greater resistance to the high temperature corrosion compared to the nickel based alloy 59 and 625. Therefore, it can be a promising alternative material to withstand in this corrosive condition. Its advantages include the high temperature strength of substrate (steel 310), low cost, low density, and good fabricability. However, the disadvantages of such as the decreasing of strength of AlFe_3 at the temperature higher than 500 °C should be noted (Houngninou et al. 2004).

3.4.3 Results for Stainless Steel 316 (Sacrificial Baffles)

The baffles made from austenitic stainless steel 316 were found to be corroded severely. The entire pieces of baffles were oxidized. This shows that the austenitic stainless steel can not withstand the corrosive conditions in this high temperature furnace. One important factor increasing its corrosion is the temperature. The baffles did not have enough surface area of heat transfer with the air cooled probes therefore it is preferably influenced by the temperature of the surrounding deposits. Corrosion products consist mainly of Fe_3O_4 , Cr_2O_3 ,

and NiO. Oxides of chromium clearly lie close to the substrate whereas oxides of iron and nickel were detected in the outer layer.

4. MATHEMATICAL MODELLING

Mathematical modelling using FLIC and FLUENT code was carried out in order to simulate the flow characteristics and inside the furnace as well as to calculate the heat transfer of the air cooled sampling probe components. The results (Figure 25) show that the surface temperatures of alloy rings were in a range of 363–440°C. This calculation supports the experimental findings showing that hot corrosion did not take place on the probe surface. The modelling shows that the coated coupons founded under the deposit could be surrounded by the deposit having temperature up to 615°C. This means that these coupons experienced higher surface temperatures than the alloy rings on the probes.

The modelling work shows that baffles can divert the particles from the probe preventing deposition and erosion corrosion. However, the temperature of the baffle itself is very high since the heat transfer surface connected with the main tube is too small. The installation of the baffle by welding it to the main tube increases the local surface temperature of the main tube by approximately 1.74%. This finding raises a concern about the use of sacrificial baffles in the industry. The welding points possibly become the source of localized corrosion which potentially punctures the superheater tube.

5. CONCLUSIONS

The results from this study yielded valuable information that can be applied to the waste-to-energy industry and similar corrosive-environment processes. The results proved that 'aluminide coating' is a promising corrosion control technique for superheater materials in the waste-to-energy plants. The coating is relatively cheap and simple but it can significantly increase the corrosion resistance of selected materials. The order of corrosion resistance of materials is as follows: coated alloy 59 > coated steel 310 > alloy 625 > alloy 59 > alloy 556 steel 316. Our results showed that corrosion resistance of FeAl₃ and Fe₂Al₃ formed on a low cost stainless steel 310 is comparable to the corrosion resistance of expensive nickel-based alloys. Finally, results showed that this particular sacrificial baffle can (1) provide rooms for deposition accumulation and (2) cause a high temperature at the welding point. As a result, the deposit-induced corrosion can take place vigorously. Therefore, use of sacrificial baffles requires precautions and careful design.

6. ACKNOWLEDGEMENT

The authors would like to thank UK Engineering and Physical Science Research Council (EPSRC) and the Royal Thai Government for their financial support for this work. We would like to thank UK Incinerator industry for providing technical support for this work. We would like to thank Dr. Changkook Ryu, Dr. Yeon Bin Yang, Dr. Hailiang Du for their great contribution to this research.

7. REFERENCES

- Hansen, Lone A., et al. (2000), 'Influence of deposit formation on corrosion at a straw-fired boiler', *Fuel Processing Technology*, 64 (1-3), 189-209.
- He, J. L., et al. (2002), 'A comparative study of the cyclic thermal oxidation of PVD nickel aluminide coatings', *Surface and Coatings Technology*, 155 (1), 67-79.
- Houngminou, C., Chevalier, S., and Larpin, J. P. (2004), 'Synthesis and characterisation of pack cemented aluminide coatings on metals', *Applied Surface Science*, 236 (1-4), 256-69.
- Ishitsuka, Tetsuo and Nose, Koichi (2002), 'Stability of protective oxide films in waste incineration environment—solubility measurement of oxides in molten chlorides', *Corrosion Science*, 44 (2), 247-63.
- Jappe Frandsen, Flemming (2005), 'Utilizing biomass and waste for power production—a decade of contributing to the understanding, interpretation and analysis of deposits and corrosion products', *Fuel*, 84 (10), 1277-94.
- Kawahara, Yuuzou (2002), 'High temperature corrosion mechanisms and effect of alloying elements for materials used in waste incineration environment', *Corrosion Science*, 44 (2), 223-45.
- Li, Y. S., Niu, Y., and Wu, W. T. (2003), 'Accelerated corrosion of pure Fe, Ni, Cr and several Fe-based alloys induced by ZnCl₂-KCl at 450 [degree sign]C in oxidizing environment', *Materials Science and Engineering A*, 345 (1-2), 64-71.
- Nielsen, Hanne Philbert, et al. (2000), 'The Implications of Chlorine-Associated Corrosion on the Operation of Biomass-Fired Boilers', *Progress in Energy and Combustion Science*, 26, 283 - 98.
- Persson, Kristoffer, et al. (2007), 'High temperature corrosion in a 65 MW waste to energy plant', *Fuel Processing Technology*, 88 (11-12), 1178-82.
- Rapp, Robert A., et al. (1981), 'High temperature corrosion in energy systems', *Materials Science and Engineering*, 50 (1), 1-17.
- Srikanth, S., et al. (2003), 'Analysis of failures in boiler tubes due to fireside corrosion in a waste heat recovery boiler', *Engineering Failure Analysis*, 10 (1), 59-66.
- Streiff, Roland, et al. (1987), *High Temperature Corrosion of Materials and Coatings for Energy Systems and Turboengines* (1; Essex England: Elsevier Applied Science Publishers LTD).
- Swithenbank, J., et al. (2000), 'Future Integrated Waste, Energy and Pollution Management (WEP) Systems Exploit Pyrotechnology', *Process Safety and Environmental Protection*, 78 (5), 383-98.
- Tsaur, Charng-Cheng, Rock, James C., and Chang, Yo-Yu (2005), 'The effect of NaCl deposit and thermal cycle on an aluminide layer coated on 310 stainless steel', *Materials Chemistry and Physics*, 91 (2-3), 330-37.
- Uusitalo, M. A., Vuoristo, P. M. J., and Mantyla, T. A. (2004), 'High temperature corrosion of coatings and boiler steels below chlorine-containing salt deposits', *Corrosion Science*, 46 (6), 1311-31.
- Vassilev, Stanislav V. and Brackman-Danheux, Colette (1999), 'Characterization of refuse-derived char from municipal solid waste: 2. Occurrence, abundance and source of trace elements', *Fuel Processing Technology*, 59 (2-3), 135.
- Williams, Paul T. (2000), 'Pollutants from Incineration: An overview', *Incineration of Municipal Waste Course* (Department of Fuel and Energy, The University of Leeds).
-

Table 1 Typical chemical composition of metal alloy regarded in this study (% wt)

Alloy	Al	Co	Cr	Fe	Mn	Mo	Ni	Others
59	0.1 - 0.4	<0.3	22 - 24	< 1.5	< 0.5	15 - 16.5	Bal.	
556	0.2	18	22	Bal	1.0	3	20	W, Ta, N, La,
625	<0.4	< 1.0	20 - 23	< 5.0	< 0.5	8 - 10	Bal.	Nb+Ta
310	-	-	24 - 26	Bal	< 2.0	-	19 - 22	
316	-	-	16 - 18	Bal	< 2.0	2 - 3	10 - 14	

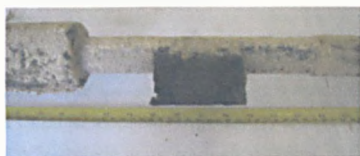


Figure 1 Baffle – wall section

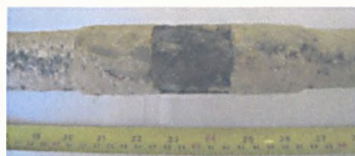


Figure 2 Alloy rings – wall section



Figure 3 Coated coupons – wall section

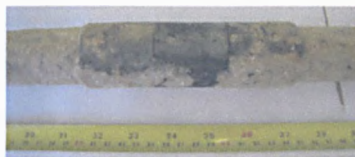


Figure 4 Alloy rings – middle section

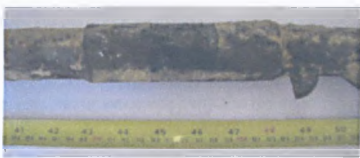


Figure 5 Alloy rings – end section



Figure 6 Coated coupons & baffle – end section

Table 2 Major elemental composition (>1%) of the deposit collected from probe No.2 (wt.%) deposit collected form superheater (SH1&2)

	Wall (556W)	Middle (556M)	End 1 (556E)	End 2 (556E)	SH1	SH2
Cl	12.72	19.98	18.65	23.26	11.10	5.45
S	6.00	6.50	6.10	7.10	2.60	7.57
Zn	0.51	0.76	0.81	0.66	1.09	2.02
K	4.92	8.70	8.45	11.4	3.31	8.19
Na	4.34	6.48	6.30	8.60	2.27	6.05
Ca	20.10	16.50	16.80	13.80	2.85	9.80
Al	1.80	1.40	1.60	1.00	0.36	1.29
Fe	0.64	0.52	0.59	0.33	23.50	4.32

Note: n.m. is 'not measured', n.detect is 'can not be detected (lower than detectable level)'

Table 3 Average corrosion rates of alloy rings from sampling probe No.2

Alloy Rings	Average Corroded Length		Corrosion Rate
		(μm)	(mm/yr)
59 - E	Front	104.43	1.13
	Rear	59.17	0.64
556 - E	Front	123.86	1.34
	Rear	240.69	2.60
625 - E	Front	69.38	0.75
	Rear	67.87	0.73

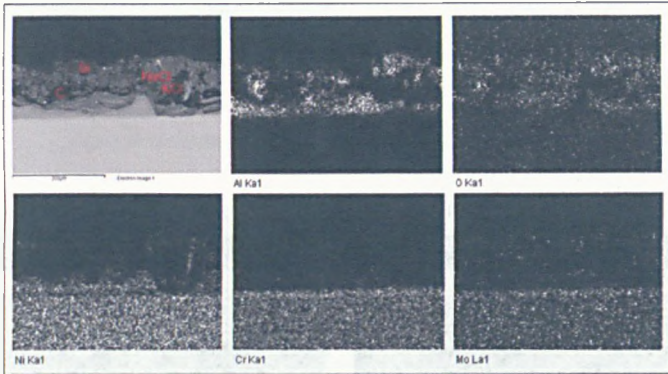


Figure 7 Elemental mapping of coated alloy 59 and its corrosion products: End/Top

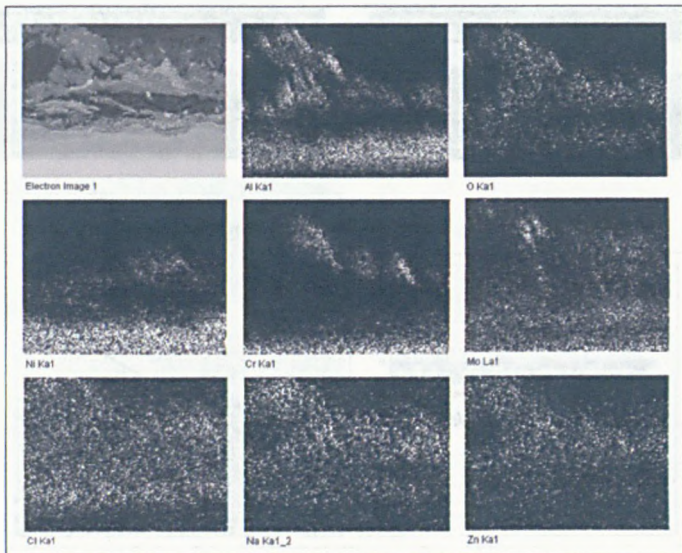


Figure 8 Elemental mapping of coated alloy 59 and its corrosion products: Wall/Top

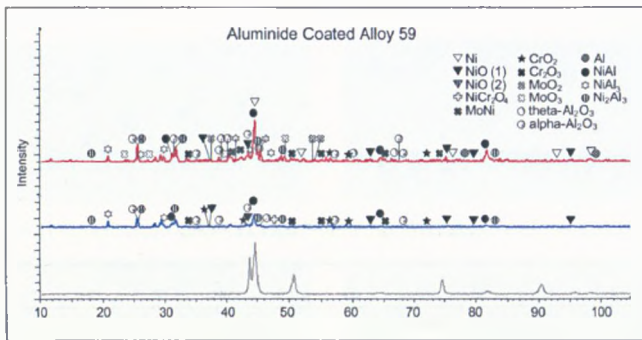


Figure 9 XRD analysis of aluminized coated alloy 59

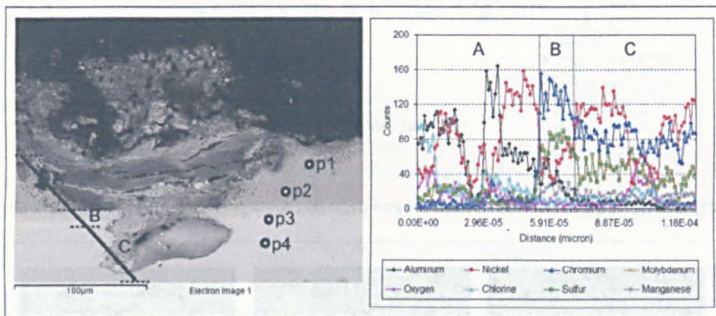


Figure 10 Results of line scan and point scanning for coated alloy 59: End/Top

Table 4 Elemental composition results of corrosion products of coated alloy 59: End/Top

Element	Atomic%				Weight%			
	P1	P2	P3	P4	P1	P2	P3	P4
C	45.31	53.26	49.61	47.53	18.83	23.83	16.37	16.18
Al	28.54	22.25	2.08	-	26.65	22.37	1.54	-
Ni	20.03	22.91	21.02	29.74	40.69	50.11	33.90	49.48
Cr	3.95	1.20	19.16	13.09	7.11	2.32	27.37	19.29
Fe	0.33	-	0.57	0.54	0.64	-	0.87	0.86
Mo	1.83	0.38	7.57	4.45	6.09	1.37	19.95	12.09
O				4.65				2.11

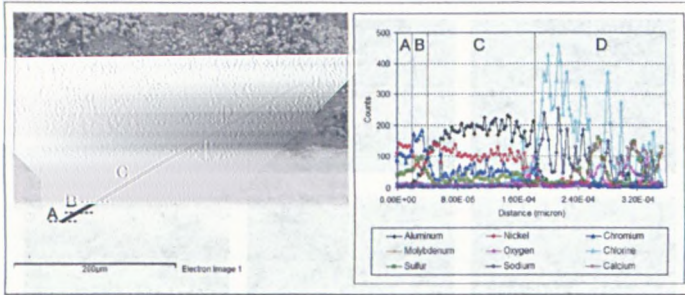


Figure 11 Line scan results of coated alloy 59: Wall/Top

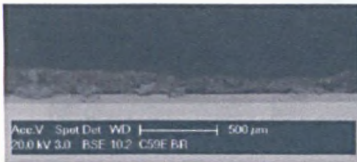


Figure 12 Coated alloy 59: End/Bottom

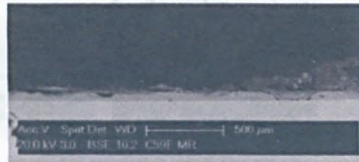


Figure 13 Coated alloy 59: End/Middle

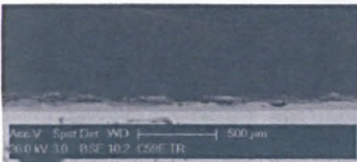


Figure 14 Coated alloy 59: End/Top

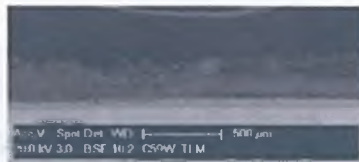


Figure 15 Coated alloy 59: Wall/Top

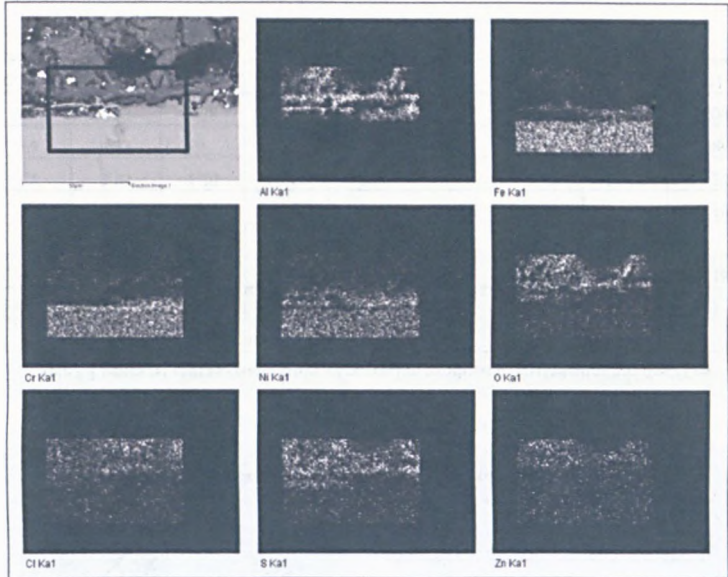


Figure 16 Elemental mapping of coated steel310 and its corrosion products: SP2 – Wall/Middle

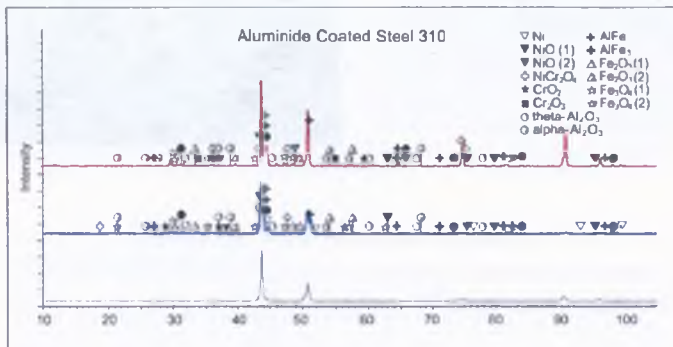


Figure 17 XRD analysis of Coated 310

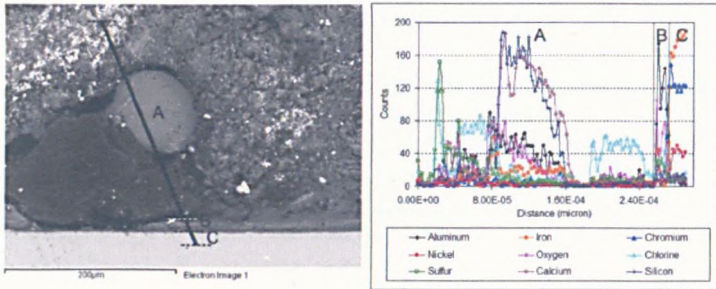


Figure 18 Line scan results of coated steel 310: SP2 – Wall/Middle (1)

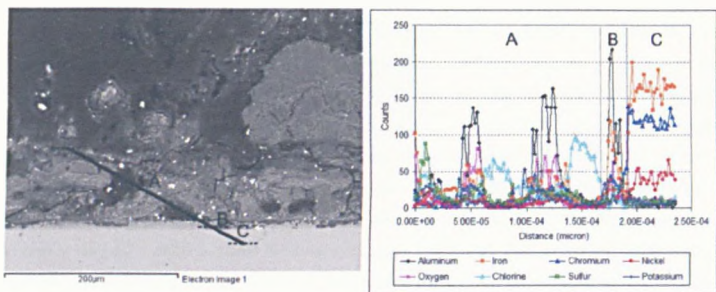


Figure 19 Line scan results of coated steel 310: SP2 – Wall/Middle (2)

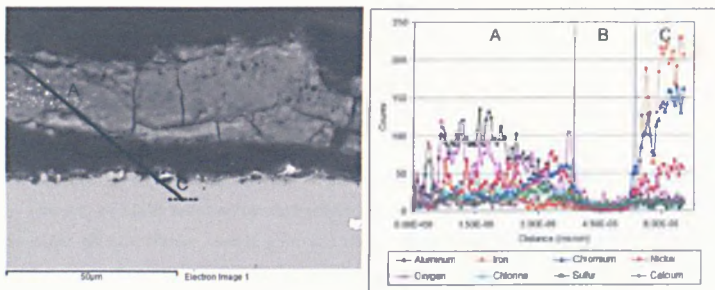


Figure 20 Line scan results of coated steel 310: SP2 – End/Middle



Figure 21 Coated steel 310: End/Middle

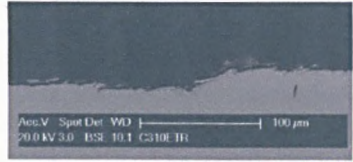


Figure 22 Coated steel 310: End/Bottom

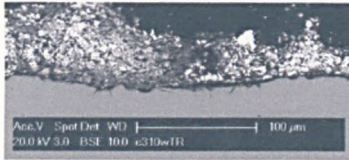


Figure 23 Coated steel 310: Wall/Top

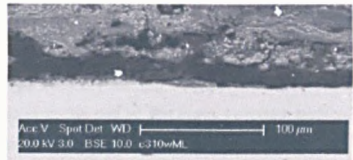


Figure 24 Coated steel 310: Wall/Middle

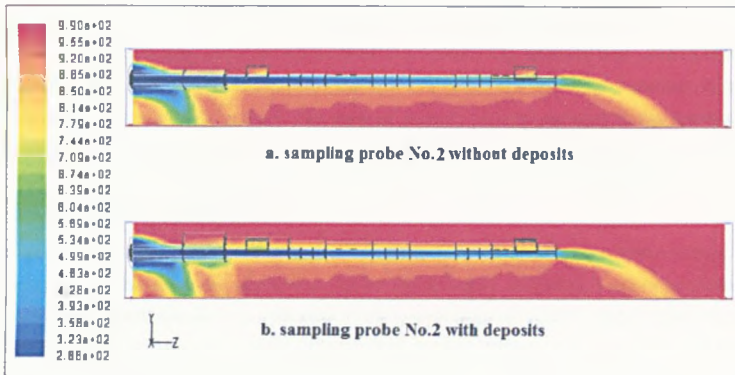


Figure 25 Contour of temperature (K) of the model 'sampling probe No.2'

CHARACTERISATION OF ASHES AND DEPOSITS FROM MUNICIPAL WASTE INCINERATION

Awassada Phongphiphat, Changkook Ryu, David Poole, Vida N Sharifi and Jim Swithenbank

Sheffield University Waste Incineration Centre (SUWIC)

Department of Chemical and Process Engineering, The University of Sheffield.

*Corresponding author. Tel: +44-114-222-7523, Fax: +44-114-222-7501,

E-mail: c.ryu@sheffield.ac.uk

ABSTRACT

Waste incineration process produces ashes through several pathways such as bottom ash, heat exchanger deposits and fly ashes. These ash particles are of various sizes and composition, and contain toxic organic inorganic compounds as well as some valuable metals for recovery. In this study, five ash samples collected from a large-scale municipal waste incinerator were characterised for particle size, surface morphology, unburned carbon and elemental composition. The samples consisted of bottom ash, superheater deposit, heat exchanger and fabric filter ashes. The bottom ash not only contained most of non- or less volatile metals, but also significant fractions of some volatile metals such as Pb and Zn. The superheater deposit was comprised of agglomerates of spherical particles sized from 10 μm to 60 μm and fine fly ashes with high concentrations of S and Zn. The concentrations of alkali metals in the superheater deposit were much higher than in the bottom ash but similar to those for heat exchanger ashes. Two heat exchanger ashes had similar particle sizes and elemental composition. However, many large particles in the economiser ash were in a thin plate form. The fabric filter ash consisted of a huge amount of particles less than 300 μm highly enriched with volatile metals and dioxins. Mass balance of the elements in the ashes was calculated using the experimental data. For Cd, 85% of the total amount was found in the fly ash.

Key words: bottom ash, fly ash, incineration, municipal waste, superheater deposit, metal partitioning

1. INTRODUCTION

Sustainable management for municipal solid waste (MSW) requires a hierarchy of reduction, reuse, recycling and energy recovery of MSW followed by environmentally sound disposal of the residues. MSW consists of putrescible, paper, plastics, textiles, metals, glass and other miscellaneous materials. After recovering valuable recyclables by segregation, the waste can be processed by thermo-chemical treatments with or without mechanical/biological treatments. Among many technologies available for energy recovery, mass burn incineration is well established in industry. It has typically about 25% of efficiency for electricity generation only, which is significantly lower than for a coal fired power plant (35%). However, more than two thirds of carbon in MSW is greenhouse gas neutral, and incineration with combined heat and power production has much higher overall energy efficiency as incineration plants are usually in the vicinity of large cities. The gas

cleaning process controls the release of various organic/inorganic pollutants well below the tightened emission regulation limits by the EU Waste Incineration Directive (2000/76/EC). PCDD/Fs have been the main focus of public concern for a few decades, but recent figures show that modern incinerators are no longer a significant source of dioxins (DEFRA, 2004; BMU, 2005). However, the release of submicron particulates escaped the air pollution control (APC) devices recently gained a significant environmental concern, which is common for most combustion sources using fossil fuels (Morawska and Zhang, 2002; Zhang and Morawska, 2002). They can be highly enriched with heavy metals and inhalable deep into a lung. This brings attention to the behaviour of trace metals associated with various ashes/particles generated from incineration, which is the subject of this paper.

The ashes from mass burn incineration are discharged through several pathways (Wiles, 1996). Most of the ashes (typically 80-90% by weight) are bottom ash discharged at the end of the grate. A minor portion of particles in the waste bed drops through the gaps between the grate plates as grate siftings, which are usually combined with bottom ash for disposal. Ferrous metals can be recovered from bottom ash and the rest can be used as feedstock for construction and other industry (Wiles, 1996; Maria et al., 2001; Ferreira et al., 2003).

The generation of fly ash from fossil fuels and biomass is well understood (Couch, 1994; Linak and Wendt, 1993; Jöller et al., 2005). The particles in the flue gas are generated by two mechanisms during combustion: a) entrainment of large particles into the gas flow and b) vaporisation of volatile trace elements. The former contributes to particles generally over $1\ \mu\text{m}$ and the latter to submicron. The entrained large particles contain the elements which do not vaporise and compose the matrix of the fly ash, but are also enriched on their surfaces by deposition of volatile material. The elements partially or fully vaporised during combustion undergo transformation and partitioning at the downstream as the flue gas cools down by heat recovery and gas cleaning. The conversion of these elements into the solid phase involves adsorption, condensation, coagulation and chemical transformation.

Some larger particles are transported to and held on the cold surfaces of heat exchangers before entering the gas cleaning process. The deposition mechanisms involve inertial impact, condensation and thermophoresis. The deposition is initiated typically by condensation of alkali metal compounds which creates a sticky surface for fly ash particles to accumulate on. Such deposits reduce the heat transfer to the water-steam and cause operational problems such as corrosion and formation of large clinkers.

Fly ash from combustion sources such as coal power plant (Davison et al., 1974; Anh and Lee, 2006), iron ore sinter plant (Ahn and Lee, 2006) and biomass plant (Obernberger and Brunner, 2005) are bimodal with a peak at sub-micron range ($0.1\text{-}1\ \mu\text{m}$). The air pollution control (APC) devices such as electrostatic precipitator and fabric filter are used in order to remove particles in the flue gas, in combination with injection of activated carbons and lime for adsorption of heavy metals and organic pollutants including dioxins. Although the APC devices have over 99% particle removal efficiencies by mass, they are least efficient for capturing submicron particles.

MSW differs from coal or pure biomass such as wood and straw mainly by great inhomogeneity in composition and sizes, high ash content (~25%) and high Cl content (~1%). Incineration directly burns large waste particles with excess air of typically 50-80%, which results in lower flame temperatures than for coal and biomass. The behaviour of particulates and trace elements in incineration has been studied for various

aspects, as compiled in the book by IAWG (1997). Other studies investigated the sources and partitioning of elements (Law and Gordon, 1979; Nakamura et al., 1996; Reimann, 1989; Jung et al., 2004) and enrichment of volatile elements on fine particles (Wadge et al., 1986; Chang et al., 2000). The above studies presented that lithophilic elements such as Fe, Cu, Cr and Al remain mainly in bottom ash (over 90% by weight) while enrichment of volatile elements in fly ash varies depending on their volatility. It also significantly varies for feed waste and plant process. Typically over 80% of Cd by weight is found in the fly ash while about 50% for Pb and Zn.

This paper presents the characterisation results for the bottom ash, superheater deposit and fly ashes taken from five locations in a large-scale municipal waste incinerator. The samples were analysed for the particle size distribution, unburned carbon, elemental composition and surface morphology.

2. INCINERATION PLANT AND ASH SAMPLES

2.1 Collection of ash samples

The ash samples were taken from a commercial mass burn incinerator shown in Figure 1. The waste fed by ram feeders undergoes combustion on the grate with the primary air supplied through the grate. The secondary air is injected in the form of strong jets at each side wall above the bed in order to supply turbulent mixing and additional oxygen to the combustion gas. The combustion gas passes through a pendant superheater, multi-tubular heat exchanger and economiser for energy recovery. Then, the gas enters the fabric filters with sorbents which are hydrated lime for acidic gases and activated carbon for dioxins and heavy metals. The amounts of lime and activated carbon injection are about 9 kg/ton-waste and 0.2 kg/ton-waste, respectively.

The bottom ash discharged from the grate passes through a magnetic separator to recover ferrous metals. The ash is then transported used as a capping material on landfill sites, or as an aggregate substitute for maintenance of roads. The amount of total residue is 322 kg/ton-waste. Bottom ash is about 85% of the total residues, of which 7.8% is recovered as ferrous metals (equivalent to 6.2% of the total residues).

The ashes and heat exchanger deposits used in this study were originally sampled for dioxin studies (Gan et al., 2003). They were collected four times spanning a period of six months from 5 different locations of the plant as numbered in Figure 1; (1) bottom ash, (2) deposits from superheater (SH), (3) fly ash from the convective heat exchanger (HE), (4) fly ash from the economiser (EC) and (5) fly ash from the fabric filters (FF). Approximately 1 to 5kg of each residue was sampled each time. The bottom and fly ashes represented particles generated for about an hour during each sampling while the SH deposit was accumulated for several weeks to months.

2.2 Combustion and emission characteristics of the plant

Several studies on combustion and pollutants emission have been carried out at this plant by SUWIC team; (a) the measurement of waste combustion using a novel instrumentation technique (Goodfellow, 2003; Ryu et al., 2004), (b) computational fluid dynamics (CFD) modelling on the waste combustion and gas flow (Ryu et al., 2004), (c) transient behaviour of waste combustion (Yang et al., 2005), (d) PCDD/Fs measurement and modelling (Gan et al., 2003), (e) continuous emission monitoring (CEM) of heavy metals before and after the fabric filters (Clarkson et al., 2003; Poole et al., 2005a, 2005b). These studies have provided in-depth

understanding of the waste combustion and micro-pollutants emission such as the particulates and trace elements.

The waste undergoes combustion on the grate for about 60-80 minutes at temperatures between 1000-1200°C (Ryu et al., 2004). The temperature and oxygen acquired directly from the bed using a novel measuring technique have very large fluctuations (over 800°C of temperature and over 10% dry of oxygen) during combustion due to the inhomogeneous waste particles, solid particle mixing and channelling of air through waste particles. The waste combustion is controlled by a simple on-off control of the ram feeders in order to keep the gas temperature at the radiation shaft at 850-1000°C. As the primary air supply keeps constant, the oxygen concentration in the combustion chamber fluctuates correspondingly between 6 to 14% dry. Due to the furnace geometry and secondary air injection, the gas flow field has a high velocity (7-12m/s) stream at over 1000°C developed from above the bed to the exit of the radiation shaft and thus is likely to carry a large amount of particles to the heat exchangers (Ryu et al., 2004). The residence time for the high velocity gas in the combustion chamber was about 2.5 seconds.

The gas temperature at the superheater inlet is about 650°C and drops to 310°C at the boiler exit. The temperatures at the economiser exit and at the fabric filter exit are about 135°C and 120°C, respectively.

The heavy metals in the flue gas at the entry to the fabric filter were measured continuously for several hours at a time for a period of several days in this incinerator, using SUWIC's unique CEM device with ICP-OES (Poole et al., 2005a, 2005b). The behaviour of metals in the flue gas were categorised into three types based on the temporal variation of the metal concentration and combustion conditions. Volatile bulk metals such as Na and K, which are present in most feed waste, have concentration variation in the flue gas largely due to changes in the combustion conditions. Volatile bulk metals with uneven distribution in the waste (often found in bulky wastes) such as Pb and Zn, which are present in high concentration, show more overall temporal variation than the more evenly distributed metals. Volatile trace metals such as Cd and Hg which are present only occasionally in the feed lead to occasional random peaks in an otherwise near-zero concentration profile.

Further continuous measurements were made for periods of several days in the flue gas emitted to atmosphere following clean-up (Clarkson, 2003; Poole, 2005b). These results did not show significant concentration or variation for any of the volatile metals of interest, with all monitored metals being below emissions limits, demonstrating the efficiency of the clean-up system in removing almost all metal contamination from the flue gases before release.

Gan et al. (2003) measured the PCDD/Fs concentration in the ashes and SH deposits for this plant and developed a mathematical model for PCDD/Fs concentrations by predicting their formation through the De-Novo synthesis mechanism in the heat recovery unit and removal by the fabric filter.

3. ANALYSIS METHOD

As the particle size varied widely from submicrons to a few centimetres, the samples were first sieved from 212µm to 4750µm with 19 size ranges. The amount of sample used for the sieving was 737g for the bottom ash and about 200g for the rest of ash samples. Mass loss during the sieving tests was less than 1% of the initial mass. Particles smaller than 850µm were analysed by a Malvern instrument (model: Mastersizer S).

This instrument uses low angle laser light scattering by particles detected by a number of photosensitive silicon detectors. It provides two models of analysis method: polydisperse range model (0.5-850 μm) and compressed range model (0.5-212 μm with better accuracy). The results with the polydisperse range model had a good agreement with those combined from sieving tests for 212-850 μm range and the compressed range model.

The analysis for morphology and mineralogy by using SEM (Scanning Electron Microscopy) and EDS (Energy Dispersive X-ray Spectrometer) was carried out at Sorby Centre, Sheffield University. The work was divided into 2 parts. Initially, the samples were coated with gold and analyzed by a Camscan Mark II – Link system SEM. Subsequently, the samples were mounted in epoxy resin, and then the cross-sections were diamond-polished and coated with carbon for SEM-EDS using attached a Link Analytical EXL energy dispersive spectrometer. It detects elements heavier than Na with a detection limit of approximately 0.1%.

The carbon content in ash was analysed according to British Standard 1016 Part 6 in which a sample is burned with pure oxygen at 1350°C and CO₂ released is captured by soda asbestos.

Elemental analysis was carried out by using a Spectro Genesis ICP (Inductively coupled plasma) spectrometer. The acid solvent used in digestion was a mixture of HNO₃ and HCl at the ratio of 3:1.

4. RESULTS AND DISCUSSION

4.1 Particle Size Distribution (PSD)

Figure 2 shows the accumulative PSD for the ash samples. The bottom ash was a heterogeneous mixture coarse black dust and larger slag solids. More than 57.0% of the bottom ash was larger than 4750 μm (4.7mm). When compared to data from Spanish incinerators reported in literature (Maria et al, 2001), the bottom ash in this study had less contribution of fine particles. However, the PSD varies between plants depending on the MSW feed composition, particle mixing by moving grates and subsequent treatment of bottom ash. Also, representative sampling of bottom ash is also notoriously difficult (IAWG, 1997)

The SH deposit was yellowish brown in colour and due to their hard nature, moderate physical force was required to break them down. It should be noted that that it was originally a large agglomerate on the SH surface, but the current sample consisted of agglomerated particles and disintegrated fragments. The vibration during sieving might have further broken up the particles. However, the results showed that pieces larger than 4750 μm accounted for 31.1%. Figure 3 shows the results from the Malvern instrument for particles less than 850 μm in the SH deposit and other fly ashes. It suggests that the SH deposit contains much more of fine particles than the HE and EC ashes. This is related to the mechanism of deposit formation: the sticky surface of the deposit can trap fine particles better due to their large surface area to mass ratio.

The HE and EC ashes consisted mainly of coarse (50-1000 μm) fly ash entrained in the flue gas. Although the HE ash was much darker than the EC ash, both samples had over 90% of the particles smaller than 850 μm (Figure 2) and a peak at around 500 μm (Figure 3). The volume-averaged diameters of the two ashes were 344.1 and 366.1 μm , respectively. The difference in particle shape will be discussed later with the SEM images.

The FF ash was the combined material of fly ash and injected sorbents, having light grey grains. All the particles were smaller than 350 μm . The volume-averaged particle size was 75.0 μm . The PSD of FF ash in Figure 3 shows that it is trimodal, with peaks at 120 μm , 12 μm and a tiny peak at 1 μm . Although the peak at 120 μm is for coarse fly ash, hydrated lime accounting 19% of FF ash by weight contributed to this peak. The grain size of commercial hydrated lime is less than 125 μm . The grain size of commercial activated carbon is typically less than 45 μm , but the weight fraction of activated carbon in fly ash was less than 0.5%. The peak at 12 μm is for coagulated fine particles. The volume fraction at the last peak was 0.38%. However, in terms of particle number fraction, 82% of FF ash was submicron. This was common for other ash samples analysed by the Malvern instrument (78% for the bottom ash, about 80% for the rest). The PM10 content for the samples was 3.3% by volume for the HE ash, 2.4% for the EC ash and 22.1% for the FF ash.

4.2 Elemental composition

Table 1 lists the unburned carbon content (average of three tests), dioxin concentration and trace element concentrations (average of two tests) in the ash samples. The unburned carbon content in the bottom ash was 3.95% which evidenced good combustion efficiency. Its value for the SH deposit, HE and EC ashes were all around 2%. The carbon content increased to 4.45% in the FF ash mainly due to the activated carbon injection and organic micropollutants adsorbed.

The bulk inorganic elements in the ash samples were Fe, Ca, Al as well as Si which was not analysed here. The concentrations of Mg, Na, K, S, P, Ti and Zn were also significant (over 2000ppm).

The comparison of elemental composition between the ash samples shows two distinct behaviours of trace elements depending on their volatilities. Non- and less volatile elements such as Ca, Al, Mg, Ti, Ni and Cr were equally distributed in the bottom ash and in the rest of the ashes as they were transported by entrainment of particles into the gas flow from the waste bed. Considering that the bottom ash is about 85% of the total ash, most of these non- or less volatile elements remained in the bottom ash. In case of Fe which is also non-volatile, the concentration in the bottom ash was significantly higher than in the fly ashes. It suggests that certain waste materials made of steel are not bound to the organic compounds but present separately. Cu also showed similar behaviour to Fe but it has an evaporation route by CuCl_2 (boiling point 993 $^\circ\text{C}$) which acts as catalysts for De Novo synthesis of PCDD/Fs (AIWG, 1997). Ca became the most abundant element in the residues except the bottom ash. Its concentration in the FF ash further increased to over 24% due to lime injection.

All the volatile elements were enriched in the FF ash but their behaviour in the other ashes were different. Sb and Cd were significantly enriched only in the FF ash and depleted in the rest of the samples. However, most other volatile elements still had a significant concentration in the bottom ash. Alkali metals (Na and K) were enriched in all the ash samples except for the bottom ash. Their compounds including KOH and chlorides vaporise in the waste bed and stay in the gas phase in the superheater region. These may condense on the cooler superheater surfaces and thus enhance deposition of other fly ash particles. S and Zn were also enriched in the SH deposit, although the weight fraction of the SH deposit in the total ash was negligible. The concentration of S increased by several times in the SH deposits. This is presumably due to sorption of SO_2 and condensation of volatilised species as metal sulphates during the prolonged exposure of the deposit to the

combustion gas. Sulphates condense at relatively high temperatures compared with chlorides, and are predicted to become more thermodynamically favoured as temperature decreases (Linak and Wendt, 1993; Poole et al., 2005b). It also suggests that the elemental composition of the deposits in the superheater and heat exchangers will vary depending on the gas temperature.

Overall, the two fly ashes from HE and EC have similar composition to the bottom ash except for alkali metals enriched and Fe and Cu depleted. The SH deposit has several times higher concentrations of S and Zn but similar levels of alkali metals to the HE and EC ashes. The FF ash was enriched with volatile metals such as Pb, Cd, K, Zn and Sb. Hg which is the most volatile element appeared only in the fly ash at a very low concentration (1.05 ppm). During the continuous monitoring of trace metals in the flue gas in this plant, Hg was observed occasionally in the pre-cleanup gas but not in the emitted gas (Clarkson et al., 2003; Poole et al., 2005a, 2005b). PCDD/Fs also increased significantly in the FF ash by adsorption to activated carbon and fine particles (Gan et al., 2003).

Table 2 summarises the amount and weight fraction of each element in bottom and FF ashes for 1 ton of input waste. The partitioning of elements was calculated from the weight fraction of bottom ash (85.3%) and FF ash (14.7%) in the total ignoring the contribution of the other ashes. Data for flue gas acquired from the UK pollution inventory was also listed in Table 2. The mass fraction of volatile metals for FF ash ranged from 25–85%. Cd has the highest mass fraction (85%) appeared for FF ash. The partitioning for most elements is in the same range as reported in Jung et al's study (2004). However, Pb in the FF ash (26%) was slightly lower than in the above study (32-57%). This is attributable to the difference in the MSW feed composition and operating conditions. The fraction of K and S in FF ash in our study was about 45%. The amount of Fe in the bottom ash per 1 ton of waste was 28.6kg of which a large proportion can be recovered by magnetic separation. The amount of ferrous metals the plant recovered was 19.9kg per ton of waste.

4.3 Morphology and Mineralogy of Ash Samples

Figure 4 shows the SEM images of the SH deposit. It was agglomerates of irregular-shaped fly ashes and spherical or polygon particles as shown in Figure 4a, unlike coal fly ash which is mainly composed of spherical particles (Saikia et al., 2006; Ahn and Lee, 2006). This is due to the variable components of MSW, greater ash entrainment, and also the low operating temperature of incineration. The spherical particles were clearly identified in Figure 4b. Their particle size ranged typically from 10 to 60µm. The spherical particles that are formed under the high temperatures appear as smooth spheres of molten material, while those formed under the lower temperatures have irregular shapes (Jiménez and Ballester, 2005). The surface of those particles (Figure 4c) was sintered agglomerates of about 1µm sized polygon particles.

Figure 5 shows the SEM-EDS results for SH deposit. Figure 5a is for the cross-section of a large spherical particle (diameter of 200µm). Partially fused particles enclosed other particles and voids inside while transforming into a sphere due to surface tension. However, the EDS spectra were very similar between the surface and the inner, having Ca and Si as major elements. K, Cl, S, Al, Fe, Cr, Mg, P, Ti and Zn were also found at all points. Figure 5b is for typical spheres and irregular shaped particles. Small spheres had a smooth cross-section due to complete fusion. All the elements appeared in Figure 5a were also found but the major elements varied between points. Ca-Si-Al and Si-K-Al appeared to be the main combination of the particles.

Ca-S were main elements at some points which was expected to be mainly CaSO_4 . In Figure 5, no clear difference was found between the surface and the inner of spherical particles.

Figures 6 and 7 shows the SEM images of HE and EC ashes. A variety of particles sized from over $300\mu\text{m}$ to submicron can be seen in both ashes. Although their PSD were similar, the EC ash contained more particles in form of plates. As the drag force on such particles is higher than on round particles, they can be carried over much further. Spherical particles appeared in SH deposit were also found but covered with fine particles. The SEM-EDS results for the EC ash shown in Figure 8 had very simple elemental composition, compared to the SH deposit. The main combinations of elements in large ash particles were Ca-Si-Al and Si-K-Al.

The FF ash contained much less large particles over $100\mu\text{m}$ and a large amount of smaller particles in irregular porous shapes, shown in Figure 9a. Several spherical particles sized around $50\mu\text{m}$ were also identified, of which some are lime particles. Figure 9b is for some fly ash particles which clearly shows the agglomeration of finer particles. Figure 10 shows lime particles adsorbed Cl (at Points 1 and 3) from SEM-EDS. Lime contains a few percent of impurities such as Al_2O_3 , Fe_2O_4 and MgO (Fernández et al., 1997) which were detected together as trace. Point 2 is on a typical large ash particle.

5. CONCLUSIONS

Five ash samples from different locations of a MSWI process were characterised for unburned carbon content, particle size, surface morphology and elemental composition. While volatile metals were depleted in the bottom ash by temperatures of $1000\text{-}1200^\circ\text{C}$ during combustion, Fe and Cu were enriched in the bottom ash due to the incombustible materials not bound to the combustible. The other non-volatile elements were distributed equally in all the samples.

The SH deposit consisted of fly ash trapped and spherical particles due to surface tension of partially fused materials by hot gas. The elemental composition of SH deposit was similar to the HE and EC ashes except highly enriched S and some volatile metals such as Zn.

The fly ashes from the HE, EC and FF consisted of two different types of particle: large spherical, polygon or plate shaped particles and a huge number of fine particles. Although the PSD was similar to the HE ash with a volume mean diameter of about $350\mu\text{m}$, the EC ash contained large particles of a thin plate form. These two ashes had increased concentrations of alkali metals.

The FF ash particles were smaller than $300\mu\text{m}$ with volume-averaged size of $75\mu\text{m}$. However, 82% of particle number fraction was in submicron range. The volatile elements were found at significant concentrations in the FF ash, such as Cd with 85% of the total amount. Over 50% of Sb and As were found in the FF ash. The weight fraction of Pb and Zn in their totals was not significant in contrary to their high volatility, which agreed reasonably well with the findings from other studies.

6. ACKNOWLEDGEMENT

This study was funded by UK EPSRC (Engineering and Physical Sciences Research Council) and the Royal Thai Government. The authors would like to thank the operators of the waste incineration plant for their support and collaboration.

7. REFERENCES

- Ahn, Y.C., Lee, J.K., 2006. Physical, chemical, and electrical analysis of aerosol particles generated from industrial plants. *Journal of Aerosol Science* 37, 187-202.
- BMU (Federal Ministry for the Environment, Nature Conservation and Nuclear Safety), Waste incineration- a potential danger?, BMU, 2005, Germany. available at http://www.bmu.de/files/pdfs/allgemein/application/pdf/muellverbrennung_dioxin_en.pdf
- Chang, M.B., Huang, C.K., Wu, H.T., Lin, J.J., Chang, S.H., 2001. Characteristics of heavy metals on particles with different sizes from municipal solid waste incineration, *Journal of Hazardous Materials* A79, 229-239.
- Clarkson, P.J., Poole, D.J., Ryu, C.K., Sharifi, V.N., Swithenbank, J., Waarlo, H.J., Ardel, D., Falk, H., 2003. Continuous measurement of metals in flue gas using ICP-OES. *Analytical and Bioanalytical Chemistry* 377, 39-47.
- Couch, G., 1994. Understanding slagging and fouling in PF combustion. London, UK: IEA Coal Research.
- Davison, R., Natusch, F.S., Wallace, J.R., 1974. Trace elements in fly ash - dependence of concentration on particle size. *Environmental Science and Technology* 8, 1107-1113.
- DEFRA (Department of Environment, Food and Rural Affairs), Review of environmental and health effects of waste management: Municipal solid waste and similar wastes, DEFRA, May 2004, London, UK.
- Fernández J., Renedo J., Garea A., Viguri J., Irabien J.A., 1997. Preparation and characterization of fly ash/hydrated lime sorbents for SO₂ removal, *Powder Technology* 94, 133-139.
- Ferreira, C., Ribeiro, A. Ottosen, L., 2003. Possible applications for municipal solid waste fly ash, *Journal of Hazardous Materials* 96, 201-216.
- Forestier, L.L., Libourel, G., 1998. Characterization of flue gas residues from municipal solid waste combustors. *Environmental Science and Technology* 32, 2250 - 2256.
- Gan, S., Goh, Y.R., Clarkson, P.J., Parracho, A., Nasserzadeh, V., Swithenbank, J., 2003. Formation and elimination of polychlorinated dibenzo-p-dioxins and polychlorinated dibenzofurans from municipal solid waste incinerators, *Combustion Science and Technology* 175, 103-124.
- Goodfellow, J.H., 2003. Lagrangian diagnostics in a hostile environment, PhD Thesis, Sheffield University, UK.
- IAWG (International Ash Working Group; A.J. Chandler, T.T. Eighmy, J. Hartlen, O. Hjelmar, D.S. Kosson, S.E. Sawell, H.A. van der Sloot, J. Vehlou). 1997. Municipal solid waste incinerator residues. *Studies in Environmental Science* 67, Elsevier Science, Amsterdam.
- Jiménez, S., Ballester, J., 2005. Influence of operating conditions and the role of sulfur in the formation of aerosols from biomass combustion. *Combustion and Flame* 140, 346-358.
- Jöller, M., Brunner, T. & Obernberger, I., 2005. Modeling of aerosol formation during biomass combustion in grate furnaces and comparison with measurements. *Energy and Fuels* 19, 311-323.
- Jung, C.H., Matsutoa, T., Tanakaa, N., Okadaa, T., 2004. Metal distribution in incineration residues of municipal solid waste (MSW) in Japan, *Waste Management* 24, 381-391.
- Law, S.L., Gordon, G.E., 1979. Source of metals in municipal incinerator emissions, *Environmental Science and Technology*, 13, 432-437.
- Linak, W.P., Wendt, J.O.L., 1993. Toxic metal emissions from incineration - mechanisms and control. *Progress in Energy and Combustion Science* 19, 145-185.
- Maria, I., Enric, V., Xavier, Q., Marilda, B., Angel, L., Felicia, P., 2001. Use of bottom ash from municipal solid waste incineration as a road material. *2001 International Ash Utilization Symposium*. Center for Applied Energy Research, University of Kentucky.
- Morawska, L., Zhang, J., 2002. Combustion sources of particles. 1. Health relevance and source signatures. *Chemosphere* 49, 1045.
- Nakamura K, Kinoshita S and Takatsuki, H., 1996. The origin and behavior of lead, cadmium and antimony in MSW incinerator. *Waste Management* 16, 509-517.

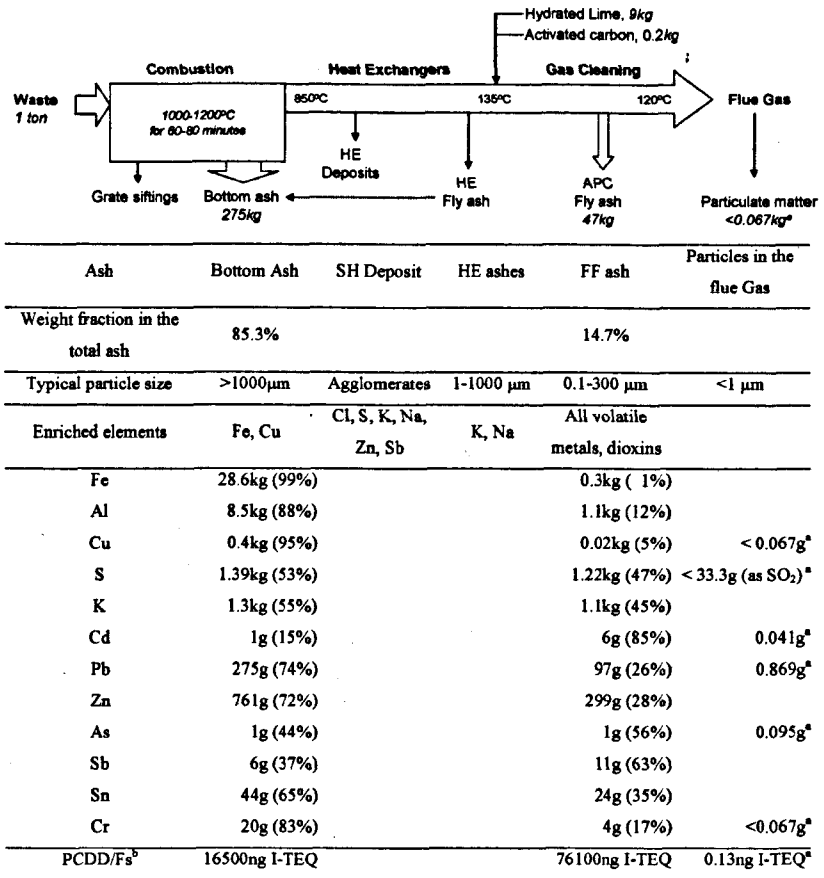
- Obernberger, I., Brunner, T., 2005. Fly ash and aerosol formation in biomass combustion processes - an introduction. In: Obernberger, I. & Brunner, T. (eds.), *Aerosol in biomass combustion: formation, characterisation, behaviour, analysis, emissions, health effects.*, Vol. 6, pp. 1 - 11. Medienfabrik Graz, Steiermarkische Landesdruckerei GmbH.
- Poole, D.J., Sharifi, V.N., Swithenbank, J., Ardelt, D., 2005a. Identification of metal concentration fluctuations in waste-to-energy plant flue gases- a novel application for ICP-OES. *Journal of Analytical Atomic Spectrometry* 20, 932-938.
- Poole, D. J., 2005b. Identification and control of metal pollutant spikes in municipal solid waste incinerators. PhD Thesis, The University of Sheffield, Sheffield, UK.
- Reimann, D.O., 1989. Heavy metals in domestic refuse and their distribution in incinerator residues. *Waste Management and Research* 7, 57-62.
- Ryu, C., Yang, Y.B., Nasserzadeh, V., Swithenbank, J., 2004. Thermal reaction modeling of a large municipal solid waste incinerator. *Combustion Science and Technology* 176, 1891-1907.
- Saikia, N., Kato, S., Kojima, T. 2006. Compositions and leaching behaviours of combustion residues. *Fuel* 85, 264-271.
- Wadge A., Hutton M., Peterson, P.J., 1986. The concentrations and particle size relationships of selected trace elements in fly ashes from U.K. coal-fired power plants and a refuse incinerator. *The Sciences of the Total Environment* 54, 13-27.
- Wiles, C.C., 1996. Municipal solid waste combustion ash: State-of-the-knowledge. *Journal of Hazardous Materials* 47, 325-344.
- Yang, Y.B., Goodfellow, J., Nasserzadeh, V., Swithenbank, J., 2005. Study on the transient process of waste fuel incineration in a full-scale moving-bed furnace. *Combustion Science and Technology* 177, 127-150.
- Zhang, J., Morawska, L., 2002. Combustion sources of particles: 2. Emission factors and measurement methods. *Chemosphere* 49, 1059-1074.

Table 1. Results of full elemental analysis of various combustion residues.

	Bottom ash	Superheater deposit	Heat exchanger ash	Economiser ash	Fabric filter ash
Unburned Carbon (%)	3.95	2.00	1.72	2.32	4.45
Dioxin (I-TEQ ng/g) ^a	0.06	0.07	0.08	0.12	1.62
<i>Elements (ppm)</i>					
Ag	2.1	5.7	6.6	3.9	28.4
Al	31000	22200	28800	40800	24000
As	3.8	25.7	7.1	3.3	27.5
Ba	639	299	704	1043	477
Ca	81320	148300	107600	102100	225000
Cd	3.7	19.8	25.6	6.25	127
Co	14.1	14.3	14.7	17.1	13.2
Cr	74.5	174	115	100	86.2
Cu	1459	713	436	1440	438
Fe	104000	8500	18800	17300	6400
K	4820	17200	17200	10420	23300
Mg	7130	9790	8680	9290	6710
Mn	753	561	689	656	468
Mo	8.1	15.2	16.2	14.0	15.9
Na	5535	14460	10330	9600	15250
Ni	73	41.7	52.5	102	41.1
P	4050	7550	5500	7000	3950
Pb	999	144	587	182	2060
S	5050	71000	7200	7900	26000
Sb	23.6	110	68.5	42.5	233
Sn	158	244	227	112	504
Sr	182.9	196.0	199.7	219.9	262
Ti	2190	2680	2430	3360	2000
Tl	< 0.1	< 0.1	< 0.1	< 0.1	1
V	51.7	41.1	57.3	83.5	59.4
Zn	2770	7850	3020	1710	6370

a: Gan et al. (2003)

Table 2. Summary of particles and metals emission per 1 ton of input waste in the incineration plant.



a: from annual emission data of the plant.

a: calculated from data presented in Gan et al's study (2003).

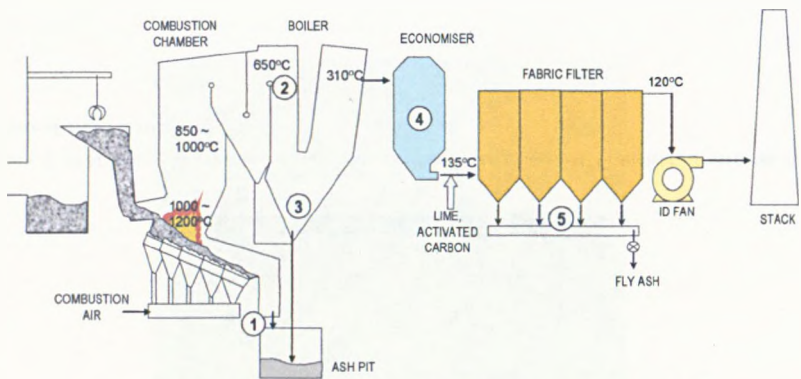


Figure 1. Incineration process and locations of five ash samples collected.

1: bottom ash, 2: superheater(SH) deposit, 3: heat exchanger (HE) ash, 4: economiser (EC) ash, 5: fabric filter (FF) ash.

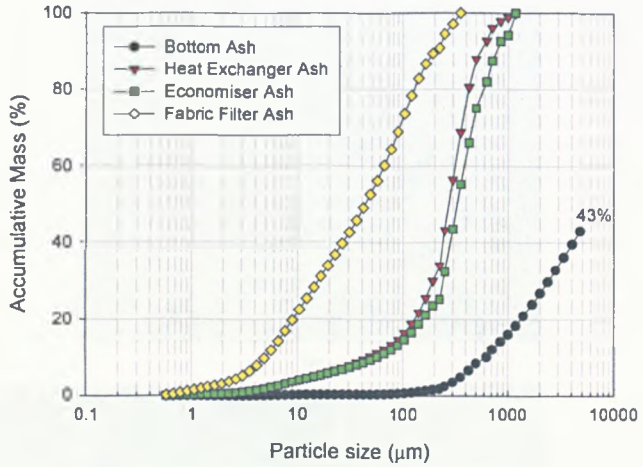
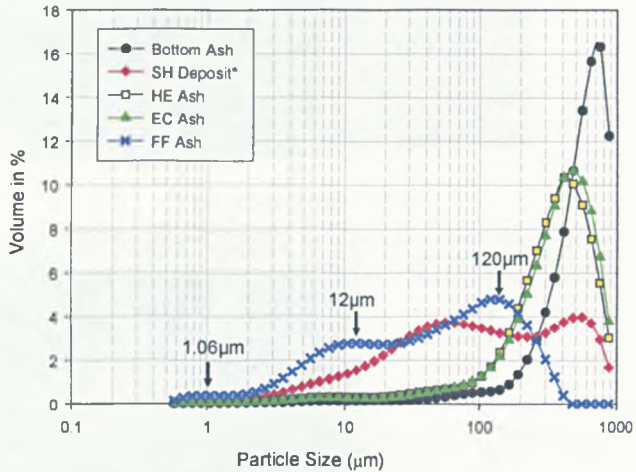
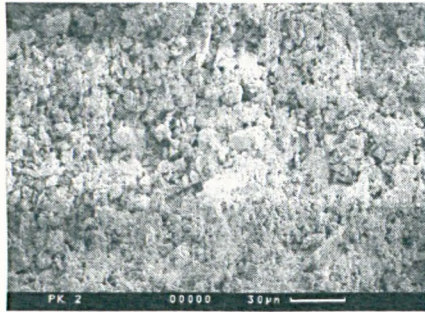


Figure 2. Accumulative particle size distribution of the ash samples.

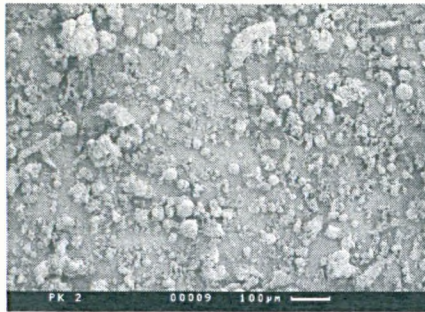


*as collected which includes fragments from large agglomerates.

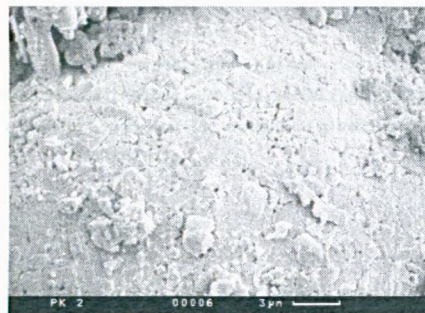
Figure 3. Size distribution for particles smaller than 850 μm.



(a)

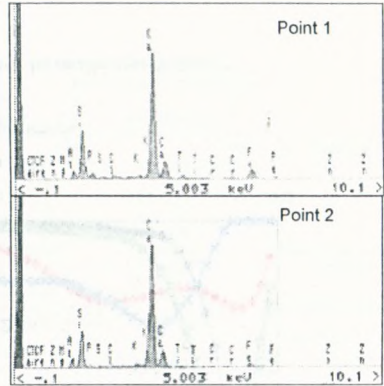
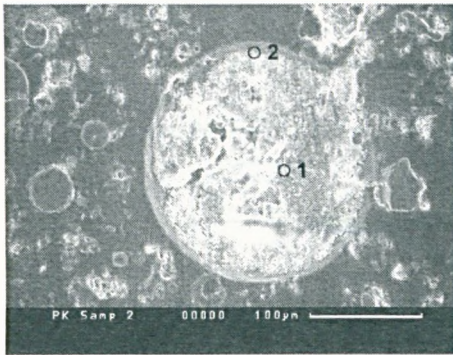


(b)

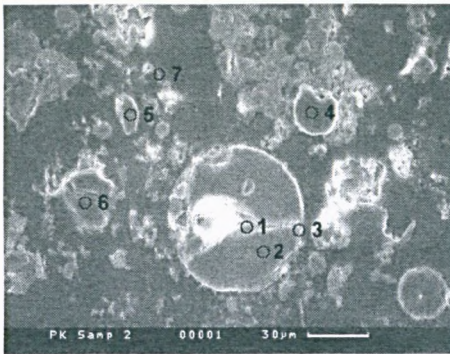


(c)

Figure 4. SEM images of superheater deposit (a: surface of large deposit, b: individual particles, c: surface of round particle)



(a)



Pt	Major elements
1	Ca, Cr, S, Ti
2	Ca, Si
3	Ca, Si
4	Si, K, Al
5	Si
6	Ca, S
7	Ca, Si, Al

Common at all points: Ca, Si, S, K, Cl, Al, Fe, Cr, Mg, P, Ti, Zn

(b)

Figure 5 SEM-EDS analysis for SH deposit.

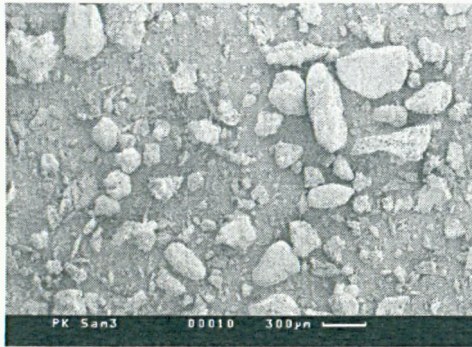


Figure 6. SEM images of HE ash.

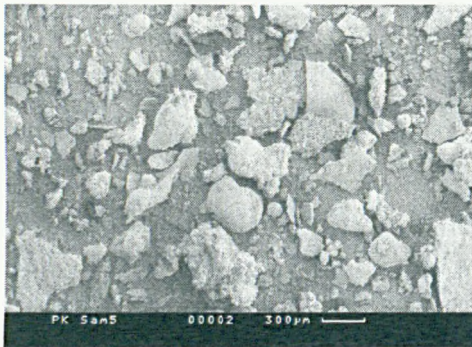
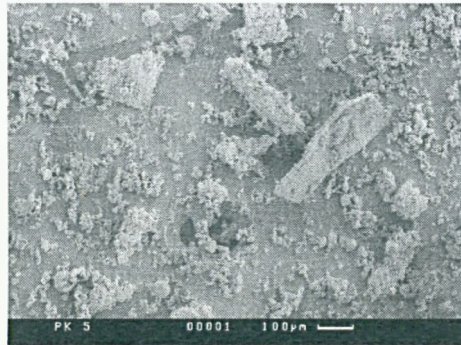


Figure 7. SEM images of EC ash.

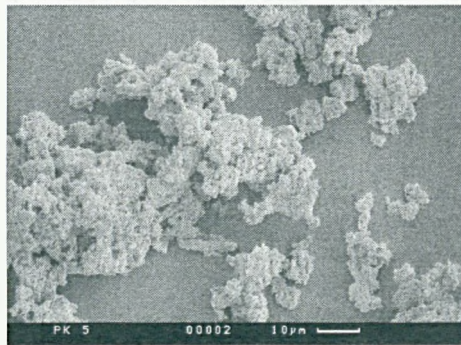


Pt	Major elements
1	Si, K, Al
2	Ca, Si, Al
3	Ca, Si, Al
4	Si, Ca, Al
5	Si, K, Al
6	Ca, Si, Al
7	Ca, Si, Al, K, Mg
8	Si

Figure 8. SEM-EDS analysis for EC ash.



(a)



(b)

Figure 9. SEM images of FF ash.



Figure 10. SEM-EDS analysis for FF ash.

Pt	Major elements
1	Cl, Ca, K, Fe, Si, Al, Mg
2	Ca, P, Si, K, Ti, Zn
3	Cl, Ca, K